Nonlinear finite element modelling of degradation and failure in folded core composite sandwich structures

A thesis accepted by the Faculty of Aerospace Engineering and Geodesy
of the Universität Stuttgart in partial fulfilment
of the requirements for the degree of
Doctor of Engineering Sciences (Dr.-Ing.)

by

Sebastian Volker Kilchert
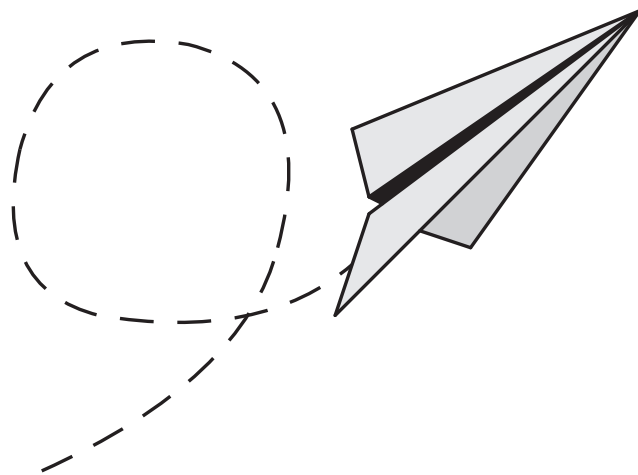
born in Berlin

Committee chair: Prof. Dr.-Ing. Heinz Voggenreiter

Committee member: Prof. Dr.-Ing. Klaus Drechsler

Date of defence: 6th of August, 2013

Institute of Aircraft Design
University of Stuttgart
2013

"Simplicity is the ultimate sophistication."

Leonardo da Vinci (1452-1519) was the first Western inventor to describe folded planes and ornithopters made of paper parchment.

Vorwort

Die vorliegende Arbeit entstand im Zeitraum von 2006 bis 2012 auf Basis meiner Tätigkeit als wissenschaftlicher Mitarbeiter am Institut für Bauweisen- und Konstruktionsforschung des Deutschen Zentrums für Luft- und Raumfahrt (DLR).

Besonderen Dank möchte ich an dieser Stelle Prof. Dr.-Ing. Heinz Voggenreiter ausprechen, der mich während der Entstehung der Arbeit fachlich und strategisch betreut hat und damit nicht nur meine wissenschaftliche, sondern auch persönliche Entwicklung gefördert hat. Weiterhin danke ich meinem Mitberichter Prof. Dr.-Ing. Klaus Drechsler für seine Zeit und Unterstützung. Für die Übernahme des Vorsitzes der Prüfungskommission danke ich Prof. Dr.-Ing. Alfred Kleusberg.

Mein größter Dank geht an meinen fachlichen Betreuer Dr. phil. Alastair F. Johnson, der mich die ganzen Jahre der Entstehung der Arbeit beraten und unterstützt hat und mich bei meiner Reise in die Welt der Wissenschaft von Anfang an begleitet hat.

Meinen Kollegen am DLR möchte ich mich für die gute Zusammenarbeit und die tolle Zeit bedanken. Durch unser freundschaftliches Miteinander habe ich mich am DLR stets zu Hause gefühlt. Namentlich danken möchte ich hier Christof Kindervater, der mich insbesondere während meines "Geisterdaseins" nach Verlassen des Instituts unterstützt hat, dem "Foldcore Competence Team" Ralf Sturm und Matthias Waimer für die Diskussionen zu allen Aspekten meiner Promotion, Sebastian Nowotny, Matthias Horn, Markus Kaden für Ihre Zeit bei Brainstorming mit Kaffee, Matthew David for polishing my English language skills, Raouf Jemmali für seine wunderbaren CT-Aufnahmen, Harald Kraft, Albert Reiter und Hussam Abu El-hija für die Hilfe bei der experimentellen Materialcharakterisierung, sowie Dr.-Ing. Nathalie Toso für die Unterstützung bei der Deckschicht-Modellierung.

In Rahmen dieser Arbeit durfte ich die Diplomarbeit von Fritz Lülf betreuen, dem ich für seine Arbeiten an der Optimierung von Faltwabengeometrien danke.

Den Partnern aus dem EU-Forschungsprojekt CELPACT danke ich für die wissenschaftliche Zusammenarbeit, für die tolle Gemeinschaft und die schönen Erfahrungen in der internationalen Forschungslandschaft. Insbesondere möchte ich an dieser Stelle Dr.-Ing. Sebastian Fischer danken für die gute, institutsübergreifende Zusammenarbeit, sowie für unsere freundschaftliche Beziehung. Dr.-Ing. Sebastian Heimbs danke ich für die vielen Denkanstöße und die kollegiale Zusammenarbeit. Des Weiteren möchte ich hier Michael Klaus von der RWTH Aachen, sowie Dr. Emmanuel Baranger und Christophe Cluzel von der LMT Cachan für die Bereitstellung Ihrer experimentellen Ergebnisse danken.

Wesentliche Teile der Arbeit entstanden im Rahmen des EU-Projektes CELPACT (2006-2009). Für diese Unterstützung danke ich der Europäischen Kommission.

Ich möchte hier auch meinen Eltern und Schwiegereltern danken, die mir immer mit Zuspruch und Ratschlägen beiseite standen. Der größte Dank gilt meiner Frau Nicole für ihren moralischen Zuspruch und Unterstützung. Ich danke ihr auch für die vielen Wochenenden und Urlaubstage, die ich statt mit ihr und unseren Kindern zur Fertigstellung der Promotion an den Instituten verbracht habe.

Freiburg im Breisgau, August 2013

Sebastian Kilchert

Contents

Abbreviations

2D	Two-dimensional
3D	Three-dimensional
APDL	ANSYS parameter design language
BEM	Boundary element method
BT	Belytschko-Tsay formulation
BWC	Belytschko-Wong-Chiang formulation
CCT	Cylinder collapse test
CDM	Continuum damage mechanics
CELPACT	Cellular Structures for Impact Performance
CFL	Courant-Friedrichs-Lewy condition
CFRP	Carbon fibre reinforced polymer
CT	Computed tomography
CV	Coefficient of variation
DELIGHT	Developing Lightweight Modules for Transport Systems
DOF	Degree of freedom
EET	Element elimination technique
EMIR	Engineering mehrfunktionaler Integralstrukturen CFK-Rumpf
FCT	Foldcore compression test
FDM	Finite difference method
FEM	Finite element method
FST	Foldcore shear test
FVM	Finite volume method
GFRP	Glass fibre reinforced polymer

HT	Hughes-Tezduyar formulation
IFB	Institute of Aircraft Design (Universität Stuttgart)
ILB	Department of Aerospace and Lightweight Structures (RWTH)
MCI	Microsopic cut-image
PMI	Polymethacrylimide
PVC	Polyvinyl chloride
RWTH	RWTH Aachen University
SAN	Styrene-acrylonitrile
SANDCORE	Coordination Action on Advanced Sandwich Structures in the Transportation Industry
TCT	Tensile coupon test
UD	Uni-directional

Kurzfassung

In den letzten Jahrzehnten haben Faserverbund-Bauweisen im Flugzeugbau weite Verbreitung gefunden. Dabei sind vor allem Sekundärstrukturen aus Faserverbund realisiert worden. Neuerdings ist die Anwendung von Faserverbund-Bauweisen in Primärstrukturen wie z.B. Flugzeugrümpfen immer weiter in den Vordergrund gerückt. Eine vielversprechende Bauweise für Primärstukturen sind Sandwichstrukturen mit Wabenkern und Deckschichten aus Faserverbund. Diese zeichnen sich durch hohe spezifische Steifigkeit und Festigkeit aus, sind aber aufgrund ihrer vergleichsweise dünnen Deckschichten anfällig auf Impaktbelastungen. Eine effiziente Auslegung auf Impakt ist daher ein kritischer Aspekt des Sandwichdesigns. Aufgrund des hohen Aufwands einer experimentellen Charakterisierung des Impaktsverhaltens besteht ein zunehmend großes Interesse den Umfang der experimentellen Testreihen durch den Einsatz von numerischen Methoden zu reduzieren. Eine Voraussetzung dafür ist die Bereitstellung leistungsstarker Simulationsmethoden für die Modellierung des komplexen Materialverhaltens bei Schädigung und Versagens der Sandwichstruktur.

In diesem Kontext untersucht die vorliegende Arbeit die numerische Modellierung von Sandwichstrukturen mit Faltwabenkern aus Aramidpapier und Deckschichten aus Faserverbund unter quasistatischen und Impakt-Lastfällen. Dazu werden bereits bestehende Ansätze, die zelluläre Sandwichstrukturen mit Meso-Modellen aus Schalenelementen abbilden, an Faltwaben aus Aramidpapier angepasst und weiterentwickelt. Aufgrund der Komplexität der in der Sandwichstruktur unter Impaktbelastung auftretenden Schädigungs- und Versagensmechanismen ist die numerische Modellierung des Impaktsverhalten in drei aufeinander aufbauenden Teilschritten entwickelt worden.

Innerhalb des ersten Teilschritt wurde die numerische Modellierung von Aramidpapier untersucht. Zur Charakterisierung der Papiereigenschaften wurden Strukturanalysen mittels Mikroskopie und Computertomographie durchgeführt und das mechanische Verhalten bis zum Versagen bestimmt. Dabei wurde eine merkliche Variation der mechanischen Eigenschaften aufgrund der inhomogenen Faserverteilung in Dickenrichtung festgellt. Basierend auf diesen Beobachtungen wird ein Modellierungsansatz mit mehrlagigen Schalenelementen vorgestellt, in dem die Variationen in Dickenrichtung berücksichtigt werden können. Die dazu benötigten Materialeigenschaften der einzelnen Lagen des Schalenelements, werden anhand einer inversen Berechnung von den experimentell bestimmen, globalen Aramidpapiereigenschaften hergeleitet. Der Vergleich mit Coupon-Zugtests und Zylindderbeulversuchen zeigt, dass der vorgeschlagene Modellierungsansatz das Materialverhalten von Aramidpapier auch im nicht-elastischen Bereich gut vorhersagen kann. Insbesondere das zur Modellierung von Impaktbelastungen wichtige Beulverhalten im Fall von Druckbelastungen wird qualitativ gut abgebildet.

Der entwickelte Ansatz zur Modellierung von Aramidpapier wird in einem zweiten Teilschritt erweitert, sodass Faltwabenstrukturen abgebildet werden können. Dazu wird ein Parametermodell vorgestellt, mit dem Faltwabengeometrien aus mehrlagigen Schalenelemente erstellt werden können. Die deutlich irreguläre Faltwabenstruktur wird über ein sogenannten ‚Node-Shaking' Ansatz berücksichtigt. Der Vergleich zu Benchmarktests (Faltwaben unter Druck- und Schubbelastungen) zeigt, dass die Kräfte und Verformungen bei Beginn des Ausbeulens der Zellwände gut repräsentiert sind und insbesondere das instabile Kollapsverhalten der Faltwabe gut wiedergegeben wird. Allerdings zeigt das Modell Schwächen bei der Vorhersage der stark ansteigenden Spannungen bei verdichteten Faltwaben.

In dem dritten Teilschritt wird das entwickelte Faltwabenmodel auf Impakt-Lastfälle angewandt. Dazu wurden Impaktversuche im Fallturm (Impaktenergien von 60–400 J) und mit einer Gaskanonenanlage (Impaktenergien von 20–800 J) durchgeführt. Anhand der experimentell bestimmten Kenndaten wurde das Faltwabenmodell bewertet. Das Impaktmodell zeigte dabei eine gute Übereinstimmung mit den experimentell beobachteten Schadensbildern und Impaktverläufen. Die Bedeutung einer guten Repräsentation des Faltwabenkerns zeigte sich auch daran, dass in den numerischen Ergebnissen ein deutlicher Anteil der kinetischen Energie von bis zu 50% in elastische und plastische Verformung des Kerns umgewandelt wurde.

Abstract

Over the last decades the application of fibre composite designs in aircraft construction has increased rapidly. However, in large aircrafts most fibre composite components are secondary structures. There is considerable interest to extend the application of fibre composite designs to primary structures, such as a fuselage. A promising design for primary structures are sandwich structures with cellular cores and fibre composite face sheets. Sandwich structures benefit from high specific stiffness and strength. However, due to the low thickness of their face sheets they are vulnerable to impact loads. An efficient dimensioning towards impact loads is therefore a critical aspect of sandwich design. Because of the considerable costs of an experimental characterisation of impact behaviour, there is a growing interest to reduce the number of required experimental tests by the use of numerical methods. A prerequisite for this is the availability of high-performance numerical methods, which are needed to model the complex damage and failure mechanisms of sandwich structures subjected to impact loads.

In this context, the present research thesis investigates the numerical modelling of sandwich structures with aramid paper foldcore and fibre composite face sheets in quasi-static and impact load cases. For that purpose, existing approaches reproducing cellular sandwich structures on the basis of shell-based meso-models are adapted to aramid paper foldcores and further developed. Due to the complexity of damage and failure mechanisms in sandwich structures under impact loads, the numerical modelling of impact behaviour is developed in three successive steps.

Firstly, the numerical modelling of aramid paper was investigated. The properties of the aramid paper were characterised on basis of structural analysis using microscopy and computed tomography and determination of the mechanical behaviour up to failure. In the process a notable variation of mechanical properties due to the inhomogeneous fibre distribution in thickness direction was observed. Based on these observations a modelling approach with multi-layered shell elements is presented, which considers the paper's inhomgeneous nature in thickness direction. The required material properties of the individual layers are derived from the experimentally determined global aramid paper properties using an inverse approach. The comparison to tensile coupon tests and cylinder collapse tests shows, that the proposed modelling approach can predict the material behaviour of aramid paper for non-elastic states until total failure. In particular the instable buckling modes occurring under compressive loads, which are important for impact modelling, are well represented.

In the second step, the developed modelling approach for aramid paper is expanded in order to represent foldcore structures. For that purpose a parametric model is presented, which is used to generate foldcore geometries composed of multi-layered shell elements. The significantly irregulare structure of a foldcore is considered by a so-called 'node-shaking'

approach. The comparison with benchmark tests (compression and shearing of foldcores) shows, that the forces and and deformations at initiation of buckling and in particular the instable collapse behaviour of the foldcore are well represented. However, the numerical model underestimates the considerable increase in stress in case of densified foldcores.

In the third step, the developed foldcore model is applied to impact load cases. For that purpose impact test series were performed with a drop tower apparatus (Impact energies: 60–400 J) and a gas gun facility (Impact energies: 20–800 J). The foldcore model was then evaluated by comparison to experimentally determined impact characteristica. The impact model demonstrated good agreement with the experimentally observed damage patterns and courses of impact events. The relevance of a good representation of the foldcore can also be seen in the fact that a considerable part of the initial kinetic energy, up to 50%, was converted into elastic and plastic deformation of the core.

1. Introduction

The application of composite materials to modern aircraft structures has grown steadily with each generation of aircraft. Existing composite aircraft structures adopt conventional design principles of skin/frame/stringer developed for aluminium lightweight construction. Current research is focusing on integrated design concepts which factor the different properties of composites. A promising approach for a next generation aircraft fuselage are twin-walled sandwich structures which provide improved shell bending stiffness and far higher strength/weight ratios than single skin designs (cf. research project EMIR [1]).

The weight reduction by structural optimisation is a driving principle in aircraft design. In case of aircraft fuselages a twin-walled sandwich allows highly efficient new fuselage concepts with a reduced number of frames and without stringers. Innovative twin-walled approaches may achieve weight savings of about 24%-29% compared to an aluminium reference fuselage as described by Hermann et al. [79].

A major challenge for an application of sandwich structures in primary aircraft structures is the impact safety. Impact events in aviation hereby include a wide range of foreign object impacts such as bird strike, tyre rubber, runway debris, metal fragments and hail. In the case of sandwich structures the improvement of impact properties is more significant compared to monolithic structures as their reduced skin thickness and low core strength lead to increased impact vulnerability. The present thesis was realised within the scope of EU Project CEL-PACT 'Cellular structures for impact performance' [3] which examines advanced sandwich core materials with improved impact properties in order to address these issues. The purpose of this research was to enhance the impact resistance of sandwich structures by improved design of high performance, low weight cores. New core materials under investigation were, amongst others, folded composite cores.

The introduction of reliable modelling and finite element (FE) simulation of sandwich structures and cellular cores such as the foldcore offer the potential to improve the design process of new sandwich structures with tailored properties and reduce development costs. FE codes with validated models provide the means to design and optimise these structures even for complex load cases such as impact events. The need for expensive test specimen development, which is caused by an almost infinite number of core materials, cell geometries, face sheet materials and sandwich constructions, impact conditions, etc. can be significantly reduced.

A major requirement for the accuracy of numerical results is a correct modelling of material properties and the present thesis aims to improve the constitutive material models and numerical descriptions used for sandwich structures with the new foldcore material. Both quasi-static and dynamic load cases are considered. To establish new materials and improve

the representation of the numerical materials models an extensive experimental investigation of the core cell wall material, the core, the composite face sheets and sandwich structure under a variety of loading conditions was required.

1.1. Aims and objectives

This work presents contributions towards the improved modelling of foldcore cell wall material and foldcores under quasi-static and dynamic load conditions, which reproduce the behaviour of materials and structures from the initial elastic behaviour until full failure. These improvement are based on observations made in experimental studies to characterise the mechanical and structural properties of the foldcore cell wall material and in foldcore sandwich structures. The capability of the proposed material models and current FE techniques with regard to modelling composite-foldcore sandwiches in quasi-static and dynamic load cases is assessed on basis of a comprehensive test program investigating various load cases.
The aims of this research thesis are:

- Experimental investigation of the properties of aramid paper which is used as foldcore cell wall material.

- Experimental characterisation of the quasi-static and dynamic foldcore benchmark behaviour.

- Investigation of the hard and soft body impact response of composite foldcore sandwich panels.

- Development of a suitable material modelling approach for the foldcore cell wall material which can represent the constitutive behaviour from initial elasticity until full failure.

- Development of a modelling strategy to correctly predict foldcore degradation and failure in quasi-static (crushing, shear) and dynamic (low-velocity and high-velocity impact) load cases.

- Stepwise validation of above modelling strategy by comparison to experimental benchmark tests.

1.2. Thesis summary

Chapter 2

The state of the art in sandwich structures and their design is summarised in this chapter. Available sandwich materials and core types are discussed with special emphasis on aramid

paper foldcores, which are the focus of this research work. Subsequently analytical and numerical methods for sandwich design are summarised. The current numerical approaches to model impact on sandwich structures are reviewed. Finally, the thesis structure based on the literature research is presented.

Chapter 3

In this chapter the modelling of aramid paper is investigated. To this end an experimental characterisation of the aramid paper's properties up to failure is presented. This includes an analysis of the microstructure of the aramid paper by microscopic cut-images and computed tomography. Based on the experimental findings a layered shell model approach is proposed, which considers the considerably non-uniform fibre distibution in the paper's thickness direction. The required material properties of the individual shell layers are derived from the globally measured paper properties on basis of an inverse approach. In a subsequent section the validity and efficiency of the proposed aramid paper model is evaluated by comparison of experiment and simulation of several benchmark tests, such as paper coupon test and cylinder collapse test.

Chapter 4

In this chapter the previously presented layered shell model approach is extended to represent aramid paper foldcore structures. For that purpose a parametric description of the foldcore's geometry is presented, which is the used to create a numerical model based on the aramid paper model. The considerable existence of irregularities in an aramid paper foldcore is discussed and a consideration of these irregularities by the so-called 'node-shaking' approach is proposed. Finally the foldcore model is evaluated by comparing numerical and experimental results of compression and shear behaviour of foldcores.

Chapter 5

In this chapter the numerical foldcore model presented in chapter 4 is applied impact load cases. For that purpose the behaviour of foldcore sandwich panels with carbon fibre composite skins subjected to low-velocity and high-velocity impact are at first experimentally investigated. The adaption of the foldcore model is presented and investigated in a parameter study. In the final section the predictions of the numerical model are compared to the experimental results. The quality of the numerical predictions is evaluated on basis of the observed representation of the governing deformation and failure mechanisms.

Chapter 6

In this chapter the limitations and validity of the experimental and numerical results and methods presented in chapters 3–5 are discussed. The benefit and disadvantages of the developed improvements to the modelling of aramid paper and foldcore structures are reviewed.

Chapter 7

In this chapter the contributions produced by this work are summerised. Subsequently, future areas of research are suggested to address limitations encountered during the presented research work and to investigate the properties of foldcore materials further.

2. State of the art

2.1. Overview

This chapter offers a general overview on the state of the art in sandwich structures. For that purpose available sandwich materials are discussed with special emphasis on sandwich core materials. Subsequently the reader is introduced to analytical methods in sandwich engineering. This is followed by a section reviewing the numerical analysis of sandwich structures, which includes a brief introduction to explicit finite element methods and a discussion of established modelling approaches for impact on sandwich structures. Finally the modelling strategy adopted in this work is summarised.
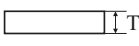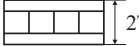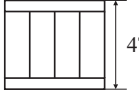
2.2. Sandwich structures

Sandwich structures are a laminate of different materials, which are joined together. Typically a low weight core material is inserted between two stiff face sheets, hence the term 'sandwich'. Each component of the sandwich structure has separate structural functions: the face sheets carry the in-plane tensile and compressive forces caused by bending loads. The core reinforces the face sheets against buckling by carrying shear forces between the face sheets as well as local out-of-plane loads. The basic idea is to maximise the second moment of area by increasing the Huygens-Steiner fraction. As a result sandwich structures offer excellent strength and stiffness properties in bending at low weight, as shown in table 2.1 taken from Bitzer [27].

The table compares the relative strength and stiffness of several honeycomb structures, which are made from a 1.6 mm thick piece of aluminium split in half as the top and bottom face sheets of the sandwich. The sandwich with four times the thickness of a flat aluminium plate is 37 times stiffer in bending and 7 times stronger, but has at the same time only a weight increased by 9 %. According to Hermann et al. [79] weight savings of about 24–29 % can be achieved for aircraft fuselages using a twin-walled sandwich compared to aluminium reference fuselages.

As discussed in [27, 61, 68] sandwich structures offer further advantages beside their weight efficiency. Compared to locally discontinuous stiffened structures such as skin-stringer-frame designs they retain a smooth surface under load, as the stability related buckling of the load carrying face sheets is considerably reduced by the continuous attachment to the core. Another benefit is the increased fatigue resistance compared to skin-stringer-frame designs. The primary reason is that sandwich structures require significantly less rivetted joints, which

Table 2.1.: Honeycomb sandwich efficiency, taken from Bitzer [27].

| Property	Unit	T	2T	4T
Relative stiffness	[-]	1	7	37
Deflection	[mm]	25.4	3.6	0.7
Relative bending strength	[-]	1	3	7
Weight	[N/m^2]	43.6	46.8	47.6

are a major cause for stress concentrations and thus induced premature failure. Furthermore sandwich structures exhibit excellent damping and insulation properties (vs. thermal, vibration), as delineated in [61, 147].

The key advantage, which is their excellent strength and stiffness properties at low weight, in combination with their other advantages promotes the application of sandwich structures in a broad range of lightweight designs. Examples of their use can be found in aviation [27, 61, 75, 79, 137], spaceflight [46, 136, 137], transportation [2, 4, 143], motor sports [111], civil engineering [112], wind energy [98, 146], sporting equipment [27, 117] and packaging [156].

However, there are some limitations of sandwich structures which need to be mentioned. The tailored multi-material composition typically results in higher cost of sandwich composites compared to conventional materials. The fabrication process is complex and time-consuming. Due to the buckling resistant design with large Huygens-Steiner fractions a sandwich structure has a considerably larger thickness than monolithic structures. Furthermore sandwich structures are difficult to repair, due to their adhesively bonded architecture in combination with their multi-material setup. If an adhesive is used to bind the face sheets to the core, the adhesive layer can also have considerably influence on the failure of a sandwich structure. Therefore the properties of a sandwich structure depends on the properties of the core and face sheets, their relative thickness and the bonding characteristics between them.

In particular relevant for the present work is the vulnerability of sandwich structures to impact loads, as the sandwich face sheets are significantly thinner than a monolithic plate made of the same material. A localised impact load leads to considerable deformation of the loaded face sheet and the intermediate core which in particular may exceed the allowable limits of the weaker core material.

Impact safety is a critical aspect of the design of primary aircraft structures. At the present time, the application of sandwich structures in aviation is mainly limited to secondary structures. Secondary structures are characterised by the fact that their failure does not lead to a catastrophic damage to the aircraft. Examples for typical sandwich applications in secondary structures are spoiler/ailerons, flap track fairings, leading and trailing edge panels, cabin floor panels, radomes, fuselage belly fairings, pylon/nacelle structures, etc. In figure 2.1a the secondary structures in an Airbus A380 are depicted as summarised by Hermann et al. [79]. It
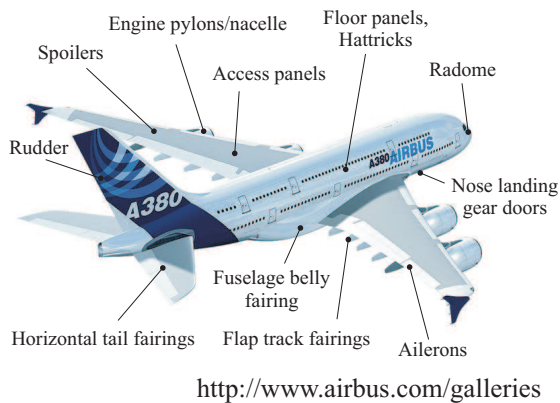
(a) Secondary sandwich structures in A380

(b) Beechcraft Premier I

Figure 2.1.: Examples for sandwich application in A380 (taken from Hermann et al. [79]) and picture of the Beechcraft Premier Ia (taken from the Hawker-Beechcraft website [5]).

is noted that an exception is the Beechcraft Premier I illustrated in figure 2.1b, which is a light jet aircraft for 6-7 passengers made by Hawker Beechcraft. Here the whole fuselage, which is a primary structure, is composed of a carbon fibre/epoxy honeycomb sandwich.

There is considerable interest to improve the impact properties of sandwich structures in order to advance the application of sandwich structures in primary structures so that aircraft designs can take full benefit of their excellent light-weight potential. The present work has been created within the framework of the EU Project CELPACT 'Cellular structures for impact performance' [3]. The objective of CELPACT was to improve the vulnerability and damage tolerance due to foreign object impact on sandwich structures by the use of new core materials. The present work focuses here on folded composite cores which are presented subsequently along with common core types in aviation such as honeycomb and foam cores.

Core types

A comprehensive overview on existing core types for sandwich structures is found in [147], which mainly refers to foam/solid cores (ships, aircraft), honeycomb cores (aircraft, satellites), truss cores (buildings, bridges) and web cores (Johnson et al. [93]) as common core types. The predominant core material in aviation are honeycomb cores, which are comprehensively reviewed in the works of Bitzer [27] and Funke [61]. A further core material in aviation are foam cores, which have been utilised successfully for several aerospace structures as described by Seibert [137]. Honeycomb cores can be fabricated from a broad range of metallic and non-metallic base materials, such as aluminium, steel, titanium, fibreglass, carbon fabrics, Nomex®, Kraft paper etc. Current non-metallic materials for foam cores are typically thermoplastics (Kilchert [99]) such as polymethacrylimide (PMI), polyvinyl chloride (PVC), styrene-acrylonitrile (SAN) , etc. In some cases also metallic foam cores, such as aluminium

Table 2.2.: Overview on common core types in sandwich structures (Data is taken from Bitzer [27] and Kilchert [99]).

Core type	Density [kg/m^3]	Compressive Modulus [MPa]	Compressive Strength [MPa]	Shear Modulus [MPa]	Shear Strength [MPa]
Aluminium honeycomb	50	520	2.1	310	1.4
Nomex honeycomb	48	140	2.2	40	1.2
Glassfibre honeycomb	48	160	2.8	130	1.3
Rohacell RI foam	52	75	0.8	24	0.8
Klegecell R45 foam	45	60	0.54	19	0.55
Divinycell HT foam	50	75	0.7	19	0.55
Airex C70 foam	48	44	0.6	15	0.55
ALPORAS foam	250	700	1.5	300	1.2
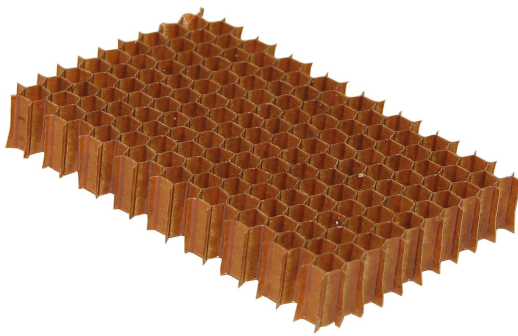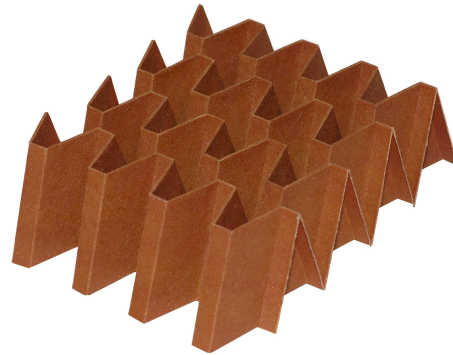
(a) Honeycomb   (b) Foldcore

Figure 2.2.: Pictures of a honycomb core and a foldcore.

foam (ALPORAS®, ALUCORE®) or steel foam are used. The properties of common honeycomb and foam core materials are summarised in table 2.2.

As discussed above the main load direction of sandwich cores are the out-of-plane normal and shear loads. In that direction the weight-specific stiffness and strength of honeycomb cores are much better than the weight-specific stiffness and strength of foam cores. Consequently honeycomb cores, as illustrated in figure 2.2a, are preferred whenever the mechanical properties of the core are a relevant factor of the sandwich design. The incentive to use foam cores is their superior behaviour in insulation as well as their closed cell structure, which reduces the accumulation of moisture. Humidity accumulation is one of the main drawbacks of honeycomb cores.

The present work investigates a novel folded sandwich core material -foldcore- which is depicted in figure 2.2b. The foldcore avoids some of the honeycomb disadvantages while

a) Imprint of fold pattern   b) Folding to three-dimensional structure   c) Finishing treatment (Curing, coating, etc.)
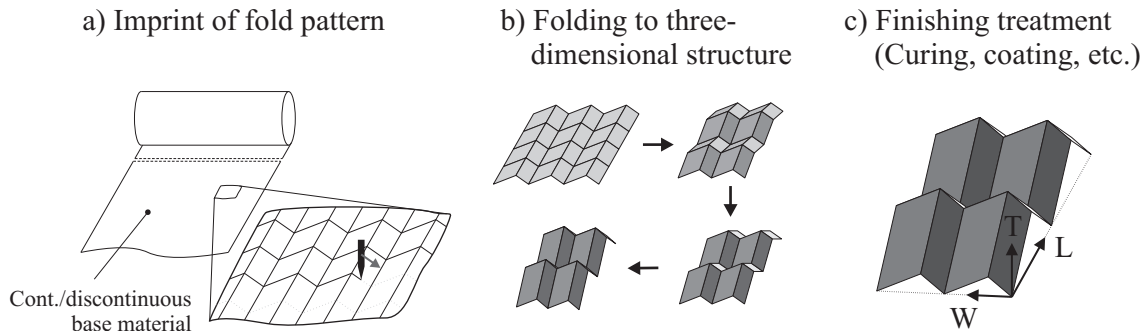
Cont./discontinuous base material

Figure 2.3.: Manufacturing process of a foldcore as used in Institute of Aircraft Design (IFB), Universität Stuttgart.

maintaining the excellent mechanical properties of honeycomb cores: The foldcore solves the problem of humidity accumulation by featuring an open cellular design which allows it to vent the foldcore (Klett et al. [104, 105]). The vulnerability to impact loads is partially addressed by the adaptiveness of the foldcore's unit cell geometry and by using base materials with high energy absorption. Compared to common honeycomb production processes which are comprehensively presented by Bitzer [27] a foldcore can be manufactured very cost-efficiently as shown by Kehrle and Drechsler [97].

Manufacturing of foldcores is based on a simple folding process in which a plane sheet of material is folded into a three-dimensional structure. The foldcore can be produced both in a continuous and a discontinuous way. Both methods follow a similar process which is schematically illustrated in figure 2.3. In the first step the fold pattern is imprinted into a base material. In the second step the imprinted material is folded into its three-dimensional form using an origami-like process. The plane faces of the folded structure thereby remain free of distortion. Subsequently finishing treatments such as curing and surface treatment are applied if needed. The density of typical folded cores made of aramid paper ranges from 25 kg/m^3 to 150 kg/m^3 depending on fold geometry.

The foldcores investigated in the present work are plane fold geometries with simple, repetitive arrangement of folds. It is noted that the process also allows foldcore structures with varying height or curvature which can be generated on basis of adjusted folding patterns, as discussed in the works of Klett et al. [105] and Hachenberg et al. [71]. Typically foldcores are orthotropic in in-plane direction as a result of the fold geometry. The local foldcore co-ordinates are referred to T-, W- and L-direction as shown in the figure. The applicable base materials for foldcore structures are in principle similar to the materials adopted in honeycomb structures. Most prevalent are paper-like materials (Aramid paper, as investigated in Fischer et al. [54], Kraft paper), composites (Glass, aramid, carbon as presented in Heimbs et al. [76]) and metals (Aluminium, titan, as investigatd in Hecht [74] and Fischer et al. [53]).

The Institute of Aircraft Design of the 'Universität Stuttgart', which provided the fold-cores investigated in the present work mainly focuses on foldcores made of aramid paper pre-

Table 2.3.: Overview on uni-directional fibre composite face sheet materials (The data is taken from the works of Funke [61] and Daniel and Ishai [37]).

Type	Density [g/cm^3]	Longitudinal Modulus [GPa]	Longitudinal Strength [MPa]	Transverse Modulus [GPa]	Transverse Strength [MPa]
Carbon/Epoxy	1.6	147	2280	10	46
S-Glass/Epoxy	2.0	45	1725	11	49
Kevlar/Epoxy	1.4	80	1400	6	30
Aluminium	2.7	70	140–480	70	140–480

pregs. In principle aramid paper is comparable to common honeycomb base materials made of aramid fibres such as Nomex®. However there are some differences which are caused by the different fabrication processes of honeycomb cores and foldcores: in case of honeycomb cores the block web material, which contains only a small amount of resin, is repeatedly dipped in liquid resin and then cured, whereas in case of foldcores the base material comes in form of pre-impregnated aramid paper, which is then folded and cured. As a result, the resin absorption in the base material of foldcores differs from the resin absorbtion in the base material of honeycomb cores, which leads to slightly different material properties, as will be shown in chapter 3.

Face sheet

An overview on existing materials for face sheets of sandwich structures can be found in [147]. The main function of face sheets is to carry the in-plane tensile and compressive forces caused by bending loads. This implies materials with large in-plane stiffness and strength. In aircraft structures this is given for a wide range of non-metallic materials such as carbon, glass fibre composites as well as for metallic materials such as steel, aluminium, titanium, magnesium. The mechanical properties of common face sheet materials are illustrated in table 2.3. In particular composite materials have gained in importance in the recent years. An exhaustive review of the properties of common composite materials is given in the works of Funke [61] and of Daniel and Ishai [37].

A detailed investigation on face sheet materials would have exceeded the scope of the present work as there is a wide range of materials available for the design of light-weight face sheets, whereas the present work mainly focuses on core behaviour. However the properties of sandwich face sheets have a considerable influence on the impact behaviour of a sandwich structure. Therefore, to provide a realistic setup for the impact cases on sandwich structures studied in chapter 5 a reference face sheet material is used. This reference face sheet is a quasi-isotropic lay-up of 16 UD carbon fibre composite plies, which was based on composite face sheet setups employed in design concepts for sandwich fuselages in the research project EMIR [1].

2.3. Analytical methods in sandwich structures

In the following a brief introduction to analytical design of sandwich structures is given, which is based on the comprehensive accounts given by Bitzer [27] and by Heimbs [75]. The overview includes approximate and exact formulations for sandwich stiffnesses and stresses. For the sake of simplicity presented results are limited to face sheets of similar thickness and material. For a more detailed description the reader is referred to the work of Bitzer [27].

In the following, the z-axis indicates the sandwich's out-of-plane orientation whereas the x- and y-axis point along the in-plane orientations. It is noted, that in this work also an alternative nomenclature (TLW) is used in case of foldcore and honeycomb sandwich structures, where the T-direction is parallel to the z-axis and the L- and W-directions are aligned to the sandwich in-plane orientations.

The sandwich dimensions and properties are illustrated in figure 2.4, which depicts approximated and exact stress distributions in a sandwich structure under normal, bending and shear loads. The sandwich height is signified by h, the sandwich width is w, the thickness of a face sheet is given by t_f and the thickness of the core is labelled t_c. For the present cases, the face sheet and core are assumed to be isotropic materials. The modulus of the face sheet is E_f and the modulus of the core is E_c.

Figure 2.4a illustrates a sandwich structure under a normal load F. If the dimensions and the modulus of face sheet and core is known, the axial stiffness $(EA)^{Normal}$ becomes

$$(EA)^{Normal} = 2E_f t_f w + E_c t_c w. \tag{2.1}$$

The stresses in face sheet $\sigma_{f,y}$ and core $\sigma_{c,y}$ are then

$$\sigma_{f,y} = \frac{E_f F}{(EA)^{Normal}} \qquad \text{and} \qquad \sigma_{c,y} = \frac{E_c F}{(EA)^{Normal}}. \tag{2.2}$$

Often it is assumed that the stiffness of the core is considerably lower than the stiffness of the face sheet ($E_c t_c \ll E_f t_f$) which allows to neglect the stresses in the core. Using this approximation above equations 2.1 and 2.2 reduce to

$$(EA)^{Normal} \approx 2E_f t_f w \qquad \text{as well as} \tag{2.3}$$

$$\sigma_{f,y} \approx \frac{2F}{t_f} \qquad \text{and} \qquad \sigma_{c,y} \approx 0. \tag{2.4}$$

The second figure 2.4b depicts the sandwich structure under a flexural load M. For this case the flexural stiffness $(EI)^{Flexural}$ of the sandwich is

$$(EI)^{Flexural} = \frac{E_f t_f w h^2}{2\lambda_f} + \frac{1}{12}\left(\frac{2E_f w t_f^3}{\lambda_f} + \frac{E_c w t_c^3}{\lambda_c}\right), \tag{2.5}$$

where the term λ signifies the Poisson's ratio effect, which makes a wide beam stiffer than a narrow beam. In case of a beam λ becomes 1, whereas in case of a plate the term has values of
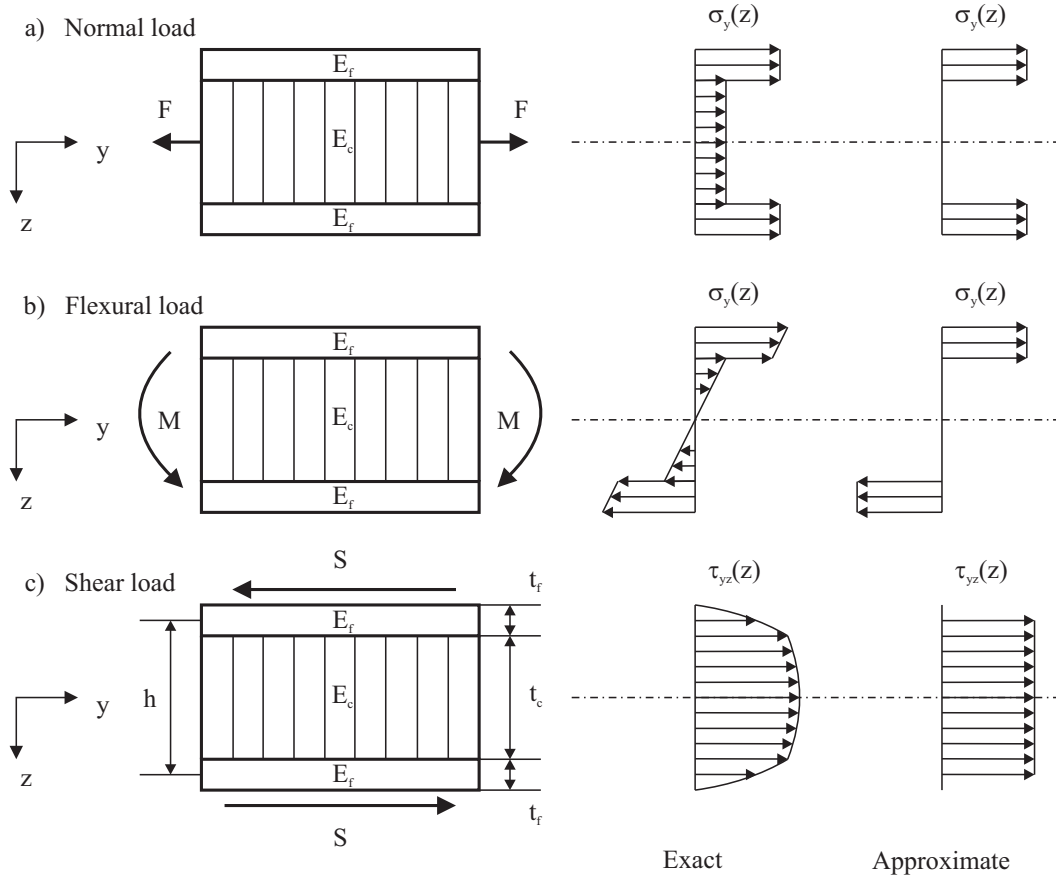
Figure 2.4.: Approximate and exact normal, bending and shear stresses in a sandwich panel as presented by Bitzer [27].

0.89 for aluminium, 0.91 for steel and 0.98 for fibreglass, as stated in the work of Bitzer [27]. Generally, if a beam's width is seven times larger than its thickness and larger than one-third of the span it is assumed to behave as a plate. With equation 2.5 the stresses in face sheet $\sigma_{f,y}(z)$ and core $\sigma_{c,y}(z)$ become

$$\sigma_{f,y}(z) = \frac{E_f M z}{(EI)^{Flexural}} \qquad \text{and} \qquad \sigma_{c,y}(z) = \frac{E_c M z}{(EI)^{Flexural}}. \qquad (2.6)$$

Above equations 2.5 and 2.6 can be simplified by assuming that the modulus of the core is significantly smaller than the modulus of the face sheets ($E_c \ll E_f$). Furthermore in case of thin face sheets ($t_f \ll t_c$) the stress distribution in the face sheet can be considered constant. Using these approximations the sandwich flexural stiffness $(EI)^{Flexural}$ and stresses in face sheet $\sigma_{f,y}(z)$ and core $\sigma_{c,y}(z)$ are given by
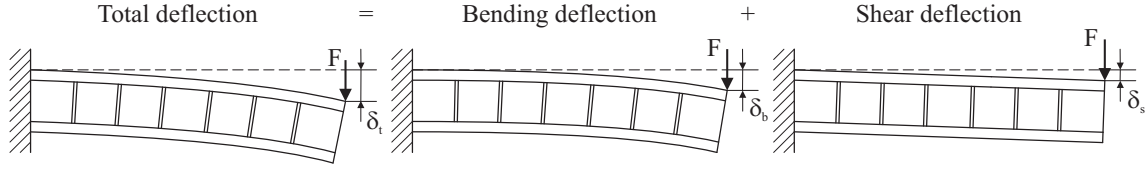
Figure 2.5.: Deflection of a sandwich beam taken from Zenkert [159].

$$(EI)^{Flexural} \approx \frac{E_f t_f w h^2}{2\lambda_f}, \tag{2.7}$$

$$\sigma_{f,y}(z) \approx \frac{2Mz\lambda_f}{t_f h^2} \qquad \text{and} \qquad \sigma_{c,y}(z) \approx 0. \tag{2.8}$$

In the third figure 2.4c a sandwich structure is illustrated which is loaded in shear by a load S. The shear stress distribution in face sheets $\tau_{f,yz}(z)$ and core $\tau_{c,yz}(z)$ can be expressed as

$$\tau_{f,yz}(z) = \frac{SE_f}{2\left(EI\right)^{Flexural}} \left(t_f^2 + t_f t_c + \frac{t_c^2}{2} - z^2 \right) \qquad \text{and} \tag{2.9}$$

$$\tau_{c,yz}(z) = \frac{S}{(EI)^{Flexural}} \left(\frac{E_f t_f(t_f + t_c)}{2} + \frac{E_c}{2} \left(\frac{t_c^2}{4} - z^2 \right) \right), \tag{2.10}$$

By assuming that the core modulus is very small ($E_c \ll E_f$) and the face sheets are sufficiently thin ($t_f \ll t_c$) the equations 2.9 and 2.10 reduce to

$$\tau_{c,yz}(z) = \tau_{f,yz}(z) \approx \frac{S}{hw}, \tag{2.11}$$

where z ranges from $-h/2$ to $h/2$. Above relations for the sandwich stiffnesses can be used to calculate the deflection of a sandwich beam. In case of a sandwich panel subjected to a out-of-plane load the total deflection is composed of a bending deflection and a shear deflection, as illustrated in figure 2.5. The total deflection δ_t is the sum of the bending deflection δ_b and shear deflection δ_s and can be expressed as

$$\delta_b = K_b \frac{FL^3}{(EI)^{Flexural}} + K_s \frac{FL}{hwG_c}. \tag{2.12}$$

The parameters K_b and K_s are deflection constants depending on the support of the sandwich beam. Values of K_b and K_s for various sandwich setups can be found in the work of Bitzer [27]. L is the length of the sandwich beam and G_c is the shear modulus of the core.

Above relations for stresses, stiffnesses and deflections can be used to estimate the elastic behaviour of a sandwich based on the properties of its face sheets and core. However it is difficult to analytically predict failure behaviour of sandwich structures due to their complex nature. The common failure modes of sandwich panels and their causes are summarised in

table 2.4. Literature dealing with failure in sandwich structures [27, 159] provides equations which allow to calculate critical stresses for various failure modes, such as wrinkling (local buckling of face sheets), dimpling (local buckling into core cells) in case of cellular cores, transverse shear failure, etc.

There exist several analytical solutions to predict the impact response of composite sandwich structures. Soden [141] modelled core crushing using an indentation model that consists of an elastic face sheet resting on an elastic perfectly-plastic foundation. However this type of approach remains limited as core crushing and damage in the face sheets is neglected. Analytical approaches which may consider these phenomena are spring-mass models and energy-balance models as found in the research works of Abrate [8] and Aminanda et al. [15]:

Spring-mass models use springs to represent the effective structural stiffness of a impactor-sandwich plate system, where the elastic response of the sandwich plate is solved from the dynamics equations of the system. The energy-balance model evaluates the conservation of the total energy in the system to solve for the maximum impact load. The sum of the deformation energies at maximum deflection is set equal to the kinetic energy of the impactor. By that the deformation energies can be quantified and determined separately. Both models have been adopted to sandwich plates with fibrous core (Anderson [17]), foam core (Zhou and Stronge [163]) and honeycomb core (Zhou and Stronge [163], Castanié [33]) to predict the force on the impactor.

However, these elastic models are limited to predict the onset of damage and are restricted in case of prediction of the evolution of damage. Modified spring-mass models have been proposed by Foo et al. [60] to account for damage, but they are heavily based on additional experimentally determined data. In summary, most existing models are valid for elastic impact events, but the impact response of the structure after the onset of damage is not well dealt with.

Another restriction is that these analytical approaches are only valid for well defined impact load cases. By contrast a sandwich structure subjected to impact fails under a complex combination of various factors, such as sandwich structure geometry, impact conditions, nature of impactor, etc. In order to predict failure conditions and failure behaviour in case of impact or likewise complex load conditions it is therefore state of the art to resort to numerical approaches as for example finite element methods (FEM). These finite element methods are briefly introduced in the next section, which is then followed by a further section discussing their adaption to impact cases on sandwich structures.

## 2.4. Numerical modelling of sandwich structures

2.4.1. Introduction

Numerical methods have been applied to numerous problems in engineering and science and have become become a reliable design tool. Beside the widely-used finite element method (FEM) there exist various other methods such as finite difference method (FDM), finite volume
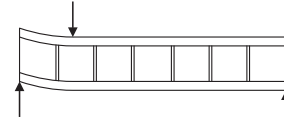
Table 2.4.: Sandwich failure modes, taken from Bitzer [27].

1. face sheet failure
Initial failure may occur in either compression or tension face sheet. Caused by insufficient panel thickness, face sheet thickness or face sheet strength.

Tensile failure in facesheet
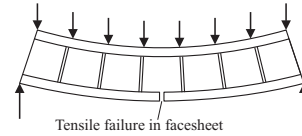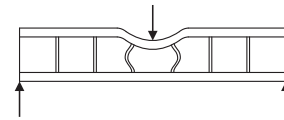
2. Transverse shear failure
Caused by insufficient core shear strength or panel thickness.
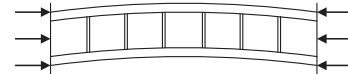
3. Flexural crushing of core
Caused by insufficient core flatwise compressive strength or excessive beam deflection.
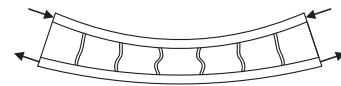
4. Local crushing of core
Caused by low core compression strength.

5. General buckling
Caused by insufficient panel thickness or insufficient core shear rigidity.

6. Shear crimping
Sometimes occurs following and as a consequence of general buckling. Caused by low core shear modulus or low adhesive shear strength.
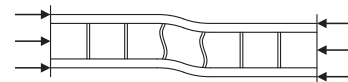
7. Face sheet wrinkling
The face sheet buckles as a plate on an elastic foundation. It may buckle inward or outward depending on relative strengths of core in compression and adhesive in flatwise tension.

Adhesive bond failure

Core compression failure
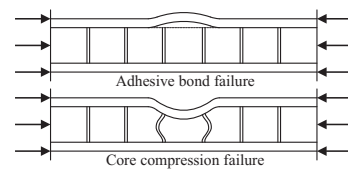
8. Intracell buckling (dimpling)
Applicable to cellular cores only. Occurs with thin face sheets and large core cells. This effect may cause failure by propagating across adjacent cells, thus inducing face wrinkling.

Facesheets buckle into core cells
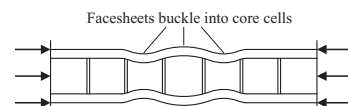
method (FVM), boundary element method (BEM) and meshless methods. However in case of impact simulations the FEM are prevalent. The FEM is comprehensively discussed in the textbook of Wriggers [155]. In comparison to time-consuming and expensive experimental approaches, they allow a short-term and inexpensive analysis of stress and deformation in complex structures with simultaneous consideration of material degradation and failure. In the FEM the geometry of a continuous body is discretised, which means the segmentation into a set of nodes and elements. The physical quantities are calculated directly at the nodes, whereas the distribution of the physical quantities between the nodes is described by elemental shape functions. In case of solid mechanics the FEM needs to solve the dynamic equilibrium equations

$$\mathbf{m\ddot{u}} + \mathbf{c\dot{u}} + \mathbf{ku} = \mathbf{f}_{ext}(t). \tag{2.13}$$

In above equation the term $\mathbf{m\ddot{u}}$ refers to inertia, the term $\mathbf{c\dot{u}}$ refers to damping, the term $\mathbf{ku}$ refers to the stiffness and $\mathbf{f}_{ext}(t)$ are the external forces. As the dynamic equilibrium equation is a function of the time it is also necessary to discretise the time, which means that equation 2.13 is solved at discrete points in time. For that purpose two different time integration methods can be used, which are the implicit and the explicit time integration.

The difference between both integration schemes is that the explicit method uses equation 2.13 at time t to predict a solution at time $t + \Delta t$. In the process the system of equations is uncoupled. The size of a time increment Δt depends on the largest eigenfrequency of the system, which typically implies very small time increments. As the solution of the differential equation is approximated (conditionally stable) it drifts from the exact solution in case of a very large number of time increments. In order to achieve convergence the Courant-Friedrichs-Lewy condition (CFL condition) has to be fullfilled. It states that the timestep Δt must be less than the time a wave needs to travel between adjacent nodal points. The one-dimensional case the CFL condition for example requires

$$\frac{v \times \Delta t}{\Delta l} \leq C, \tag{2.14}$$

where v is the velocity of a wave and Δl is the distance between two adjacent nodes. The term C refers to a characteristic magnitude which depends on the particular differential equation to be solved.

The implicit method attempts to satisfy the equation 2.13 at time t after the solution at time $t - \Delta t$ has been found. For that purpose the whole system of equations has to be solved at each time increment which also means that the global stiffness matrix has to be inverted at large numerical costs. However it is unconditionally stable and the size of the time interval is only limited by the convergence conditions. Therefore the time increments are typically considerably larger than in the explicit method. In figure 2.6 the differences between both integration methods are also schematically illustrated.

There exist various commercial numerical codes which use implicit (ANSYS, NAS-TRAN, ABAQUS implicit, etc.) and explicit (PAM-CRASH, LS-DYNA, ABAQUS explicit, AUTODYN, etc.) integration schemes. Implicit methods are suitable for quasi-static and
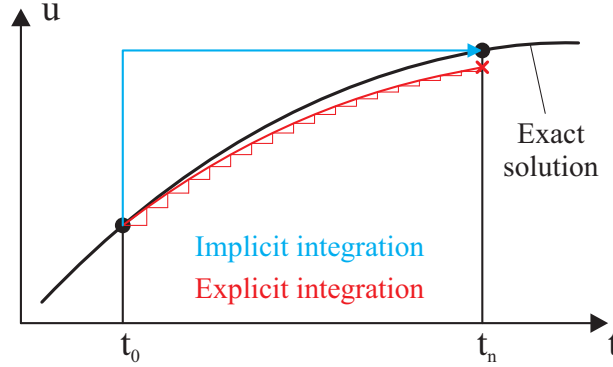
Figure 2.6.: Schematic illustration of implicit and explicit time integration scheme.

slowly evolving events. Typically they need one or very few time increments to obtain a solution. They are limited in case of notably non-linear problems as the size of a time increment has to be considerably reduced in order to converge to a correct solution. In contrast, explicit methods are appropriate for highly non-linear problems with very short time duration, as for example impact and crash events. As the time increment in an explicit time integration is very small, they need a large number of time increments to obtain a solution. The present work mainly focuses on the modelling of impact problems, therefore it uses the explicit time integration method. An introduction to explicit time integration methods can be found in the text books of Wilson [152] and Wriggers [155]. The kinetic relations and the dynamic equilibrium equations of a given time increment can be used to calculate the solution of the following time increment. An example for this approach is the finite difference scheme, after which the displacements at $t + \Delta t$ can be expressed by

$$\ddot{\mathbf{u}}_t = \mathbf{m}^{-1}\left(\mathbf{f}_{ext,t}(\mathrm{t}) - \mathbf{d}\dot{\mathbf{u}}_t - \mathbf{k}\mathbf{u}_t\right) \qquad \text{(Acceleration)}, \qquad (2.15)$$

$$\dot{\mathbf{u}}_{t+1/2\Delta t} = \dot{\mathbf{u}}_{t-1/2\Delta t} + \ddot{\mathbf{u}}_t \Delta t \qquad \text{(Velocity)}, \qquad (2.16)$$

$$\mathbf{u}_{t+\Delta t} = \mathbf{u}_t + \dot{\mathbf{u}}_{t+1/2\Delta t}\Delta t \qquad \text{(Displacement)}. \qquad (2.17)$$

Above equations have to be solved in each time increment for each degree of freedom (DOF). The approach corresponds to a piecewise propagation of the updated displacements and loads (element by element) through the body. From the displacements the nodal forces at $t + \Delta t$ can be calculated. The repeated application of equations 2.15–2.17 allows to solve for a series of time increments if the initial conditions are known.

The above discussed methods of integration are only conditionally stable, if the time increment is smaller than a so-called critical time increment t_{crit}. The critical time increment is based on the largest eigenfrequency of the system and is commonly defined as

$$\Delta t_{crit} = k \left(\frac{L}{c} \right), \tag{2.18}$$

where L is the characteristic element length of the smallest element. The factor k is often used in commercial codes to ensure stability in case of non-linearity. c is the material sound speed, which is

$$c = \sqrt{\frac{E(1-\nu)}{\rho(1+\nu)(1-2\nu)}} \tag{2.19}$$

in case of solid elements,

$$c = \sqrt{\frac{E(1-\nu)}{\rho(1-\nu^2)}} \tag{2.20}$$

in case of shell elements and

$$c = \sqrt{\frac{E}{\rho(1-\nu^2)}} \tag{2.21}$$

in case of solid-shell elements. The smaller the element size and the stiffer the material, the smaller becomes the critical time increment. Therefore, the computation time of an explicit time integration scheme mainly depends on element size and number of integration points. In order to limit the computation time, explicit analyses often run with single precision (cf. [48]). It is also noted, that explicit analyses often use a reduced integration technique with one-point quadrature instead of a full integration. This reduced integration avoids locking phenomena but leads instead to zero-energy modes commonly called 'hourglass-modes', which can cause numerical instability through uncontrolled oscillations. For these cases commercial codes provide hourglass control algorithms, which minimise this effect of one-point quadrature elements (PAM-CRASH manuals [47, 48]). Reduced integration typically results in a reduced computation time.

2.4.2. Modelling impact on cellular sandwich structures with FEM

An important question is how to correctly represent the behaviour of cellular sandwich structures (such as foldcore and honeycomb) in impact. Generally the physical phenomena associated with impact damage and progressive collapse of composite sandwich structures are complex and therefore simulation tools for design and analysis as well as predictive models are being widely investigated. Key issues are the development of constitutive laws for modelling composites in-ply and delamination failures of the face sheets, suitable models for complex sandwich cores and the efficient implementation of the material models into explicit FE codes.

There are several approaches in literature which aim to describe sandwich structures with face sheets and core numerically. A very basic approach is to model the sandwich setup

with a stack of three shell elements representing face sheets and core or a single multilayered shell where face sheets and core are represented by individual layers. A parameter study investigating different setups of this approach using linear elastic material properties for face sheets and core was performed by Manet [115]. The shell-based approach is in particular suited to reproduce the elastic bending behaviour of very large sandwich structures. However it is noted that the shell-based method limits the consideration of local damage and failure and therefore is not well qualified to model impact events.

It is noted, that Kärger et al. [106] modified the shell-based approach to provide efficient simulation of damage resistance of honeycomb sandwich panels subjected to low-velocity impact. By using an element formulation which accounts for the full 3D stress state and implementing a failure analysis based on a progressive damage mechanics approach the onset of damage is correctly predicted. Damage progression is not considered by the model.

Another straight-forward method is a homogenisation, which replaces the cellular core with an equivalent continuum model of three-dimensional solid elements. By the homogenisation the constitutive behaviour of the solid element setup is adapted to the effective properties measured for the respective cellular core. The face sheets are represented by shell elements. This approach has been investigations in various publications. Besant et al. [25] and Heimbs [75] used homogenised solid elements to predict the crushing behaviour of honeycombs. The honeycomb was modelled as fully anisotropic material completely uncoupled in all directions and linear-perfect plastic material behaviour. Similar approaches have been used by several other researchers [11, 76, 83, 118] to model impact on foam and honeycomb sandwich panels. PAM-CRASH [48, 49] provides three material models (Material type 31 and Material type 41, 42) based on homogenisation, which have been specifically designed to reproduce the nonlinear behaviour of honeycombs. They allow to implement the constitutive behaviour of highly anisotropic materials. Both material models assume a fully uncoupled material behaviour in all directions.

However in case of honeycombs or foldcores, these models suffer from a certain drawback, as schematically illustrated in figure 2.7: The common stress-strain curves in out-of-plane compression and shear demonstrate an initially stiff behaviour and a sudden considerable degradation in material properties caused by cell wall buckling and folding. This is schematically illustrated for a compression case in figure 2.7a, where (I) signifies the initial stress peak, (II) signifies the decreased stress level during which the foldcore interfolds and collapses and (III) marks a significant increase in stiffness due to complete densification and compaction of the cell wall material.

Implementing this stress-strain curves into the material model causes each individual element to react like the whole foldcore/honeycomb. The result is an atypical stress-strain response of a mesh where several rows of elements are distributed in the sandwich's out-of-plane direction. This is exemplified for a mesh with three rows of elements as depicted in figure 2.7b, which is loaded in compression. The elements behave like a single element until the peak stress is met (IV). However, as soon as a single row of elements is degrading, the other rows are unloaded to the considerably lower collapse stress level. Once the degraded row of elements reaches the densification phase and the increasing stress is equal to the peak

a) Foldcore compression   b) Recurring stress peaks   c) Cut-off of the stress peak

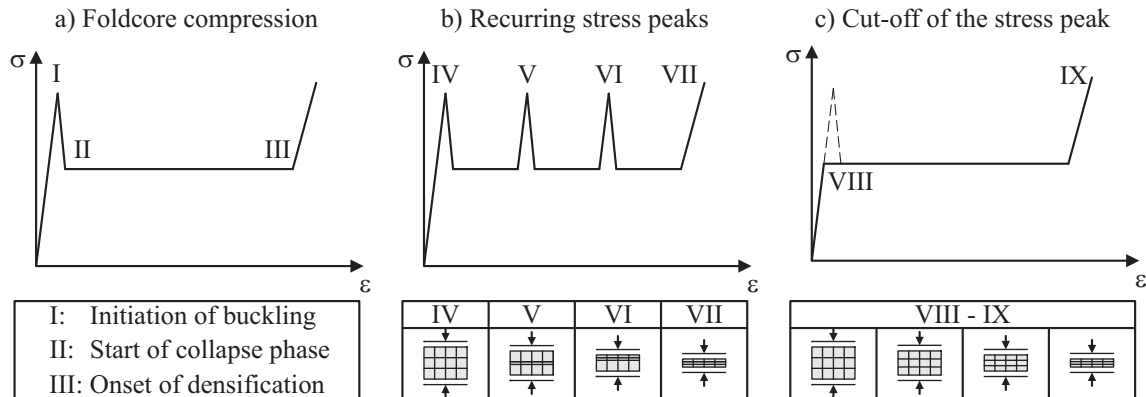| I: | Initiation of buckling |
| II: | Start of collapse phase |
| III: | Onset of densification |

Figure 2.7.: Schematic illustration of a) the characteristic foldcore/honeycomb behaviour in compression b) recurring stress peaks caused by homogenised element instability c) avoidance of instability by cutting off the stress peak.

stress the second row of elements begins to degrade (V). This sequence is repeated until all rows of elements are collapsed (VII) and after which the stress now further increases in all elements beyond peak stress magnitude.

A simple workaround is to cut off the peak stress (VIII) as depicted in figure 2.7c. As the stress in the material is now continuously increasing the consecutive full failure of elements/rows of elements is avoided. However the material model then underestimates the stress levels at which the collapse of the foldcore/honeycomb is initiated. This approach gives a good approximation of energy absorption, which is important if sandwich cores are used for example as crash absorbers. However the approach is limited in case of impact, as core failure is localised and a correct representation of the peak stress is important.

Therefore a homogenised model is a convenient way to represent the real core geometrically, but it is limited if it is used to model core damage and degradation. The main reason is that in each homogenised element the constitutive behaviour of a whole foldcore is implemented, whereas in the model it represents only a small, local part of it. Another limitation may also be that it cannot reproduce the exact damage propagation caused by the discontinuous surfaces of a cellular core in contact with the face sheets.

In recent years the increase in computational power has promoted the meso-model approach, which models the core explicitly with shell elements to obtain more realistic distributions of stresses and strains. Considerable research has been invested in the design of shell-based meso models and their respective cell wall material models. The focus of this research is mainly aimed at modelling of the quasi-static behaviour of cellular cores (primarily in compression and shear) as well as on the prediction of impact behaviour of cellular sandwich structures.

The crushing of aluminium honeycomb cores with the explicit code PAM-CRASH was modelled by Chawla et al. [34] who studied the influence of modelling parameters like loading

rate, element size and material models. The aluminium cell wall was presumed to be isotropic and nonlinear elastic-plastic. Aminanda et al. [14] investigated the crushing of Nomex®, paper and aluminium honeycomb cores experimentally, numerically and analytically. A comparable modelling approach can be found in the work of Aktay et al. [12] where experimental and numerical analyses of the crushing of aluminium and Nomex® honeycomb cores where performed as well as in the work of Foo et al. [59] where impact on Nomex® honeycomb cores was researched. All data from the open literature demonstrate that large compressive deformations of cores with fibre network type cell walls and which are mainly governed by buckling and bending, can be modelled using explicit codes in combination with an elastic-(perfect) plastic material model. Similar conclusions were drawn by Lamb [111] who simulated a range of different load conditions on honeycomb sandwich structures for crash absorption in Formula 1 applications.

Less research exists regarding the modelling of the cell-wall behaviour of foldcore structures. Nguyen et al. [121] modelled spherical impact on aluminium honeycomb and foldcore sandwich structures in LS-DYNA using an isotropic non-linear elastic-plastic cell wall model. First results showed substantial potential but were abandoned due to excessive computational time consumption. Heimbs et al. [76,77] compared explicit simulation and experiment of aramid and carbon composite foldcore crushing and impact behaviour. The folding and kinking cell walls of the aramid paper structure were satisfactorily modelled on basis of an isotropic elastic-perfect plastic cell wall model. However the post-failure behaviour of the carbon composite foldcore which is mainly governed by crushing cell walls was difficult to represent.

A slightly different approach was employed by Buitrago et al. [32] to model an aluminium honeycomb sandwich structure. Here the face sheets were modelled using a fine mesh of solid elements and the honeycomb core was modelled with the shell-based meso-model. Far from the impact location the honeycomb core was represented by homogenised solid elements. Good agreement of experiment and simulation was reported for impact with high velocities.

An important advantage of the meso-model approach is, that due to the detailed representation of the cellular structure the damage initiation and propagation can be modelled accurately until total failure based on the implemented material degradation and failure mechanisms of the cell wall. A further advantage is that the cellular structure can be directly represented by fold geometry and cell wall material behaviour. Therefore there is no need to tediously determine the complex constitutive behaviour of cores with different fold geometry separately. However it is noted that the meso-model approach requires a significant number of elements of small size for its detailed mesh structure. The computational costs are considerably larger than in the other approaches.

2.4.3. Thesis structure based on literature review

The present work follows the research reviewed into the development of an FE methodology, which tries to represent the behaviour of a foldcore sandwich structures in various load environments. These load environments include quasi-static compression and shear loads as well as dynamic load states caused by low- and high-velocity impact. In order to give a precise

reproduction of the mechanical and structural behaviour in all load cases the detailed meso-model modelling approach discussed in section 2.4.2 is proposed. The motivation is that the meso-model approach has the best performance in describing all relevant physical mechanisms and is able to conveniently handle large numbers of different foldcore geometries.

For the implementation of a shell based meso-model accurate numerical descriptions of the respective geometries and material behaviours which range from initial elastic behaviour up to –if required– total failure are necessary. Additionally several other factors can influence the modelling results, such as skin-core interface, sliding and friction, material irregularities, boundary conditions, numerical inaccuracies, etc. In summary, the physical and numerical mechanism governing response of a composite foldcore sandwich model are very complex, especially in case of impact. In order to provide reliable results the development of a meso-model for impact on sandwich structures is realised in three sub-parts, which build on each other. The first part includes the modelling of the cell wall material, the second part covers the description of foldcore structures and the third part extends the foldcore model to impact. This partitioning allows to evaluate the individual model characteristics separately.

In summary the required work steps in this thesis are:

- Cell wall material: This part is discussed in chapter 3 and focuses on the development of a shell-based material model which captures the characteristics of aramid paper cell wall material. For this purpose the mechanical properties of aramid paper are characterised then a suitable material description is derived. Subsequently the capability of the material model is evaluated by comparison to experimental data.

- Foldcore structure: This part is discussed in chapter 4 and deals with the adoption of the previously developed cell-wall material model to foldcore structures. For this purpose the geometrical and mechanical characteristics of foldcore panels are measured. Based on the geometrical description of a foldcore including its irregularities a shell-based foldcore model is developed. For evaluation the model is subsequently compared to foldcore benchmark tests.

- Impact on sandwich panel: This part is discussed in chapter 5 and describes the extension of the previously established foldcore model to impact. Additionally, the impact behaviour of foldcore sandwich structures is experimentally characterised in order to assess and evaluate the predictive capabilities of the model.

3. Aramid paper

3.1. Overview

This chapter gives an overview on the properties of aramid paper and how aramid paper is modelled in this work. In the first section the characteristics of its constituents are briefly summarised. Subsequently, the structure of aramid paper is discussed on basis of microscopic cut-images (MCI) and computed tomography (CT). The second section of the chapter deals with the measurement of the paper's mechanical properties, which are required for the numerical representation of aramid paper. For this purpose several test series, such as tensile coupon, cylinder crush, thick-walled beam shear and vibration bending tests are presented and discussed. The third section of this chapter then deals with the constitutive description of the aramid paper. The main part of this section discusses the design of a constitutive model for the aramid paper. The main challenges are the considerable orthotropy of the aramid paper and the necessity to reproduce the non-linear mechanical behaviour up to total failure. Finally in the last section the validity and efficiency of the cell wall model is assessed by comparison of experiment and simulation of selected benchmark tests, such as paper coupon test and cylinder collapse test.

3.2. Introduction to aramid paper

In this section the constituents of the aramid paper, the aramid fibre and the phenolic resin are discussed and basic data on their material characteristics are given. The fabrication process of aramid paper is briefly summarised. Subsequently, the microscopic structure of the aramid paper is reviewed and basic mechanisms in the paper-like material are discussed.

3.2.1. Aramid fibre

A factor considerably contributing to the particular mechanical characteristics of the aramid paper is the nature of the reinforcing fibre. The **ar**omatic poly**amid**e was developed by E. I. DuPont de Nemours, Inc. at the beginning of the 1970s. Aramid fibres are man-made high-performance fibres with excellent thermal resistance. Nowadays aramid fibres are widely used and there is much data on their behaviour and properties available in the literature [52,61,150, 157].

Typically aramid fibres are sub-divided into p-aramids and m-aramids. P-aramid fibres were developed in the 1960s and 1970s. They offer high strength and high modulus and are ty-

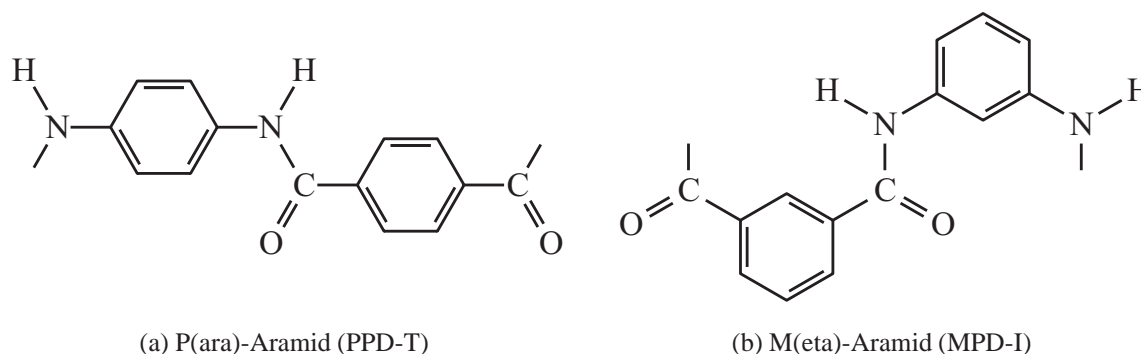(a) P(ara)-Aramid (PPD-T)   (b) M(eta)-Aramid (MPD-I)

Figure 3.1.: Aromatic polyamide, as presented by Yang [157].

pically employed as reinforcement in composite materials. Common tradenames of p-aramid fibre products are Twaron® (Twaron is a registered trademark of Akzo Nobel, Inc.), Technora® (Technora is a registered trademark of Teijin Ltd.) and Kevlar® (Kevlar is a registered trademark of E. I. DuPont de Nemours, Inc.). The chemical formula of p-aramid is illustrated in figure 3.1a.

The other member of the aramid family are m-aramid fibres, which were developed in the 1960s. They demonstrate less strength and modulus compared to p-aramid fibres. In many aspects m-aramid is similar to conventional textile fibres and can be formed into stiff, durable papers. Common tradenames of m-aramid fibre products are Nomex® (Nomex is a registered trademark of E. I. DuPont de Nemours, Inc.) and Teijinconex® (Teijinconex is a registered trademark of Teijin Ltd.). The chemical formula of m-aramid is illustrated in figure 3.1b.

These two types of aramid fibres have several important properties, which were summarised by Wardle [150] as follows. The main characteristics of both types are their excellent fracture toughness and damage tolerance as well as the high tensile strength and modulus which is well comparable to inorganic fibres such as glass and carbon. In combination with their low specific density they are an unusually light, strong and stiff material with high resistance to impact damage. Another prominent quality is the negative coefficient of thermal expansion. In combination with a matrix material with positive coefficient it is possible to create laminates which have very low thermal expansion. The properties of aramid fibres are compared to the properties of other fibre products in table 3.1.

However the compressive and transverse properties of aramid fibres are comparatively low. The chain structure of the polymer molecules is vulnerable to kinking and collapse, which results in significant plastic deformation in the form of kink bands (Andrews et al. [18]). As a result the stress-strain response in fibre direction is considerably asymmetric as it is delineated for a aramid fibre yarn (Kevlar® 49) in figure 3.2. In compression the aramid fibre yields at relatively low strain and subsequently shows a (perfect) plastic behaviour, whereas in tension the fibre behaves linear elastic and shows a very high strength. The behaviour in bending and shear is comparable to the compressive behaviour.

Table 3.1.: Properties of different fibre products taken from Daniel and Ishai [37] and DuPont technical guide [45].

Material	Type	Density [g/cm^3]	Tens. modulus [GPa]	Tens. strength [GPa]	Failure strain [%]
Kevlar 49	p-aramid	1.44	112.4	3.0	2.4
AS-4	High-tenacity carbon	1.8	235	3.1	1.4
Glass	S-glass	2.49	85	4.6	5.4
Boron	Boron fibre	2.35	395	3.5	-
Steel	Steel wire	7.75	200	1.96	2.0
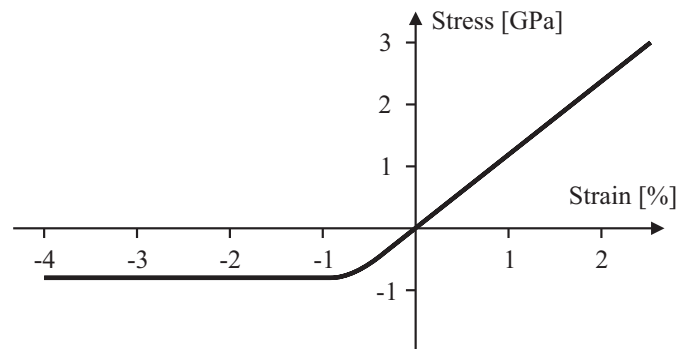
Figure 3.2.: Typical stress-strain-behaviour of Kevlar® 49 yarn, taken from Flemming et al. [57].

Because of their considerable toughness aramid fibres are difficult to process. Typically fabrics have to be cut with special cutting tools and aramid fibre reinforced laminates have to be handled e. g. with water-jet cutting processes in order to obtain satisfying cut surfaces. Aramid fibres tend to absorb humidity and are vulnerable to ultraviolet radiation. It is also difficult to attain a good bond between fibre and matrix and typically the adhesion of different matrix materials to aramid fibres is weaker compared to glass and carbon fibres.

The main characteristics of aramid fires, which are excellent toughness and low weight, make them an ideal material for impact absorption (Wardle [150], Fink [52]). The area of application ranges from low velocity impact to impact cases with very high velocities. Typical examples are impact resistent structures in transport vehicles such as aircrafts, helicopters, automotive vehicles, railway vehicles, etc. and ballistic protection equipment.
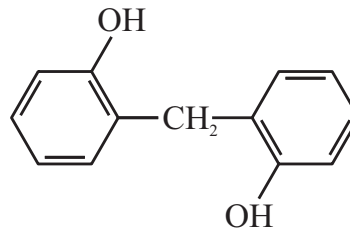
Figure 3.3.: Phenolic resin, as presented in the Phenolic Resins Technology Handbook [123].

Table 3.2.: Properties of different matrix materials taken from Daniel and Ishai [37] and the Phenolic Resins Technology Handbook [123].

Material	Density [g/cm^3]	Modulus [GPa]	Tensile strength [MPa]	Compressive strength [MPa]
Phenolic resin	1.1	5-6	34-55	69-138
Epoxy (3501-6)	1.27	4.3	69	200
PEEK	1.32	3.7	96	-
Polyester	1.1-1.5	3.2-3.5	40-90	90-250
Vinylester (Derakane)	1.15	3-4	65-90	127
Polymides	1.4-1.9	3.1-4.9	70-120	-

3.2.2. Phenolic resin

The properties of phenolic resin in this section have been summarised based on informations taken from the Phenolic Resins Technology Handbook [123]. Phenolic resins are a type of synthetic thermosetting resin invented by Dr. Leo Baekeland in 1907. They are produced by polymerising phenol and formaldehyde under separation of water. The occurrence of water as by-product leads to a certain undesired porosity. Their main characteristics are high temperature resistence, high strength and low smoke generation in case of fire. They also offer a good price/performance profile. The chemical formula of phenolic resin is illustrated in figure 3.3.

Phenolic resins are relatively stiff and non-ductile. Their material behaviour is typically more brittle compared to other resins used in fibre composites such as for example epoxy. The stress-strain curve in tension is essentially a straight line up to the yield point. In compression they show considerable plasticity after an initial elastic phase, which approximates perfect-plastic behaviour before failure. The compressive failure strength is 2-3 times higher than the tensile failure strength. Typical properties of different composite matrix materials are listed in table 3.2.

The percentage of phenolic resin in common fibre composites is relatively low. Their application is limited due to the release of volatile substances (water) during curing and their comparatively brittle behaviour, which makes the adoption as structural components difficult.
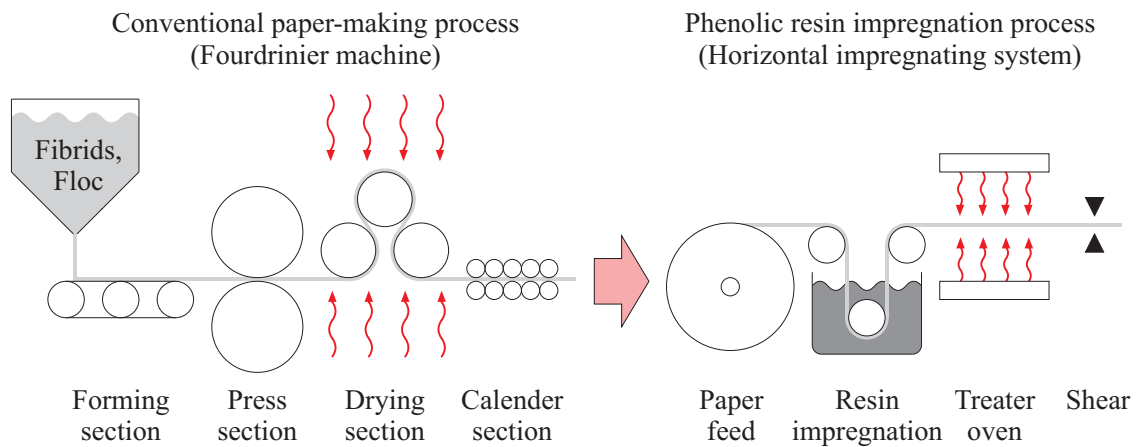
Figure 3.4.: Illustration of the paper-making process and the phenolic resin impregnation process.

Their outstanding property is the excellent thermal resistance and low flammability compared to other resin matrix materials. This, in combination with the good impact resistance, which they share with other resin matrices, makes phenolic resins interesting for applications, where fire safety is important. Typical examples are structures in aviation, mass-transit, marine, off-shore and construction.

3.2.3. Manufacturing of aramid paper

In the scope of this work the primarily investigated paper structure is the 'aramid paper', which is a development similar to the prevalent honeycomb material. The manufacturing process of the investigated aramid paper comprehends of three individual steps. A schematic overview on the first two process steps is given figure 3.4. In the first step an aramid fibre pulp is machined into a raw aramid fibre paper form on basis of a conventional paper-making process (Yang [157], Fink [52]). The aramid fibre pulp is produced from two forms of the aramid polymer. Small fibrous binder particles (fibrids) derived directly from the polymer under high shear conditions are thereby mixed with short fibres (floc) which are cut to length from a fibre filament.

The floc and fibrids are combined in a water based slurry from which a continuous fibre fleece is produced (Forming section). The fibre fleece is subsequently milled (Press section), which generally causes the fibres to be more orientated in the machine direction. In this context machine direction is defined parallel to the milling direction and cross-machine direction signifies the perpendicular orientation. The remaining moisture is removed by a drying process (Drying section). The final densification and internal bonding is achieved by high temperature calendaring (Calender section). The resulting paper is mechanically strong and has good electrical properties.

During the second step the aramid fibre paper is impregnated with phenolic resin, a process which is for example delineated by Brydson [31]. For that purpose the aramid paper is typically machined in a horizontal impregnating system, where the dry aramid paper is immersed in a resin dip and then transported via a roller system through a metering device, where the excess resin is deposited. Subsequent heat tratment allows the fabrication of aramid paper prepreg.

In the third step the aramid paper prepreg is brought into its final structural shape. In the present work this shape corresponds to the fold structure of the foldcore sandwich core. The folded aramid paper prepreg is then subjected to a heat treatment in which it is cured in its final form. The cured aramid prepreg is called 'aramid paper'. The mass per area of the cured aramid paper is about 240 g/m^2.

3.2.4. Composition and structure of aramid paper

The aramid paper consists of randomly orientated aramid fibres bonded together by phenolic resin. As its abbreviation 'aramid paper' already indicates it shares some basic properties and behaviours of a 'common' paper structure. A paper material as defined by Bristow and Kolseth [29] is a two-dimensional fibre network. It mainly depends on the elastic and strength properties of the fibres, the bond between the fibres and the geometrical characteristics of the fibre network. The geometrical characteristics include fibre length, fibre cross-sectional shape, fibre orientation distribution, fibre curl and the quantity and formation of the fibre-to-fibre bonds. In general a paper structure exhibits some unique characteristics:

- Anisotropy: The anisotropy depends mainly on the inhomogeneous character of the fibre network. Dependent on the manufacturing process the fibres generally lie parallel to the plane of the paper. Secondly a non-uniform, in-plane orientation distribution of the fibres is caused by the milling process. In general the anisotropy in thickness direction is considerably more pronounced than in planar direction.

- Planar nature of paper: The magnitude of the dimensional size in thickness direction compared to the planar dimensions is very small. In fact the difference in scale of the paper's thickness relative to the characteristic length of the fibre network structure is marginal. This inherent geometrical nature poses quite a challenge when experimentally evaluating the through-thickness properties.

- Inhomogenity: In reality a fibre network such as paper exhibits an uneven distribution of mass density and local thickness. The main reason is the irregular orientation and allocation of individual fibres and fibre flocs. In case of aramid paper the phenolic resin matrix which has a weight proportion twice as much as the aramid fibres additionally causes considerable inhomogenity especially through-thickness direction of the paper.

A photography of plain writing paper is added in figure 3.5a to point out the astonishing visual conformance to the aramid paper depicted in figure 3.5b. The dimensions of the photographies

(a) Writing paper

(b) Impregnated aramid paper

(c) Unimpregantd aramid paper

(d) Impregnated aramid paper

(e) Impregnated aramid paper
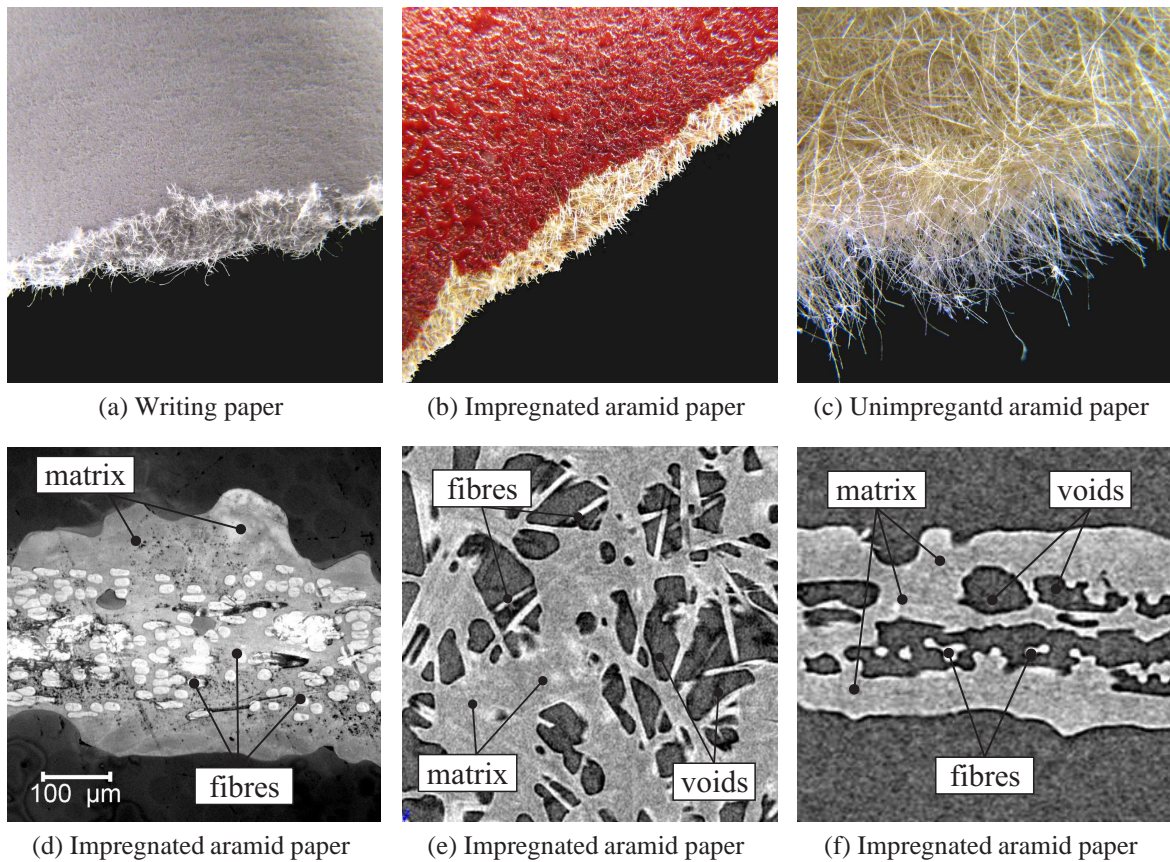

(f) Impregnated aramid paper

Figure 3.5.: (a) Standard writing paper (80 g) made of cellulose pulp (b) Impregnated and cured aramid paper (c) Uncured aramid paper prior to impregnation with phenolic resin (d) Microscopic image of aramid paper cross-section (e) Computer tomography of aramid paper midplane (f) Computer tomography of aramid paper cross-section.

in the top row of figure 3.5 are about 10 mm. In figure 3.5c the cured aramid fibre fleece prior to the infiltration with phenolic resin is illustrated. The fibre network character is clearly noticeable (by the naked eye). Variation in fibre length and fibre curl can be observed.

A study of micrographic images of aramid paper cross-section as depicted in figure 3.5d leads to following observations: The distribution of fibres in out-of-plane direction of the paper is inhomogeneous. The fibres are concentrated in the papers midplane showing an almost constant fibre dispersion in thickness direction which measures about 0.2 mm. An irregular distribution of pure resin film can be observed on the surface of the aramid paper which measures about 50 % of the total local thickness. This irregular pattern of resin film causes significant variation in paper thickness, which ranges from 0.2 mm to 0.4 mm.

In figure 3.5e and 3.5f the top-view of an impregnated aramid paper midplane as well as the cross-section of an aramid paper are visualised by computed tomography. The distribution

of phenolic resin in the fibre reinforcement is highly irregular and there is a significant number of voids. The voids are mainly located in the fibre reinforced region. Considerably less voids are observed in the pure resin film, which covers the surfaces of the fibre reinforcement. It is noted, that the polished cut image of figure 3.5d generally shows less voids. A reason may be, that the grinding process of the cut surfaces tends to disperse the phenolic resin to some degree.

On basis of the examination of a sequence of micrographic images an average paper thickness of 0.30 mm can be approximated. The measured data is consistent with the observations made by Baranger et al. [20] who also investigated fibre direction distribution in the plane of the paper. The surface fibre rate in machine direction was observed to be more pronounced than the surface fibre rate in cross-machine direction with 7.9 % compared to 5.1 %.

3.3. Experimental characterisation

This section presents test series which aim to evaluate the paper's mechanical properties ranging from behaviour under general loading conditions up to total failure. The main intent is to provide sufficient mechanical data to design a material model which is capable to reproduce all types of quasi-static as well as dynamic load events. In consideration of this motive it is necessary to determine the elastic properties as well as the occurrence of damage and plasticity prior to total failure. Due to the intrinsic properties of aramid fibre composites, which differ especially in the post-elastic regime, the strong tensile behaviour and the weak compressive behaviour have to be measured separately. Finally an approach to quantify the effect of the inhomogeneous fibre distribution in out-of-plane direction is proposed. Partial aspects of the presented work have been published by the author in the research works of Kilchert et al. [101] and Fischer et al. [54, 55].

To characterise the mechanical behaviour of paper material it is necessary to expend considerable effort on design of specimen and test setup in order to overcome the difficulties given by its inherent mechanical characteristics. Due to its fibre network structure and planar nature the practicable minimum size of specimen is limited and especially the evaluation of compressive and out-of-plane properties is challenging. There is a broad consensus that paper behaves as an orthotropic material [29, 51, 133] which leaves nine elastic constants to be determined as given by

$$
\begin{pmatrix} \varepsilon_{xx} \\ \varepsilon_{yy} \\ \varepsilon_{zz} \\ 2\varepsilon_{yz} \\ 2\varepsilon_{xz} \\ 2\varepsilon_{xy} \end{pmatrix} = \begin{pmatrix} \frac{1}{E_x} & -\frac{\nu_{xy}}{E_x} & -\frac{\nu_{xz}}{E_x} & 0 & 0 & 0 \\ -\frac{\nu_{xy}}{E_y} & \frac{1}{E_y} & -\frac{\nu_{yz}}{E_y} & 0 & 0 & 0 \\ -\frac{\nu_{xz}}{E_z} & -\frac{\nu_{yz}}{E_z} & \frac{1}{E_z} & 0 & 0 & 0 \\ 0 & 0 & 0 & \frac{1}{G_{yz}} & 0 & 0 \\ 0 & 0 & 0 & 0 & \frac{1}{G_{zx}} & 0 \\ 0 & 0 & 0 & 0 & 0 & \frac{1}{G_{xy}} \end{pmatrix} \begin{pmatrix} \sigma_{xx} \\ \sigma_{yy} \\ \sigma_{zz} \\ \sigma_{yz} \\ \sigma_{xz} \\ \sigma_{xy} \end{pmatrix}. \tag{3.1}
$$

The x- and y-axes signify the in-plane directions and the z-axis signifies the out-of-plane direction. The variables σ_{ij} are the stresses and the variables ε_{ij} are the strains. The elastic constants are the normal moduli E_x, E_y, E_z, the shear moduli G_{yz}, G_{zx}, G_{xy} and the Poisson's ratios ν_{yz}, ν_{zx}, ν_{xy}. A method to determine all nine orthotropic elastic constants of machine-made paper was detailed by Mann et al. [116]. The in-plane normal stiffnesses of Nomex® paper have been investigated by Foo et al. [58] and all in-plane moduli for tensile and compressive loading of Nomex® paper have been established by Hähnel and Wolf [80]. It is noted that the scope of the following section is limited due to availability of test machines to the determination of the most relevant elastic constants which are the in-plane constants E_x, E_y, ν_{xy} and G_{xy}. The stiffness and strength in out-of-plane direction is typically 50 to 100 times smaller than the in-plane properties. The two Poisson's ratios ν_{xz}, ν_{yz} for the coupling between the in-plane and thickness directions are very close to zero whereas their corresponding ratios ν_{zx}, ν_{zy} are large.

The elastic moduli and damage behaviour in normal in-plane directions was investigated on basis of tensile coupon tests and ring crush tests. On basis of thick-walled beam shear test the in-plane shear behaviour of the aramid paper was determined. Test data of vibration bending tests taken from Baranger et al. [20] is presented to provide insight on how the inhomogeneous distribution of fibres in the out-of-plane direction is affecting the elastic behaviour of the aramid paper.

3.3.1. Tensile coupon test

The purpose of the tensile coupon test is to determine the in-plane tensile behaviour of the aramid paper. In the following the measurement of tensile normal modulus, the Poisson's ratios, the tensile failure stresses and the tensile stress vs. tensile strain response in both in-plane orientations is delineated and discussed. Additionally the amount of plasticity is evaluated using cyclic loaded coupon specimens.

The quasi-static tensile test series was conducted on a Zwick universal testing device. The preparation and performance of the coupon tests are in accordance to ISO 1924-2 [43] with minor modifications. The specimens are tapered along their length to a minimum width of 10 mm to avoid failure in adjacency of the clamping. An emphasis must be placed on the grips to minimise slippage. Satisfactory results were achieved with aluminium tabs at the clamping brackets. The specimen were prepared such that the fibre network was either axially loaded in machine direction or in cross-machine direction. The test setup is depicted in figure 3.6 and the test conditions are summarised in table 3.3.

A challenge presents the measurement of the specimen's elongation as the stiffness is considerably affected by traditional methods such as strain gauges. An elegant way out of this dilemma is offered by optical measurement methods which follow the relative displacement of a speckle pattern applied to the specimen. On basis of the pattern's time-dependent variation the displacement and strain fields of the monitored area can be calculated in all three dimensions. It is noted that the observed strain distribution during testing varied over the speimen area as can be seen in figure 3.7. The contour plots show the strain distribution after start of

Figure 3.6.: Test device

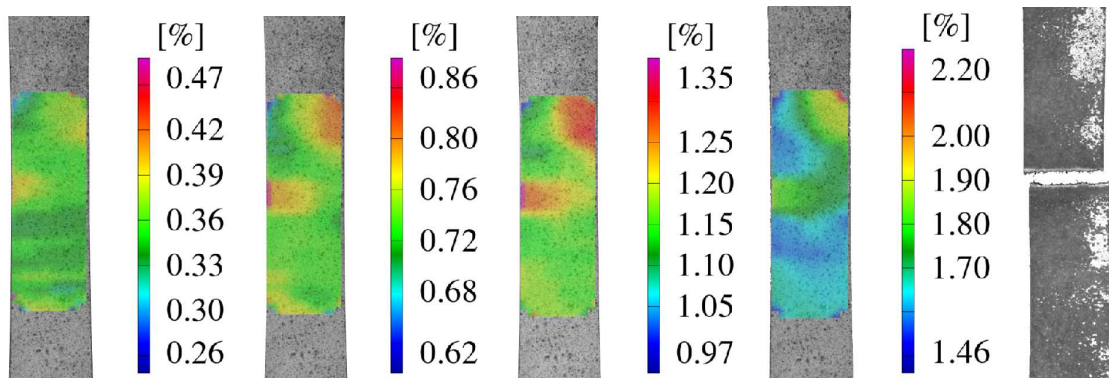| Test method:	A	Coupon test
	B	Cyclic coupon test
Test standard:		DIN EN ISO 1924-2
Test rate:		2 mm / min
Specimen material:		Aramid paper
Specimen dimension:		250x15x0.30 mm
Number of specimen:	A	10
	B	10

Table 3.3.: Test specifications

Figure 3.7.: Contour plots of longitudinal strain from test initiation until briefly before failure of specimen and photography of failed specimen.

the test and just before total failure. The quality of distribution was consistent during the entire test duration. This non-uniform behaviour is mainly caused by the irregular paper thickness and fibre network properties as illustrated in section 3.2.4. A global strain can be defined by computing the average of the non-uniform strain in a sufficiently large area.

Figure 3.8 shows the averaged stress-strain behaviour of 5 specimens loaded axially in machine direction and of 5 specimens loaded axially in cross-machine direction. The highlighted curves signify the averaged values of the individual test curves, which are printed in light colours. The presented stresses and strains are values averaged over all sub sets, which are located on the narrow waist of the specimen. Stress is the load measured with a 5 kN sensor divided by the sectional area of the sample whereas the strain is the global strain described above. The optical strain measurement captures the normal strain in both in-plane directions which permits the calculation of the in-plane Poisson's ratios, if it is assumed that the stiffness
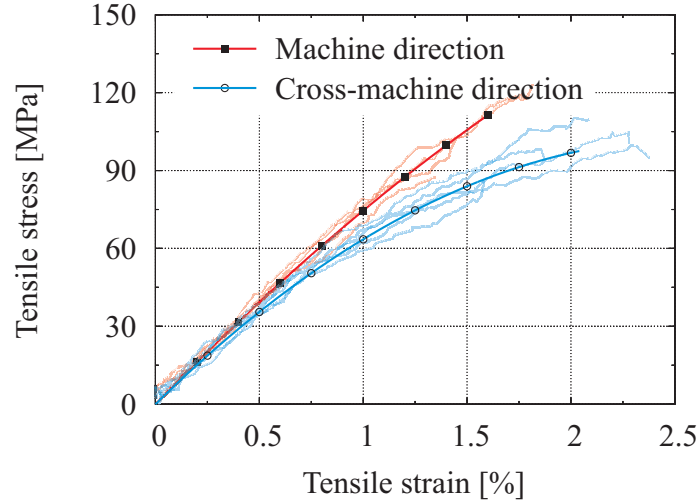
Figure 3.8.: Averaged longitudinal stress-strain-curve of tensile aramid paper specimen loaded in machine and cross-machine direction.

and Poisson's ratios in out-of-plane are very small and can be neglected. In case of infinitesimal linear elasticity the in-plane Poisson's ratios are calculated as

$$\nu_{xy} = -\frac{\varepsilon_{yy}}{\varepsilon_{xx}} \qquad \text{and} \qquad \nu_{yx} = -\frac{\varepsilon_{xx}}{\varepsilon_{yy}}. \tag{3.2}$$

It is noted that considerable scatter from the averaged curves can be observed in figures 3.8 and 3.9 if the individual test curves are compared.

   Figure 3.9 shows the distribution of the longitudinal stress versus the strain measured in transverse direction. Typically the stress-strain behaviour of a specimen is mainly (nonlinear) elastic until sudden failure by fracture. The elastic modulus in machine direction is observed to be approximately 8 % larger than the modulus in cross-machine direction whereas the failure stress in machine direction is 3.5 % higher than in cross-machine direction. By contrast the failure strain in cross-machine direction is about 1.2 times the failure strain in machine direction.

   Again the influence of in-plane orthotropy observed in section 3.2.4 is apparent. Generally the strain energy is transmitted to adjacent fibres within the network through the sites of bonding. The fibre segments are prevalently orientated in machine direction and thus offer considerable stiffness and large maximum stress if loaded accordingly. In case of loading in cross-machine direction a large number of fibre segments first align themselves in load direction before gradually starting to transfer loads. During alignment in load direction substantial matrix cracking and debonding of fibres and matrix occurs. The resulting damage in the network structure leads to lower maximum stress levels. The fibre alignment process permits a significant increase in maximum strain where the specimen fails if the majority of fibres are straightened and met their individual load limit. In both cases damage occurs first as cracks in
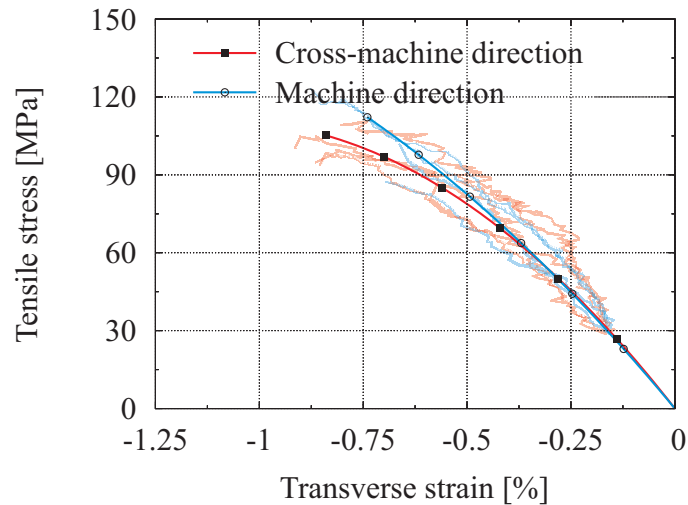
Figure 3.9.: Averaged longitudinal stress vs. transversal strain in machine and in cross-
machine direction.

the external resin coating, followed by matrix cracking and fibre debonding until eventually
the specimen fails due to fibre breaking.

The assumption that the appearance of matrix damage varies depending on the respective
load direction is also supported by observations made in cyclic tension tests. The stress-strain
behaviour of single specimens in machine and cross-machine direction is illustrated in figures
3.10 and 3.11. The observed plasticity is approximately 14 % in the machine direction and
approximately 23 % in the cross-machine direction. During the experiment a continuous de-
gradation of the stiffness was visible, which is already initiated at low loads. This observation
is inconsistent with the general behaviour measured for (straight) unidirectional aramid fibres
loaded in tension, which are essentially linear elastic until failure. An explanation of the ob-
served behaviour is that the plasticity is predominantly caused by fibre segment realignment
and associated local matrix damage. The larger the number of fibre segments is, which are
orientated such that they are initially able to transfer loads, the less fibre realignment and
matrix degradation occurs.

Table 3.4 summarises the mechanical benchmark parameters determined for in-plane
behaviour of aramid paper. The presented data is based on average values of the measured
material test curves. Naturally a considerable scatter of about 4–14 % exists caused by the
inhomogeneous nature of the paper. The elastic moduli have been measured from the secant
of the averaged stress-strain values at 0.3–0.6 %. The main reason to derive the stiffness
properties from small stress and strain values is to consider the observed non-linear elasticity
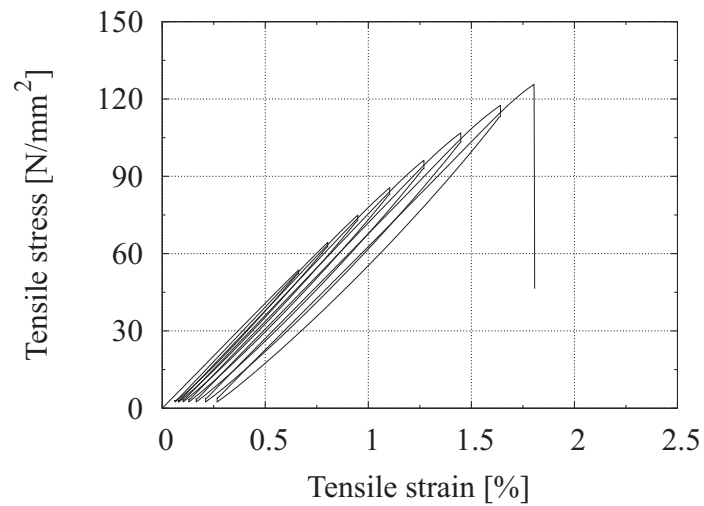and degradation in stiffness, which occur at small loads.

Figure 3.10.: Cyclic stress-strain-curve of tensile aramid paper specimen loaded in cross-machine direction.
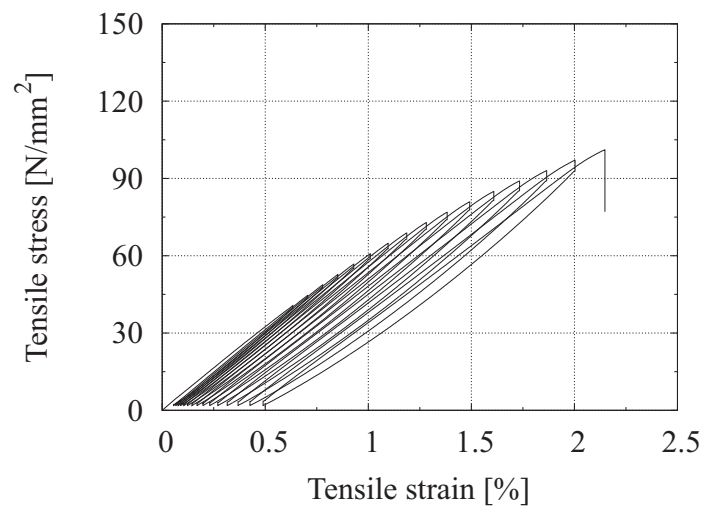

Figure 3.11.: Cyclic stress-strain-curve of tensile aramid paper specimen loaded in cross-machine direction.

Table 3.4.: Tensile properties of aramid paper measured in tensile coupon test. The coefficients of variation are presented in parentheses.

Orientation	Elastic modulus [GPa]	Poisson's ratio [-]	Tensile failure stress [MPa]	Tensile failure strain [%]	Plasticity [%]
MD	7.7 (5%)	0.3 (-)	111 (13%)	1.6 (13%)	14 (-)
CD	7.1 (4%)	0.4 (-)	97.5 (8%)	2.04 (14%)	23 (-)

3.3.2. Cylinder crush test

The cylinder crush test is used to determine the in-plane compressive behaviour of the aramid paper. In the following the measurement of compressive normal modulus, the compressive yield stresses and the compressive stress vs. compressive strain response in both in-plane orientations is described and discussed.

The quasi-static cylinder crush test series was realised with a Zwick universal testing device. Generally the compressive behaviour of paper-like materials can be investigated mechanically (Uesaka [148], Fellers [50] and Haraldson et al. [73]) with methods like ring crush test (DIN 53134 [42]), short span test (ISO 9895 [88]) and support test (ASTME E9-09 [19]). Underlying motive of these tests is to overcome the structural instability due to the marginal out-of-plane expansion of the paper which makes the determination of the compressive material behaviour considerably difficult. The main challenge is to separate the material behaviour from the structural behaviour, especially in the post-elastic region. To avoid the prevalent instability due to buckling either the unsupported axial length of the specimen needs to be reduced or the area moment of inertia needs to be increased. An example for a reduction of unsupported length is the short span test where the basic idea is that crushing of the specimen occurs before any buckling of the specimen can take place. Another method is to support the paper material in compression on each its sides against buckling as it is done for different kinds of support tests. A third alternative is the compression of cylindrical specimen where the substantial increase in area moment of inertia is employed as for example demonstrated by ring crush tests.

The reason for choosing cylinder crush tests in this work was that they allow to determine the aramid paper compressive properties up to failure on basis of a convenient approach. The underlying theory of the cylinder crush test is as follows: If the height of a cylinder with constant radius and thickness is decreased, the stress level at which buckling occurs increases. Eventually a height will be found where the stress at which instability occurs is equal to the compression strength of the material. With further decrease in height, the cylinder is crushed before it buckles, and the maximum stress sustained by the cylinder remains constant at the compressive strength of the material, as depicted in figure 3.13. Therefore it is important, that the cylinder dimensions given by height, radius and wall thickness are chosen such that crushing failure rather than buckling failure occurs. There are a number of effects which

(a) Cylinder specimen and method of fixation   (b) Crushed cylinder wall
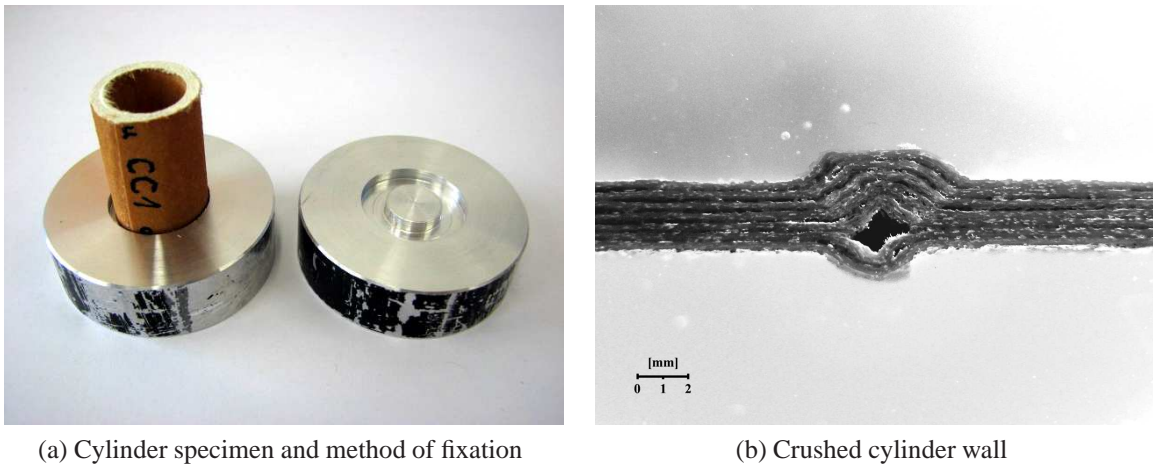
Figure 3.12.: (a) Illustration of cylinder crush specimen and its method of fixation (b) Close-up view showing the cross-section of a crushed cylinder wall.
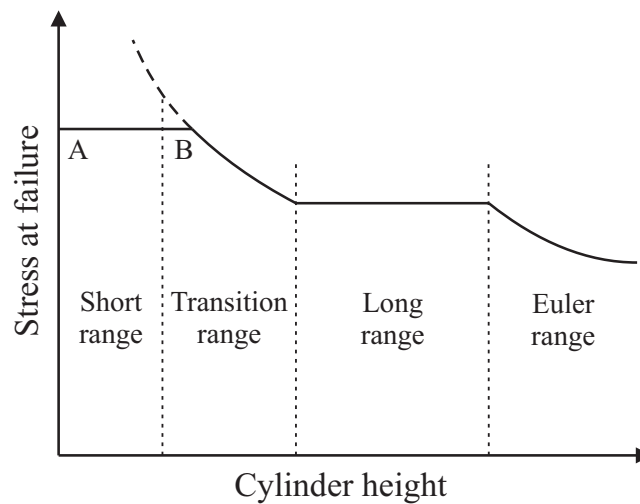

Figure 3.13.: Stress at failure versus height of cylinder, taken from Fellers [50].

impair to some extent the results of the cylinder crush tests. It is possible that high stresses may develop in the aramid paper perpendicular to the loading direction, which in turn may seriously decrease the load at failure of the cylinder. Another factor is the impact of the seam structure created by the fabrication of the cylinder which can cause considerable non-axis-symmetric deformation.

Based on the ring crush test described in DIN 53134 [42] cylinder crush specimens were produced with small height and thick cylinder walls consisting of seven plys of aramid paper. The hollow cylinder was formed by rolling the aramid paper prepreg around a teflon tube and subsequently bonding the paper prepreg layers together during the curing process. In the pro-
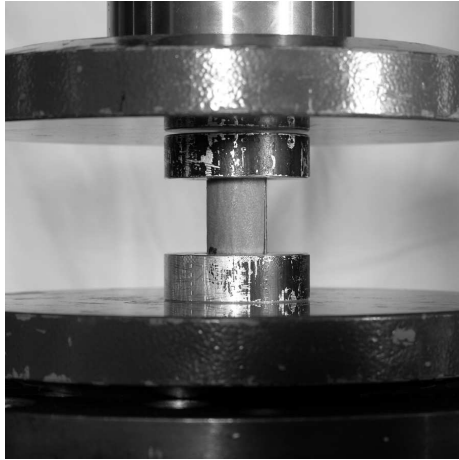
Test method:	Ring crush test
Test standard:	ISO 12192
Test rate:	1 mm / min
Sample material:	Aramid paper
Sample dimension:	Height: 30 mm
	Inner radius:
	Ø15.6–16.2 mm
	Outer radius:
	Ø20.0–20.9 mm
Number of specimen:	10

Figure 3.14.: Test device   Table 3.5.: Test specifications

cess the prepreg layers are compressed only by the residual stresses due to initial tight rolling. The length of the rolled paper strip was chosen such that the endings of the strip at inner and outer diameter are located at the same circumferential position. The test setup is depicted in figure 3.14 and the test conditions are summarised in table 3.5. The load environment was displacement controlled with a compression velocity of 1 mm/min. The boundary conditions of a fixed end are ensured by bonding the top and bottom of the cylinder to prepared notches within the clamping device with epoxy resin. The specimen and upper and lower clamping devices with notched surfaces are illustrated in figure 3.12a. Particular consideration was used to confirm the parallelism of the clamping devices by separate distance pieces. The cylindric specimen were prepared such that the fibre network was either axially loaded in machine direction or in cross-machine direction.

Figure 3.15 depicts the averaged stress-strain behaviour of 5 specimens loaded axially in machine direction and of 5 specimens loaded axially in cross-machine direction. Stress is the load measured with the 100 kN sensor divided by the sectional area of the sample and strain is the displacement of the transverse divided by the initial cylinder height. The cylinder is compressed elastically until peak load whereas it depicts similar continuous degradation from linear elasticity as observed during the tensile coupon tests. It is noted, that the peak compressive stress is about half the level of the maximum tensile stress, as it is also observed for compressive testing of paperboard. Subsequently, the cylinder begins to collapse around a ring-shaped initial zone at a constant stress level which remained constant up to strains of about 20 % at which the execution of the experiment was stopped. The constant stress level during collapse phase is about the same magnitude for machine and cross-machine direction. The delineated compression behaviour was reproducible for all samples of the test series.

The picture sequence illustrated in figure 3.16 depicts the external deformation of the cylinder specimen during the crush test at strains ranging from 0 % to 25 %. At yield stress the cylinder typically fails by forming a kink band and then briefly after starts to buckle locally in
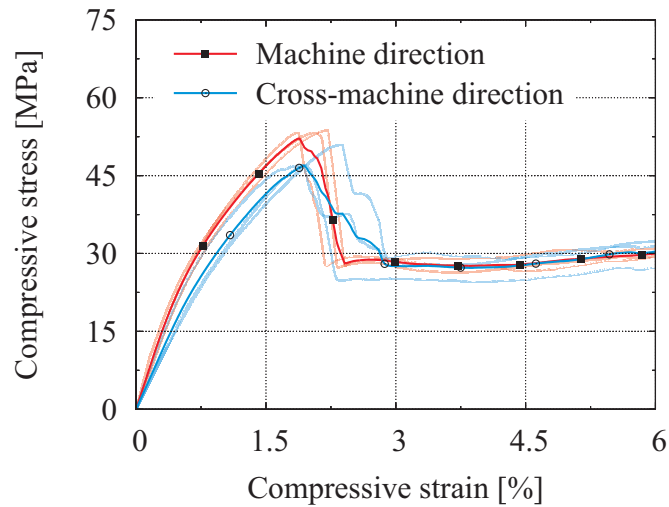
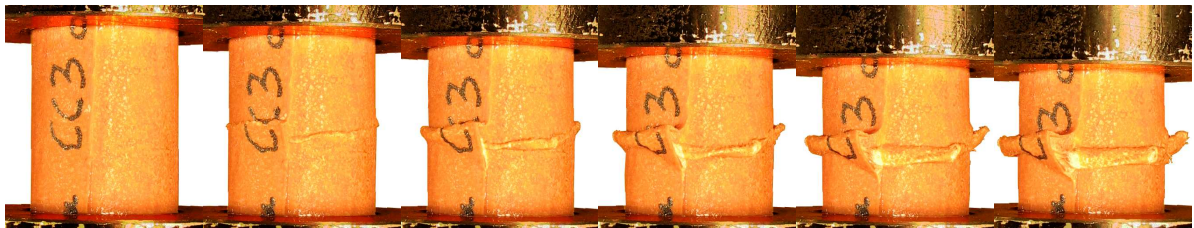Figure 3.15.: Stress-strain-curve in machine and cross-machine direction.

Figure 3.16.: Picture sequence of cylinder crush test at compressive strains of about 0 %, 5 %, 10 %, 15 %, 20 %, 25 %.

the yield zone. In the process debonding between two or in some cases several paper plys can be observed, which is initiated in the yield zone. Figure 3.12b shows a cut image focussed on the yield region of the cylinder wall cross-section, which illustrates a debonding between the fifth and the sixth paper ply.

The occurrence of debonding explains the considerable decrease in stress level after reaching the yield strength as the separated wall sections have a lower area moment of inertia. The lower collapse stress is an obvious indicator that the structure effects the stress-strain-behaviour after reaching the yield strength. However, the constant stress level during collapse indicates, that similar to the behaviour of UD aramid laminates in compression the aramid paper behaves perfectly-plastic after reaching the yield strength.

Table 3.6 summarises the mechanical benchmark parameters, which have been determined for the in-plane compressive behaviour of aramid paper. The presented data is based on average values of the measured test data. The elastic moduli have been determined from the gradients of the averaged stress-strain curves in the origin. As for the tensile tests a considerable scatter of about 1–9 % has been observed during the experiments. The elastic moduli

Table 3.6.: Compressive properties of aramid paper measured in cylinder crush tests. The
             coefficients of variation are presented in parentheses.

Orientation	Elastic modulus [GPa]	Yield strength [MPa]	Yield strain [%]	Collapse stress level [MPa]
MD	4.7 (4%)	53 (0,5%)	1.9 (6%)	29.5 (3%)
CD	4.2 (9%)	47 (3%)	2.0 (8%)	29.5 (7%)

have been measured from the secant of the averaged stress-strain values at 0.3–0.6 %. The
main reason to derive the stiffness properties from small stress and strain values is to consider
the observed non-linear elasticity and degradation in stiffness, which occur at small loads.

3.3.3. Thick-walled beam shear test

The thick-walled beam shear test was used to determine the in-plane shear behaviour of the
aramid paper. In the following the measurement of shear modulus and the shear stress vs.
shear strain response is presented and discussed.

It is noted, that similar to the measurement of the compressive in-plane behaviour, the
measurement of the in-plane shear properties is complicated because of the paper's structural
instability due to buckling. Possible solutions to prevent the buckling modes are either to
constrain the paper's degree of freedom in out-of-plane direction or to reinforce the specimen's
moment of inertia. The thick-walled beam shear tests presented here were performed by the
CELPACT partner 'Universität Stuttgart' (Institute of Aircraft Design) using specimens with
an enhanced moment of inertia. For that purpose 24 plys of aramid paper were bonded together
during the curing process to form a single specimen.

In lateral direction, the thick-walled beam specimen was then glued to face sheets made
of glass fibre composite. The face sheets were bolted to the loading jaws, which moved re-
latively to each other at a relative velocity of 1 mm/min. The preparation of the universal
testing device was based on DIN 53294. The test device is illustrated in figure 3.17 and the
test specifications are presented in table 3.7.

Figure 3.18 illustrates the averaged stress-strain response of ten thick-walled beam speci-
men. The shear stiffness was measured at low shear strains of about 0.1 %. It is noted that the
shear strain γ is given as the change in angle measured for the thick-walled beam specimen.
The shear stress is calculated by dividing the measured force by the transverse cross-sectional
area of the thick-walled beam specimen.

The shear modulus given in table 3.8 correlates to the average modulus and Poisson's
ratio measured in tensile direction. This indicates, that in-plane shear is governed by similar
mechanisms as observed in the aramid paper tests in tension. In the stress-strain curve it
can be observed, that the initially linear-elastic stress-strain relationship begins to degrade at
comparatively low strains. This degradation caused by re-alignment of fibres with localised
damage in the matrix conforms to the damage behaviour noticed in the above test series.
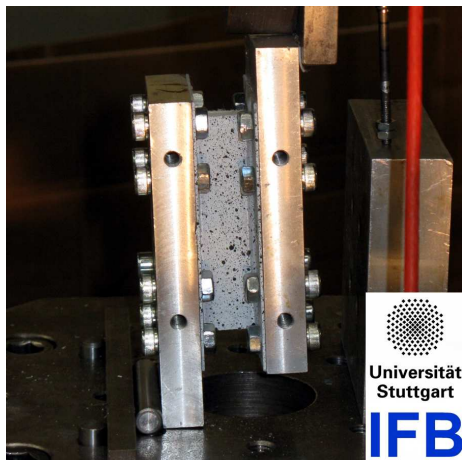
Figure 3.17.: Test device

Test method:	Beam shear test
Test standard:	DIN 53294
Test rate:	1 mm / min
Sample material:	Beam with 24 layers
	of aramid paper
Sample dimension:	80 x 20 x 6.3 mm
Number of specimen:	10

Table 3.7.: Test specifications
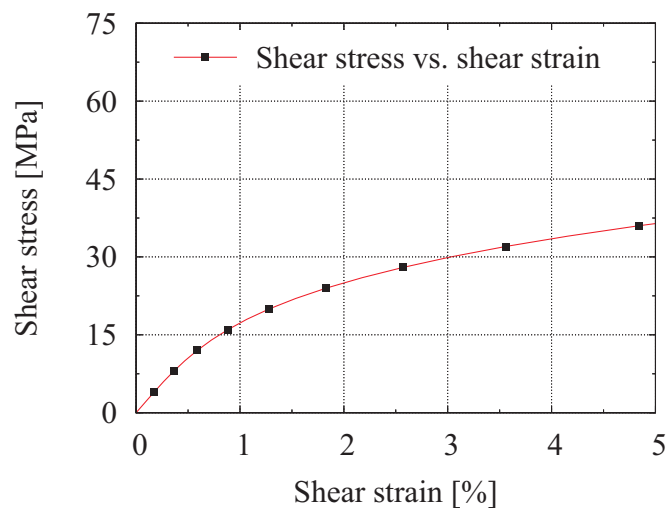
Figure 3.18.: Averaged stress-strain-curve of thick walled beam shear test measured by Universität Stuttgart (Institute of Aircraft Design).

At larger strains, the stress-strain curve approaches a constant stress level. It is noted, that the maximum stresses are larger than the stresses measured in the compressive test series but lower than the maximum stresses measured in the tensile test series. This observation and the good correlation of the determined shear stiffness to the elastic moduli measured in tension indicate, that the shear behaviour is fibre reinforcement dominated similar to the tensile behaviour.

Table 3.8.: Shear modulus measured in the thick-walled beam shear test, Universität Stuttgart
(Institute of Aircraft Design). The coefficient of variation is presented in parentheses.

In-plane Shear modulus [GPa]	Length [mm]	Width [mm]	Thickness [mm]
2.3 (24%)	80	20	6.3

3.3.4. Vibration bending test

The free vibration bending test was performed to characterise the flexural elastic stiffness of
the aramid paper. The test series was performed by the CELPACT partner 'LMT Cachan'
(Winterberger [153], EU-project CELPACT [21]). The test method bases on determining the
elastic stiffness by the frequency response of the natural vibration of a beam. A brief overview
on this method is given by Digilov [41]. In principal, the frequency response through the fast
Fourier transform gives the fundamental frequency f_0. In case of a beam with rectangular
cross-section, the frequency f_0 is given by

$$f_0 = \frac{\omega}{2\pi L^2}\sqrt{\frac{(EI)^{Flexural}}{\rho A}}, \tag{3.3}$$

where ω is the modal eigenvalue, L is the free length of the cantilever span, A is the cross-
sectional area of the beam and ρ is the density of the aramid paper. $(EI)^{Flexural}$ is the flexural
stiffness, where I is the area moment of inertia and E is the modulus. In figure 3.19 a sche-
matic plot of the test setup is depicted and in table 3.9 the specifications of the test are sum-
marised. The paper strip is restrained at one side whereas the other side can oscillate freely.
A laser velocimeter measures the displacement at the free end. The oscillation is stimulated
by a deflection of the free end by 15 mm. It is noted that the test have been performed in the
machine direction.

Figure 3.20 illustrates the oscillation of the free end versus the time in a linear and a
semi-log plot. The logarithmic decrement δ observed in the semi-log plot can be used to
calculate the damping factor ξ as

$$\xi = \frac{\delta}{2\pi}. \tag{3.4}$$

On basis of equation 3.3 and 3.4 a global elastic rigidity of 159 Nmm^2 and a flexural modulus
of 4.7 GPa is computed. The magnitude of the evaluated flexural modulus of 4.7 GPa is lower
than expected on basis of the tensile properties measured in section 3.3.1 and larger than
expected on basis of the compressive properties measured in section 3.3.2. An explanation
for this deviance is the inhomogeneous setup of aramid paper in out-of-plane direction which
results in a concentration of the reinforcing fibres close to the neutral axis. The data reported
by LMT Cachan are given in table 3.10.
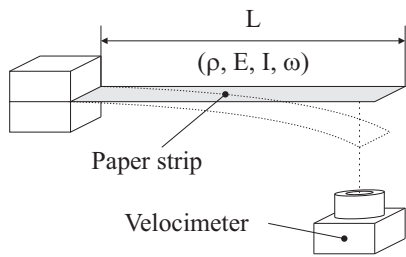
Test method:	Vibration bending test
Test standard:	-
Initial amplitude:	15 mm
Sample material:	Aramid paper strip
Sample dimension:	Width: 15 mm
	Thickness: 0.3 mm
Number of specimen:	5

LMT Cachan

Figure 3.19.: Test device   Table 3.9.: Test specifications
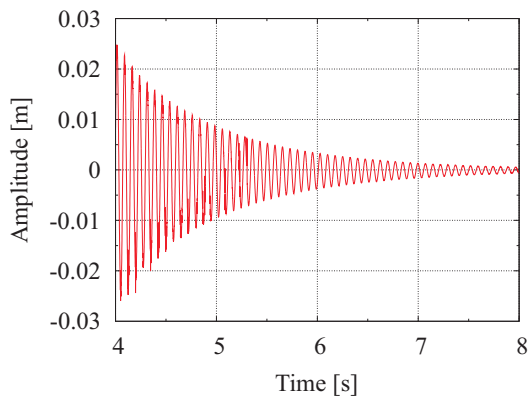
(a) Evolution of oscillation over the time   (b) Evolution of the amplitude over the time
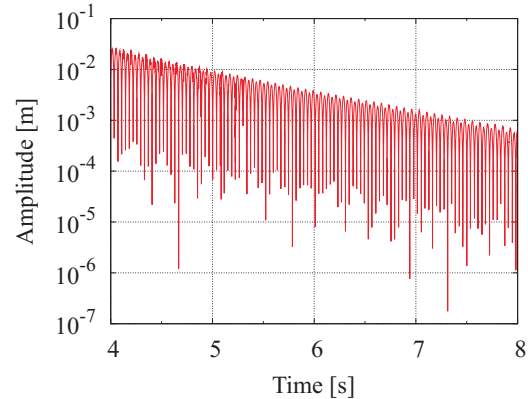
Figure 3.20.: Oscillation behaviour of vibration bending test, LMT Cachan.

Table 3.10.: Flexural modulus, area moment of inertia and rigidity measured in the vibration bending test (LMT Cachan).

Flexural modulus (MD) [GPa]	Area moment of inertia [mm^4]	Flexural stiffness (MD) [Nmm^2]	Damping factor [-]
4.7	0.03375	159	0.011

3.4. Numerical model

In order to design a meso-model for foldcore structures which can reproduce the deformation of the individual folds, a detailed modelling of the cell wall behaviour is necessary. In the present case the interest is to integrate the relevant characteristics of aramid paper as specified in sections 3.2.4 and 3.3 into a simple, effective cell wall model. In this regard a paradox is evident between the concept of modelling that requires the aramid paper to be a preferably homogeneous material whereas in reality the aramid paper reveals a great degree of heterogeneity in composition, shape and distribution.

Considerable work has been dedicated to this contradiction in modelling approach and reality. Several theoretical descriptions of a fibre network such as paper have been proposed by the researchers of traditional papers and can be found amongst others in [129, 134]. The present work follows the shell-based meso-model approach which was used by various researchers to successfully model local failure mechanisms of cell wall failure in cellular cores as discussed in section 2.4.2. In these works the nature of an aramid paper (Nomex®) cell wall is commonly assumed to be isotropic elastic-perfect plastic. In this section a cell wall model is presented which is based on the presented research. In addition the model offers further refinement to these concepts which can be classified into four main elements:

- Layered shell model: Modelling of the non-uniform nature of the aramid paper in out-of-plane direction on basis of a layered shell model. The different layers represent the characteristic properties of the fibre reinforced region and the pure resin film on the paper's surfaces.

- Elastic properties of the fibre reinforced layer: Development of an orthotropic stiffness matrix following the experimental observations made in sections 3.2.4 and 3.3.

- Elastic properties of the pure resin layer: Description of the elastic properties by an isotropic stiffness matrix based on the experimental observations made in section 3.3.

- Stiffness degradation: Implementation of a stiffness degradation which can reproduce the different non-elastic properties in tension and compression, based on the observations in section 3.3.

To establish the constitutive equations, it is important to know about the fundamental mechanics of the material. Section 3.4.1 summarises the experimental data from section 3.3. The basic setup of the of the layered shell approach is delineated in section 3.4.2. In section 3.4.3 the development of the elastic constitutive parameter of the individual layers is discussed. The The derivation of non-elastic parameters is presented in section 3.4.5. Finally the element elimination technique used to erode failed elements is briefly sketched. Partial aspects of the presented work have been published in [54, 101].

Table 3.11.: Elastic properties measured experimentally as discussed in section 3.3.

Tensile coupon test				Cylinder crush test		Vib. bending test	Beam shear test
Modulus		PR		Modulus		Modulus	Modulus
E_{MD}	E_{CD}	ν_{MD}	E_{CD}	E_{MD}	E_{CD}	$E_{MD/CD}$	$E_{MD/CD}$
[GPa]	[GPa]	[-]	[-]	[GPa]	[GPa]	[GPa]	[GPa]
7.7	7.1	0.3	0.4	5.0	4.6	4.7	2.3

3.4.1. Experimentally measured aramid paper properties

In-plane properties

The experimental data on elastic properties as presented in section 3.3 are given in table 3.11. It is noted, that the constitutive behaviour of the aramid paper is expected to be orthotropic. Generally, the elastic coefficients derived by tensile coupon tests and cylinder crush tests reveal, that a slight in-plane orthotropy exists. As discussed in section 3.3.3, the shear modulus shows good correlation to the in-plane tensile properties.

Notable is, that the modulus measured in the vibration bending test predicts significantly lower stiffness than expected from the measured tensile and compressive moduli. Additionally the moduli in machine and cross-machine direction measured in the vibration bending test are virtually similar, whereas the moduli derived on basis of the tensile coupon test and cylinder crush test show notable dependence on machine or cross-machine direction. These discrepancies can be explained by inhomogeneous in-plane properties through thickness and are considered based on a layered shell model as delineated in the following section 3.4.3.

Out-of-plane properties

The planar nature and the limited practicable minimum size of a paper specimen compared to its thickness make the determination of its out-of-plane properties by usual mechanical means almost impossible. An alternative approach are ultrasonic methods as proposed by Mann et al. [116]. Depending on its dimensions the paper sample is assumed to follow orthotropic beam/plate wave theory. By measuring the wave velocities of an oscillating sample the elastic constants can be directly determined. However in the scope of this work the ultrasonic method was not available. Based on the values found for traditional paper and paperboard (Fellers and Coffin [51], Mann et al. [116]) an approximation of the actual values was assumed and implemented into the layered shell model approach discussed in 3.4.4.

Similarly, the vulnerability of paper to buckling makes it difficult to mechanically determine the in-plane shear properties and it is virtually impossible to identify the out-of-plane shear properties. Generally, the aforementioned methods which employ the wave theory to measure the normal out-of-plane properties are again applicable. By Uesaka [148] the interlaminar and in-plane shear moduli are measured on basis of the torsions pendulum method, which establishes the elastic constants on the same principles as the ultrasonic measurements
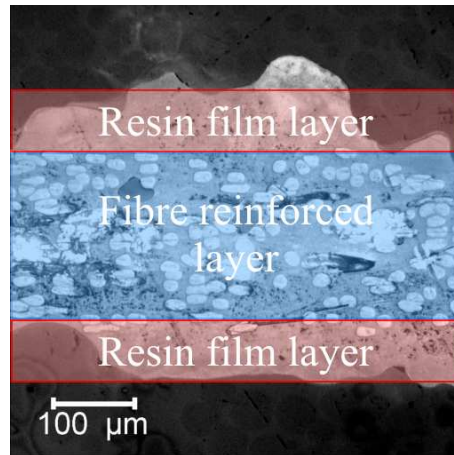
Figure 3.21.: Schematic setup of the layered shell model.

proposed by Mann et al. [116]. In this work the out-of-plane shear properties are approximated based on the layered shell model approach discussed in 3.4.4.

3.4.2. Layered shell model - Setup

In section 3.2.4 the out-of-plane distribution of fibres was observed to be considerably inhomogeneous. The fibres are primarily located close to the paper's centreline whereas a film with irregular patches of resin is found on the surface of the paper. The thickness of the resin film layer amounts to a significant proportion of the total paper thickness. As a consequence the normal in-plane paper stiffnesses are varying with strong properties in the fibre reinforced centre region and weak properties in the resin film region. Clearly a model with constant in-plane stiffness over the thickness is in this case limited and can not adequately reproduce the actual paper stiffnesses for all load conditions.

In order to adapt to this inhomogeneity the introduction of a layered shell model is proposed. The layered shell concept is typically employed to reproduce the layup of multiple plys of uni-directional composite materials and is adopted by many researchers [87, 122, 131, 132]. In these approaches, each layer represents an individual composite ply and its orientation. Similarly, in case of the aramid paper, the fibre reinforced region and the resin film region can be regarded as individual layers with different constitutive properties. The aramid paper is then assumed to be a layup of different continuous layers as schematically illustrated in figure 3.21, with isotropic or orthotropic stiffness properties. The fibre reinforced centre region is represented by an individual layer (E_{Fr}^T, E_{Fr}^C, A_{Fr}, I_{Fr}^T and I_{Fr}^C) with characteristic tensile and compressive properties of an aramid fibre composite. The irregular resin film on the paper surfaces is assumed to be an isotropic region (E_{Film}, A_{Film}, I_{Film}). It is noted that a comparable approach for aramid paper was independently investigated by Winterberger [153]. Subsequently, the nature of both layers is briefly summarised.
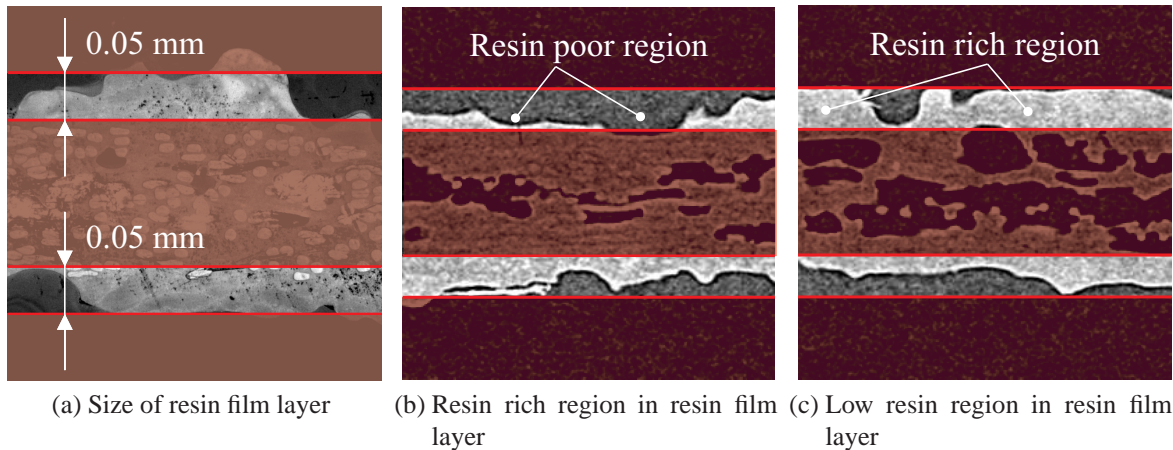
(a) Size of resin film layer (b) Resin rich region in resin film layer (c) Low resin region in resin film layer

Figure 3.22.: Computed tomography images of aramid paper cross-section showing region with low and high amount of resin in the resin film layer.

Resin film layer

The term 'resin film layer' describes the surface regions of the aramid paper. It mainly consists of the film of resin, which settled on the fibre reinforcement during the production process. Although mainly composed of phenolic resin it contains a certain number of voids and infrequent inclusion of aramid fibre reinforcement in particular close to the fibre reinforced region. The resin film layer assumes regular geometric shape with a constant thickness of 0.05 mm, as illustrated in figure 3.22a. This is a simplification, as in reality the material has an irregular distribution of thickness, with local resin rich and resin poor regions, as shown in figure 3.22b and 3.22c. The description of material behaviour is based on the main constituent of the resin film layer, which is the phenolic resin.

Fibre reinforced layer

The term 'fibre reinforced layer' signifies the midplane region of the aramid paper. Here the aramid fibre reinforcement is uniformly distributed at a remarkably constant thickness of about 0.2 mm, as depicted in figure 3.23a. The fibres are bonded to each other by the paper-making process as well as by patches of resin. The infiltration of the fibre-network with resin is partial and there is a considerable existence of voids. The amount of voids varies, which is showed exemplary in figure 3.23b and 3.23c, where a region with high resin absorption and a region with low resin absorption are depicted. The description of material behaviour is based on the main constituents of the fibre reinforced layer, which is the aramid fibre and the phenolic resin.

3.4.3. Layered shell model - Derivation of in-plane stiffnesses

It is not possible to gain information of individual aramid paper layer stiffnesses by means of mechanical testing due to their indivisibility. As a consequence the in-plane stiffnesses of the

(a) Size of fibre reinforced layer   (b) Low resin absorption   (c) High resin absorption
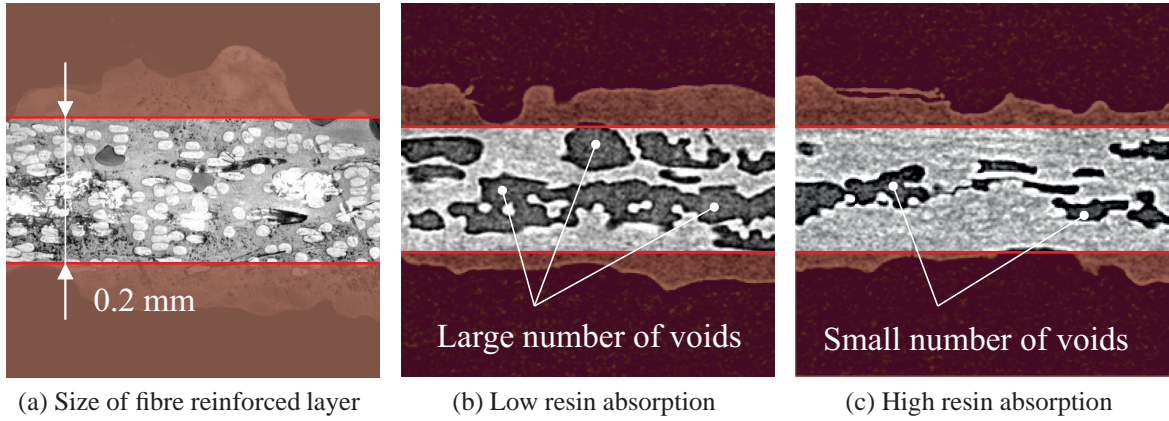
Figure 3.23.: Computer tomographies of aramid paper cross-section showing regions with low and high resin absorption in the fibre reinforced layer.

two layer types have to be computed by inverse methods. For that purpose the global tensile, compressive and flexural properties of the entire paper have been measured experimentally as presented in section 3.3. It is noted that the tested specimen were of beam-like nature so that elastic beam behaviour can be used to describe the stress distributions in the experimental setups. Figure 3.24 illustrates the different stress-strain distributions of the theoretical layered model setup in case of tensile and compressive normal loading in y-direction as well as bending about the z-axis. Based on elastic beam theory the global in-plane properties are now correlated to the in-plane properties of the individual layers.

The subsequently presented correlations are equally valid in both in-plane orientations of the aramid paper. The two outer resin film layers are assumed to have identical geometrical dimensions which is a simplification as the shape of upper and lower resin film layers is generally differing slightly. The fibre reinforced centre layer is signified with subscript 'Fr' and the resin film layer is signified with subscript 'Film'. The correlation between global paper stiffness and the moduli of the individual layers is given by

$$(EA)^{Normal} = \sum_{i=1}^{n} \int_{A_i} E_i dA_i \qquad \text{and} \qquad (3.5)$$

$$(EI)^{Flexural} = \sum_{i=1}^{n} \int_{A_i} E_i \bar{z}_i^2 dA_i, \qquad (3.6)$$

where A_i signifies the cross-sectional area of the ith layer and $\bar{z}$ the position of the neutral line. The global normal and flexural stiffnesses have been experimentally measured as delineated in 3.3.1 and 3.3.4 and are given in table 3.12. It is noted, that the axial stiffnesses in tension and compression are differing due to the intrinsic aramid fibre properties.

Knowing the geometrical dimensions of the individual aramid paper layers, equation 3.5 and equation 3.6 can be used to calculate the stiffnesses of the fibre reinforced layer E_{Fr}^{T} and E_{Fr}^{C} as well as of the pure resin layer E_{Film}. In order to solve the flexural stiffness correlation
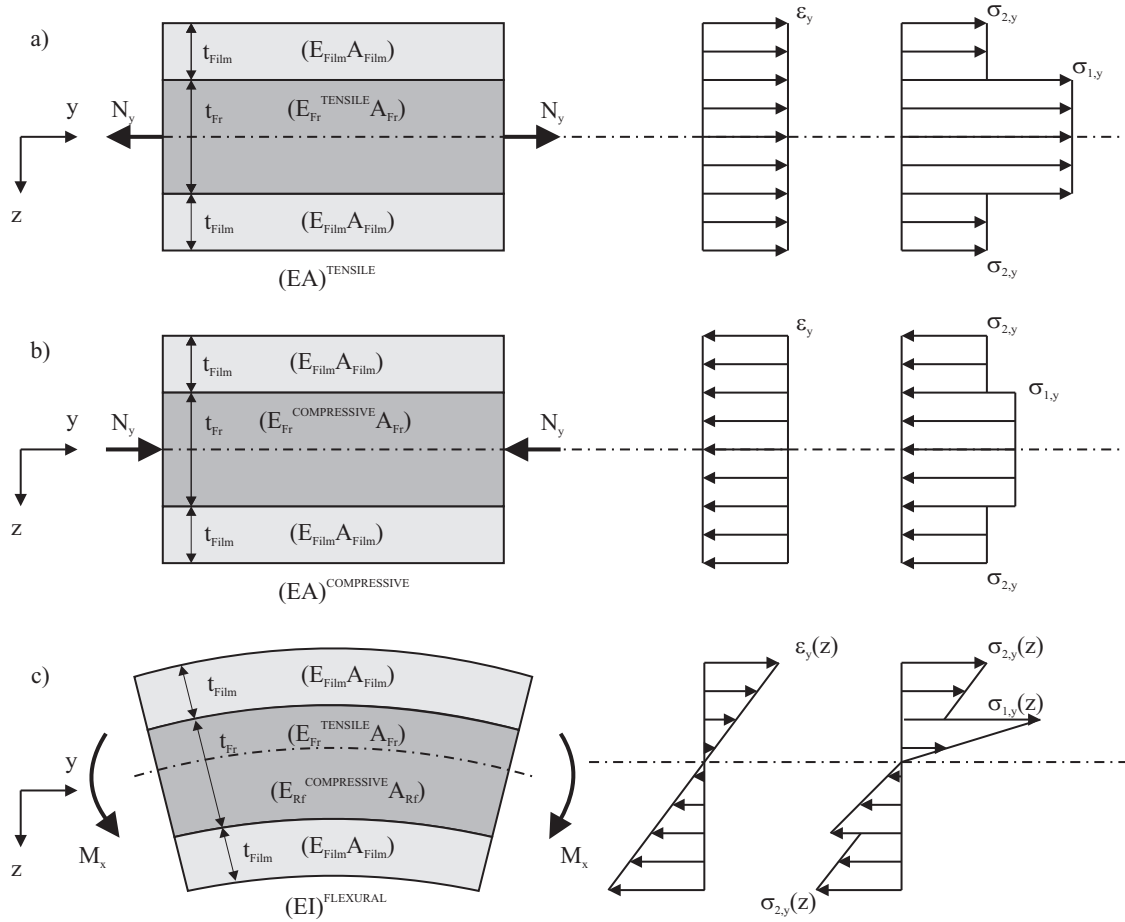
Figure 3.24.: Tensile (a), compressive (b) and flexual (c) stress-strain distribution in layered model.

Table 3.12.: Global stiffnesses under tensile, compressive and flexual loading as measured in section 3.3 for an average paper thickness of 0.3 mm and specimen width of 15 mm.

$(EA)^T$–MD [kN]	$(EA)^C$–MD [kN]	$(EI)^F$–MD [Nmm^2]	$(EA)^T$–CD [kN]	$(EA)^C$–CD [kN]	$(EI)^F$–CD [Nmm^2]
34.6	22.4	159	31.9	20.9	157

Figure 3.25.: Substitution of paper cross-section by an equivalent cross-section with a uniform
              stiffness.

given by equation 3.6 it is necessary to compute the position of the neutral line. Due to the
difference in stiffness of the fibre reinforced layer in tensile and compressive direction the
neutral line deviates from the axis of gravity. This can be done be employing the simple
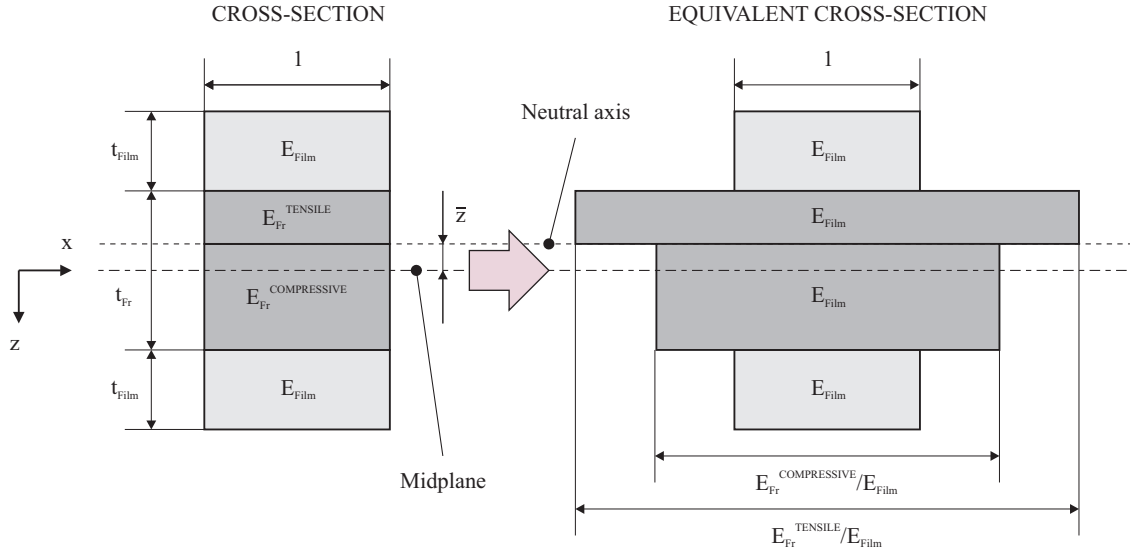equivalent width technique as illustrated in figure 3.25.

Here a equivalent cross-section with uniform stiffness is chosen, such that the mechanical
properties correspond to the original material. The distance between midplane and neutral line
$\overline{z}$ becomes

$$\overline{z} = \frac{1}{A} \sum_{i=1}^{n} \int_{A_i} \overline{z}_i dA_i, \tag{3.7}$$

where factor A is the global cross-sectional area and the subscript i indicates individual layers.
If the known geometrical dimensions are implemented in equations 3.5, 3.6 and 3.7 the relation
between global properties and layer properties can be calculated. Equation 3.7 then becomes

$$4\left(E_{Fr}^{T} - E_{Fr}^{C}\right)\overline{z}^2 - 4\left(4E_{Film}t_{Film} + E_{Fr}^{T}t_{Fr} + E_{Fr}^{C}t_{Fr}\right)\overline{z} + \left(E_{Fr}^{T} - E_{Fr}^{C}\right)t_{Fr}^2 = 0. \tag{3.8}$$

Thickness t_{Film} is the thickness of the resin film layer and thickness t_{Fr} is the thickness of
the fibre reinforced layer. The tensile and compressive stiffnesses of the aramid paper layers
implemented in equation 3.5 result in

$$E_{Paper}^{T} = \frac{E_{Fr}^{T}t_{Fr} + 2E_{Film}t_{Film}}{t_{Fr} + 2t_{Film}} \qquad \text{and} \tag{3.9}$$

Table 3.13.: Elastic in-plane properties of the fibre reinforced layer with a thickness of $t_{Fr} = 0.2$ mm and resin film layer with a thickness of $t_{Film} = 0.05$ mm.

Orientation	E^T_{Fr} [GPa]	E^C_{Fr} [GPa]	E_{Film} [GPa]	$\overline{z}$ [mm]
MD	9.2	5.1	4.7	0.011
CD	8.3	4.7	4.7	0.011

$$E^C_{Paper} = \frac{E^C_{Fr}t_{Fr} + 2E_{Film}t_{Film}}{t_{Fr} + 2t_{Film}}. \tag{3.10}$$

Similarly, equation 3.6 can be expressed as

$$\left(4t^3_{Film} + 3t^2_{Fr}t_{Film} + 6t_{Fr}t^2_{Film} + 12t_{Film}\overline{z}^2\right) \cdot \left(E^F_{Paper} - E_{Film}\right) + \cdots$$
$$+ \quad 2\left(t_{Fr} - \overline{z}\right)^3 \cdot \left(E^F_{Paper} - E^T_{Fr}\right) + 2\left(t_{Fr} + \overline{z}\right)^3 \cdot \left(E^F_{Paper} - E^C_{Fr}\right) = 0. \tag{3.11}$$

If equations 3.9 and 3.10 are inserted in equations 3.8 and 3.11 a two-dimensional, nonlinear equation system can be established. The rather complex relations are solved iteratively on basis of the multi-dimensional Newton-Raphson method. The basic principles of the Newton-Raphson algorithm are discussed in detail in appendix A. The computed stiffnesses E^T_{Fr}, E^C_{Fr} and E_{Film} as well as the position of the neutral line $\overline{z}$ are summarised in table 3.13. It is noted that stiffness of the resin film layer and the position of the neutral line are quite comparable, whereas the stiffnesses of the fibre reinforced layer are varying depending on their in-plane orientation.

3.4.4. Layered shell model - Elastic properties

Knowing the in-plane stiffnesses leaves seven undetermined elastic constitutive layer constants. However, the experimental determination of the missing constants is beyond the scope of this work. As a compromise the missing constants are approximated based on the determined values and the knowledge on the structural nature of the aramid paper. The estimation of the missing elastic constitutive parameter is discussed in the following sections 'Resin film layer' and 'Fibre reinforced layer'.

Resin film layer

The resin film layer simplifies the comparatively inhomogeneous distributed resin film on the aramid paper surfaces to a homogeneous layer with uniform properties. Therefore, the derived constitutive magnitudes of this layer represent a superposition of the influences of heterogeneously distributed resin patches and voids as well as sporadic fibre inclusions. The elastic properties of the resin film layer are derived based on following assumptions:

Table 3.14.: Material properties of the resin film layer.

Stiffness E_{Film} [GPa]	Poisson's ratio ν_{Film} [-]	Layer thickness t_{Film} [mm]
4.7	0.35	0.05

- The material behaviour of the resin film layer is isotropic.

- The resin film layer has similar behaviour under tension and compression.

- The layer in-plane stiffnesses are determined inversely as discussed in section 3.4.3.

- The Poisson's ratio conforms to the Poisson's ratio measured for the whole aramid paper.

The assumption of isotropy in the resin film layer is rational, as the orthotropy of the aramid paper is mainly caused by the fibre-reinforcement whereas the phenolic resin itself is isotropic. However, it is noted that a minor in-plane alignment of the resin film due to the milling process is neglected. The intrinsic material properties of the phenolic resin, which is the dominant component of the resin film layer also give equal behaviour in tension and compression.

The elastic parameters used in this work are given in table 3.14. The thickness of the resin film layer is determined by optical observation of the microscopic cut-images and is identified to have an average magnitude of about 0.05 mm. The Poisson's ratio of the resin film layer is equal to the mean value of the Poisson's ratio measured for the whole aramid paper during the tensile coupon test delineated in section 3.3.1. It is noted that the mean Poisson's ratio is 0.35 which is close to the Poisson's ratio typically observed for samples of pure phenolic resin (cf. Phenolic Resins Technology Handbook [123]).

Fibre reinforced layer

The fibre reinforced layer represents the region with constant thickness in the middle of the aramid paper where the aramid fibres are mainly distributed. To characterise the (orthotropic) stiffness of the fibre reinforcement layer following simplifications are made:

- The material behaviour of the fibre reinforced layer is orthotropic.

- The in-plane orthotropy of the aramid paper is caused by the fibre reinforced layer.

- There is no fibre reinforcement in out-of-plane direction.

- The layer in-plane stiffnesses are determined inversely as discussed in section 3.4.3.

- Different in-plane stiffnesses in tension and compression.

The in-plane normal stiffnesses are derived inversely as discussed in section 3.4.3. The in-plane Poisson's ratio is set to the mean value of the Poisson's ratios measured during the tensile coupon test delineated in section 3.3.1. The in-plane shear stiffness is derived from the shear stiffness experimentally measured for the aramid paper and the resin film layer shear stiffness by using equation

$$(GA)^{Aramidpaper} = \sum_{i=1}^{n} \int_{A_i} G_i dA_i,$$ (3.12)

where A_i is the cross-sectional area of the ith layer and G_i is the layer's shear modulus. By implementing the shear stiffness G_{Film} of the pure resin layer and the thicknesses t_{Film} and t_{Fr} the relation for the shear stiffness G_{Fr} of the fibre reinforced layer becomes

$$G_{Fr} = G + \frac{2t_{Film}}{t_{Fr}} (G - G_{Film}).$$ (3.13)

It is noted, that the resulting magnitude of the in-plane shear stiffness corresponds to the tensile stiffnesses of the fibre reinforced layer. This conforms with the observations in the thick-walled beam shear tests (Section 3.3.3), where the shear behaviour was mainly dominated by the load carrying capacity of the aramid fibre reinforcement.

The out-of-plane stiffnesses is difficult to characterise, as it involves matrix stiffness as well as fibre stiffness. The composition of the fibre reinforced region is highly irregular with scattered patches of phenolic resin joining the aramid fibres which leads to a significant existence of large voids. This limits the use of conventional analytical descriptions for transverse elastic properties of fibre composites as can be found in the book of Daniel and Ishai [37]. In this work it is assumed that there is no fibre reinforcement in out-of-plane direction and the out-of-plane normal and shear moduli are dominated by the matrix behaviour. It is further assumed that the resin film layer represents a behaviour comparable to a 'pure' matrix behaviour. These assumptions allow to set the out-of-plane stiffnesses and Poisson's ratios of the fibre reinforced layer equal to the stiffnesses and Poisson's ratios of the resin film layer.

The elastic parameters of the fibre reinforced layer are illustrated in table 3.15. The 1- and 2-direction signify the in-plane orientation, whereas the 3-direction signifies the out-of-plane orientation. The thickness of the fibre reinforced layer observed in microscopic cut-images is remarkably constant with a value of about 0.2 mm. It is noted, that the computed stiffness in normal compression is equal or smaller than the stiffness calculated for the resin film layer. This characteristic is attributed to the substantial occurrence of voids in the fibre reinforced region compared to a relatively continuous distribution of resin in the resin film region (cf. Figures 3.5e and 3.5f in section 3.2.4). In tension the fibres elongate and carry considerable loads. In compression the fibres which are unsupported within the voids are primarily kinking and tend to carry marginal loads.

Table 3.15.: Elastic properties derived for fibre reinforced layer.

Direction	E_1	E_2	E_3	G_{12}	G_{13}	G_{23}	ν_{12}	ν_{13}	ν_{23}
	[GPa]	[GPa]	[GPa]	[GPa]	[GPa]	[GPa]	[-]	[-]	[-]
Tensile	9.2	8.3	4.7	2.6	1.7	1.7	0.35	0.35	0.35
Compressive	5.1	4.7	4.7	-	-	-	-	-	-

3.4.5. Layered shell model - Stiffness degradation

In between the initial elastic behaviour and total failure the aramid paper shows multifaceted and complex damage modes, which include for instance matrix cracking and rupturing, matrix-fibre debonding, fibre straightening and fibre fracture. The intent of this section is to present the concentration of the most noteworthy damage characteristics into a straightforward damage model. The main objective for the introduction of the damage model was to allow a realistic reproduction of the effects occurring during cell wall buckling. The cell wall buckling is mainly controlled by the in-plane tensile and compressive behaviour of the aramid paper and for a good representation it is necessary to correctly reproduce the respective unique properties in both the fibre layer and the resin film layer. For that purpose a damage model provided by PAM-CRASH, the unidirectional composite bi-phase ply (Type 0) description was utilised. It offers adequate flexibility to be adapted to the required material and damage behaviours, which can be summarised as follows:

- The aramid paper exhibits considerably different failure modes for either loading in tension or compression respectively.

- In case of tensile loading the aramid paper shows a comparatively small continuous decrease in stiffness caused by the damage occurring during fibre alignment in load direction. After an ultimate strain is met, the aramid paper fails suddenly in a brittle mode.

- In case of compressive loading the aramid paper behaves 'perfectly plastic' after an initial elastic phase.

- The aramid paper demonstrates a continuous orthotropic material behaviour as presented in subsection 3.4.1.

- The inhomogeneous through thickness properties are described on basis of a multi-layer shell approach as illustrated in subsection 3.4.4.

The definition of a damage function for the PAM-CRASH unidirectional composite bi-phase ply (Type 0) model is briefly summarised in the following. The derivation of the damage functions for the resin film layer and the fibre reinforced layer is presented subsequently. The damage functions are derived from the in-plane stress-strain data observed in the tensile and

compressive test series presented in section 3.3.1 and 3.3.2. For that purpose a virtual global damage function is constructed which composes of the superposition of the individual layer curves. The experimental curves are fitted to the virtual global damage function. The breakdown of global damage function into the two seperate damage functions for resin film layer and fibre reinforced layer is based on the characteristics observed for the material behaviour of each layer region.

Degenerated Bi-Phase damage model (PAM-CRASH)

The bi-phase ply model is primarily a heterogeneous material model adapted to uni-directional continuous fibre reinforced composites or composite fabrics (PAM-CRASH [47–49]). A typical multi-directional laminate lay-up is modeled by stacking through the thickness several uni-directional ply layers with orientation corresponding to the fibre alignment in the original laminate. The stiffness and strength of the individual plys are calculated by superimposing the effects of an orthotropic matrix material and of a one-dimensional fibre material. For each material (fibre, matrix) a seperate modulus damage behaviour can be defined.

In the presented case, the properties of the one dimensional fibre material are set to zero which results in a quasi homogenuous orthotropic ply description given by the matrix material definition with a micro-fracturing brittle damage model. The thus degenerated ply model has an elastic stress-strain matrix C_0^{Global} given by

$$C_0^{Global} = C_0^{Fibre} + C_0^{Matrix}, \tag{3.14}$$

where $C_0^{Fibre} = 0$ and C_0^{Matrix} is given by the orthotropic elastic constants summarised in tables 3.14 and 3.15 in section 3.4.4. By introducing a modulus damage function $d(\varepsilon')$ the elastic stress-strain matrix C_0^{Matrix} is modified and results in the instantaneuous stress-strain matrix C^{Global}, which is expressed as

$$C^{Global} = (1 - d(\varepsilon')) \, C_0^{Matrix}. \tag{3.15}$$

As the damage parameter d is a scalar which depends on the strain it is necessary to express the strain tensor in a scalar form. For that purpose the second invariant of the deviatoric strain tensor $\sqrt{J_2}$ is used. This definition implies that the major part of the deformation energy is based on distortion whereas the volumetric change is small. This precondition is assumed to be valid, as although the modulus damage function affects the complete stress-strain matrix, it depends mainly on the in-plane strain state where Poisson ratios between 0.3 and 0.4 have been measured. Generally volume damage is physically associated with tensile loading only which causes tensile volumetric strain with correlated flaw growth and coalescence. Compressive volumetric strain will not cause volume damage in most cases, however. The term $\sqrt{J_2}$ is in the following referred to as equivalent strain ε'.

The damage function $d(\varepsilon')$ is classified in seperate sections defined by the equivalent strain parameters ε'_1, ε'_i and ε'_u as depicted in figure 3.26. The damage function is equal to zero at initation and increases monotonically to a value of one at failure. It is noted that different
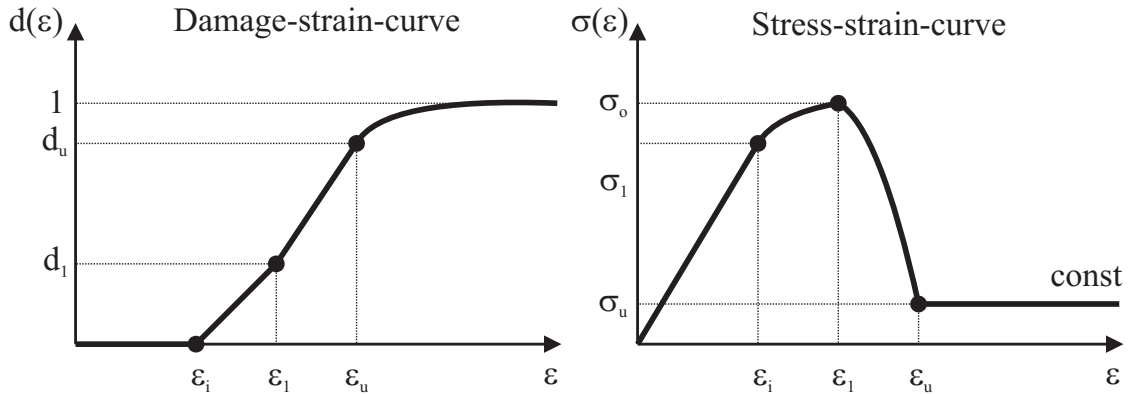
Range	Damage function	Stress-strain-relation
$0 < \varepsilon' < \varepsilon'_i$	$d = 0$	$E_0 \varepsilon'$
$\varepsilon'_i < \varepsilon' < \varepsilon'_1$	$\frac{\varepsilon' - \varepsilon'_i}{\varepsilon'_1 - \varepsilon'_i} d_1$	$E_0 \varepsilon' \left(1 - \frac{d_1}{\varepsilon'_1 - \varepsilon'_i} \left(\varepsilon' - \varepsilon'_i\right)\right)$
$\varepsilon'_1 < \varepsilon' < \varepsilon'_u$	$\frac{\varepsilon' - \varepsilon'_1}{\varepsilon'_u - \varepsilon'_1} \left(d_u - d_1\right) + d_1$	$E_0 \varepsilon' \left(1 - d_1 \frac{d_u - d_1}{\varepsilon'_u - \varepsilon'_1} \left(\varepsilon' - \varepsilon'_i\right)\right)$
$\varepsilon'_u < \varepsilon' < \infty$	$1 - \left(1 - d_u\right) \frac{\varepsilon'_u}{\varepsilon'}$	$E_0 \varepsilon'_u \left(1 - d_u\right) = \text{const}$

Figure 3.26.: Correlation strain, damage and stress-strain behaviour of modulus damage function, taken from PAM-CRASH Solver Notes [48].

tensile and compressive damage functions can be defined by individual sets of parameters. Generally two sections of linear modulus degradation are specified after an initial elastic section. After an ultimate equivalent strain ε'_u is met the damage function increases such that the residual stress level remains constant.

Resin film layer

The shape of the damage function correlates to the non-linear behaviour of phenolic resin, which is the main constituent of the resin layer. However it is noted that the resin film layer represents a homogenisation of an irregular material region with considerable voids and defects. Therefore the damage behaviour of the resin film layer is less brittle than behaviour of pure homogeneous phenolic resin.

The fit of the damage function is based on the assumption, that the aramid paper in compression is purely matrix dominated. Resin film layer and fibre reinforced layer behave similar in an elastic 'perfect-plastic' mode. Based on these assumptions, the stress-strain curve and the yield stress observed in the cylinder crush tests (see section 3.3.2) are directly used to fit the stress-strain behaviour of the resin film layer.

The evolution of damage in tension is considered to be identical to the damage evolution in compression. It is noted that this is a simplification. Typically polymers demonstrate a
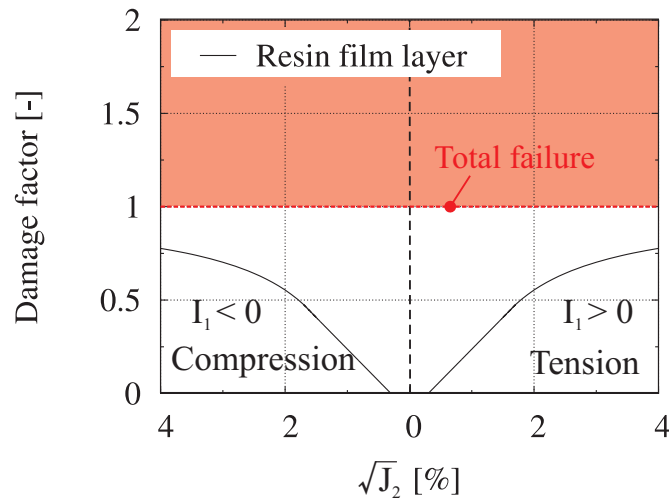
Figure 3.27.: Evolution of the damage scalar vs. $\sqrt{J_2}$ as defined for the resin film layer.
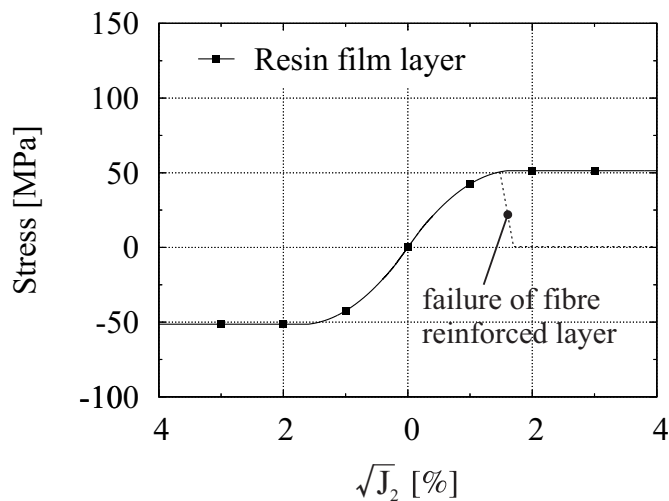

Figure 3.28.: Evolution of the normal stress vs. $\sqrt{J_2}$ for an uniaxially loaded resin film layer.

lower damage evolution and lower yield in tension as in compression. However it is extremely difficult to determine the impact of the irregular distribution of material on its damage evolution. Therefore above simplification is justified as a 'rough' estimation of the damage behaviour, which the resin film region shows in tension.

The damage function of the resin film is illustrated in figure 3.27. It is observed, that damage is initiated at low strains $\sqrt{J_2} = 0.2\,\%$, which conforms to the observations in section 3.3. The damage scalar increases linearly until a strain of $\sqrt{J_2} = 1.7\,\%$. At larger $\sqrt{J_2}$ the damage is controlled such that a constant stress vs. strain response is generated. The resulting stress-strain behaviour for an uni-axially loaded resin film with elastic material properties as
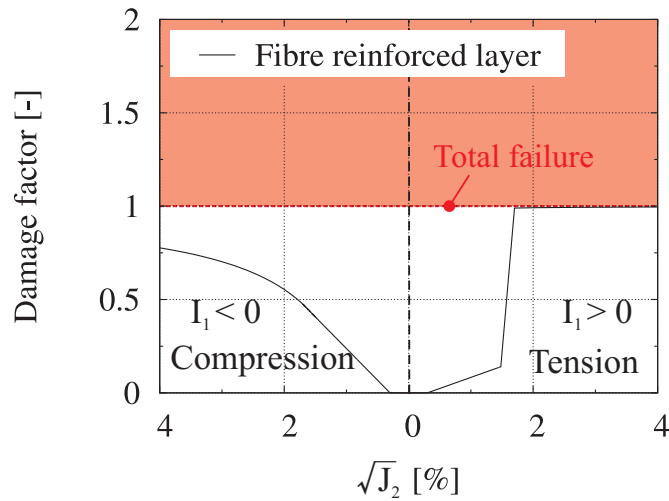
Figure 3.29.: Evolution of the damage scalar vs. $\sqrt{J_2}$ as defined for the fibre reinforced layer.

derived in sections 3.4.3-3.4.4 is given in figure 3.28. It is noted that the resin film layer fails in tension in a brittle mode at about $\sqrt{J_2} = 1.5\,\%$, due to the element failure criteria defined in the fibre reinforced layer.

Fibre reinforced layer

The damage function of the fibre reinforced layer conforms to the behaviour of a typical aramid fibre composite, with brittle failure in tension and elastic-'perfect plastic' behaviour in compression. Comparable to the resin film layer, the fibre reinforced layer behaves softer than a common aramid fibre composite, which may be explained by the significant number of voids. The damage function in the compressive domain is fitted analogously to the damage function of the resin film layer: The evolution of damage in compression is matrix dominated and results in an elastic 'perfect-plastic' stress-strain-relation.

The damage evolution in tension is fitted such that the combined response of resin film layer and fibre reinforced layer conforms to the tensile test curves delineated in section 3.3.1. It is assumed that the aramid fibre reinforcement generally behaves linear elastic and the observed degradation is caused by local matrix damage and fibre realignment which is represented by the consolidated damage parameter d. If the fibre reinforced layer is fully damaged in tension the whole element is assumed to have failed.

The damage function of the fibre reinforced layer is depicted in figure 3.29. Similarly to the resin film layer, the fibre reinforced layer shows a cumulative micro-damage behaviour in both tension and compression which is initiated at small loads and then continuously increases. If a specific strain threshold $\sqrt{J_2} = 1.5\,\%$ is exceeded in tension the material fails in a brittle mode. In compression the damage scalar increases linearly until a strain of $\sqrt{J_2} = 1.7\,\%$. For larger $\sqrt{J_2}$ the damage is controlled such that a constant stress vs. strain response is generated.
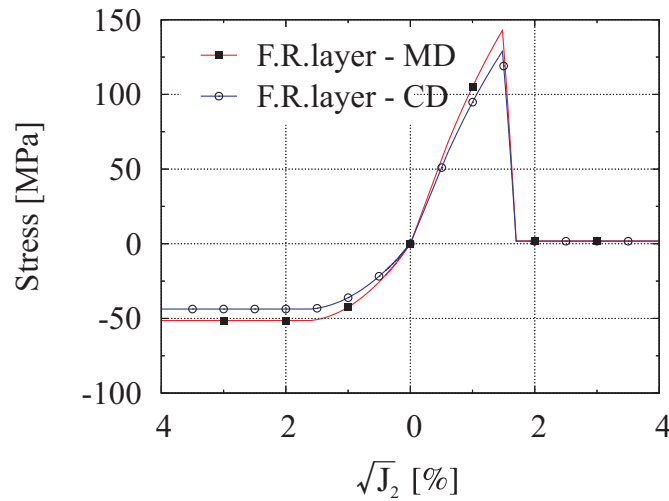
Figure 3.30.: Evolution of the normal stress vs. $\sqrt{J_2}$ for an uniaxially loaded fibre reinforced layer.

The corresponding stress-strain-relation for an uniaxial normal load case is delineated in 3.30. It is based on the elastic material properties derived in sections 3.4.3-3.4.4. The different behaviour is caused by the orthotropic in-plane stiffness of the fibre reinforced layer. It is noted that the damage evolution itself is by definition isotropic.

Stiffness degradation due to interaction of resin film and fibre reinforced layer

The stiffness degradation of the whole layered element is controlled by the damage evolution in its individual layers. However, as discussed above, fitting of the individual layer's damage functions is based on the combined response of the individual layers. This is due to the fact that the experimental data was measured for the aramid paper composite, whereas there is only limited experimental data on the behaviour of its constituents and individual layer regions.

The stress-strain behaviour of a layered shell element with 4 layers (2x resin film, 2x fibre reinforced) is illustrated in figure 3.31 for an uniaxial load in MD direction and in 3.32 for an uniaxial load in CD direction. The fibre reinforced region is represented by two layers due to numerical reasons. A single layer representing the fibre reinforced region will be located directly on the element's midline, which might cause inaccuracies. The figures include the curves of the single layers as well as the experimental data based on the tensile coupon tests and the cylinder crush tests.

The relevant characteristics of the damage function curve fit are marked in the figures. In tension and compression the material model reproduces the initial culmulative micro-damage observed in the experiments. In tension the material model shows brittle failure and subsequent element elimination which conforms to the results of the tensile coupon tests. In compression the material model represents a 'perfect-plastic' behaviour, which is initiated at
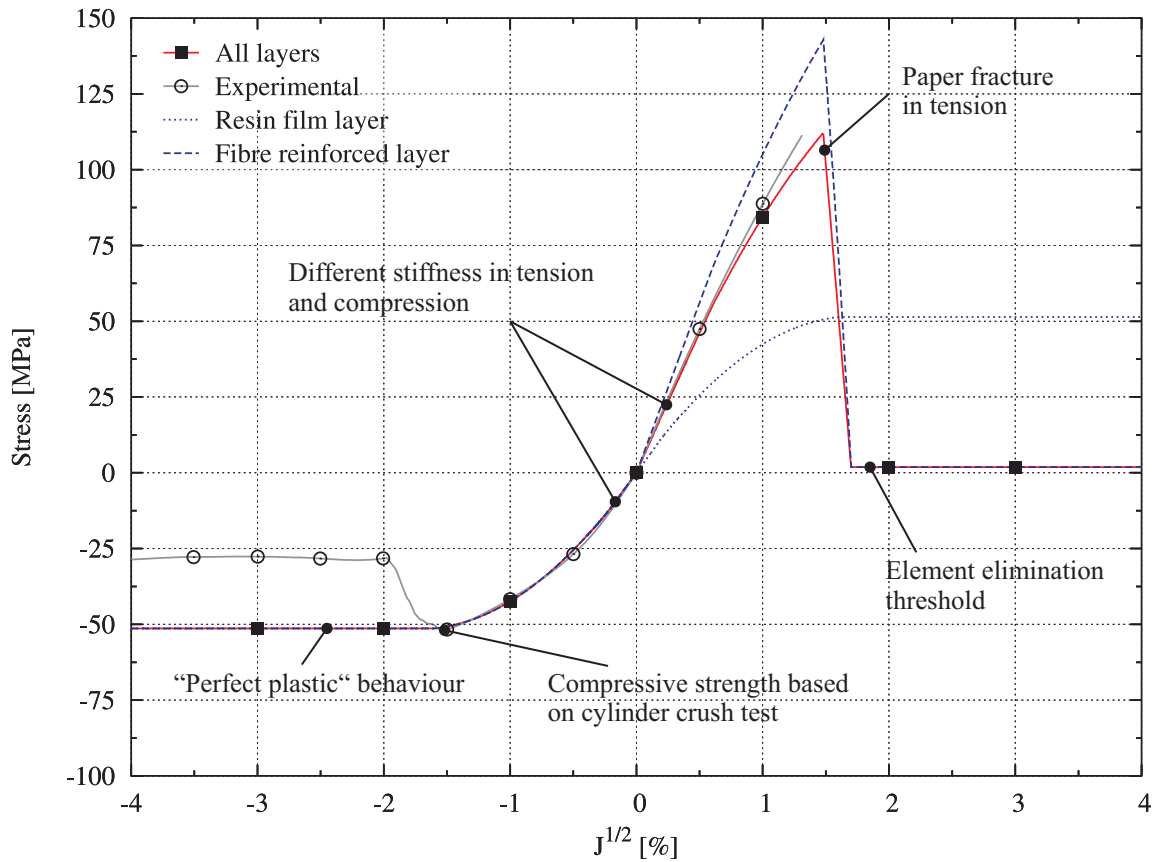
Figure 3.31.: Evolution of the normal stress vs. $\sqrt{J_2}$ for a 4-layer aramid paper element ($t_{Film} = 0.05mm$, $t_{Fr} = 0.2mm$). The aramid paper is loaded uniaxially in normal MD direction.

the compressive yield measured in the cylinder crush tests. The subsequent drop in stress observed in the experimental curve is mainly caused by structural failure mechanisms and it is reasonable to assume a constant stress level (cf. section 3.3.2).

3.4.6. Element elimination

The above presented material description of an aramid paper is supplemented by an element erosion mechanism called 'Element elimination technique (EET)'. A comprehensive overview on the element elimination technique can be found in the review of Mishnaevsky and Schmauder [120] where several methods to represent damage growth and crack propagation in continuum meso-mechanical FE modelling are reviewed. In summary, the element elimination technique permits to remove elements from the calculation if a specified failure condition is met. For a removed element all components of the stress tensors are set to zero which results in no loads being transmitted by this element to neighbouring non-eliminated elements.
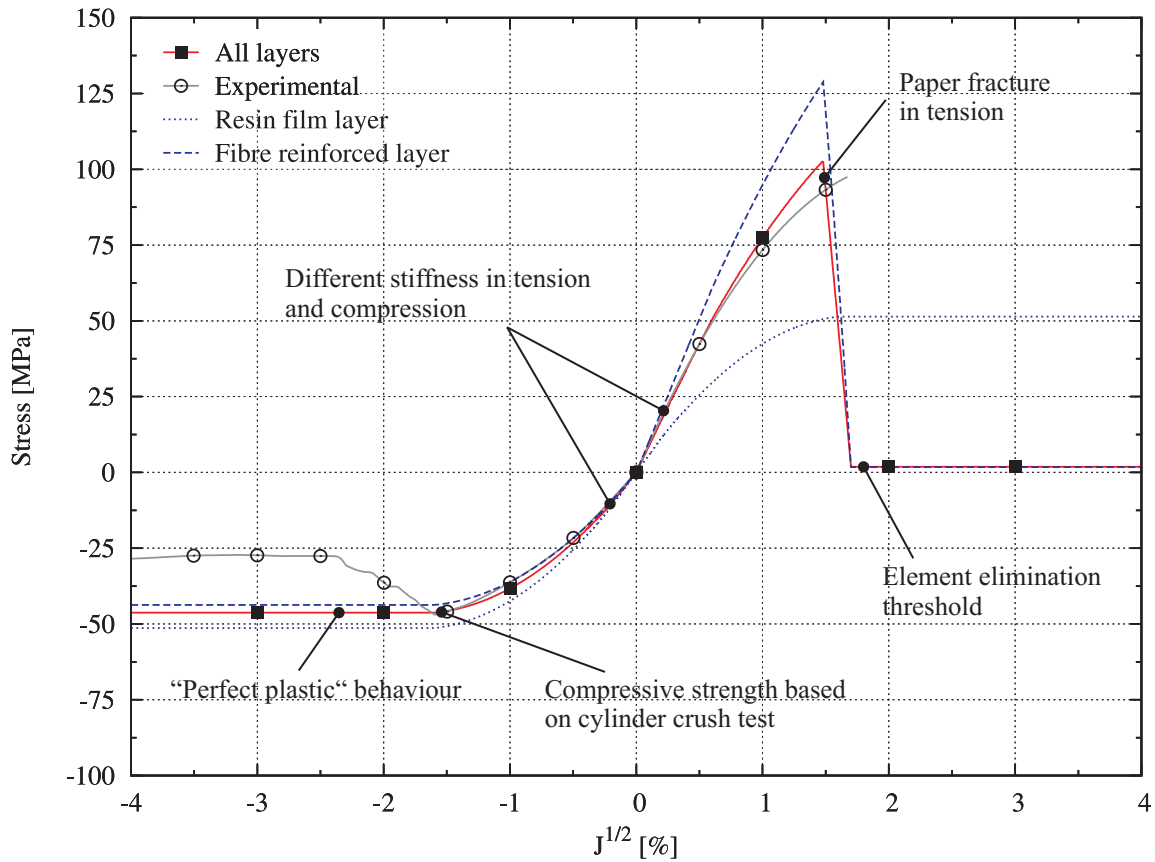
Figure 3.32.: Evolution of the normal stress vs. $\sqrt{J_2}$ for a 4-layer aramid paper element ($t_{Film} = 0.05mm$, $t_{Fr} = 0.2mm$. The aramid paper is loaded uniaxially in normal CD direction.

This means, that an eliminated element stops to interact with neighbouring elements but is not actually removed from the FE mesh. Typically the stresses are set equal to zero over a number of time steps to avoid numerical problems due to the significant local loss of equilibrium. The elastic moduli in the eliminated elements are set to zero in the last relaxation step.

The element elimination technique is incorporated in most commercial FE codes, such as PAM-CRASH, ABAQUS, LS-DYNA, etc. In the present work the element elimination is used to erode plies or elements which have considerably degraded and assumed damage values close to full degradation (Damage scalar $d > 0.99$) in order to prevent over-expanded elements. The element elimination is triggered, if certain treshhold strains in the fibre reinforced layer are met. These treshhold strains range from >20 % (normal) to >90 % (shear). It is noted, that the treshhold values have no direct physical meaning and are large compared to failure strains observed in the experiments. However, as the elements are essentially fully degraded at lower strains and offer minmal resistance to deformation this difference has negligible impact on the simulation results.
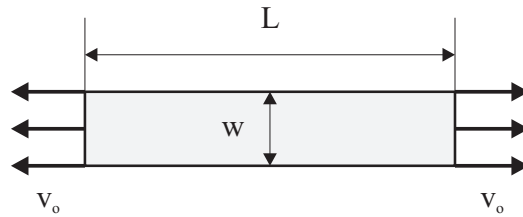
Figure 3.33.: Schematic plot of FE model setup of tensile coupon test.

3.5. Model evaluation

To assess the capacity and quality of the aramid paper model the predictions of the finite element model are carefully compared to the results of selected benchmark tests. This includes tensile coupon tests and crush tests of large thin-walled cylinders. It is noted, that the test environment was quasi-static contrary to the dynamic nature of the explicit FE simulations. The simulation of a structure or test specimen under quasi-static loads with an explicit, dynamic FE model is admissible if the dynamic inertia effects are within acceptable bounds. In this regard the time scale of the dynamic model has to be chosen so that the kinetic energy is small compared to the internal energy. Generally the kinetic energy should be less than 1 % of total energy.

3.5.1. Modelling of tensile coupon test (TCT)

To assess the material models capability in tension the conditions of the tensile coupon tests in section 3.3.1 are reproduced with a FE model using the multilayered shell approach presented in section 3.4.

Experimental and finite element model setup

Details on the experimental test setup can be found in section 3.3.1. The geometrical dimensions of the numerical model are depicted in figure 3.33 with width w = 15 mm and length L = 100 mm. The width of 15 mm corresponds to the waist width of the test specimen which has a minor curvature. A strip representing the centre section of the respective tensile specimen was loaded axially with a constant velocity v_0 of 1 m/s. To avoid excessive oscillations due to rapid initial acceleration the velocity v_0 is approached at simulation begin during a start-up time interval of $\delta t = 0.01$ ms. The element size is 1 mm.

The numerical model of a tensile specimen with a uniform mesh typically fails at the ends of a specimen where the velocity boundary conditions are applied causing inconsistent edge effects. By implementation of a marginal irregular mesh structure generated with node shaking the location of damage initiation is randomised. Main reason for the introduction of node
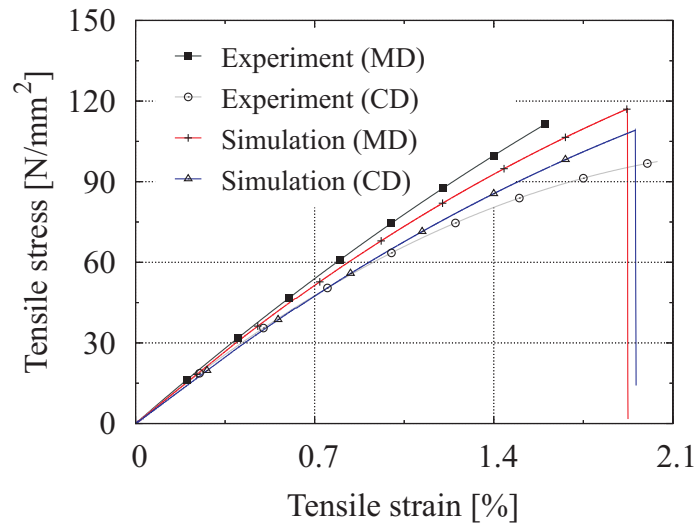
Figure 3.34.: Comparison of experimental and numeric stress-strain-curves.

shaking were minor numerical variations in the strain field caused by the the slightly deformed element shapes which override the impact of the edge effects occuring at the specimens tips. It is noted, that the effect of node shaking on the stress-strain response was negligible, which is a result of the shift in lateral position being strongly decreased by the tensile load in in-plane direction.

Comparison and discussion

Figure 3.34 illustrates the stress-strain-behaviour of numerical model and experiment in both orthotropic in-plane directions. Generally the curves give a good view on the input and output values of the model, as tensile behaviour of the model is calibrated on basis of the tensile coupon tests. In table 3.16 the failure properties observed in simulation and experiment are compared. The variations of the numerically calculated properties from the mean values measured experimentally are given. The deviation between numerical properties and experimental mean values ranges from 4–20% which correspondes roughly to the COV observed in the experiments, which amounted to 8–14%. It is noted that the variation of the numerical results caused by the node-shaking was very small ($\rightarrow$0%) and therefore negligible.

The deviation of the numerical results from the experimentally observed mean values is mainly caused by inherent limitations of the material model: the representation of the difference in stress magnitude between both in-plane orientations is limited as the model is only capable to consider the difference in stiffness. The difference in damage behaviour between both directions as it is observed in the experiment is underestimated as the scalar damage variable represents isotropic damage behaviour and does not account for orthotropic damage

Table 3.16.: Comparison of tensile failure properties of aramid paper observed in experiment and simulation. The experimental values (measured failure properties and COV) are presented in parentheses.

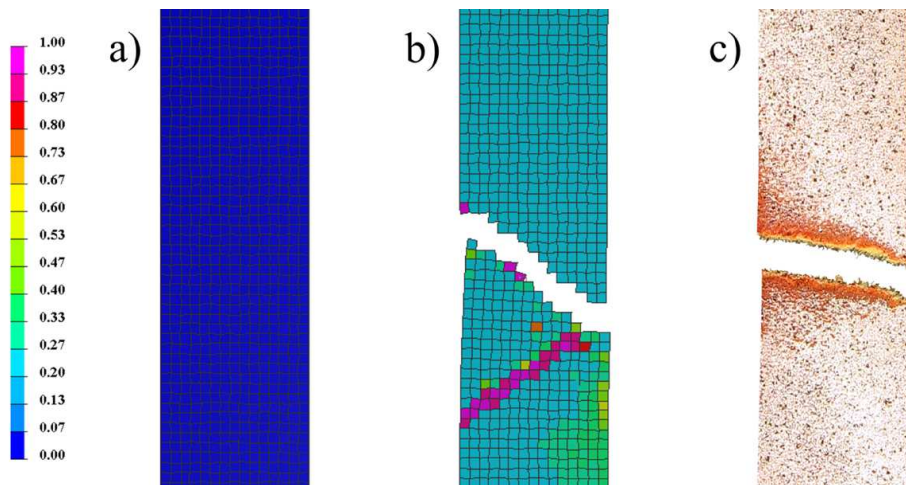| Orientation	Tensile failure stress [MPa]	Variation of failure stress -	Tensile failure strain [MPa]	Variation of failure strain -
MD	117 (111)	5% (13%)	1.92 (1.6)	20% (13%)
CD	109 (97.5)	12% (8%)	1.95 (2.04)	4% (14%)

Figure 3.35.: Contour-plot of scalar damage variable in unloaded state (a) and briefly after failure (b) / Photography of failed tensile test specimen (c).

occurrence. Another result of the isotropic damage is the constant failure strain in in-plane direction which differs from the range of failure strains observed in the experiment.

The planar damage evolution is depicted in figure 3.35a for the initial state and in figure 3.35b briefly after failure. The contour plot shows a small global damage accumulation due to the constant stiffness degradation. The damage which leads to failure is localised and propagates rapidly from the element which first reaches the failure strain. The failing element is located exclusively at the specimen free edge and the damage spreads at an angle of approximately 45°. However in the experiment in most cases a fracture angle of 90° is observed, which is depicted in figure 3.35c. It is assumed that this discrepancy is caused by the inappropriate simplification that damage is governed by exclusively by the second invariant of the deviatoric strain tensor. This presumption is accurate for the range before failure strain is reached as mainly damage due to shear deformation by fibre realignment is caused. However the failure mode by tearing as observed in the experiment may depend considerably on the volumetric strain which is neglected in the damage model.

In summary the numerical results differ to some extend from the experimentally observed behaviour. These deviations are caused by inherent limitations of the material model. However the overall analogy of numerical and experimental stress-strain-behaviour is satisfying. The constant degradation of the stress-strain-curve observed in the experiment is well represented by the gradual increase in damage initiated a small strains. The deviation of numerical and experimental results is in the range of or below the COV observed in the experiments.

3.5.2. Cylinder collapse test (CCT)

The purpose of the comparison of cylinder collapse behaviour in experiment and simulation is the evaluation and validation of the buckling behaviour of the developed aramid paper material model. The idea of the cylinder collapse test is to create a load environment for a paper-like material in which the buckling behaviour depends on only few manageable influencing factors and in which repeatable experimental results can be easily measured. The thin cylinder structure fails mainly due to buckling and collapse in contrast to the thick-walled structures used for the cylinder crush test presented in section 3.3.2 which were designed to fail due to crushing.

There is comprehensive knowledge on the compression and collapse of thin-walled cylinder structures in the literature. Main focus of the research is the energy absorption behaviour of crash absorbers with cylindrical and other geometries. The failure mechanisms here differ depending on the employed material and geometry. Composite tubes typically fail as reported in the research of Mamalis et al. [114] under a progressive crushing mode with micro fragmentation as well as in a fracture mode resulting in brittle failure.

However, although the aramid paper categorises as a fibre composite it demonstrates a failure behaviour comparable to the modes observed for metal and plastic tubes, which demonstrate a progressive folding and hinging during crushing. A brief overview on different crushing modes of aluminium tubes is given by Pled et al. [130], who observed concertina, diamond and mixed as well as Euler-type buckling modes. All these modes can be induced with aramid paper tubes, depending on geometry and boundary conditions. An elaborate investigation on fold formation in axis-symmetric collapse of round (aluminium) tubes based on analytical, numerical and experimental methods is also given by Gupta et al. [69, 70].

Experimental and finite element model setup

As briefly summarised in section 3.3.2 the buckling behaviour of a cylinder bases primarily on cylinder height, cylinder diameter, wall thickness and material properties. In comparison to the cylinder crush test of section 3.3.2 the height and diameter of the cylinder are increased whereas the wall thickness is reduced. The dimensions of the cylinder specimen are within the long range region as depicted in figure 3.13 on page 37 and cylinder wall buckling is expected as main failure mode.

The quasi-static tensile test series was performed on a universal testing device. An illustration of the test setup and the specifications of the cylinder specimen is given in figure 3.17.
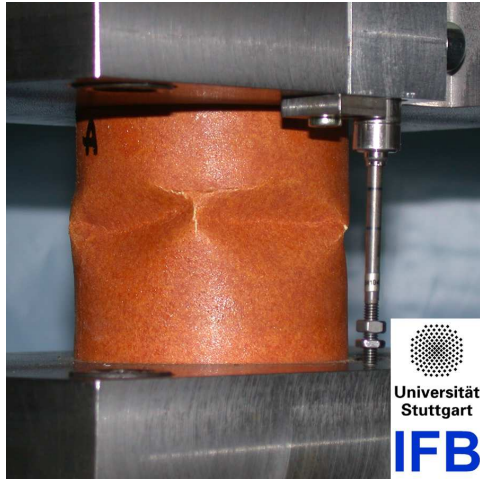
Test method:	Cylinder collapse test
Test standard:	-
Test rate:	1.0 mm / min
Sample material:	Aramid paper
Sample dimension:	Ø70 mm, 70 mm
Number of specimen:	10

Figure 3.36.: Test device   Table 3.17.: Test specifications

The hollow cylinder is formed by rolling the aramid paper prepreg around a Teflon tube and subsequently bonding the paper prepreg layers together in the curing process resulting in cylinder walls of three bonded plies. Particular care was taken to ensure that the ends of the rolled paper strip at inner and outer diameter are located at the same circumferential position. The aramid paper strip is rolled in cross-machine direction of its fibre network so that the machine direction points along the cylinder axis.

The cylinder is clamped to the test device by tightening with tension rings the upper and lower cylinder parts to cylindrical aluminium supports, which gives a fixed support at both cylinder ends. The load environment was displacement controlled with a compression velocity of 1 mm/min. Stress is the load divided by the sectional area of the sample and strain is the displacement of the transverse divided by the initial cylinder height.

The schematic setup of the numeric model is illustrated in figure 3.37. The cylinder is compressed with a constant velocity v_0 of 1.0 m/s. The other degree of freedom of the nodes at top and bottom end of the cylinder are constrained to zero displacement. The height H of the cylinder is 70 mm and the diameter d is 70 mm. The cylinder wall with three bonded plies is represented by shell elements with a setup of twelve layers as depicted in the figure. The layered shell element assumes perfect bonding between the individual layers and no delamination between the layers is considered. The element size is 1.5 mm whereas the mesh is slightly distorted on basis of the node shaking approach discussed in section 4.3.3 with an maximum deflection of 0.05 mm lateral and 0.0025 mm normal to the face plane.

Comparison and discussion

Figure 3.38 illustrates the stress-strain-behaviour of numerical model and the experimental result of an individual specimen in direction of the applied displacement condition. Typically the stress-strain behaviour of a specimen observed during experiment is mainly (nonlinear)
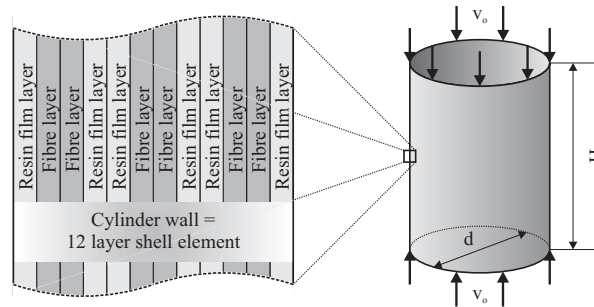
Figure 3.37.: Schematic plot of FE model setup of cylinder collapse test.

Table 3.18.: Failure properties of the cylinder observed in the simulation. The experimental values (measured failure properties and COV) are presented in parentheses.

Orientation	Failure stress [MPa]	Variation of failure stress -	Collapse stress [MPa]	Variation of collapse stress -
MD	43.4 (48.5)	10% (4%)	8.1 (8.6)	6% (13%)

elastic until sudden instability by buckling initiated collapse. Similar to the behaviour observed for tensile coupon test (Section 3.3.1) and cylinder crush test (Section 3.3.2) a small constant degradation of the stress-strain-curve is visible within the initial elastic regime. At a peak stress of about 48 MPa the specimen starts to buckle and collapses in a diamond-shaped buckling mode with five distinct folds as can be seen in figure 3.39a and 3.39c. With growing compressive deformation the amplitude of the five folds increases at a constant stress level of about 8-9 MPa.

The variation of the numerical results caused by the node-shaking with discussed maximum deflection was very small ($\rightarrow$0%). This was unexpected as there is a considerable difference to the numerical results of model with perfect mesh (no node-shaking normal to the face plane). The negligible variation of the numerical results of models with node shaking was attributed to the uniform distribution of stochastic deflections in the scale of the cylinder structure due to the large number of nodes.

The scatter observed in the experiment ranged from 4% to 13% (COV). These values are compared to the variation of the numerical results from the experimental mean values as depicted in table 3.18. The deviation of the numerically calculated peak stress is more than twice as much as the coeeficient of variation observed in the experiment. However, it is noted that although the peak stress is observed to deviate, the mode of collapse and number of formed folds as well as the average stress-strain-behaviour during collapse are well comparable to the experiments. The accurate prediction of the buckling initiation and collapse behaviour is a good indication that the aramid paper model captures the significant buckling mechanism.
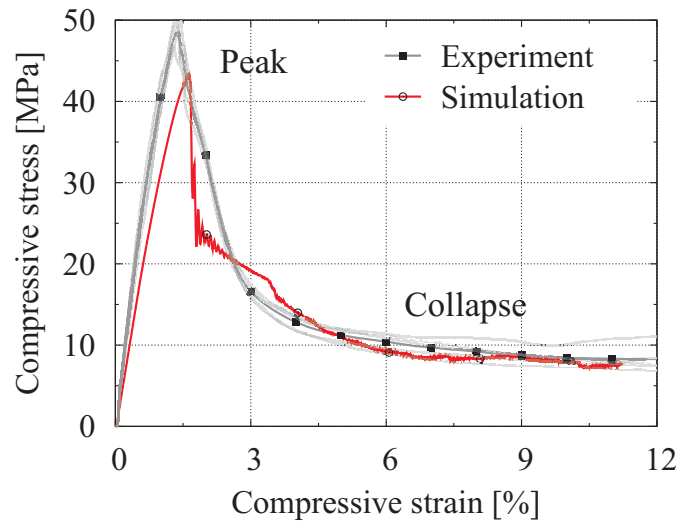
Figure 3.38.: Compressive stress vs. compressive strain of cylinder collapse simulation and experiment.

In summary, in the numerical model the initial collapse and subsequent drop in stress level is predicted to be more excessive as the actual behaviour observed in the experiment. This is a hint that the model overestimates the buckling behaviour of the aramid paper during initial collapse. Both numerical simulation and experiment show the formation of a diamond shaped buckling mode with five distinctive folds which shows that the buckling and collapse at later stages is well represented. It is noted that the cylinder collapse test gives no information on the buckling behaviour at fold edges, which have a considerable impact on buckling.

3.5.3. Summary of evaluation of aramid paper model

In above sections 3.5.1 and 3.5.2 the experimental investigation of two different aramid paper specimens is compared to FE models which use the layered shell model derived in chapter 3.4. Altogether the layered shell model gave good results for both benchmark load cases (Tensile coupon test (TCT) and cylinder collapse test (CCT)). The initial elastic behaviour in tension (TCT) and in compression (CCT) showed good agreement to the experiments. The small culmulative damage during the initial 'elastic' phase is observed to be well represented in all load cases. In case of compression (CCT) the peak stress is slightly underestimated by the layered shell model.

The evolution and occurrence of buckling is generally well captured, as the comparison of experiment and model showed in case of cell wall buckling (CCT). It is noted that the buckling observed in the CCT case predicted a stronger instability compared to the observations in the experiment. The local increase of damage in highly loaded regions of the aramid paper is well represented. In case of uniaxial tensile loading (TCT) the model predicted the correct fai-
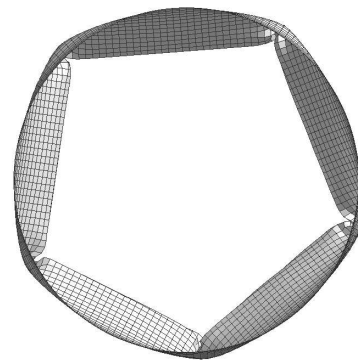
(a) Side-view of experiment
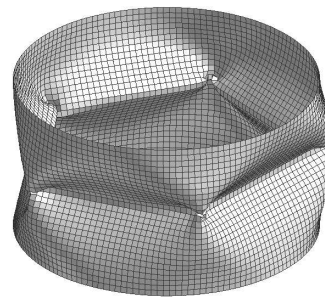
(b) Side-view of simulation

(c) Top-view of experiment

(d) Top-view of simulation

Figure 3.39.: Side-view and top-view of experiment (a,c) and simulation (b,d) of a collapsed large cylinder specimen.

lure strains and stresses but with 45° compared to 90° a considerable deviation of the fracture angle.

4. Folded sandwich cores

4.1. Overview

This chapter expands the previously presented aramid paper model to foldcore structures. The first part discusses the experimental characterisation of the foldcore's mechanical behaviour. This includes compression and shear tests. Furthermore the coefficient of kinetic friction is measured for different material combinations. In the subsequent section a parametric approach to describe the foldcore's geometry is presented, which is then used to create a numerical model based on the aramid paper model. The existence of numerous irregularities in a foldcore structure is highlighted and their inclusion in a numerical model is discussed. The quality of the numerical model is then studied on basis of a parameter study, which investigates effects of integration method and element size. The possibility of strain rate effects is discussed. Finally the foldcore model is validated by comparing numerical and experimental results of the foldcore compression and shear tests.

4.2. Experimental characterisation

To assess the capacity and quality of a numerical foldcore model, it is necessary to characterise the mechanical behaviour of a foldcore. For that purpose the foldcore is tested under compressive and shear load conditions. Subsequently test setup and results of these foldcore compression tests (FCT) and foldcore shear tests (FST) are discussed. Furthermore the kinetic friction behaviour of aramid paper is measured. The friction properties are necessary to describe the effect of contact events in case of large deformations of the foldcore folds. It is noted that also the friction behaviour between aramid paper and several other materials, such as steel, aluminium and carbon composite was tested. These additional information on friction are relevant for the impact modelling presented in chapter 5.

4.2.1. Foldcore compression test (FCT)

The understanding and modelling of the crushing behaviour is fundamental to the description of impact behaviour of cellular cores such as honeycomb and foldcores. During core crushing, a cellular structure fails in a complex combination of fold formation and cell wall fracture in which the interconnected and deformed cell walls reinforce each other. This phenomenon is known for its energy-absorbing capacities and has been analysed by various researchers

[58, 75, 151, 160]. Compressive behaviour of a foldcore in T-direction is the most important property for normal impact on sandwich structures.

The basic foldcore characteristics in compression are comparable to the compressive behaviour of honeycomb, which is probably one of the most intensely researched properties of honeycomb. Hong et al. [82] investigated the quasi-static crush behaviour of aluminium honeycomb specimen under pure compressive and combined loads. Furthermore, The compressive, tensile and shear behaviour of Nomex® honeycomb cores was comprehensively characterised by Zhand and Ashby [160] and Foo et al. [58]. Similar research was performed by Aktay et al. [12] and Castanié et al. [33], who also modelled Nomex® honeycomb compression and low-energy impact on basis of finite element methods employing shell and spring elements. All of them reported the typical stress-strain behaviour of a honeycomb under compression where the compressive stress initially increases almost linear elastically until the cell wall edges start to buckle or fracture. The stress then drops to a lower level at which the compressive stress remains nearly constant. At very large strains the stress increases again due to densification of the core.

Foldcore properties in compression have been investigated by Heimbs et al. [77] who compared quasi-static crushing tests of foldcores with dynamic finite element simulation. Kintscher et al. [102, 103] did an extensive experimental study of foldcore properties under single and combined loads. Both reported foldcore compressive behaviour to be very similar to the one observed for honeycomb cores. The presented compression test in this section has been published in advance by Heimbs et al. [77].

The quasi-static foldcore compression test series was performed on a Zwick 1484 universal testing device. The basic test device is depicted in figure 4.1 together with the test specifications. Four specimens were compressed composed of type 31 foldcores with 5x13 unit cells and glass fibre composite face sheets bonded together with adhesive. The 'Type' specification is a foldcore geometry definition adopted in the CELPACT research project. The corresponding foldcore dimensions can be found in table 4.5 on page 81. The sandwich plates are compressed in T-direction with a constant velocity of 2.0 mm/min. The technical stress is calculated by dividing the force measured at the load sensor by the theoretically computed area. The strain is given by the displacement of the crosshead divided by the initial foldcore height.

Figure 4.2a depicts the average stress-strain behaviour of the foldcores loaded in compression in direction of the applied load. The scatter observed in the compression test is small. For the mean peak stress (3.1 MPa) a coefficient of variation of 0.8% was calculated. An initial elastic increase of stress is observed until a specific peak stress is met. During this increase a small cumulative degradation of the stress-strain curve is noticeable, similar to the degradation behaviour observed in the tensile coupon test and cylinder crush series in section 3.3. Briefly before the peak stress is reached the first foldcore faces start to buckle. Once buckling of the faces has begun to extend to the fold edges the specimen collapses at peak stress. The stress level then drops to a relatively constant stress magnitude labelled crush stress. The so-called crush zone signifies strains between 5 % and 40 %. Within the crush zone the buckling of the foldcore structure and the formation of small cracks at the fold edges are observed. For large
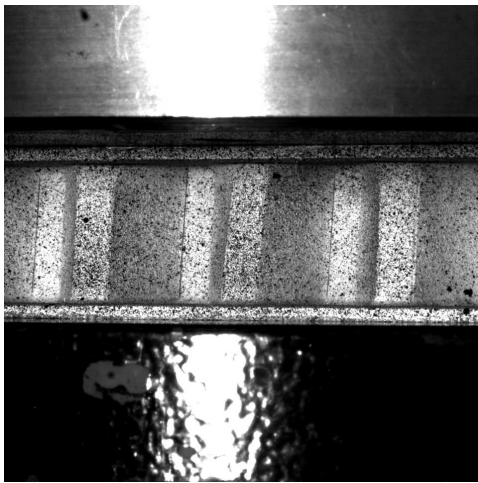
Test method:	Foldcore compression test
Test standard:	-
Test rate:	2 mm / min
Sample material:	Type 31 foldcore
Sample dimension:	5x13 unit cells, 20 mm height
Number of specimen:	4

Figure 4.1.: Test device   Table 4.1.: Test specifications
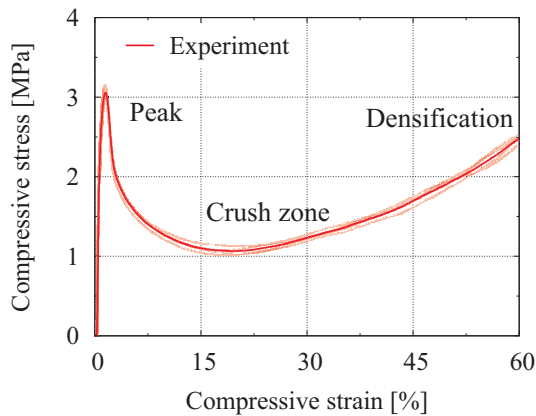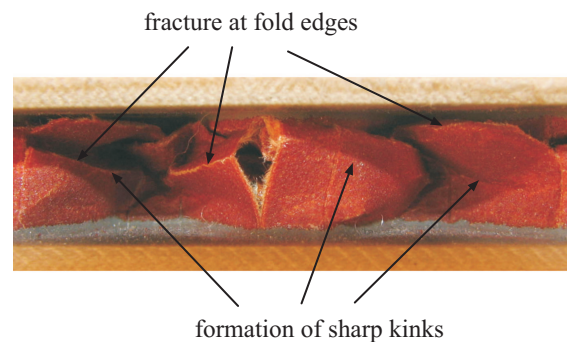
(a) Compressive stress-strain response   (b) Sideview of crushed foldcore

Figure 4.2.: (a) Compressive stress vs. compressive strain in foldcore compression experiment, (b) Sideview of crushed foldcore which was tested until densification.

strains (>40 %) the considerably deformed foldcore faces begin to interact with each other. This structural behaviour, which is called 'densification' is accompanied with a gradual increase of stress. During densification the formation of sharp kinks with considerable cracks and fractures at the fold edges is observed in the foldcore structure, as presented in figure 4.2b.

4.2.2. Foldcore shear test (FST)

The responses to shear in TL- and TW-direction are the two other dominant properties of a foldcore subjected to impact. The foldcore shear behaviour resembles the shear behaviour of honeycombs with respect to the global stress-strain response as well as the deformation and

Figure 4.3.: Test device

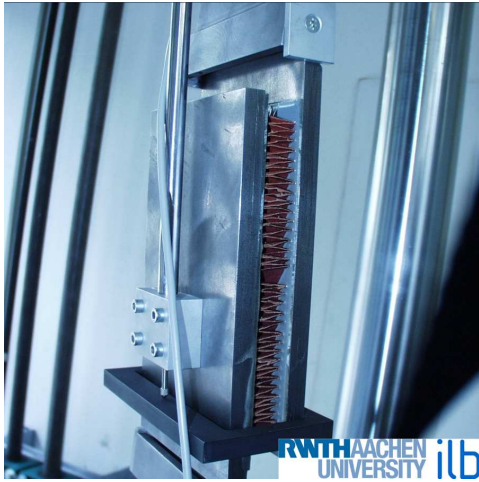| Test method:	Foldcore shear test
Test standard:	DIN 53294
	ASTM C273
Test rate:	0.5 mm / min
Sample material:	Type 21 foldcore
Sample dimension:	TL: 19x5 unit cells,
	20 mm height
	TW: 10x8 unit cells,
	20 mm height
Number of specimen:	TL: 5 / TW: 5

Table 4.2.: Test specifications

damage evolution of the base material. However, there is noticeable deviation in the observed characteristics, which mainly originates from the different geometry and dimensions between honeycomb cores and foldcores.

Longitudinal shear of aluminium honeycombs (TL- and TW-direction) was investigated experimentally and analytically by several research groups [107, 126, 127]. For a wide range of Nomex honeycombs the collapse behaviour under both shear and compression (TL-, TW- and T-direction) was numerically and experimentally analysed by Zhang and Ashby [160]. On basis of a representative unit cell the transverse shear behaviour of a honeycomb sandwich panel was numerically examined by Grediac [65]. All of them reported similar shear behaviour, with an initial elastic increase in stress until a peak stress is reached. The stress then drops considerably due to face buckling and plastic deformation of the cell walls. Following the decrease, several studies observed a constant shear stress level for increasing shear strain, whereas other studies observed a continuously decreasing residual stress. At large strains the stress approaches zero caused by interface debonding and cell wall fracture.

The shear behaviour of foldcores was investigated by Kintscher et al. [102, 103] who performed an extensive experimental study of foldcore properties under single and combined loads. The foldcore shear behaviour was reported to be comparable to the one observed for honeycomb cores. It is noted, that for both honeycomb core and foldcore an in-plane orthotropy was observed due to the different fold symmetries in L- and W-direction.

The presented shear tests on foldcore structures have been performed by the CELPACT partner RWTH Aachen (Department of Aerospace and Lightweight Structures). The quasi-static test series was performed on a Schenk Hydropuls 160 kN universal testing machine. The basic test setup is illustrated in figure 4.3 and the test specifications are given in figure 4.2. Five foldcore specimen (Type 21, 19x5 unit cells) were loaded in TL-direction and five foldcore specimen (Type 21, 10 x 8) were loaded in TW-direction.
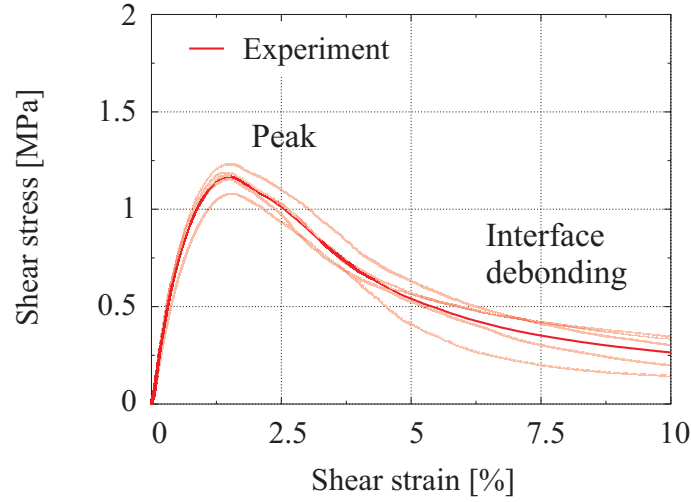
Figure 4.4.: Stress-strain-curves of foldcore shear test in TL-direction.

The foldcore dimensions corresponding to the 'Type' specification can be found in table 4.5 on page 81. The glass fibre reinforced polymer (GFRP) face sheets of the foldcore were adhesively bonded to rigid steel plates, which moved parallel to each other with a velocity of 0.5 mm/min. The technical stress is computed by dividing the force measured at the load sensor by the theoretically computed area of 19x5 unit cells and 10x8 unit cells respectively. The displacement is measured by an extensometer (HBM W20TK). The engineering shear strain $\gamma_{TL,TW}$ is calculated by dividing the transverse displacement by the initial foldcore height. The tensorial shear strain $\varepsilon_{TL,TW}$ is calculated with

$$\varepsilon_{TL,TW} = \frac{\gamma_{TL,TW}}{2}. \tag{4.1}$$

In figures 4.4 and 4.5 the average stress-tensorial shear strain responses of foldcores loaded in TL- and TW-direction are illustrated. An average scatter was observed in both shear directions. The COV calculated for mean peak stress in TL-direction (1.2 MPa) was 5% and the COV calculated for the mean peak stress in TW-direction (1.2 MPa) was 3%. The experimental curves demonstrate similar elementary characteristics in both in-plane orientations: Initially, the stress increases mainly elastically in addition to a small cumulative degradation of stiffness, which has also been observed in the other test series. Briefly after the foldcore faces start to buckle a peak stress is met. The stress level drops rapidly as soon as the initial face buckling extends to the fold edges. In case of further increasing strains the stress level eventually approaches zero due to extensive interface debonding (TL-direction) and face fracturing (TW-direction).
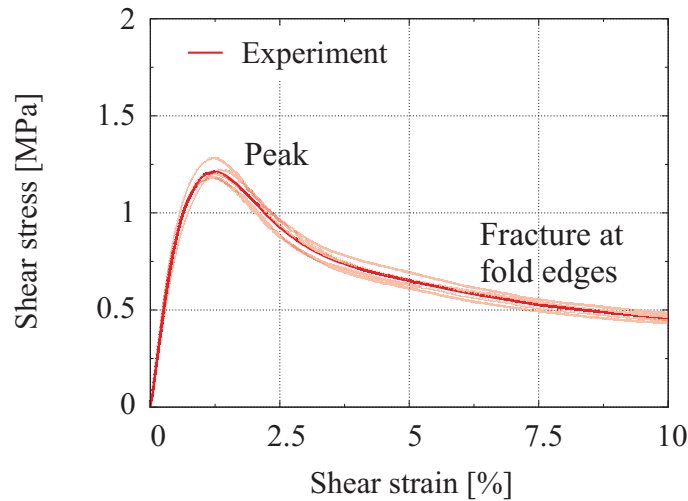
Figure 4.5.: Stress-strain-curves of foldcore shear test in TW-direction.

4.2.3. Friction on sliding interfaces

The failure of a foldcore sandwich structure coincides with considerable contact and sliding of its components. In particular the interaction of deforming foldcore faces results in multiple contact and sliding. If there is significant foldcore crushing additional contact occurs between the face sheets and the twisted foldcore faces. In case of impact there is also extensive contact between the target structure (Foldcore, face sheets) and the impactor. Therefore the friction associated with the sliding on these interfaces has significant influence on the simulation results. The effect of different friction coefficients on the results of a hard body impact model is shown in section 5.3.5 on page 146.

Typically the frictional force on a sliding interface is described by Coulomb friction which means that the frictional force is proportional to the applied normal force, independently of the contact area. In case of kinetic friction the correlation between frictional force F_f and normal force N is given by

$$F_f = \mu_k N, \tag{4.2}$$

where μ_k is the coefficient of kinetic fricton. In case of the present materials (aramid paper, carbon fibre reinforced polymer) it is difficult to find data on the required coefficient of kinetic friction in the literature. The main reason is the large range of factors affecting the frictional behaviour of composites, e. g. resin and fibre types, consistency of the surface, arrangement of the intrinsic components, which make a generic description difficult. Briscoe and Motamedia [28] determined the coefficient of interfibre-interyarn friction of Kevlar® 49 to be 0.22. Brown and Burgoyne [30] measured a friction coefficient of 0.11 for Kevlar® 49 yarns sliding on aluminium.
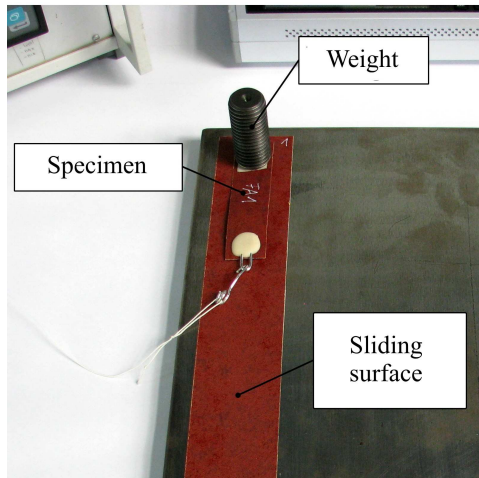
Figure 4.6.: Test device

Test method:	Measurement of coeff. of friction
Sample material:	Aramid paper
	Carbon composite
Sliding surface	Aramid paper
	Carbon composite
	Steel
	Aluminium
Number of specimen:	80

Table 4.3.: Test specifications

A significant amount of information on frictional parameters originates from tribologal studies. Zhang et al. [161] investigated the friction of a carbon fabric reinforced phenolic composite sliding on steel rings and found a coefficient of friction of 0.3. In the work of Schön [135] a frictional coefficient of 0.23–0.3 was determined for a carbon/epoxy composite (quasi-isotropic lay-up) on aluminium. The coefficient of friction of Nomex® fabrics sliding on steel discs was measured to be 0.136 by Su et al. [142]. However, the frictional parameters provided by tribology have to be considered with caution as they are typically determined for different surface topologies, pressure, temperatures, sliding velocities, etc, which can result in a significantly differing frictional behaviour.

In order to provide reliable data on the friction behaviour of the material types investigated in this work a basic friction test series was performed. For that purpose 48 strips of aramid paper and 32 strips of carbon composite were prepared, which were pulled at constant velocity along different sliding surfaces (Aramid paper, carbon composite, steel and aluminium). The drag load required to pull a strip equals the frictional force. It was measured by a force meter which was attached to the strip. The normal force was applied by a weight (1.7 kg and 3.6 kg) positioned on top of the strip. The test setup is depicted in figure 4.6 and the test conditions are summarised in table 4.3.

In a test cycle the drag load is increased until the strip begins to move. During a so-called sliding phase the strip is then moved at constant velocity for a time period. Subsequently the drag load is again reduced to zero. This procedure is repeated several times. The drag force measured during the sliding phase is the frictional force. For a better understanding, two force-time curves are pictured in figure 4.7. They show the frictional force measured for aramid paper sliding on aramid paper and a normal weight of 1.7 kg and 3.6 kg, respectively. It is noted that there is hardly any initial peak load due to static friction observable at begin of the sliding phase.
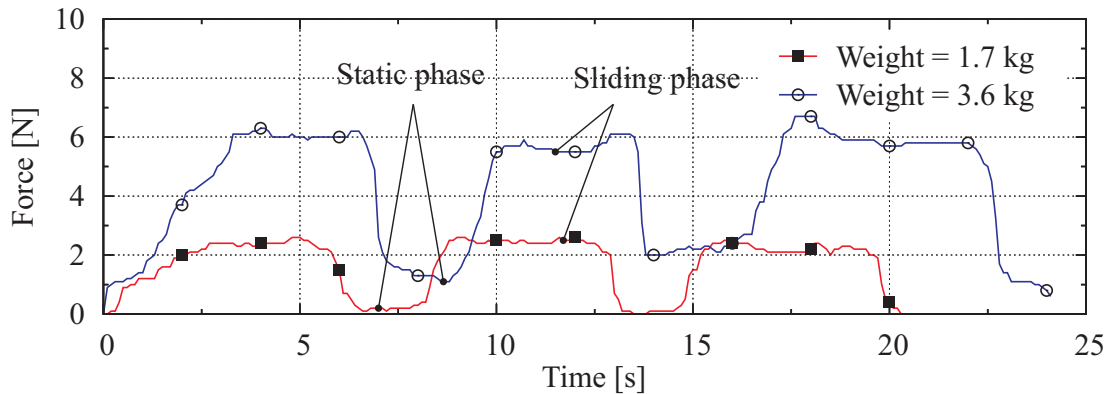
Figure 4.7.: Force-time plot of aramid paper sliding on aramid paper for an object mass of 1.7 kg and 3.6 kg.

Table 4.4.: Overview on measured coefficients of friction

Strip surface	Sliding surface	Number of specimen	Friction coefficient	Standard deviation
Aramid paper	Aramid paper	16	0.2	0.03
Aramid paper	Steel	8	0.42	0.03
Aramid paper	Aluminium	8	0.39	0.07
Aramid paper	Carbon composite	14 (16)	0.18	0.02
Carbon composite	Carbon composite	13 (16)	0.18	0.06
Carbon composite	Steel	8	0.29	0.07
Carbon composite	Aluminium	8	0.3	0.04

The measured coefficients of friction are summarised in table 4.4. If not stated otherwise, the in table 4.4 presented magnitudes for Coulomb friction are used in the numerical models of this work. The coefficients of friction determined for a composite surface sliding on a composite surface (Carbon composite, aramid composite) range from 0.17 to 0.18. These magnitudes are lower than those measured for a composite surface sliding on a metal surface (Steel, aluminium) which range 0.29 from 0.42. It is noted that the coefficient of friction of 0.42 measured for a aramid paper surface sliding on a steel surface is considerably larger than the value of 0.136 reported by Su et al. [142] for Nomex®. Reasons for this disagreement are differences in normal load (16.5–35 N vs. 235–430 N), velocity (0.03 m/s vs. 0.26 m/s) surface structure (The surface of aramid paper is exclusively composed of phenolic resin), contact temperature (20 °C vs. 62–240 °C) and time duration (~30 sec vs. 2h).

4.3. Numerical model

In this section the aramid paper model derived in chapter 3 is applied to foldcore geometries. For this purpose a parametric foldcore unit cell is presented. The existence and representation of imperfections and irregularities in a foldcore structure are outlined subsequently. The dependency of the foldcore model on numerical factors such as integration method and element size is quantified on basis of a parameter study and the consequences on the numerical adequacy and reliability of the model are discussed. Finally a brief overview on strain-rate dependent behaviour of the foldcore structure caused by micro-inertial effects is given.

4.3.1. Foldcore geometry

In the following a the geometric description of a foldcore structure is presented, which can then be meshed by shell elements using the aramid paper model presented in chapter 3. The geometrical foldcore desrciption is based on existing research [44, 71, 158], in which a description for the ideal geometry of repetitive folded structures was presented. Generally a folded geometry without curvature is composed of a recurrent fold pattern, which repeats itself along the planar directions. Different folding patterns of complex three-dimensional folded structures are depicted in figure 4.8. The foldcore schemes investigated in this work are denominated as the zig-zag type (Figure 4.8a) and the extended type (Figure 4.8b). The recurrent fold pattern can be used to define a unit cell as illustrated in figure 4.9 for the zig-zag and the expanded foldcore types. Typically the orientation of a foldcore is signified with the parameter T, L and W, where T is the out-of-plane direction representing the foldcore's thickness and L, W are the in-plane directions representing the foldcore's length and width.

In the work of Hachenberg et al. [71] it was shown, that a set of four independent geometric parameters determines a unit cell of zig-zag foldcore geometry and five independent parameter define an expanded foldcore geometry. Additionally a method to describe curved foldcore geometries was proposed. However, the foldcore mesh geometries presented here are confined to flat surfaces of parallel geometry although it is generally feasible to generate curved shapes with varying spacing between the surfaces. The parameters defining the geometric model are the folded core height H, the zigzag opening angle γ and the spacing parameters a and L. The extended foldcore includes the additional dimension s. Each individual foldcore face occupies a respective fraction of the sandwich core volume V^*. In figure 4.10a the volume taken by a zigzag type foldcore face is depicted. In figure 4.10b the volume occupied by the extended face in W-direction of a extended type foldcore is shown. If the cell wall thickness t_{wall} and the cell wall density ρ_{wall} are known an average core density ρ^* can be calculated with

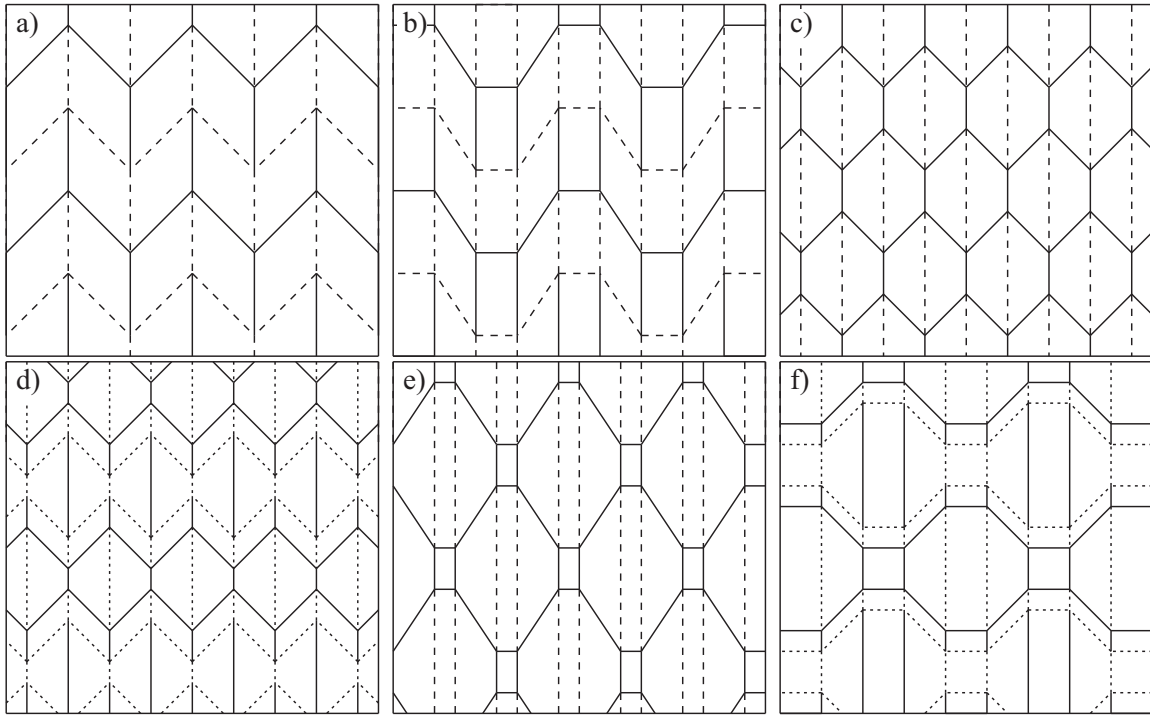$$\rho* = \frac{V_{wall}}{V^*}\rho_{wall},$$

(4.3)

Figure 4.8.: Typical folding schemes for a variety of folded structures taken from Hachenberg et al. [71].
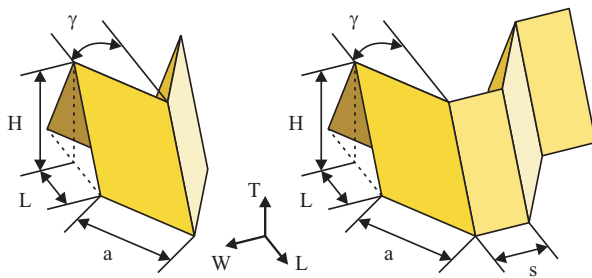

Figure 4.9.: Unit cell of a zig-zag foldcore and an expanded foldcore.
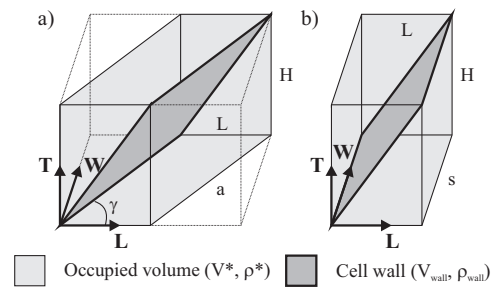

Figure 4.10.: Volume occupied by an individual foldcore face.

where V_{wall} is the cell wall volume and V^* is the average core volume of a unit cell. The cell wall volume V_{wall}^{Zigzag} and the average core volume $V^{*Zigzag}$ of a zigzag type unit cell are given by

$$V_{wall}^{Zigzag} = 4a\sqrt{L^2sin^2\gamma + H^2}t_{wall} \qquad \text{and} \qquad V^{*Zigzag} = 4LHasin\gamma. \qquad (4.4)$$

The cell wall volume V_{wall}^{Ext} and the average core volume V^{*Ext} of a extended type unit cell are defined by

$$V_{wall}^{Ext} = 4\left(a\sqrt{L^2sin^2\gamma + H^2} + s\sqrt{L^2 + H^2}\right)t_{wall} \qquad \text{and} \qquad V^{*Ext} = 4LH\left(asin\gamma + s\right).$$
$$(4.5)$$

By combining equations 4.4 in case of zigzag type and 4.5 in case of extended type respectively one of the independent geometric parameter can be substituted by the average core density ρ^*. The resulting correlations can be written as

$$\rho^{*Zigzag} = \frac{\sqrt{L^2sin^2\gamma}t_{wall}}{LHsin\gamma}\rho_{wall} \qquad \text{and} \qquad (4.6)$$

$$\rho^{*Ext} = \frac{\left(s\sqrt{H^2 + L^2} + asin\gamma\sqrt{L^2sin^2\gamma + H^2}\right)t_{wall}}{LH\left(s + asin^2\gamma\right)}\rho_{wall}. \qquad (4.7)$$

It is noted that in case of zig-zag cores the average core density $\rho^{*Zigzag}$ is independent of the geometric parameter a. The average core density is a fundamental design criterion of sandwich cores and it is generally convenient to utilise the average core density as a parameter to define the unit cell. In course of the presented work, the above formulation was adopted to mathematically describe the investigated foldcore geometries.

Typically the foldcore mesh is generated in ANSYS on basis of a apdl-script in which the input of the geometric parameter, the global foldcore dimensions and the mesh characteristics constitutes the position of the nodes and their respective elements. The basic procedure of model generation in PAM-CRASH is briefly summarised appendix B. It is noted, that the specific foldcore geometries in this work are referred to as Type 'x' foldcores, where 'x' specifies the number given in table 4.5. This notation has been adopted during the CELPACT project [3] during which the impact behaviour and performance of the thus defined set of different foldcore geometries was investigated. Results of the numerical investigations performed in the CELPACT project are presented in section 4.4 and section 5.4 of this thesis.

4.3.2. Imperfections in a foldcore structure

During observation of a genuine foldcore sample it becomes apparent that its structure is neither uniform in geometry nor free of imperfections and irregularities. Three types of imperfections can be observed. Firstly irregularities, which directly originate from the non-uniform consistency of the cell wall material. A rough indication of the irregular nature of the aramid

Table 4.5.: Foldcore geometry specification as employed in EU-project CELPACT [3].

Number	H [mm]	a [mm]	γ [°]	s [mm]	$\rho*$ [kg/m^3]	t_{wall} [mm]	Variation
1	10	12.5	30.5	5	137.5	0.306	H
2	15	12.5	30.5	5	137.5	0.306	H
3	20	12.5	30.5	5	137.5	0.306	H
4	25	12.5	30.5	5	137.5	0.306	H
5	30	12.5	30.5	5	137.5	0.306	H
6	20	5.0	30.5	5	137.5	0.306	a
7	20	8.75	30.5	5	137.5	0.306	a
8	20	12.5	30.5	5	137.5	0.306	a
9	20	16.25	30.5	5	137.5	0.306	a
10	20	20	30.5	5	137.5	0.306	a
11	20	12.5	1.0	5	137.5	0.306	γ
12	20	12.5	15.75	5	137.5	0.306	γ
13	20	12.5	30.5	5	137.5	0.306	γ
14	20	12.5	45.25	5	137.5	0.306	γ
15	20	12.5	60.0	0	137.5	0.306	γ
16	20	12.5	30.5	2.5	137.5	0.306	s
17	20	12.5	30.5	5	137.5	0.306	s
18	20	12.5	30.5	7.5	137.5	0.306	s
19	20	12.5	30.5	10	137.5	0.306	s
20	20	12.5	30.5	5	75.0	0.306	s
21	20	12.5	30.5	5	106.25	0.306	$\rho*$
22	20	12.5	30.5	5	137.5	0.306	$\rho*$
23	20	12.5	30.5	5	168.75	0.306	$\rho*$
24	20	12.5	30.5	5	200.0	0.306	$\rho*$
25	20	12.5	30.5	5	137.5	0.063	$\rho*$
26	20	12.5	30.5	5	137.5	0.126	t_{wall}
27	20	12.5	30.5	5	137.5	0.201	t_{wall}
28	20	12.5	30.5	5	137.5	0.268	t_{wall}
29	20	12.5	30.5	5	137.5	0.306	t_{wall}
30	20	12.5	30.5	5	137.5	0.306	t_{wall}
31	20	12.5	30.5	5	112.97	0.306	Additional
32	20	12.5	3.12	5	137.5	0.306	Blocked

(a) Cell wall material

(b) Top view

(c) Curved faces

(d) Foldcore edges
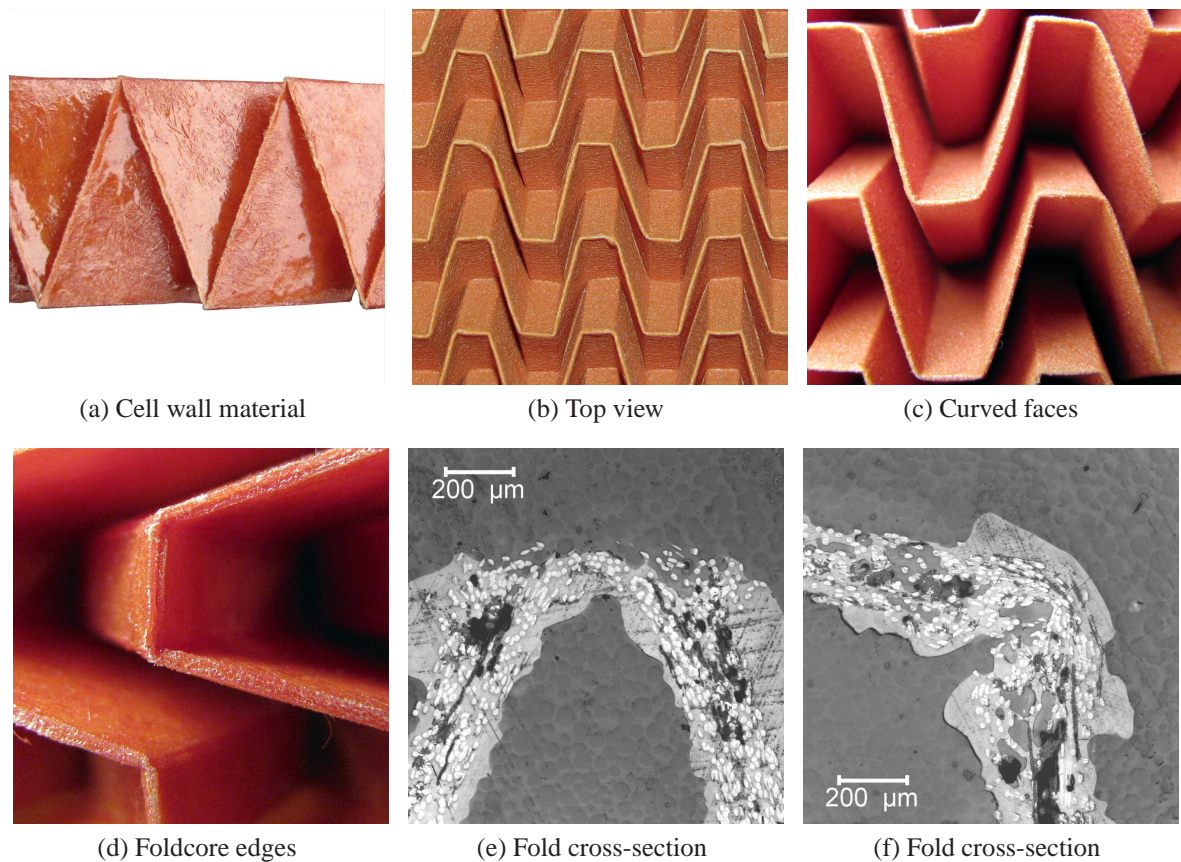

(e) Fold cross-section

(f) Fold cross-section

Figure 4.11.: Imperfections observed in foldcore specimen: (a) Top view on skewed fold-
core geometry (b) Warped foldcore faces (c) Foldcore cell wall material (Aramid
paper) demonstrates considerable non-uniform properties (d) Truncated aramid
paper at foldcore edges (e-f) Microscopic image of the cross-section of the fold
between two foldcore faces showing (e) open cut on outer surface and (f) closed
cut on inner surface.

paper is given in figure 4.11a where randomly oriented fibres and resin patches can be ob-
served at the paper faces. The distinctive characteristics of the aramid paper with substantial
existence of irregularities are discussed in detail in chapter 3. The modelling of the paper
material's inherent inhomogenities is presented in chapter 3.4.

Local cuts at the fold edges are separately considered as a second type of imperfection.
The cuts are caused by the embossment of the fold pattern into the aramid paper prepreg
and the subsequent folding process. In figure 4.11d a close-up photography of a foldcore
cell shows the cut structure at the foldcore edges which is observable by the naked eye. The
microscopic images of the cross-section of two foldcore edges depicts an open cut positioned
at the exterior of the fold and a closed cut positioned at the fold interior. Generally the cut
depths range between 40–80 % of the total cell wall thickness.

It is noted, that degradation of the aramid paper at the face edges due to the embossing process is not considered in the subsequently discussed modelling approach. However, in the quasi-static foldcore experiments of section 4 it is observable, that cracks and tears are predominantly initiated at the face edges, where the material is weakened and where significantly loads are occurring. Therefore it is expected that although the adopted finite element approach may reproduce crack initiation at face edges due to the existing load concentration, it will overestimate the stiffness and strength properties of the face edges due to the neglect of initial edge degradation.

Another type of imperfection is the noticeable variation of the foldcore geometry. Common variations are uneven cell walls and deviation of the face size from the perfect shape due to the folding process as depicted in figure 4.11b as well as considerable curvature of the faces in unloaded state as observable in figure 4.11c. The effect of this type of imperfection on the foldcore's load response is examined in the following.

4.3.3. Representation of foldcore imperfections

In contrast to the previously discussed imperfections observed in real foldcore structures the geometry of a meso-model generated by the geometrical approach is perfect. An uniform foldcore geometry is expected to influence simulation results and was investigated by Heimbs et al. [77]. Here the implementation of inhomogenities in FE models which reproduced buckling and crushing of aramid paper and carbon composite foldcore specimen in compression was investigated. Different approaches were examined such as random variation of mesh geometry as well as modification of the cell wall properties. It was found that the geometrical imperfections influence the buckling load of the single cell walls and the whole structure's strength especially in case of the carbon composite foldcores. It was also observed that neglect of imperfections can cause discrepancies due to uniform unit cell behaviour.

In the presented work the effect of the geometrical inhomogenities are modelled on basis of random variations of the mesh geometry. Two variation approaches have been investigated. The approach signified as 'node-shaking' is depicted in figure 4.12. Here the local imperfections are represented by random modifications of all nodal coordinates with the exception of the nodes at the paper wall edges. In-plane of the cell wall the nodal positions are relocated from their original positions at a distance which randomly ranges between the maximum negative and positive magnitude d_{max}^{NS}. Out-of-plane of the cell wall the nodal positions are randomly varied on basis of a reduced minimum/maximum magnitude αd_{max}^{NS} with the ratio factor α having a value of 0.05.

The second approach is denominated as 'geometry shaking'. The top view on a foldcore geometry distorted with 'geometry shaking' approach is illustrated in figure 4.13. Here the corner positions of the cell wall faces are randomly varied prior to meshing. In direction of the sandwich's L- and W-orientation the corner positions are randomly dislocated between a maximum negative and positive magnitude d_{max}^{GS}. In the sandwich T-direction the corner positions are randomly varied on basis of a reduced minimum/maximum magnitude βd_{max}^{GS} with ratio factor β being equal to 0.25.
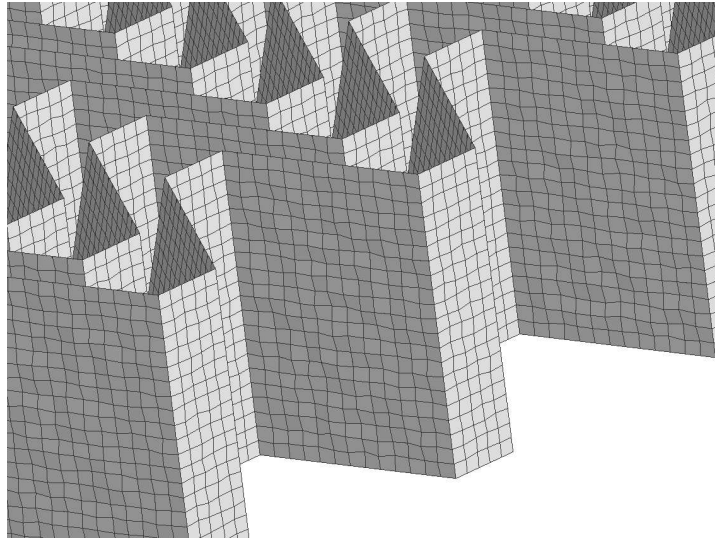
Figure 4.12.: Illustration of randomly distorted node positions in node shaking approach (Maximum deviation: 0.4 mm in-plane of paper and 0.1 mm out-of-plane of paper).
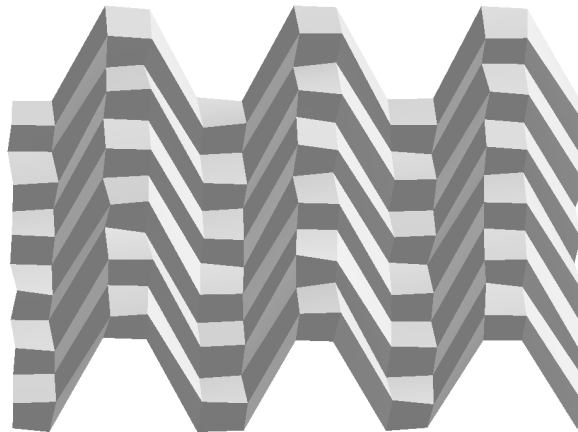

Figure 4.13.: Top-view on distorted geometry of a foldcore in geometry shaking approach (Maximum deviation: 4 mm in L- and W-direction and 1 mm in T-direction).
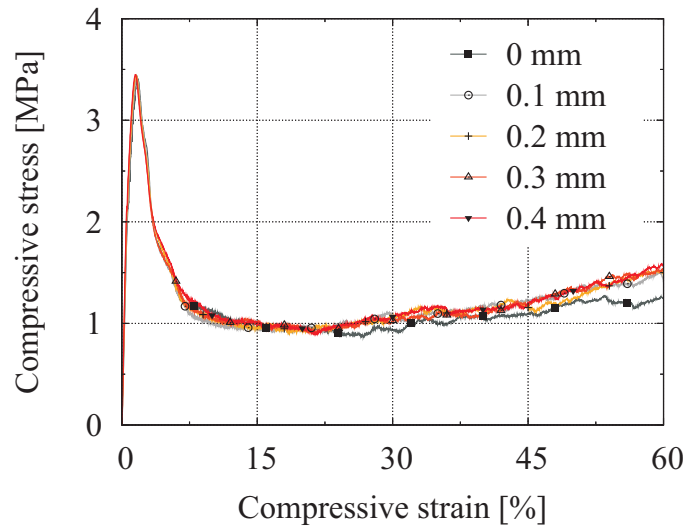
Figure 4.14.: Comparison of stress-strain-curve of foldcore in compression with perfect fold-core geometry and node-shaking with values of $d_{max}^{NS} = 0.1$ mm, 0.2 mm, 0.3 mm and 0.4 mm.

Figures 4.14 and 4.15 show the stress-strain behaviour of a foldcore specimen in compression modelled with a perfect geometry and with 'node-shaking' and 'geometry-shaking' approaches using different d_{max}. For the aramid paper the material model developed in chapter 3.4 was implemented. Generally it can be observed, that for the investigated conditions the effect of the different geometrical inhomogenities on the simulation results is very small and the stress-strain-curve of the modified geometry is comparable to a uniform geometry. This contravenes to some extend observations made in the PhD thesis of Aktay [10] and by Heimbs et al. [77].

In case of the honeycomb structures reported by Aktay [10] the differing results caused by the consideration of geometrical inhomogenities may originate from the difference in orientation of the individual cell wall structure of foldcores and honeycomb cores. In a honeycomb core under compression the respective cell wall faces are loaded parallel to their planes. A slight deviation of the geometry in out-of-plane direction of the face provokes a considerable decrease of stability as it introduces a load in lateral direction of the face. In a foldcore under compression, the faces are loaded in normal and in lateral direction due to their inclined orientation. A deviation of the foldcore geometry has therefore a lesser effect on the global stability of the foldcore.

Heimbs et al. [77] observed an impact due to consideration of geometrical inhomogenities in particular for carbon composite foldcores. Carbon composite foldcores are generally significantly stiffer than aramid paper foldcores and also exhibit a larger amount of global geometrical irregularities in the foldcore structure. These characteristics might explain the different observations made for the effect of consideration of inhomogenities.
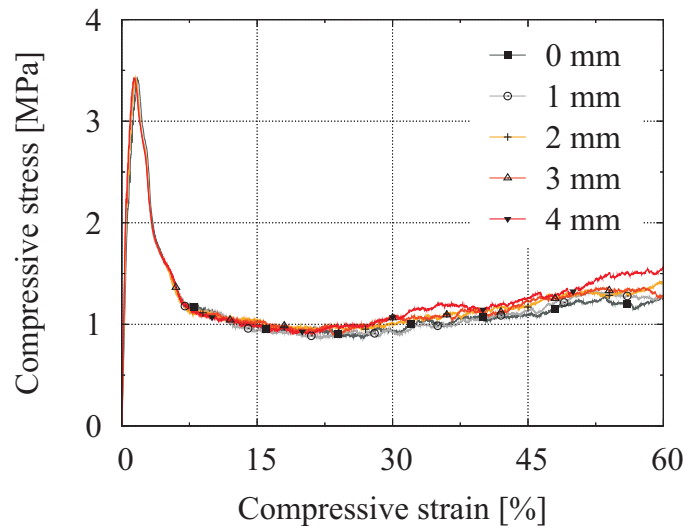
Figure 4.15.: Comparison of stress-strain-curve of foldcore in compression with perfect fold-
core geometry and geometry-shaking with values of $d_{max}^{GS} = 1.0$ mm, 2.0 mm,
3.0 mm and 4.0 mm.

(a) Perfect geometry   (b) Node-shaking
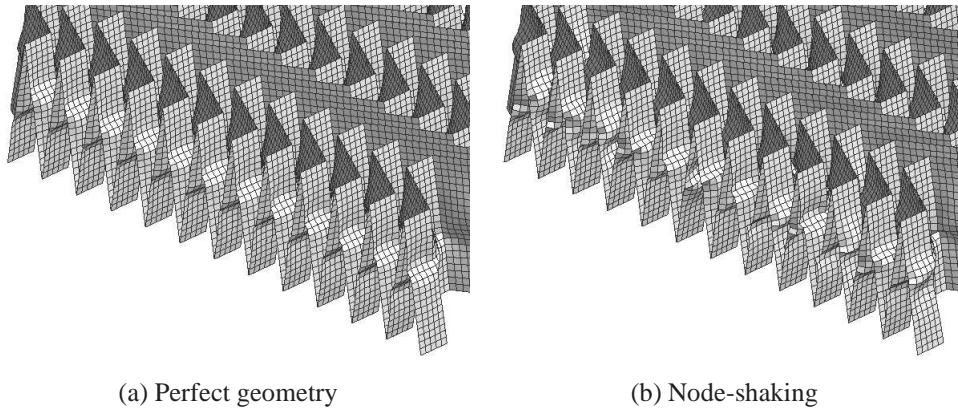
Figure 4.16.: Buckling and deformation plots of an uniform geometry and a node-shaked geo-
metry.

However, while a perfect foldcore structure tends to buckle uniformly for each repeating
unit cell, a modified node structure demonstrates slightly different buckling for each unit cell
and thus avoids discrepancies, which can result from uniform behaviour. This behaviour is
illustrated in figure 4.16, where the buckling pattern of an uniform and a 'node-shaked' fold-
core geometry are depicted. The perfect geometry shows identical buckling for each unit cell,
whereas the modified geometries exhibit a preferable irregular buckling as it is also observed
in reality.

An implication of the observed behaviour is that although the random modification of geometry has negligible effect on the stress-strain-curves, it is desirable to consider irregularities in the geometrical model, as it results in a physically realistic irregular folding/buckling mode in the core. For this purpose, both 'node-shaking' and 'geometry-shaking' demonstrate qualitative comparable results. In the present work, inhomogenities are generally considered by the 'node-shaking' approach with a d_{max}^{NS} of 0.1 mm and an α of 0.05.

4.3.4. Numerical effects and influences

In the following a parameter study is presented, which investigates the influence of several numerical factors on the FE models results. The study uses a representative setup reproducing foldcore compression. There are several incentives to select foldcore compression as a characteristic reference case: Foldcore compression is straightforward to implement and experimentally and numerically well-established. Most notably is that the deformation and failure mechanisms observed for foldcore compression correspond well to effects observed for impact cases whilst reducing the influencing factors given that properties of face sheets and adhesive bonds can be neglected and the load environment is comparatively simple.

Element type and Hourglass energy

In this subsection the adequacy of different shell formulations based on Mindlin shell theory [119] and provided by PAM-CRASH to reproduce foldcore load scenarios is investigated. The desired shell formulation is required to balance computational cost with numerical accuracy, especially in case of considerable shell bending and rigid body motion, as is expected to occur in the foldcore model. The parameter model used for the investigation employs the aramid paper material model discussed in chapter 3 and reproduces foldcore compression between two rigid surfaces at constant velocity. Relevant characteristics for assessment are the initial elastic behaviour as well as the buckling and collapse behaviour of the foldcore.

The four types of PAM-CRASH shell formulations analysed are a reduced Belytschko-Tsay (BT) formulation, a fully integrated Hughes-Tezduyar formulation as well as a reduced and a fully integrated Belytschko-Wong-Chiang formulation [47]. The Belytschko-Tsay shell formulation employs a bilinear (four node) quadrilateral shell which is based on a uniform reduced integration approach as proposed by Hughes et al. [85] and further developed by Belytschko et al. [23]. The Belytschko-Tsay formulation is remarkably computationally efficient and offers in general satisfactory accuracy. However it suffers from zero-energy modes which are a consequence of under-integration. In most cases, the impact of the zero-energy modes can be effectively reduced by addition of an algorithm as proposed by Flanagan and Belytschko [56].

The Hughes-Tezduyar (HT) shell formulation uses a fully integrated bilinear (four node) quadrilateral shell which adopts an enhanced transverse shear strain rate field as developed by Hughes and Tezduyar [86]. The assumed strain field avoids the shear locking commonly observed in fully integrated shells. The Hughes-Tezduyar formulation has no zero-energy
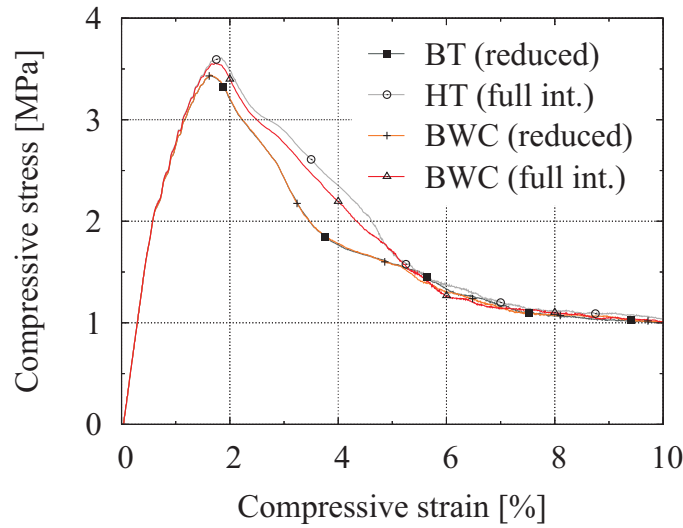
Figure 4.17.: Compressive stress-strain-curve of a foldcore loaded in compression which is
             computed with different shell element formulations (Belytschko-Tsay (BT),
             Hughes-Tezduyar (HT) and Belytschko-Wong-Chiang (BWC)).

modes due to its full quadrature. However as a direct consequence of full integration the formulation is computationally expensive.

The Belytschko-Wong-Chiang (BWC) shell formulation (Belytschko and Leviathan [22]) adds a nodal projection as described by Belytschko et al. [24] to the Belytschko-Tsay formulation. The projection enforces invariance of the internal power to rigid body motion and drill rotation, which results in improved behaviour for warped elements. The Belytschko-Wong-Chiang formulation is implemented for reduced as well as fully integrated bilinear (four node) quadrilateral elements. The full rank element has no zero-energy modes but it requires a considerable increase in CPU time. In case of the full rank element the shear field is assumed on an approach based on Bathe and Dvorkin to avoid shear locking.

The effect of the individual shell formulation are illustrated in figure 4.17, which depicts the stress-strain-behaviour of several FE simulation of a foldcore parameter model in compression. In summary it is observed that the stress-strain-behaviour during initial buckling as well as the considerable deformation during foldcore crushing is well represented by all formulations. In case of initial buckling, the formulations with reduced integration demonstrate a marginally lower stress level than the full rank formulations. Due to the satisfactorily reproduction of buckling behaviour and the low computational time consumption, as seen in table 4.6, the Belytschko-Tsay formulation is preferred for foldcore modelling in this work.

The application of a reduced integration formulation requires a control of the zero-energy modes. Zero-energy modes are caused by the integration failing to provide stiffness to stop certain modes of deformation. They are commonly controlled by adding an analytically determined corrective stiffness or viscosity respectively to the element stiffness or force equations.
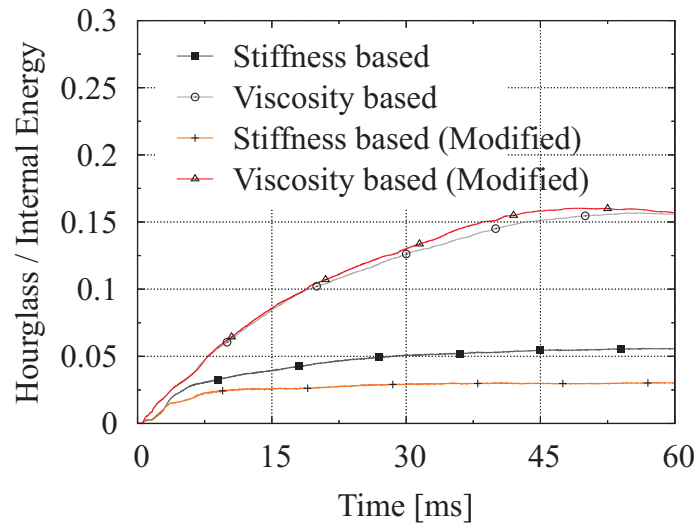
Figure 4.18.: Ratio of hourglass energy by internal energy for different zero-energy mode reduction schemes.

Table 4.6.: Time consumption of different shell formulations for implemented parameter model.

	Belytschko-Tsay	Hughes-Tezduyar	BWC reduced	BWC full rank
Time t	$6.5 \cdot 10^4$ s	$1.15 \cdot 10^5$ s	$6.4 \cdot 10^4$ s	$1.22 \cdot 10^5$ s
Ratio t/t_{BT}	1.0	1.77	0.99	1.88

In large deformation calculations, a viscous term is usually preferred to avoid building up large elastic forces in the system. For explicit calculations with small to moderate deformations, and long time periods, a stiffness form of zero-energy mode control is often preferred to prevent zero-energy modes from slowly building up in the solution.

To select an adequate zero-energy mode control for the model the ratio of hourglass energy versus internal energy of a stiffness based and a viscous based correction is compared as illustrated in figure 4.18. Those two methods can additionally be modified by adding a term, which improves the consideration of orthogonality between hourglass strain-rates and rigid body modes for strongly warped elements which undergo large rigid body rotations. Based on experience the ratio of hourglass energy versus internal energy should be less than 10 %.

In figure 4.18 a considerably lower ratio of hourglass energy versus internal energy is observed for stiffness based correction compared to the viscosity based correction. With less than 5 % the standard stiffness based method shows satisfying results which even can be improved with the modified stiffness based method which exhibits a ratio of 2.5 % and below. Due to satisfying numerical results and low computation time the finite element models in this
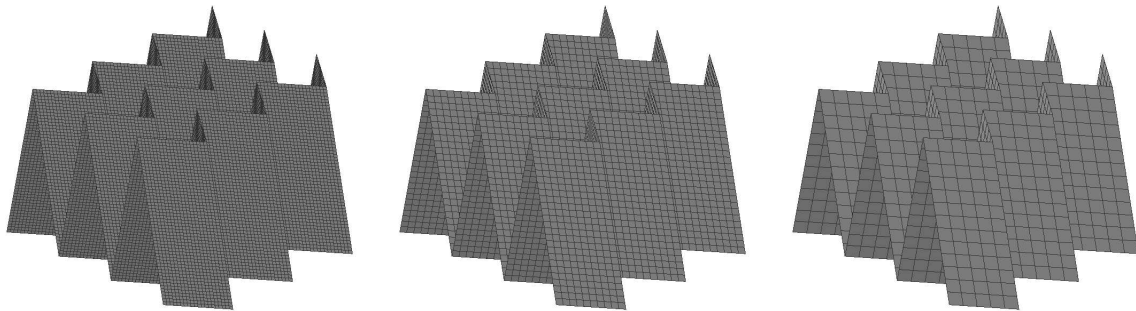
Figure 4.19.: Illustration of foldcore model meshed with different element sizes (0.5 mm, 1.0 mm, 2.0 mm).

work are discretised with Belytschko-Tsay shell elements where the zero-energy modes are controlled by the stiffness based method.

Element size

Another important numerical factor is the size dependency of shell elements within the fold-core model. A coarser mesh reduces the computational cost. However coarse meshes tend to be conservative in their estimation of buckling phenomena. This overestimation of buckling resistance is particularly strong if instability is occurring, as it is observed in case of foldcore cell walls in compression.

Mesh sensitivity of cellular structures modelled by a detailed shell element model has been observed by Heimbs et al. [77] as well as by Aktay et al. [12]. Aktay et al. [12] examined models with different mesh sizes which represent aluminium honeycomb crushing. It is reported that mesh sensitivity affects deformation modes and load-displacement-behaviour especially in case of advanced honeycomb densification. The results presented here have been partly published in the work of Heimbs et al. [77], where the mesh sensitivity of aramid paper und carbon composite foldcore models in compression was investigated. The element size is noticed to slightly affect the Young's modulus of the folded core prior to buckling. Considerable difference in buckling stresses was observed, at which a coarser mesh tends to exhibit larger stress level compared to finer meshes. It was indicated, that the element size effect is possibly coupled to the shell thickness.

The significance of mesh size towards buckling resistance is observed using the foldcore parameter model. Here the basic compression model using different mesh sizes as illustrated in figure 4.19 was investigated. The parameter study was performed for two different material models: A simple power law aluminium material model and the aramid paper model. The numerical model is set up, such that it reproduces foldcore compression between two rigid surfaces at constant velocity. The sole variable in the different material model setups is the mesh size.
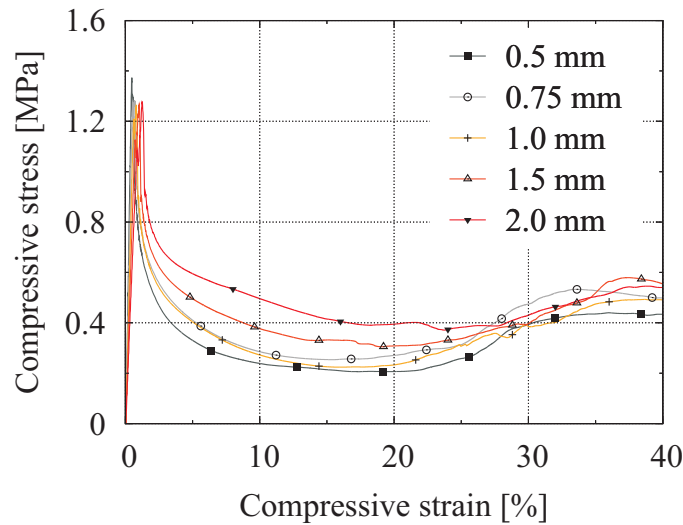
Figure 4.20.: Compressive stress-strain-curve of an aluminium foldcore loaded in compression which is discretised with different element sizes ranging from 0.5 mm up to 2.0 mm.

The stress-strain behaviour as shown in figure 4.20 for a foldcore with aluminium material model and in figure 4.22 for a foldcore with aramid paper material model reveals a considerable impact of the mesh size on simulation results. The stress level observed during buckling and crushing of the foldcore differs about 50–100 % in case of the aluminium material model and 25–50 % in case of the aramid paper material model for the examined narrow range of mesh sizes. The stress level drops with decreasing mesh size.

Two further dependencies are noticeable in figure 4.21 for the aluminium model and in figure 4.23 for the aramid paper model, which depict a close-up view of the stress-strain behaviour during the initial elastic pre-buckling phase. It is recognisable that the foldcore pre-buckling stiffness in out-of-plane direction increases slightly if the mesh size decreases. Additionally it is noticed that the maximum peak stress at buckling initiation varies by 10 % where lower values result from increasing mesh sizes. Generally it is found that the buckling region of smaller mesh sizes is more localised than the buckling region of larger meshes.

The aluminium model is more sensitive to a variation of mesh size than the aramid paper model. However it is difficult to identify an explicit model parameter which causes the mesh size dependent behaviour, as several parameter such as the elastic constants, the shell thickness, plasticity and damage are different in both models. It is thought that the effect is depending on the aspect ratio of the individual elements, which for confirmation needs to be investigated in future studies.

In summary a considerable dependency on mesh size is evident, which can be avoided only to a limited amount as it originates directly from the degrees of freedom of the mesh. A significant variance from the mesh size for which the model has been validated gives differing
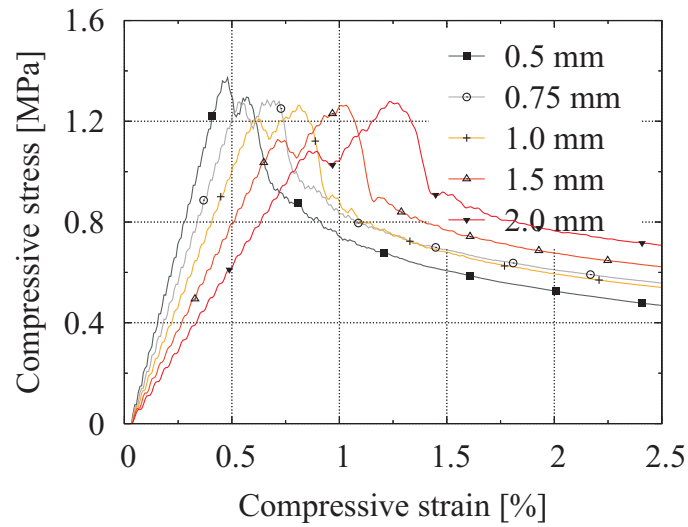
Figure 4.21.: Close-up section of initial elastic phase of the simulations depicted in figure 4.20.
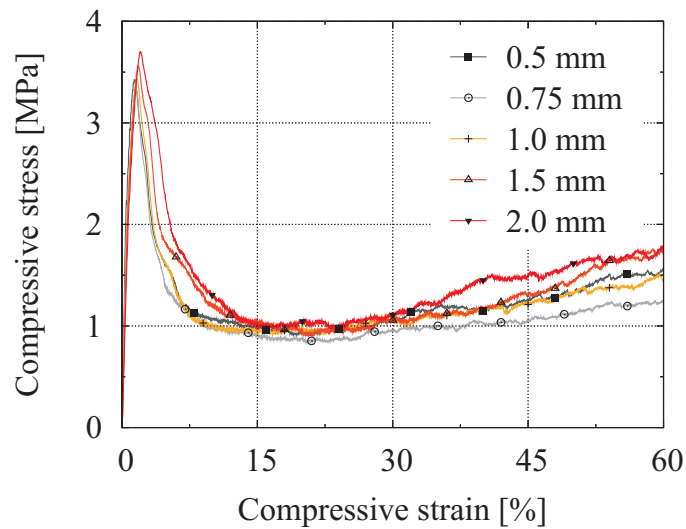

Figure 4.22.: Compressive stress-strain-curve of an aramid paper foldcore loaded in compression which is discretised with different element sizes ranging from 0.5 mm up to 2.0 mm.
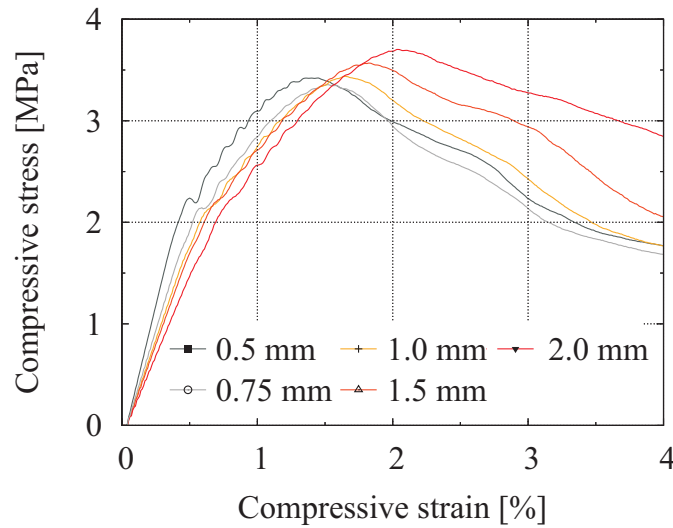
Figure 4.23.: Close-up section of initial elastic phase of the simulations depicted in figure 4.23.

results. To minimise the effect of mesh size, the employed element sizes in this work were restricted to 1.0 mm to 1.5 mm side length, with some rare occasions using element sizes up to 3.0 mm side length.

4.3.5. Strain rate effects

Most material properties (as for example stiffness moduli, Poisson's ratios, strength, etc.) used for calibration of FE models in static and dynamic codes originate from quasi-static test methods. In case of modelling dynamic events such as crash or impact it can be necessary to consider the dynamic material properties. Generally it has been observed that high strain rates result in an increase in material stiffness and strength compared to the quasi-static behaviour. The magnitude of the strain effect depends on the respective material. The strain rate $\dot{\varepsilon}$ is defined as the derivation of the strain ε with respect to the time t and can be written as

$$\dot{\varepsilon} = \frac{d\varepsilon}{dt}. \tag{4.8}$$

Commonly strain rates below 0.01 s^{-1} are defined as quasi-static. For strain rates of about 10 s^{-1} and larger the effect of dynamic loading can be observed for many materials, as for example metals. Strain rates properties of aramid yarns or fibre bundles were investigated by Wang and Xia [149] and by Tan et al. [145]. Wang and Xia loaded Kevlar® fibre bundles with strain rates between 10^{-4} s^{-1} and 1350 s^{-1}. An increase of 25 % in failure stress, 7.5 % in failure strain and 15 % in modulus was measured for strain rates of about 140 s^{-1}. In summary the aramid fibres demonstrated considerably less strain rate sensitivity compared to glass fibres with a transition range to rate dependence from rate independence at about 0.1 s^{-1} to 100 s^{-1}. Tan et al. [145]

Table 4.7.: Technical strain rates and impact velocities at which experiments are performed in this work.

Technical strain rate [s^{-1}]	Impact velocity [m/s]	Application
0.001	-	Quasi-static test (2 mm/min)
200	5	Drop tower test (2.2 m/s - 6.0 m/s)
2000	50	Gas gun test (40–110 m/s)
10^4	250	-

investigated aramid fibre yarns at strain rates from $0.3 \cdot 10^{-3}$ s^{-1} to 500 s^{-1}. At 480 s^{-1} an increase of 36 % in failure stress, 26 % in failure strain and 28 % in modulus was measured. At strain rates of about 250 s^{-1} the observed increase in properties decreased to about one-third of those values. At a strain rate of about 480 s^{-1} a change in the failure mechanism of the fibres was observed. The fibre yarns showed fracture with more lengthy fibrils splitting axially at low strain rates while exhibiting fewer and shorter fibrils at high strain rates.

A basic overview on impact velocities and their corresponding technical strain rates used in this work is given in table 4.7. The technical strain rate values are roughly calculated by

$$\dot{\varepsilon}_T = \frac{v_0}{l_0}, \qquad (4.9)$$

where v_0 is the initial velocity of loading and l_0 is the specimen dimension. It is noted that the maximum strain rates in this work are observed in the gas gun impact test as delineated in section 5.2.2. They are expected to be roughly about 2500 s^{-1}. For the drop-tower experiments illustrated in section 5.2.1 strain rates of up to 250 s^{-1} are estimated.

Strain rate effects on Nomex® honeycomb were investigated in research done by Goldsmith and Sackman [64] as well as by Aitken [9]. It is noted that the strain rate measured for honeycomb core crushing is the technical strain acting on the honeycomb divided by the time and not the local strain rates at impact location. Goldmith and Sackman [64] observed in flatwise compression test performed with a gas gun facility at high loading rates a 10 % increase in crush strength compared to quasi-static test. By Aitken [9] also a slight increase in crush strength was found in the medium technical strain rate range of 5 s^{-1}. An extensive investigation on strain rates effects in Nomex® honeycombs was presented by Heimbs et al. [78]. Here the crushing of honeycombs in out-of-plane and in-plane directions was examined for technical strain rates ranging from 10^{-3} s^{-1} to 300 s^{-1}. In this study, a technical strain rate of 300 s^{-1} corresponded roughly to an impact velocity of about 4.5 m/s at which an increase in the crush stress plateau of about 10 % was measured. However the observed rate dependency was attributed to inertial effects rather than material strain rate dependencies.

The structural setup of honeycomb and foldcores with planar faces which are orientated to each other at certain angles is comparable. Therefore it is justifiable to expect that, in case of employed impact velocities in the range of 2.2 to 110 m/s, rate dependencies are mainly
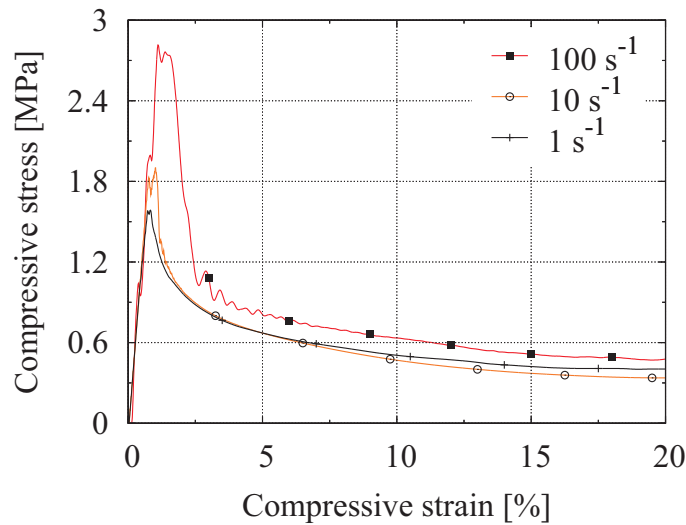
Figure 4.24.: Compressive stress-strain-curve of a foldcore loaded in compression with different load rates (100 s⁻¹, 10 s⁻¹, 1 s⁻¹).

caused by micro-inertial effects, as it was observed in above studies. Strain rate effects induced by the foldcore cell wall material can be neglected.

In section 4 a range of quasi-static experiments on foldcores are compared to dynamic simulations. A necessary condition for a successful solution of a quasi-static problem by means of an explicit, dynamic code is, however, that the problem is basically displacement-driven. For such problems the inertia forces can easily be controlled by the prescribed displacement or velocity. To assess the influence of the inertial effects on the numerical results a parameter study was performed, where simulation time and prescribed displacement velocity have been varied. The stress-strain-curves of a foldcore compression model loaded with different load rates 100 s⁻¹, 10 s⁻¹ and 1 s⁻¹ is depicted in figure 4.24. The upper and lower part of the foldcore are assumed to be fixed and a displacement load with different velocities is applied at the upper face of the foldcore. The finite element model does not consider material strain rate effects.

The presented load rate is calculated using equation 4.9, where v_0 is the velocity of compression and l_0 is the initial height of the foldcore. It is observable that increased load rates result in a stiffer initial behaviour until peak load as well as an increased stress level during foldcore collapse and crushing. The difference in behaviour is caused by inertial effects and disappears if the load rate is sufficiently reduced. The global deformation of the model with load rates of 100 s⁻¹, 10 s⁻¹ and 1 s⁻¹ at identical compressive strain of 5 % is illustrated in figure 4.26.

At 100 s⁻¹ the foldcore collapses locally at the upper end where the load is applied under formation of sharp-edged folds. If the load rate is reduced to 10 s⁻¹ and 1 s⁻¹ the buckling pattern extends until it adopts the global buckling mode which is generally observed in quasi-
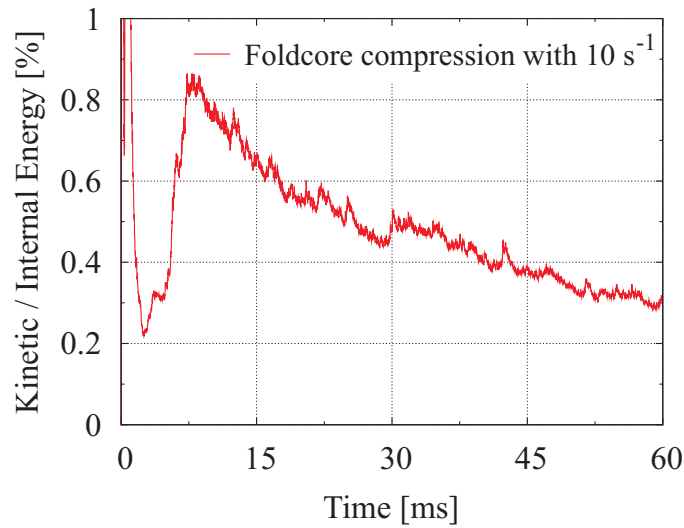
Figure 4.25.: Ratio of kinetic and internal energy of a foldcore compressed with 10 s^{-1}.
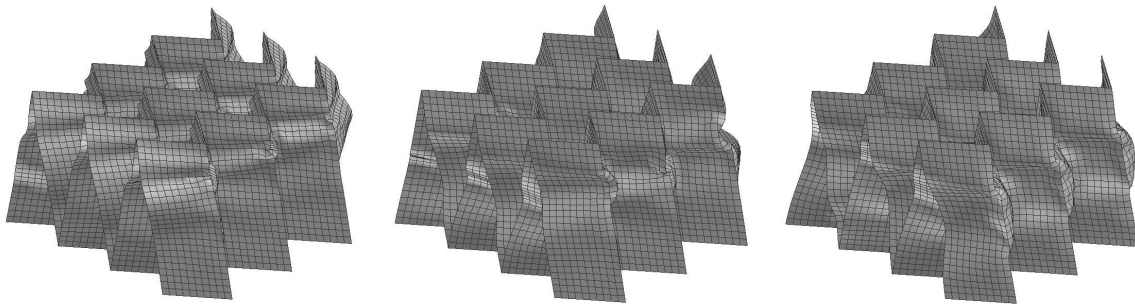
Figure 4.26.: Illustration of deformation of a foldcore model in compression with different load rates (100 s^{-1}, 10 s^{-1}, 1 s^{-1}).

static experiments. This observation indicates, that at higher strain rates (which are expected in case of impact events) the failure is localised to the contact area. There is no time for the global buckling in the foldcore wall to take place, which is seen at lower strain rates.

In summary it is noted that the stress-strain-curves and buckling behaviour approximately converge at load rates smaller than 10 s^{-1}. In conclusion quasi-static experiments are modelled in this work with load rates between 10 s^{-1} and 1 s^{-1}. Although lower load rates are generally required for quasi-static tests, the simulated load rates chosen depend on the practical balance between computation time and required model size. To this regard the time scale of the dynamic model has to be chosen so that the kinetic energy is small compared to the internal energy. In figure 4.25 the ratio of kinetic energy and internal energy is plotted against

the time for a foldcore compression model with 10 s^{-1}. It is apparent that the energy ratio is constantly less than 1 %. The initial peak of the curve is caused by the internal energy being zero at the onset of simulation.

4.4. Model evaluation

To assess the capacity and quality of the adopted foldcore modelling approach the predictions of the finite element model are carefully compared to the results of the benchmark test presented previously in section 4.2. This includes the investigation of compressive as well as of shear loading of foldcore specimen. The geometry parameters and numerical parameters used in the foldcore model are presented in table 4.8.

It is noted, that the test environment is quasi-static contrary to the dynamic nature of the explicit FE simulations. A comparison of a quasi-static problem with an explicit, dynamic model is admissible if the undesired inertia effects are within acceptable bounds, as discussed in section 4.3.5. This is assumed, as in the presented simulations the kinetic energy is below 1 % of the total energy.

4.4.1. Foldcore compression test (FCT)

The compressive behaviour of a foldcore in T-direction is the most important property for normal impact on sandwich structures. To measure the efficiency of the numerical foldcore model in this respect the numerical and experimental results of foldcore compression tests are compared. Evaluation criteria are the reproduction of global collapse behaviour of the foldcore, face and wall edge buckling as well as cell wall damage evolution.

The presented numerical model is configured as indicated in figure 4.27. A 3x6 type 31 foldcore (for type definition cf. table 4.5 on page 81) is represented by a 3D shell element structure employing the layered shell model. It is noted that the foldcore size of the numerical model with 3x6 unit cells is considerably smaller than the experimental specimen with 5x13 unit cells. However preliminary numerical studies revealed that the stress-strain-behaviour is virtually unaffected by the size reduction. The reason is, that the effect of the free boundaries at the foldcore edges is confined by the nearby internal cell wall folds. The change of ratio of free cell wall faces to joined cell wall faces is small in the range of investigated foldcore sizes.

The element size is 1 mm side length. The mesh is slightly distorted via node shaking as discussed in section 4.3.3 with an maximal deflection of 0.05 mm lateral and 0.0025 mm normal to the face plane. The foldcore model is attached to rigid surfaces with the linear TIED penalty method provided by PAM-CRASH. The possibility of face sheet-core debonding is neglected. The rigid face sheets move toward each other at a constant relative velocity v_0 of 0.2 m/s. The foldcore model uses a self contact with a coefficient of friction of 0.2 (0.17) as was determined in section 4.2.3.

Figure 4.28 depicts the stress-strain behaviour of experiment and numerical model in compression in direction of the applied load. If both curves are compared a good agreement can be observed for the initial elastic behaviour, as well as for the behaviour in the crush zone. However the difference between the peak stress of numerical and experimental results is with 10% considerably larger than the COV observed in the experiments (0.8%). The numerical model seems to overestimate the peak stress, where it predicts a peak stress of 3.4 MPa com-

Table 4.8.: Summary of geometry and numerical parameters used in the foldcore model.

| Parameter	Value	Unit	Comments
Foldcore properties			
Type	31	-	Foldcore dimensions are defined in section 4.3.1 on page 78ff. ($H = 20$ mm, $a = 12.5$ mm, $\gamma = 30.5°$, $s = 5$ mm, $\rho* = 112.97$ kg/m^3).
Type	21	-	Foldcore dimensions are defined in section 4.3.1 on page 78ff. ($H = 20$ mm, $a = 12.5$ mm, $\gamma = 30.5°$, $s = 5$ mm, $\rho* = 196.25$ kg/m^3).
Aramid paper	-	-	The elastic properties of the aramid paper are listed in section 3.4.4 on page 51ff. and the degradation is described in section 3.4.5 on page 54ff.
Numerical properties			
Node shaking	2.5–50	μm	The maximum deflection of nodal position is 2.5 μm normal and 50 μm lateral to the foldcore faces. Implementation of irregularities is discussed in section 4.3.2 on page 80ff.
Element side length	1	mm	A parametric study investigating the influence of element side length can be found in section 4.3.4 on page 90ff.
Element elimination strain	0.2–0.9	-	Element elimination is briefly discussed in section 3.4.6 on page 60f.
Friction coefficient	0.2	-	An investigation of friction can be found in section 4.2.3 on page 75ff.
Contact thickness	0.35	mm	The foldcore model uses a selfimpacting contact with edge treatment (PAM-CRASH Type 36)
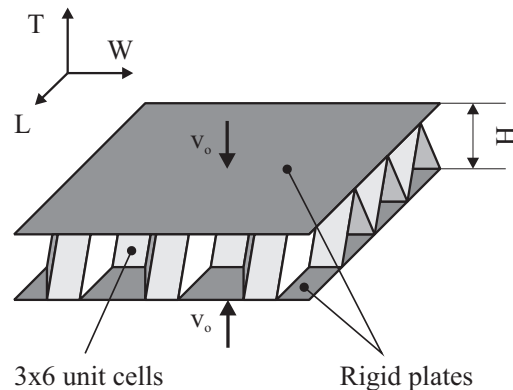
Figure 4.27.: Schematic plot of FE model setup of foldcore compression test.

pared to 3.1 MPa observed in the experiment. This difference is attributed to the neglect of the pre-damaged cell wall structure at the fold edges in the numerical model (see section 4.3.2).

Furthermore, there is a distinctive deviance in the prediction of the stress level in the densification regime, where the numerical model considerably underestimates the stress measured in the experiments. This difference is attributed to the way the material model represents the cell wall damage. In the experiments the foldcore structure during densification is observed to form sharp folds with considerable cracks and tears at the fold edges. However in between the folds the aramid paper is comparatively undamaged and retains significant stiffness. In contrast the material model cannot fully represent the formation of sharp folds and thin cracks as it reproduces damage uniformly distributed over an element. Eventually this leads to an overestimation of the distribution of damage, which in turn results in a underestimation of predicted compressive stresses.

In figure 4.29 the deformation of an experimental specimen and the numerical model is plotted for strains of 1 %, 5 % and 10 %. In figures 4.29a and 4.29b comparable initial face buckling prior to peak stress is observable for the numerical model and the experiment. In figures 4.29c and 4.29d buckling of faces and edges can be observed for both experiment and simulation. The buckling of the numerical model tends to be located approximately in the centre of the foldcore, whereas in the experiment buckling is also seen in top and bottom regions. In the experiment first initial cracks appear at fold edges. In the deformation plot of the numerical model no eliminated elements are visible. However, if the damage scalar contour plot in figure 4.30 is considered, significant occurrence of damage at similar locations as in the experiment can be observed at a strain of 2.5 %. Figures 4.29e and 4.29f show numerical model and experiment at a strain of 10 %. Both plots show comparable folding and kinking as well as frequent appearance of cracks, which, in the numerical model, is represented by elimination of elements.

Figure 4.30 illustrates the planar distribution of damage evolution of the numerical model at strains of 1 % and 2.5 %. At 1 % a low dispersal of damage is observed at foldcore faces
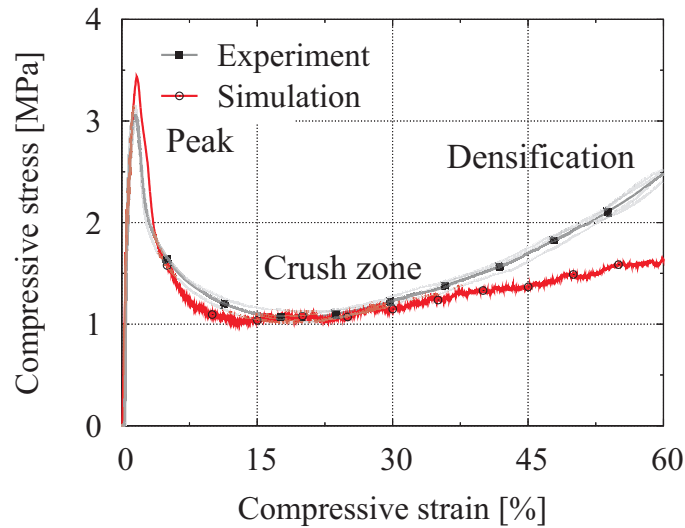
Figure 4.28.: Compressive stress vs. compressive strain of foldcore compression simulation and experiment.

and fold edges. This conforms to the cumulative damage evolution caused by fibre segment realignment and associated local matrix damage observed in the experiments. At larger strains the damage increases locally especially in regions where the cell wall is notably deformed. In particular at the fold edges, where buckling occurs, a considerable increase in damage is observed. This evolution of damage conforms with the experiments, in which first cracks usually appear at fold edges.

In summary the layered shell model gives a good reproduction of the global collapse behaviour in the initial phase as well as in during the crush regime. The initial peak stress is overestimated by an moderate extend. In case of densification it tends to overestimate the evolution of damage. This observation is also valid for the local cell wall damage evolution, which is well represented at low strains, but which predicts a too sizeable expansion of damage for large strains in the densification regime. Face and wall edge buckling is in good agreement with the experiments.

4.4.2. Foldcore shear test (FST)

The responses to shear in TL- and TW-direction are the two other important properties of a foldcore subjected to impact. To measure the efficiency of the numerical foldcore model in this respect the numerical and experimental results of foldcore shear tests are compared. Major criteria are the reproduction of the global stress-strain response and the damage processes in the paper after the initial elastic phase as well as the representation of the prevalent face and edge tearing. The numerical model is configured as indicated in figure 4.31. A 3x6 type 21 foldcore model is implemented with 3D shell elements using the layered shell model pre-

(a) Numerical model - 1 % strain (b) Experiment - 1 % strain

(c) Numerical model - 5 % strain (d) Experiment - 5 % strain

(e) Numerical model - 10 % strain (f) Experiment - 10 % strain
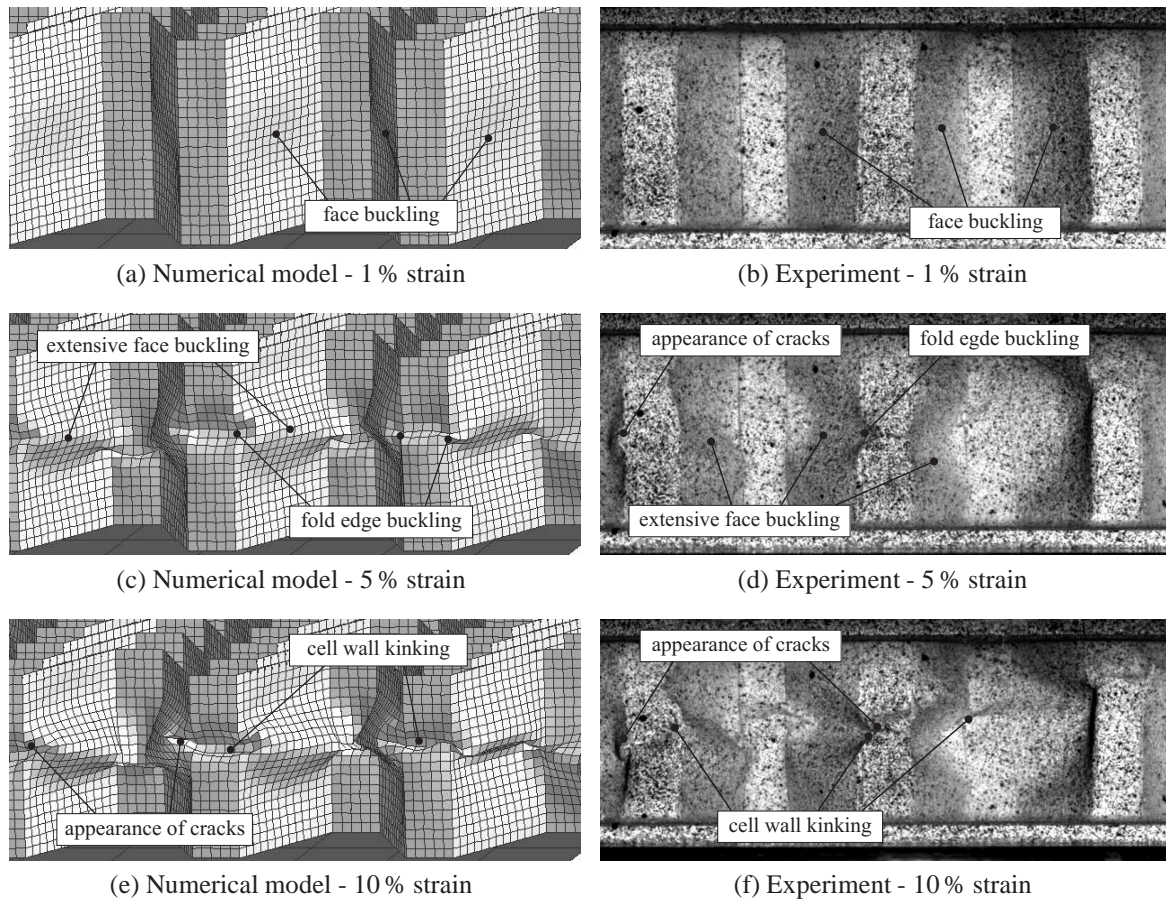
Figure 4.29.: Deformation plots of aramid paper foldcore model loaded in compression at strains of 1 %, 5 % and 10 % for simulation and experiment.

sented in chapter 3.4. Similar to the studies for the compression case, preliminary numerical models with 19x5 and 10x8 unit cells show comparable stress-strain response to a scaled down foldcore with 3x6 unit cells. The FE simulations presented here are realised with a foldcore with 3x6 unit cells.

The numerical model is meshed with elements of 1 mm side length and the nodal positions are slightly distorted based on the node shaking approach discussed in section 4.3.3. The model of the foldcore is attached to rigid face sheets with the PAM-CRASH TIED contacts. The rigid face sheets move parallel to each other at a constant velocity of 0.2 m/s. The displacement in T-direction is free. Self contact is defined similarly to the foldcore model in compression, which uses a coeffcent of friction of 0.2 (0.17, cf. section 4.2.3).

In figures 4.32 and 4.33 the stress-strain response of experiment and numerical model are illustrated. The experimental curves demonstrate similar elementary characteristics in both in-plane orientations: Initially, the stress increases mainly elastically in addition to a small cumulative degradation of stiffness, which is also observed in the other test series. Shortly
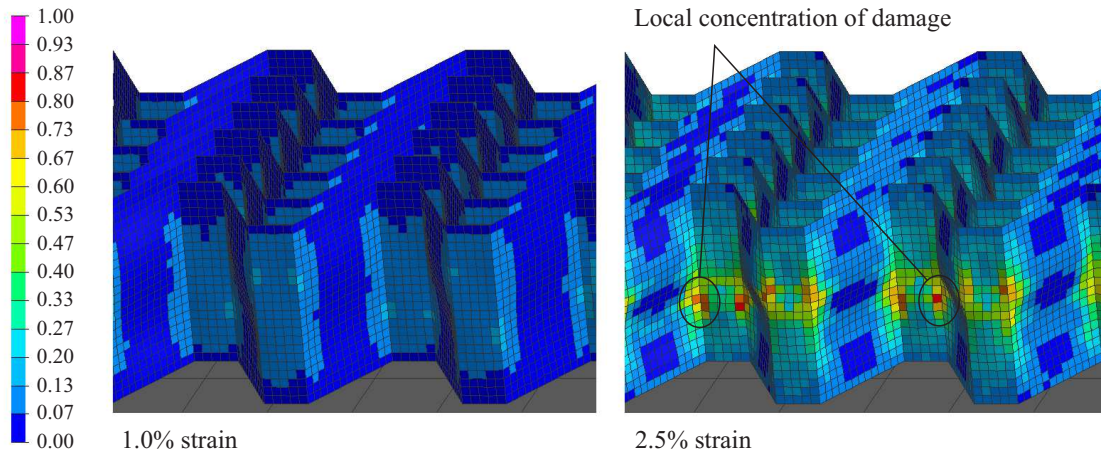
Figure 4.30.: Contour plots of the damage scalar of the fibre reinforced layer at compressive strains of 1 % and 2.5 %.

(a) Shear in TL   (b) Shear in TW
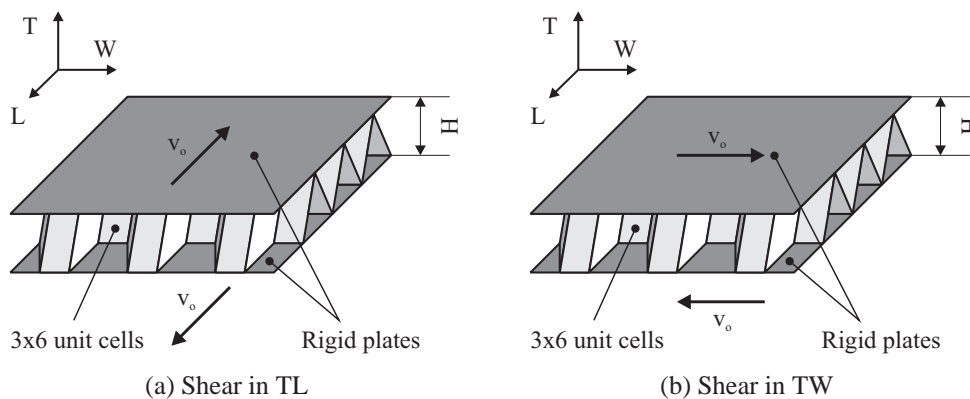
Figure 4.31.: Schematic setup of the FE model representing the foldcore shear tests.

after the foldcore faces start to buckle a peak stress is reached. The stress level drops rapidly as soon as the initial face buckling extends to the fold edges. For further increasing strains the stress level approaches zero due to extensive interface debonding (TL-direction) and face fracturing (TW-direction).

The stress-strain response of experimental and numerical results demonstrate good agreement, especially in case of larger strains. The numerical model overestimates the peak stress for both shear directions, with 1.45 MPa vs. 1.2 MPa in case of TL-direction and 1.4 MPa vs. 1.2 MPa in case of the TW-direction. The differences are considerably larger than the coefficients of variation observed in the experiment (5% in TL and 3% in TW-direction). There are two factors, which are identified to cause these differences. Firstly, the pre-damaged cell wall structure at fold edges is neglected in the numerical model, which causes an overestima-
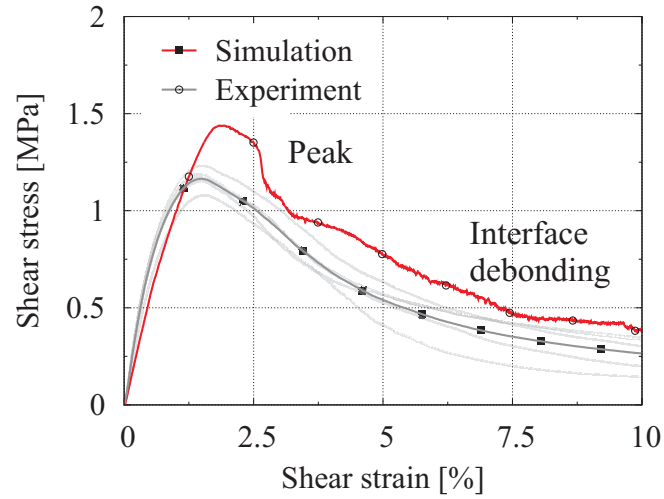
Figure 4.32.: Stress-strain-curves of experiment and simulation of foldcore shear test in TL–
          direction.
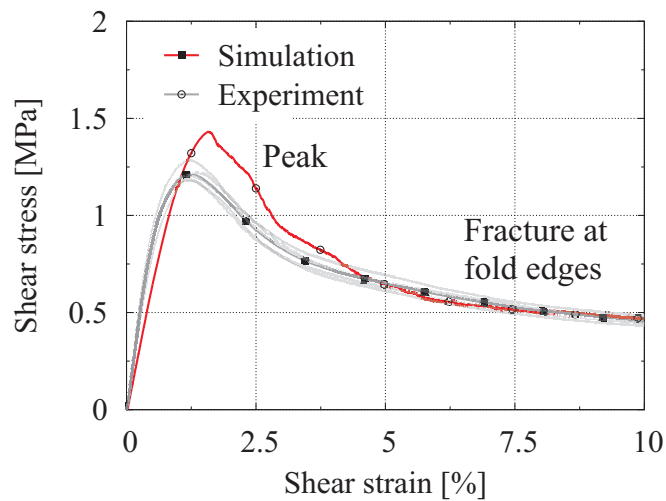
Figure 4.33.: Stress-strain-curves of experiment and simulation of foldcore shear test in TW-
          direction.

face buckling

cell buckling

extensive cell buckling

failing elements at interface

failing elements at interface

(a) Numerical model - 2.5 % strain   (b) Numerical model - 5 % strain   (c) Numerical model - 7.5 % strain

fracture at interface   face buckling

fracture at interface

fracture at interface

(d) Experiment - Small strain   (e) Experiment - Medium strain   (f) Experiment - Large strain
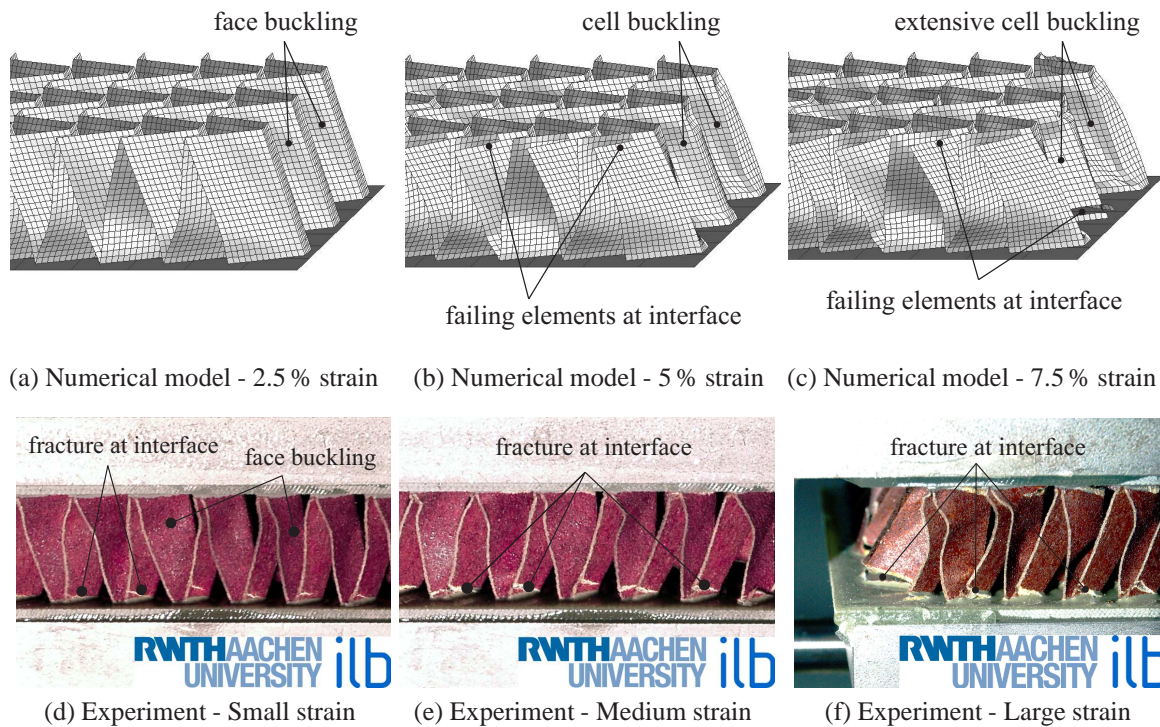
Figure 4.34.: Deformation of aramid paper foldcore model and ILB shear tests loaded in TL-shear.

tion of load level, at which the fold edge begin to rupture (Mainly observed in TW-direction). Secondly the bond between face sheet and foldcore is assumed to be a perfect bond with no fracture. In case of interface debonding the cell wall adjacent to the face sheet has to fail instead, which also results in an overestimation of load level (Mainly observed in TL-direction).

In figure 4.34 the deformation of numerical model and experimental results in TL-direction are illustrated for different strains. In case of the experiments, the first buckling is initiated at the zigzag faces (Fig. 4.34a). At large strains mainly interface debonding is observed (Fig. 4.34e–Fig. 4.34f). If the numerical and experimental deformation plots are compared, a good agreement of the buckling modes is observable. The numerical model shows extensive element degradation (Fig. 4.35) and elimination in close proximity to the regions, where the foldcore-face sheet interface is observed to fracture in the experiments. This overestimation of foldcore failure is caused by the perfect bond between face sheet and foldcore, as discussed above.

In figure 4.36 the deformation of the numerical model and the experimental results in TW-direction are illustrated for different strains. In the experiments the first buckling is initiated diagonally across the middle face of the extended foldcore (Fig. 4.36b), which is parallel to the shear load. In case of large strains fracture occurs at first at the fold edges and spreads

Figure 4.35.: Contour plots showing the evolution of the damage factor in the fibre layer for shear strains in TL-direction of 2.5 % and 5 %.

later across the faces (Fig. 4.36d and Fig. 4.36e). If numerical model and experimental results are compared, a good agreement of the buckling modes is evident. In figure 4.37 the distribution of the damage factor is plotted for different strains. The numerical model initially shows degradation mainly at the fold edges as can be observed in the contour plot at 2.5 % shear strain. However if compared to the fracture occurrence observed in the experiment, the subsequent degradation extends less in direction of the edges and is more pronounced across the foldcore faces (Fig. 4.37, 5 % shear strain). As discussed above, this deviance is attributed to the pre-damaged fold edges due to cutting in real foldcore structures, whose effect is underestimated due to the assumption of perfect fold edges in the numerical model.

In summary the layered shell model can satisfactorily represent the global stress-strain behaviour. However, it has to be noted that the numerical model overestimates the peak stresses by approximately 20 %, which is mainly caused by neglect of pre-damaged fold edges and assumption of a perfect bond between face sheet and foldcore in the numerical model. The buckling modes are well captured and the evolution of damage and fractures is comparable to the occurrence of fractures observed in the experiments.

4.4.3. Summarised evaluation of numerical foldcore model

In above sections 4.4.1-4.4.2 the experimental investigation of foldcore structures loaded in T-, TL- and TW-direction is compared to numerical foldcore models which use the layered shell model derived in chapter 3.4 in combination with the setup discussed in section 4.3. Overall the numerical model shows good results for all presented load cases (Foldcore compression test (FCT) and foldcore shear tests (FST)). It is noted, that the model has only 3 x 6 cells, whereas the tests are performed on larger foldcore structures. In the simulated structure the greater proportion of free edges means that the foldcore cells are less constrained. Thus the structure

diagonal face buckling   diagonal face buckling   extensive cell buckling

fold edge buckling   failure of elements at edges

(a) Numerical model - 2.5 % strain (b) Numerical model - 5 % strain (c) Numerical model - 7.5 % strain

diagonal face buckling   diagonal face buckling   extensive fracture
fracture at edges   fracture at edges

(d) Experiment - Small strain   (e) Experiment - Medium strain   (f) Experiment - Large strain

Figure 4.36.: Deformation of aramid paper foldcore model and ILB shear tests loaded in TW-shear.

Failure at fold edges
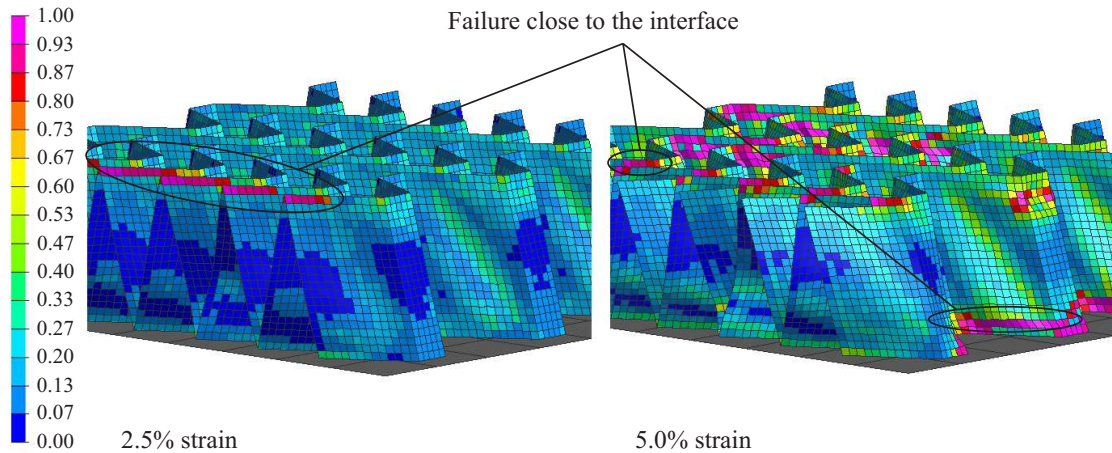

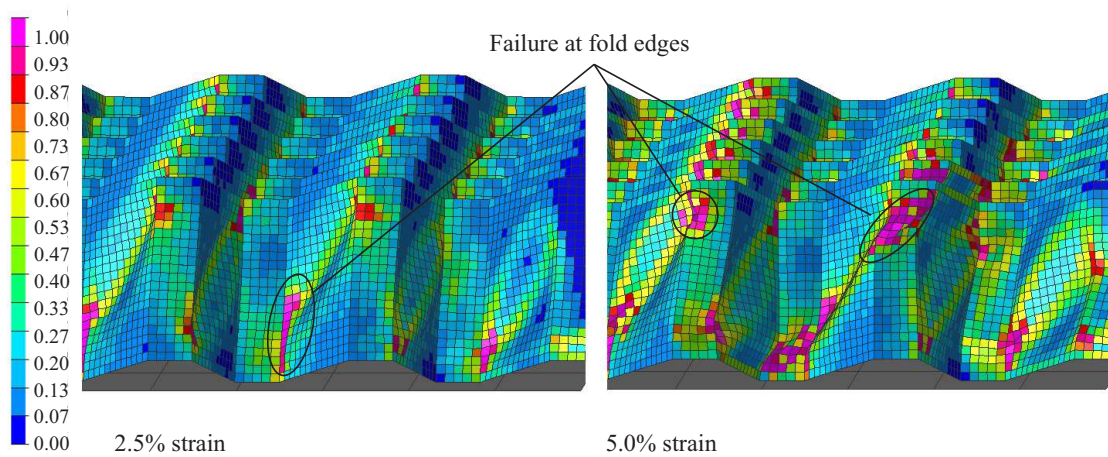2.5% strain   5.0% strain

Figure 4.37.: Contour plots showing the evolution of the damage factor in the fibre layer for shear strains in TW-direction of 2.5 % and 5 %.

is softer and allows greater wall bending/buckling before collapse. The more constrained cells in the test also fracture earlier. However preliminary studies with varying cell numbers show, that this effect can be neglected for the investigated cases.

The initial elastic behaviour in compression (FCT) shows good agreement to the experiments. The small cumulative damage during the initial 'elastic' phase is observed to be well represented in all load cases. However, in case of compression the peak stress is considerably overestimated by the modelled foldcore structures (FCT and FST). This is in contrast to the peak stress observed for the cylinder collapse test (CCT) in section 3.5.2 which was underestimated by the layered shell model. Main reasons for this overestimation are the neglect of pre-damaged fold edges and the assumption of a perfect bond between foldcore and face sheet. The evolution and occurrence of buckling is generally well captured, as the comparison of experiment and model shows in case of foldcore face and edge buckling (FCT and FST).

The initial local increase of damage in highly loaded regions of the aramid paper is well represented. This is especially observed for fold edge degradation and tearing (FCT and FST). However, in case of extensive occurrence of damage as for example in the FCT, the layered shell model significantly overestimates the occurrence of damage. This is a result of the constant distribution of damage in a single element, which degrades the whole element and therefore overestimates the planar expansion of the localised damage and fracture processes observed in real foldcore structures.

In summary the foldcore model is well suited to represent impact, as it gives a good estimation of energy absorption (load level x displacement). During impact the foldcore is expected to be considerably subjected to collapse and shear loads, whereas densification of the foldcore is localised. If the foldcore densification occurs in an extensive area (crash) the model tends to moderatly underestimate the absorbed energy. The capability of the model to predict the beginning of instability is limited, as the main indicator is the maximum load, which was generally overestimated.

5. Impact on foldcore sandwich structures

5.1. Overview

In this chapter the numerical foldcore model presented in chapter 4 is applied to impact load cases. For that purpose the behaviour of foldcore sandwich panels with carbon fibre composite skins subjected to low-velocity and high-velocity impact are at first experimentally characterised. Low-velocity impact of hard, spherical impactors is investigated on basis of a droptower test series. Additionally, high-velocity impact is analysed by means of gas gun tests for varying impactor types, shot angles, velocities and impact energies. The impact occurrence is evaluated by high speed film sequences, photography of the impact region, 2D and 3D computed tomography (CT) and in case of low-velocity impact the measurement of the load and deflection reaction.

In the subsequent section the adaption of the numerical foldcore model to impact scenarios is presented. After a brief introduction to impact modelling, the representation of the composite face sheets, of the bondline interface between foldcore and face sheets and of impactors and support is discussed. The quality of the numerical model is then studied on basis of a parameter study, which investigates effects of element size, impact location, target specimen size and coefficient of friction.

In the final section the predictions of the numerical model are compared to the experimental results previously presented in section 5.2. The first part of the section covers the comparison of low-velocity impact experiments (drop tower tests) with the numerical predictions. Subsequently the comparison of high-velocity impact experiment (gas gun tests) with the numerical prediction is discussed. In both parts the quality of the numerical predictions is evaluated on basis of the observed representation of the governing failure mechanisms.

5.2. Experimental characterisation

In general, a sandwich structure is relatively sensitive to impact loading due to the low thickness of its face skins (cf. Bitzer [27]). Therefore numerous research is aimed at evaluating the damage behaviour of sandwich beams and panels under various impact loads. A significant proportion of this research investigates impact on sandwich structures with honeycomb cores. Honeycomb sandwich structures are expected to demonstrate similar damage characteristics

as sandwich structures with folded cores, as both have a similar geometrical structure of angularly connected faces and are made of similar base materials. In the following a brief overview on the damage behaviour of honeycomb sandwich structures under impact load is provided, given that scarce literature is available on impact behaviour of foldcore sandwich structures.

Impact studies are commonly classified by the velocity of impact in low-velocity impact (0–50 m/s), high-velocity impact (50–1000 m/s) and hyper velocity impact (> 1000 m/s). Low-velocity impact tests are mainly executed with drop weight systems and servo-hydraulic impact machines. In aircraft and aerospace structures this type of impact typically results from tool drops, hail and runway debris (low speed). High-velocity impact tests are performed with gas gun systems. They reproduce impact occurrences such as bird impact, hail during flight, runway debris (high speed) and metal fragments. For hyper velocity impact test mainly two-stage light gas guns and powder guns are employed. Hyper velocity impact usually signifies occurrences such as ballistic impact and orbital debris hitting spacecraft equipment. In the following hyper velocity impact is not considered, as this work focuses on impact behaviour of potential aircraft structures, which is in the regime of low and high-velocity impact.

Low-velocity impact on honeycomb sandwich structures has been investigated by various researchers [16, 39, 128, 138]. A low-velocity impact study with a spherical drop weight to characterise the type and extent of the damage observed in a variety of sandwich configurations with carbon fibre/epoxy face sheets and foam or honeycomb cores was conducted by Anderson and Madenci [16]. Dear et al. [39] studied the damage behaviour in honeycomb sandwich panels from the onset of damage to catastrophic failure. Shin et al. [138] performed low-velocity impact tests on several configurations of sandwich panels (foam core and honeycomb core) at different impact energy levels. Similarly, Park et al. [128] investigated the damage resistance of honeycomb sandwich structures to low-velocity impact.

The findings of the researchers above can be summarised as follows: In case of composites predictions of the effects of low-velocity impact damage are difficult. The main reason is that internal damage occurs at impact energy levels lower than those required to create visible damage. Typically, the surfaces of honeycomb sandwich structures reveal very little damage at low levels of impact energy, as the main failure modes are delamination in the surface skin and core crushing. As a means to investigate the internal damage of the sandwich samples X-ray scans and ultrasonic C-scans have been very successful. Additionally the measurement of the force-time and deflection-time response allows to identify characteristic attributes such as peak load, contact time to peak load, deflection at peak load and absorbed energy.

Several researchers classified characteristic sandwich failure states such as upper skin failure, core crush, lower skin failure and perforation and have linked the different stages of failure to the force–time traces. Typical failure modes are face sheet buckling and delamination within the face sheet, debonding between face sheet and core as well as core indentation and crushing. Results have been compared with those of an equivalent static loading and showed that low-velocity impact was generally quasi-static in nature except for localised damage. Additional comprehensive and detailed summaries of similar experimental studies can be found in the review articles by Abrate [6, 8].

Although less research is available on high-velocity impact on honeycomb sandwich structures this topic has been the focus of several research groups [32, 35, 63]. Christopherson et al. [35] examined the high strain rate response of honeycomb sandwich structure filled with foam undergoing small mass impact at high velocities. Buitrago et al. [32] compared experiment and simulation of high-velocity impact on sandwich structures with honeycomb core. Goldsmith and Louie [63] researched the axial perforation of aluminium honeycombs (without face sheets) by projectiles at high impact velocities.

The response of sandwich composites to impact is investigated by comparison of impact energies and absorbed energies which is calculated by the residual velocity of a penetrating projectile. The nature of damage was also optically measured. In summary, above researchers found that once the velocity approaches a critical value, dependent upon sandwich material and geometry of the composite panel, the damage area induced by the impact situation is quite local. Christopherson et al. [35] observed the existence of a local damage area until the impact energy approaches and exceeds a respective critical energy value, after which the damaged region expands considerably. Main damage mechanism in the face sheets is fibre breakage whereas the core failure is mainly core crushing. This is in contrast to low-velocity impact situations in which a primary mode of failure is delamination. Almost no appreciable delamination of face sheet and core has been observed.

In addition, there has been some work concerning small mass impacts on sandwich composite materials, which has shown that high-velocity/low-mass impacts impart a wave-controlled response such that the load and deflection responses are out of phase and independent of the composite panels boundary conditions or size (Olsson [125]). It is noted, that parts of the experimental studies presented in this chapter have been published by the author in Heimbs et al. [76].

5.2.1. Low-velocity impact

This section describes low-velocity impact tests on foldcore sandwich panels, which were carried out at the DLR within the CELPACT project [91]. The tests were carried out on four foldcore sandwich panels with carbon composite face sheets and foldcore type 30 with 50 mm steel ball impactors (for type definition cf. table 4.5 on page 81). The panels were manufactured by 'Universität Stuttgart' (Institute of Aircraft Design). One quasi-static test was carried out at constant velocity loading to observe the sequence of failure mechanisms and measure energy absorption. This was followed by three drop tower impact tests with impact energies in the range 60–400 J. It is noted that the performed drop tower tests with ~25 kg drop weight and spherical impactor tip usually represent ground impact for example by contact with a vehicle or during baggage handling. This type of low-velocity, high energy blunt impact may also occur during maintenance when a tool or structure drops onto the sandwich panel. It allows to observe a wide range of failure modes, and thus provide experimental data suitable for detailed validation of the damage models and the FE simulation methods developed here. The failure sequence observed in the tests includes:
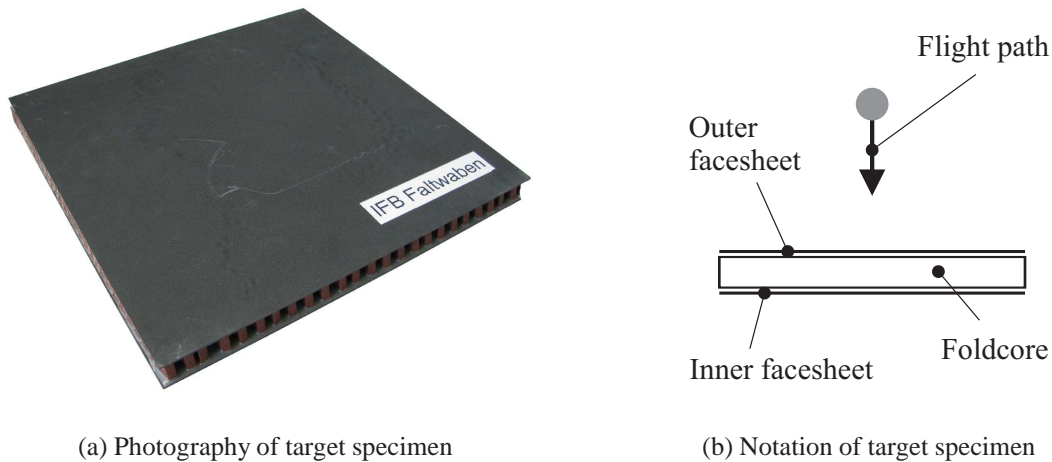
(a) Photography of target specimen   (b) Notation of target specimen

Figure 5.1.: Photography of the foldcore sandwich specimen provided by the Institut für Flug-
zeugbau, Universität Suttgart and a schematic illustration of the used notation.

- Damage on the outer face sheet,

- Perforation of the outer face sheet,

- Core damage and penetration,

- Damage on the inner face sheet and

- Perforation of the sandwich panel.

The tests were instrumented to provide dynamic force-displacement curves at the impactor,
from which energy absorption could be determined. Impact damage was assessed by high
speed video film of the test and post-test by close-up view photography and computed tomo-
graphy analysis of the impacted panels. This technique gave detailed information on internal
core damage obtained non-destructively by X-ray methods.

    The impacted specimen was a sandwich specimen with dimensions of 300x300x24 mm
as depicted in figure 5.1a. The sandwich core was a type 30 foldcore (for type definition
cf. table 4.5 on page 81). The surface face sheets were ~1.8 mm carbon composites panels
(Cytech HTS/977-2, 16 UD plies quasi-isotropic lay up). In figure 5.1b the notation used for
sandwich face sheets and core is schematically illustrated. 'Outer face sheet' signifies the
composite face sheet, which was oriented such that it was impacted first by the drop weight.
'Inner face sheet' signifies the composite face sheet which was facing away from the impacting
drop weight. In subsequent sections the quasi-static pre-test to estimate kinetic impact energy
levels, the setup and the experimental results of the low-velocity impact tests are discussed.

Figure 5.2.: Test device

Test method:	Quasi-static pre-test
Test standard:	-
Test rate:	100 mm / min
Sample material:	Type 30 foldcore
Sample dimension:	300x300x20 mm
Number of specimen:	1

Table 5.1.: Test specifications

Quasi-static pre-test

As the kinetic energy levels needed to cause characteristic damage states are initially unknown, an individual panel was first tested to ultimate failure at quasi-static loading. During the quasi-static test, the energy levels were measured for different states of indenter penetration. These measured energy levels were then used to select impact velocities for the low-velocity impact tests to provide impact kinetic energies similar to the critical energies measured in the constant velocity test.

For that purpose, the sandwich panel was loaded quasi-statically by a 50 mm diameter steel indenter up to complete penetration in a Zwick 1484 servo-hydraulic test frame. The panel was placed horizontally on the 250x250 mm aperture steel loading frame and fixed at the edge midpoints of the lower face sheet by a light clamp to prevent lateral movement, as depicted in figure 5.2. However the clamp did not prevent edge rotations in the sandwich panel. The spherical indenter was then pushed through the sandwich panel at a constant loading rate of 100 mm/min.

During the course of testing some elastic loading of the outer face sheet, then outer face sheet penetration followed by extensive core crushing and finally inner face sheet penetration was observed. The outer face sheet was fractured in a circular region of about 70 mm diameter, as can be seen in figure 5.3a. The amount of delamination can be observed in the CT image in figure 5.3b. The CT image clearly shows how localised the core failure was with foldcore cells undamaged if more than 10 mm away from the indenter. The typical foldcore cell wall failure where initial buckling is succeeded by the formation of sharp kinks and fractures was observable. The foldcore was debonded from the inner face sheet in a circular region of about 100 mm diameter whereas debonding from the upper face sheet was negligible. The inner face sheet fracture region extended along the fibres and covered the whole panel. Both inner and outer CFRP face sheets showed significant delamination failures in the damage regions, as seen on the CT image.

(a) Photography of indented panel   (b) 2D computed tomography
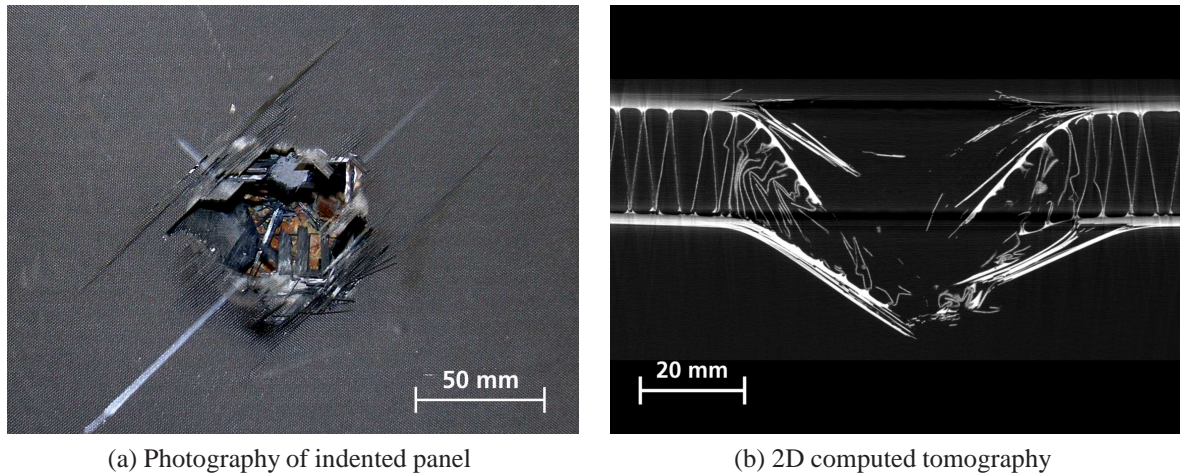
Figure 5.3.: (a) Photography of front side of indented panel (b) 2D computed tomography of push-through region of indenter.
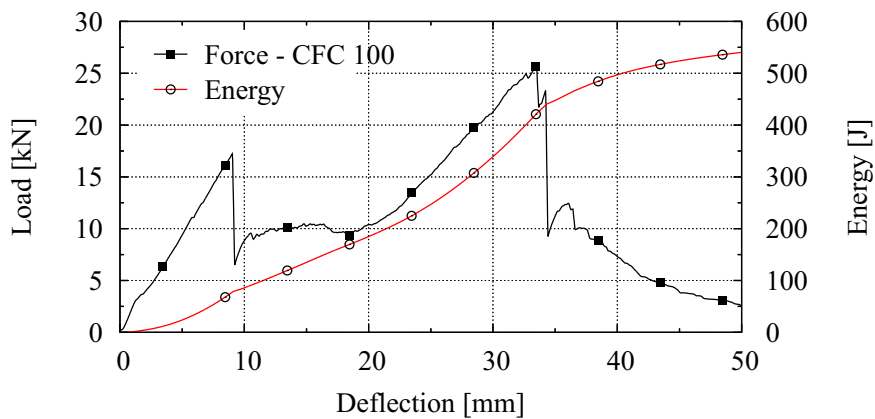
Figure 5.4.: Load-deflection and Energy-deflection curves of quasi-static test.

The failure sequence is clearly seen in measured load-deflection curves shown in figure 5.4, with elastic penetration until outer face sheet fracture at about 9 mm deformation and 17 kN load, then extensive core crushing at a constant load of about 10 kN, followed by loading of the inner face sheet at about 20 mm deformation seen by linear increasing loads up to inner face sheet penetration at about 33 mm and 26 kN load. The global deflection of the carbon composite face sheets was about 10 mm before occurrence of total failure. The absorbed energy data indicate outer face sheet penetration at about 80 J and inner face sheet penetration at about 450 J.

Based on the assumption that quasi-static and dynamic energy levels are sufficiently comparable the energy levels were selected to possibly observe rebounding with damage at
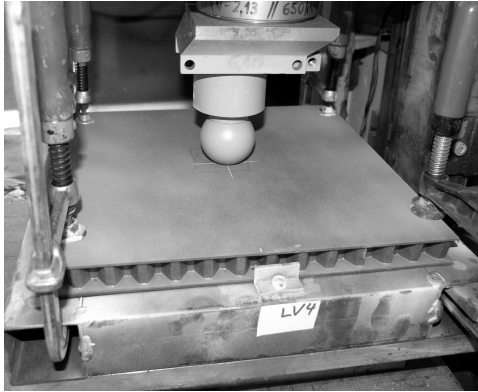
Test method:	Drop tower impact test
Test standard:	-
Impact velocity:	2.21/3.42/5.77 m/s
Core material:	Type 30 foldcore
face sheet material:	Cytech HTS/977-2
	16 UD plies
Sample dimension:	300x300x24 mm
Number of specimen:	3

Figure 5.5.: Test device   Table 5.2.: Test specifications

outer face sheet (~60 J), outer face sheet penetration and core damage (~140 J) and complete penetration of the sandwich panel (~400 J).

Setup of low-velocity impact test series

A total of three flat foldcore sandwich panels were tested for low-velocity impact with the drop tower impact setup shown in figure 5.5. The three foldcore sandwich panels had dimensions 300x300x24 mm with ~1.8 mm carbon composite face sheets (Cytech HTS/977-2, 16 UD plies quasi-isotropic lay up) and were provided with foldcore type 30 (for type definition cf. table 4.5 on page 81). For the low-velocity tests carried out here, the foldcore sandwich test panels were cut to size from a larger panel and the edges were left unsealed. The panels were placed on the same steel load frame as in the quasi-static test with the centre edge clips at the lower face sheet and 4 clamps were placed at the corners to stabilize the panel under impact loads.

The impact velocity was varied in the range 2.2–5.8 m/s to provide data on different failure modes. The total drop mass was 23.63 kg for all tests, including load cell and steel ball impactor. The steel ball impactor was 50 mm in diameter. The measured impact velocities and the corresponding impact energies are listed in table 5.3.

The force-time data was measured at the load cell located between the spherical indenter and the impact mass. The displacement-time of the cross-head was measured by an electro-magnetic device in the drop tower frame. The impact process was recorded by a high-speed camera system (PHOTRON Fastcam Ultima APX RS, Model 250k). Internal structure damage in the sandwich cores was quantified by post-test CT scans. Using CT the internal structure and damage in the sandwich cores were quantified.

Table 5.3.: Measured impact conditions.

Specimen number	Impactor type	Impactor mass	Impact velocity	Impact energy
-	-	[kg]	[m/s]	[J]
1	Steel ball	23.63	2.21	57.7
2	Steel ball	23.63	3.42	138.2
3	Steel ball	23.63	5.77	393.4
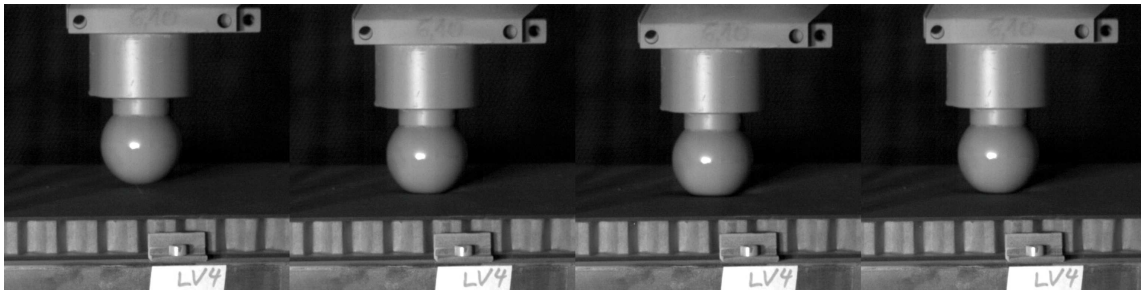
Figure 5.6.: Image sequence of impact with 60 J (Time interval: ~3.3 ms).

Experimental results

60J Impact   The measured impact velocity in this test was 2.21 m/s giving an initial kinetic energy of 57.7 J. This energy level was chosen as it is below the outer face sheet penetration energy of 80 J seen in the quasi-static test. The steel ball indented the outer face sheet before it rebounded as can be seen in figure 5.6. There was no damage visible in the close-up view of the impact region in figure 5.7a. However, the CT image of figure 5.7b confirms that the ball caused delamination damage at the contact position on the outer face sheet. Also some damage on the foldcore was observable close to the point of impact with a region diameter of about 50 mm. The damage was mainly cell wall breakage accompanied by sharp kinks and small tears very close to the impact zone. The inner face sheet had no visible damage.

Referring to figure 5.8 the peak load at outer face sheet rebound was 12.5 kN at about 8 mm displacement. The absorbed energy at rebound calculated from the load-deflection curve was about 49.3 J which was about 85 % of the impact energy calculated by the initial velocity and drop weight mass which amounted to 57.7 J. The overall impact test results in this case were consistent with those expected from the quasi-static penetration test.

140J Impact   In the presented test the measured impact velocity was 3.42 m/s corresponding to an initial kinetic energy of 138.2 J. This was chosen as an energy level at which outer face sheet penetration and core crushing was expected from the quasi-static data. In figure 5.9 an image sequence of the impact occurrence is depicted. The steel ball penetrated the outer face sheet, is slowed down and stopped by the core and rebounded subsequently. The close-up

(a) Photography of impact region

(b) 2D computed tomography

Figure 5.7.: (a) Photography of the front side of the 60 J impact specimen (b) 2D computed tomography of impact region.
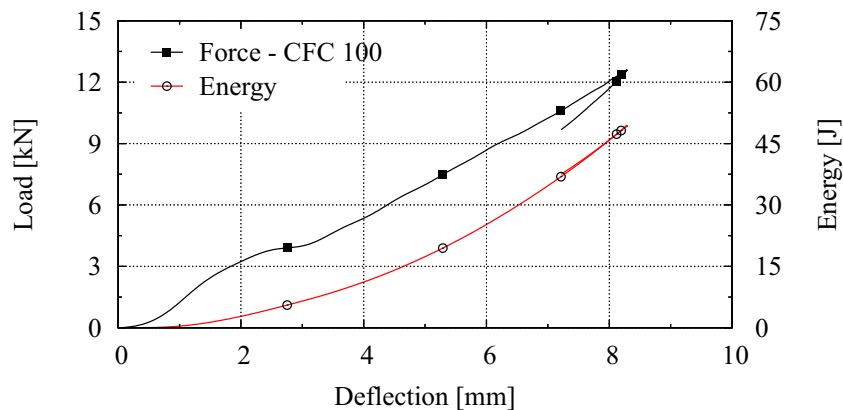
Figure 5.8.: Load-deflection and Energy-deflection curves of the 60 J impact test.

view of the impact region in figure 5.10a shows several cracks at the location of impact. The detailed CT image of core damage in figure 5.10b clearly shows that after face sheet penetration the core absorbed the remaining impact energy and protected the inner face sheet from damage. The damage of outer face sheet and core was localised at the impact zone in a diameter of about 70 mm. Within the impact region extensive face sheet delamination and core crushing was observed.

Figure 5.11 shows the measured load-deflection data and energy absorbed in impact. In the test the peak load at outer face sheet penetration was about 13.5 kN at 8 mm displacement, with a fairly constant core crush load of 9.0 kN until rebound started at about 15 mm displacement. At rebound the energy absorbed by the sandwich panel was seen to be about 120 J, of which about 50 J was absorbed by fracture and penetration of the outer carbon fibre

Figure 5.9.: Image sequence of impact with 140 J (Time interval: ~4.1 ms).

(a) Photography of impact region

(b) 2D computed tomography
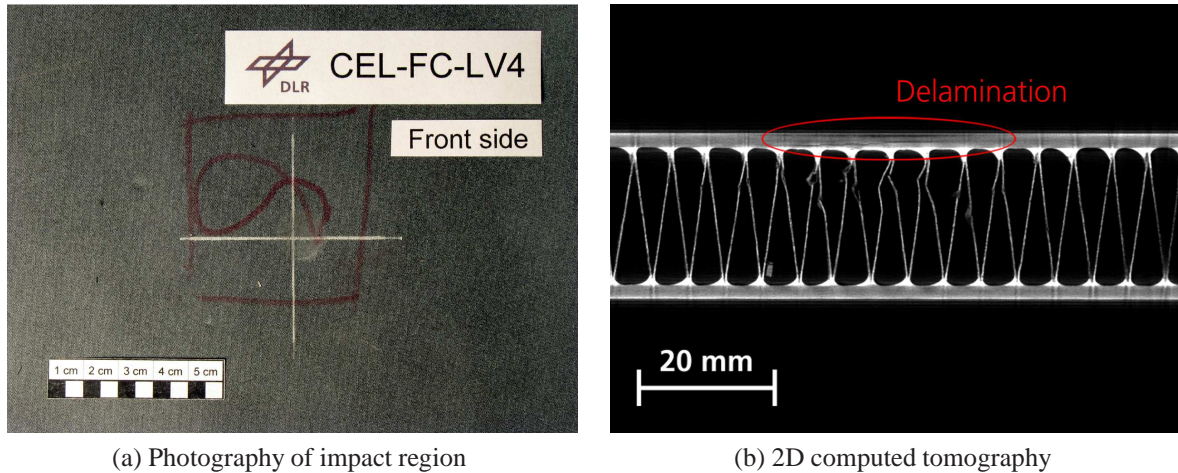
Figure 5.10.: (a) Photography of the front side of the impact specimen (b) 2D computed to-
mography of impact region.

composite face sheet. It is noted that the absorbed energy calculated from the load-deflection curve amounted to 117.5 J which was about 85 % of the impact energy calculated from the initial velocity and impactor mass which amounted to 138.2 J.

400J Impact   For the third impact test the impact velocity was measured as 5.77 m/s which resulted in an initial kinetic energy of 393.4 J. This energy level was selected as it corresponded to an almost complete penetration of the sandwich in the quasi-static test. The steel ball penetrated the outer face sheet, is slowed down by the core and stopped by the inner face sheet before it finally started to rebound as seen in figure 5.12. The topview of the impacted sample in figure 5.13a shows the severely damaged outer face sheet. The CT scans of core damage in figures 5.13b and 5.14 confirm that the ball penetrated the core as far as the inner face sheet, which appears to be undamaged suggesting it was deformed elastically to absorb the impact energy before the projectile started to rebound. However extensive core debonding from the inner face sheet was observed.

Figure 5.11.: Load-deflection and Energy-deflection curves of the 140 J impact test.

Figure 5.12.: Image sequence of impact with 400 J (Time interval: ~5 ms).

(a) Photography of impact region
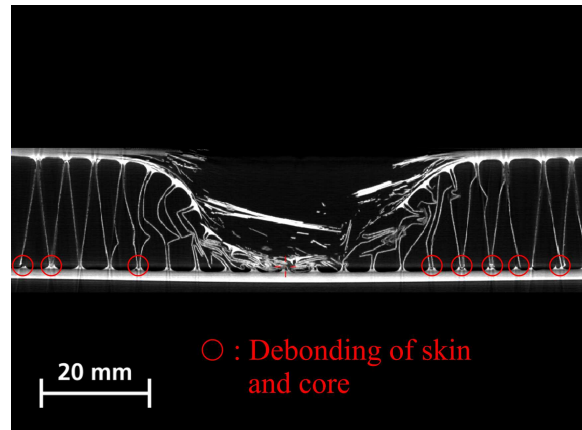
(b) 2D computed tomography

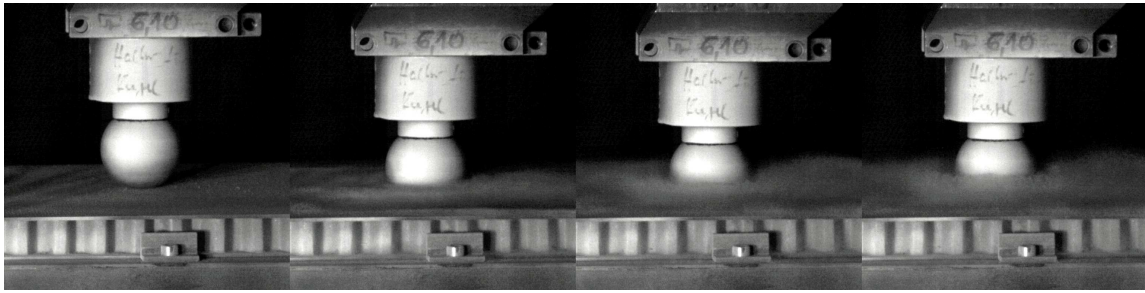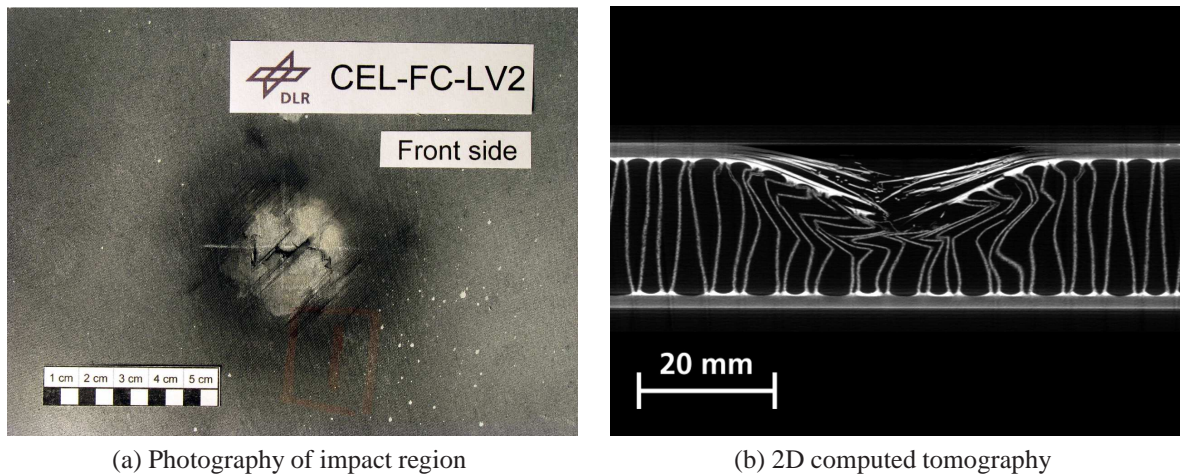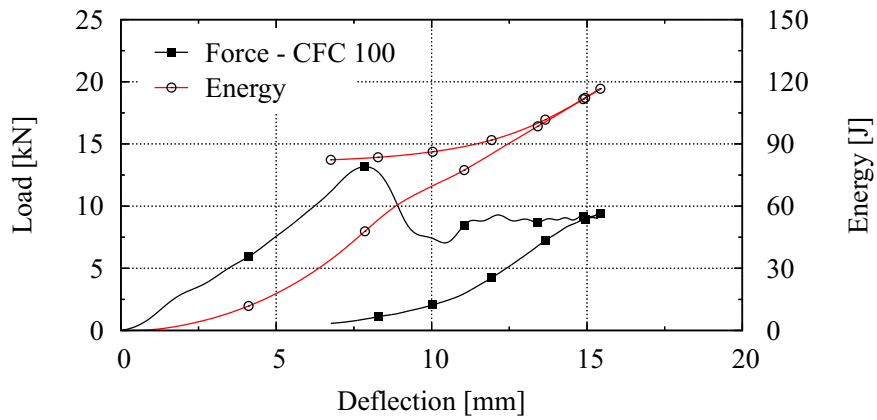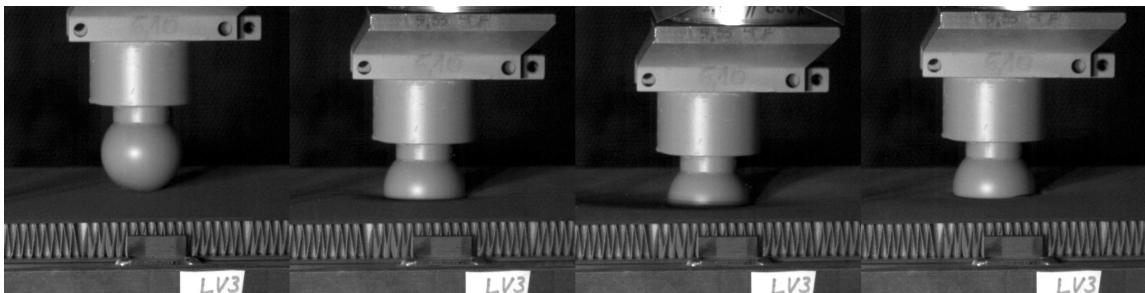Figure 5.13.: (a) Photography of the front side of the impact specimen (b) 2D computed tomography of impact region.

(a) Top view (b) Midline view (c) Side view
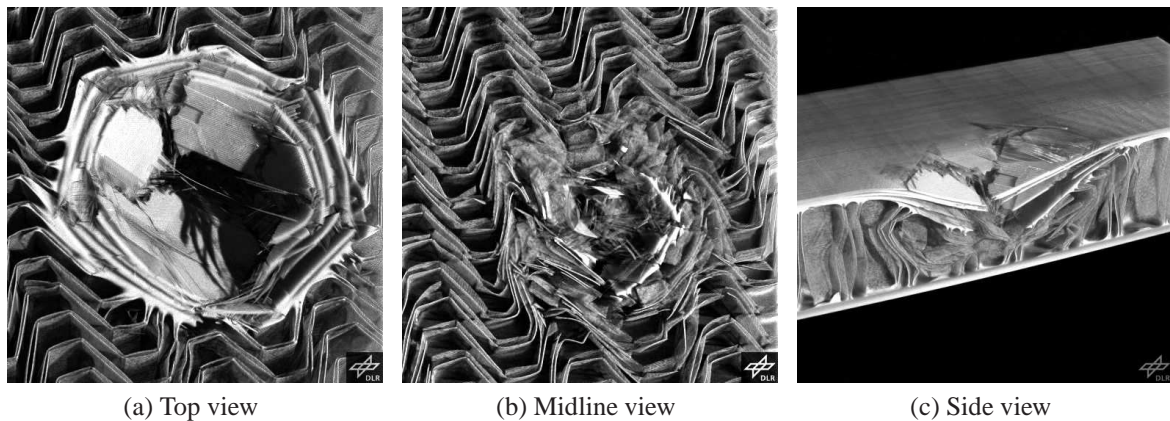
Figure 5.14.: 3D computed tomography of impact region.

Referring to figure 5.15 the peak load at outer face sheet penetration was about 13.0 kN at 8.5 mm displacement, with a fairly constant core crush load of 8.5 kN before a steady increasing load due to core compaction, crushing and inner face sheet elastic deformation until rebound started at about 35 mm displacement. At rebound the energy absorbed by the sandwich panel is seen from figure 5.15 to have been about 350 J, with an estimated 280 J absorbed by core crushing and fracture.

With 350 J the absorbed energy calculated from the load-deflection curve was about 90 % of the kinetic energy calculated from the initial velocity and impactor mass. It as concluded that the sandwich panel had better impact resistance than predicted from the constant velocity penetration test, since the inner face sheet was not damaged in the LV impact test, despite the very high energy. This may be explained by the fact that the impactor was slowed down and stopped by the core and had no energy left to penetrate the inner face sheet, whereas in the quasi-static test at constant velocity it continued on with constant velocity through the inner face sheet.

Conclusions

Figure 5.16 compares the contact force in the quasi-static test with the results from the three drop tower impact tests. It is apparent that the failure modes of the quasi-static test with outer face sheet penetration, core crushing and finally inner face sheet deformation and penetration, are reproduced in the impact tests, except for final penetration of both face sheets. However, in the test which was expected to cause almost complete penetration at impact energy of 400 J, the impactor was stopped by the sandwich core and did not damage the inner face sheet. It is also noted, that the force magnitudes and energy absorption were observed to be larger in the quasi-static test compared to the magnitudes observed in the dynamic tests.

Dynamic properties of composite materials are usually characterised by a more brittle failure behaviour, compared with quasi-static properties. Thus dynamic failure stresses are higher, but dynamic failure strains and energy absorbed at failure are usually lower. The mea-
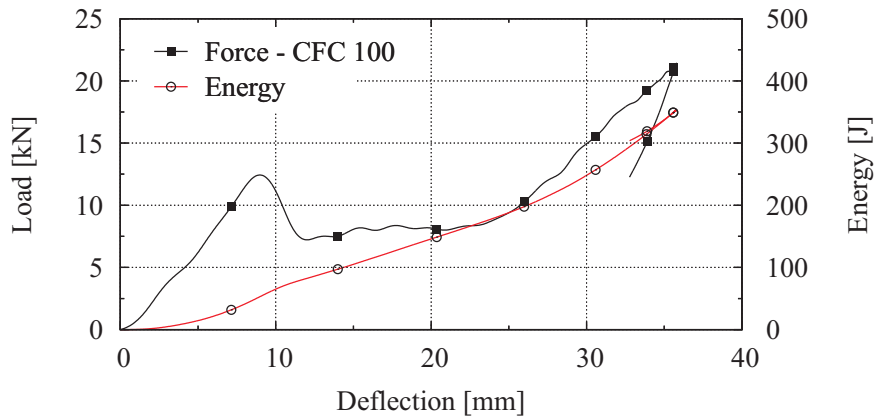
Figure 5.15.: Load-deflection and energy-deflection curves of the 400 J impact test.

sured lower dynamic core crush loads, with lower energy absorption seen here are consistent with DLR test data on crush response of composite absorber elements such as CFRP segments, reported in the research thesis of M. David [38]. M. David observed that for crush velocities in the range 1–10 m/s steady crush loads and energy absorption were typically 20–25 % below quasi-static values.

Generally, in the energy-deflection curves in figure 5.17 it can be observed, that the peak measured absorbed energy is lower than the initial kinetic energy of the impactor by a factor of about 10 %. In the dynamic tests this is the point of rebound, since in each test the impactor is stopped, then rebounds with a reduced velocity. At this point it is expected that the initial impactor kinetic energy is zero, and balanced by the strain energies, fracture energies and kinetic energy in the sandwich plate. The discrepancy here could be due to energy losses such as friction between impactor and plate, kinetic energies due to plate vibrations and in the test frame and cross-head, plus the effect of filtering on the dynamic force and displacement measurements.

Based on the experimental results typical characteristics of the dynamically loaded sandwich structure have been identified for the effective impact conditions. The observed characteristics are used to assess the quality of the subsequently presented finite element model. Significant observed characteristics are:

- The impact tests followed the same load and energy curves up to the point of impactor rebound. Two definite peak loads correlated with outer and inner face sheet failure. After outer face sheet failure the foldcore crushed at a constant load.

- Observed surface face sheet failure behaviour was interlaminar delamination and subsequent occurrence of face sheet fractures.

- The foldcore failed after initial elastic buckling in a crushing mode under formation of sharp kinks and fractures at face edges.
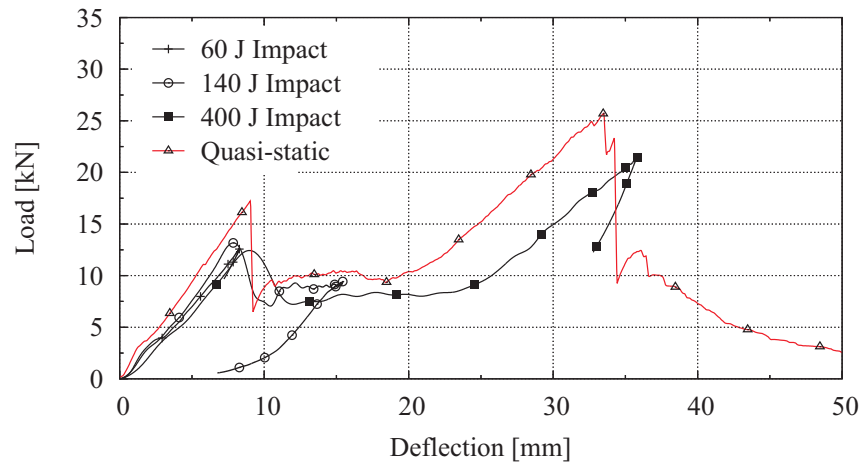
Figure 5.16.: Load-deflection curves of the low-velocity impact tests and the quasi-static pre-
test.
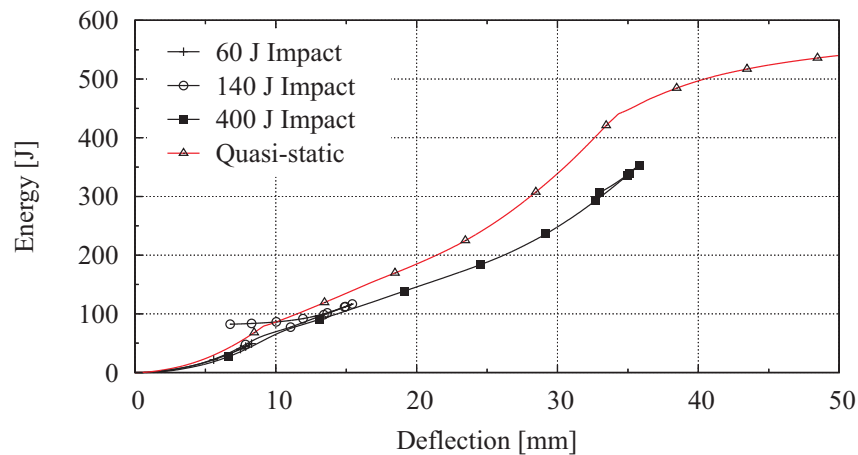
Figure 5.17.: Energy-deflection curves of the low-velocity impact tests and the quasi-static
pre-test.

- The observed damage and failure for a hard body impact was localised close to the
  impact region. For all tested impact energies the core remained undamaged if it was
  about 10–20 mm away from the impactor. An exception was the extensive debonding of
  lower face sheet and core for large impact energies. In combination with the large-scale
  damage observed in the quasi-static test this indicated that failure of the inner face sheet
  can also be expected to be more widespread.

Figure 5.18.: Photography of a gas gun test specimen.

5.2.2. High-velocity impact

This section summarises results from the high-velocity impact test series conducted on three sandwich panels, which are depicted in figure 5.18. The test were carried out at the DLR within the CELPACT project [100]. A total of three 500x500 mm flat foldcore sandwich panels were tested. The target specimen were provided by 'Universität Stuttgart' (Institute of Aircraft Design). The purpose of the test programme was to determine the critical impact energies and velocities for a given impactor to cause characteristic damage states. Different projectile types, such as

- Steel cubes,

- Steel beams and

- Rubber beams

were considered. This section briefly describes the setup of the gas gun facilities, the support conditions, the sandwich panels and the projectiles. This is followed by a summary and discussion of the test results observed for each projectile type. The high-velocity impact tests were documented by a sequence of photographs of the impact event extracted from the high speed digital video camera, photographs of the visible damage on the outer and inner face sheets and computed tomography of core and interface damage for selected impact samples.

The aim of the test programme was to determine the critical kinetic energies and impact velocities for a given projectile and test panel, causing damage on the outer face sheet, perforation of outer face sheet, core damage and penetration, damage on the inner face sheet and perforation of sandwich panel. However, such a complete characterisation requires a large number of impact tests and hence test panels. In the case of the present test series it was possible to carry out several shots per panel with the steel projectiles, since failure was localised. Thus it was possible to estimate face sheet and core damage and penetration conditions. For the rubber projectiles there was no outer face sheet penetration observed, so that the focus was on delamination or core/face sheet debonding at the impact position. After impact testing, computed tomography scans were carried out on the damaged panels. Sufficient detail was obtained to show cracking, delamination and fibre damage in the composite face sheets, face sheet-core debonding and core microdamage.

Setup of high-velocity impact test series

A gas gun with barrel diameter of 60 mm was used in this test series. It consists of a single 50 l pressure tank and a fast acting pneumatic valve to a dove-tail breech and 5 m long honed bore barrel with 60 mm diameter. The target chamber is shown in figure 5.19. On the right hand side the muzzle of the gas gun barrel is visible. An optical gate with velocity meters which is positioned directly in front of the muzzle. It is linked to a computer for calculation of the impact velocity and for synchronising the start of cameras. On the left hand side the sandwich panel specimen is positioned, which is bolted to a support frame. The projectile masses range from 0.013 to 0.1 kg and are accelerated to impact speeds up to 125 m/s by a sudden release of the pressurized air. The specimen were impacted with steel cube, steel beam and rubber beam projectiles at 90° or 60° impact angle and with 3–5 shots per panel, depending on size of damage zone.

The free flight and the impact of the projectiles on the target specimen were visualised through a high-speed video camera (PHOTRON Fastcam Ultima APX RS, Model 250k) comprising of a 10 Bit CMOS monochrome sensor with 1024x1024 pixel. The camera speed was adjusted to 12,000 frames per second (640x480 pixel). For post-test investigations of damage close-up view photography and computed tomography for selected impact samples have been performed.

The three foldcore sandwich panels have dimensions as shown schematically in figure 5.20a. The sandwich core is a foldcore type 30 as specified in table 4.5 on page 81. The sandwich face sheets are 16 UD plies with quasi-isotropic layup of Cytech HTS/977-2 carbon fibre composite (~1.8 mm thickness). The panels were supported in a vertical plane and bolted to a steel support frame inside the gas gun target chamber. In order to attach the panels securely to the supporting steel frame, each test panel was fabricated with internal edge supports of dense integral foam core at which the panel was bolted. When bolted to the support frame this gives the foldcore sandwich a test size of 400x400 mm. The angles of impact ($60°$, $90°$) are obtained by rotating the frame and panel with respect to the impact direction. For that
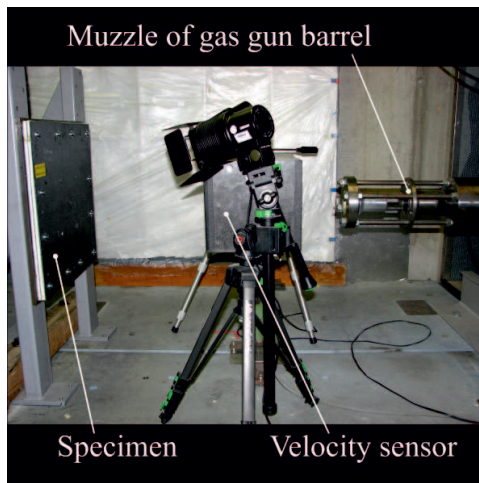
Figure 5.19.: Test device

Test method:	Gas gun impact test
Test standard:	-
Impact velocity:	40 m/s - 125 m/s
Core material:	Type 30 foldcore
face sheet material:	Cytech HTS/977-2
	16 UD plies
Sample dimension:	500x500x24 mm
Number of specimen:	3

Table 5.4.: Test specifications
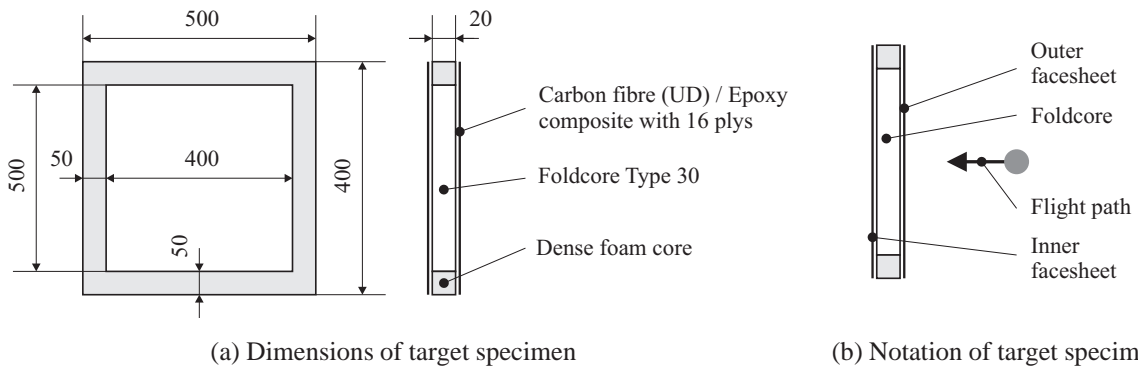
(a) Dimensions of target specimen

(b) Notation of target specimen

Figure 5.20.: Schematic illustration of the dimensions and notation of the target specimen in mm.

purpose, an adjustment device was built and fixed to the global frame for the $60°$ impact to hold the panel at the right inclination.

The notation of the sandwich face sheets and core is similar to the one used in the low-velocity impact tests, as illustrated in figure 5.20b. The 'outer face sheet' signifies the composite face sheet, which is oriented such that it is impacted first by the projectile. The 'inner face sheet' signifies the composite face sheet which is facing away from the impacting projectile.

In the test series, two types of metallic and one type of rubber projectiles were fired: A steel cube with side length 12 mm and mass 13.5 g, a steel beam with dimensions 109x30x4 mm and mass 101.7 g and a rubber beam with dimensions 132x30x25 mm and mass 103 g. In the tests the projectiles are held in sacrificial polyurethane foam cylinders inserted in aluminium alloy 'cups'. These 'sabot' devices hold the projectile in the desired orientation and form a gas tight seal against the driving gas. A cavity at the front of the sabot whose diameter and depth are adapted to the size and geometry of each projectile carries the projectile. A

(a) Steel cube   (b) Steel beam   (c) Rubber beam
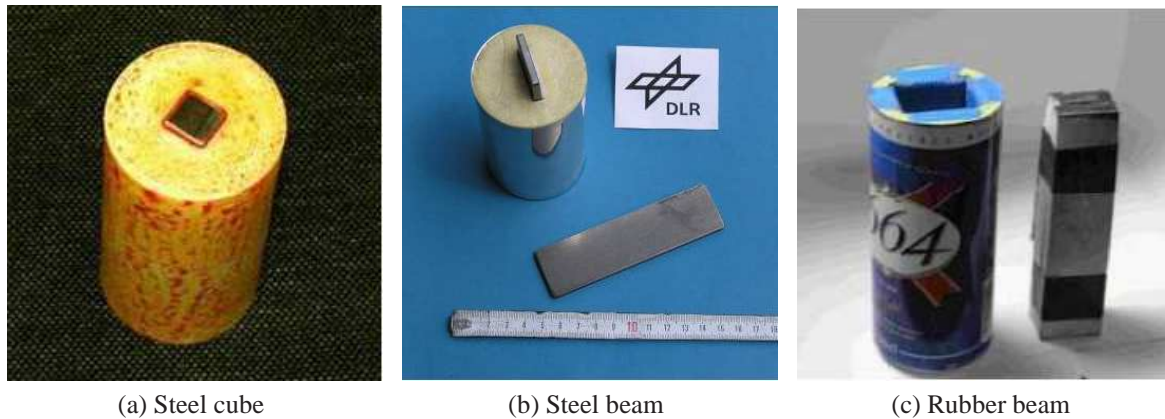
Figure 5.21.: Different types of projectiles with sabots (a) Steel cube (b) Steel beam (c) Rubber beam.

sabot stripper is fitted onto the muzzle of the barrel which restricts the muzzle opening such that the projectile can pass through unimpeded whilst the sabot is stopped. The projectiles and their sabots are shown in figure 5.21.

The steel cube projectiles represent impact of metallic objects from ground debris impacting lower parts of the fuselage. The steel beams represent engine fragments hitting the fuselage at a specific angle. The rubber beams represent burst tyre fragments, which are launched upward and impact lower parts of the fuselage. The rubber projectiles were cut from aircraft tyres provided by Airbus. In order to have a straight rubber beam with an acceptable weight of about 100 g, it was necessary to build the rubber projectiles by using two strips cut from the tyre, consisting of tyre rubber and fabric reinforcements. These two strips were attached to each other using an adhesive tape.

Steel cube impact

A total of five shots were performed on a foldcore sandwich panel with a 12 mm steel cube weighing about 13.5 g. The velocities, impact energies and test observations of each shot are listed in table 5.5. The angle of impact was normal to the panel surface with 90°. Special care was taken to prepare sabot and projectiles so that the projectiles hit the panel flat on with the face. However, projectile 4 and 5 rotated during free flight and hit the target panel with slightly inclined angle.

The test series indicated that up to 20 J impacts the projectile rebounds, with minor surface scratches, as can be seen in figure 5.22a for an impact with a kinetic energy of 20.9 J. However, the computed tomography in figure 5.23a indicates that the outer face sheet was delaminated at the location of impact. The foldcore in close proximity (10–20 mm) to the point of impact was bend and showed some kinks and cracks.

Outer face sheet perforation was in the range 20–40 J, then at 45–70 J the projectile was stopped by the foldcore, which absorbed the impact energy by folding and fracture. Figure

Table 5.5.: Overview on performed impact test with steel cube projectiles.

Shot	Mass [g]	Velocity [m/s]	Energy [J]	Comments
1	13.5	55.6	20.9	The impactor rebounded from the sandwich. The outer face sheet was damaged.
2	13.5	81.8	45.2	The outer face sheet was penetrated and the projectile was stopped by the foldcore. The projectile remained stuck in the core.
3	13.3	99.5	66.8	The outer face sheet was penetrated and the projectile remained stuck in the core. No damage was visible on inner face sheet.
4	13.3	108.1	77.2	The outer face sheet was penetrated and the projectile remained stuck in the core. No damage was visible on inner face sheet.
5	13.3	109.0	79.0	The outer face sheet was penetrated and the projectile remained stuck in the core. A crack of about 0.8 mm was visible on inner face sheet.
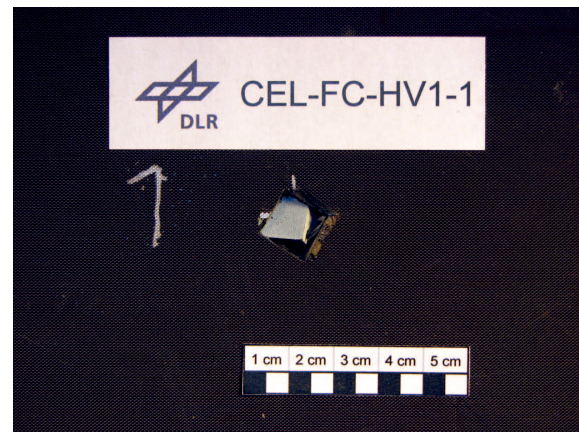
(a) 20.9 J impact   (b) 45.2 J impact

Figure 5.22.: (a) Close-up view of impact region for a kinetic energy of 20.9 J (b) Close-up view of impact region for a kinetic energy of 45.2 J.

(a) 20.9 J impact   (b) 77.2 J impact
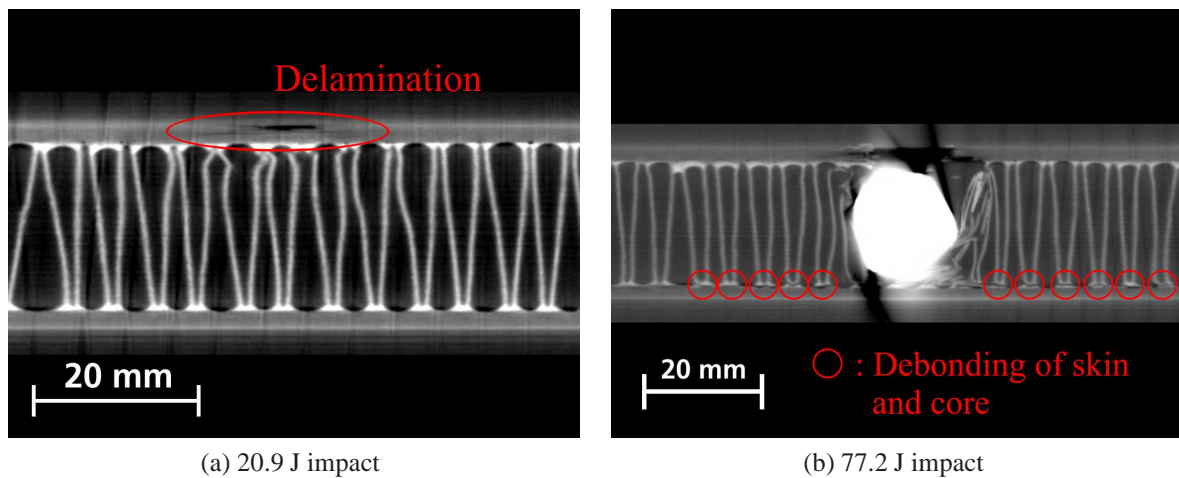
Figure 5.23.: (a) The 2D computed tomography shows the cross-section of impact region for
            a kinetic energy of 20.9 J (b) The 2D computed tomography shows the cross-
            section of impact region for a kinetic energy of 77.2 J.

5.22b depicts the outer face sheet of the target specimen, which was impacted with an kinetic energy of 45.2 J. The projectile penetrated the outer face sheet and remained stuck half way through the 20 mm thick core. The damage of the outer composite face sheet was localised, with the size and shape of the face sheet perforation corresponding to the circumference of the impacting projectile. This is confirmed by a computed tomography of the impact region's cross-section in figure 5.23a. It is clearly visible, that damage and delamination in the outer composite face sheet were limited to a region of about twice the projectiles side length in diameter. The deformation and damage in the foldcore was localised to a region of similar size, with foldcore crushing only observed directly below the projectile.

Similar observations were made for an impact with kinetic energy of 66.8 J. Here the foldcore was fully crushed by the projectile which was stopped by the inner face sheet, as can be seen in the 3D computed tomography of figure 5.24. The projectile, which remained stuck is coloured in yellow. In case of larger kinetic energies (77.2 J and 79.0 J) the added energy was mainly absorbed by bending of the inner face sheet which was accompanied by extensive face sheet-core debonding in a region of 80–100 mm in diameter, as depicted in figure 5.23b. The different extend of inner face sheet-core debonding between the 66.8 J (no debonding) and 77.2–79.0 J (considerable debonding) indicated that the foldcore absorbed energy up to about 65 J by crushing and rupturing. After 65 J the excessive energy was absorbed by the inner face sheet. In the tests it was not possible to penetrate the sandwich with the employed kinetic energies, as this required hard body impacts above 80 J (> 109 m/s) for the 12 mm steel cube.

(a) 66.8 J impact   (b) 66.8 J impact

Figure 5.24.: 3D computed tomography of 66.8 J impact. The images show an iso-view, with a cut-plane (a) adjacent to the outer composite face sheet (b) adjacent to the inner composite face sheet.

Table 5.6.: Overview on performed impact test with steel beam projectiles.

Shot	Mass [g]	Velocity [m/s]	Energy [J]	Comments
1	101.7	39.3	78.7	The outer face sheet was penetrated. The projectile rotated during penetration and remained stuck in the core. No damage was visible on the inner surface
2	101.7	67.9	234.7	The projectile penetrated the sample
3	101.7	86.3	372.0	The projectile penetrated the sample

Steel beam impact

Three shots with steel beam projectiles with dimensions of 109x30x4 mm were carried out. The velocities, impact energies and test observations of each shot are listed in table 5.6. Generally, the considerably larger mass of the projectile resulted in much higher kinetic energy levels than in the tests with the small steel cubes. The target specimen was positioned such that the projectiles hit the specimen with an inclined impact angle of $60°$. The beam was aligned with the sabot so that it impacts the panel end on. By rotating the beam in the sabot, it was possible to vary the angle between the face of the beam and the foldcore directions.

The first shot with an kinetic energy of 78.7 J showed that the beam penetrated the outer face sheet and was stopped by the core and inner face sheet, which is very similar to the result for the steel cube. However at the higher kinetic energies of 234.7 J and 372 J, the beam passed straight through the sandwich panel. This was a severe load case because the beam was in the

(a) Front side

(b) Back side

Figure 5.25.: Photography of the front side (a) and back side (b) of the target specimen which was impacted with a kinetic energy of 234.7 J.

(a) Side view
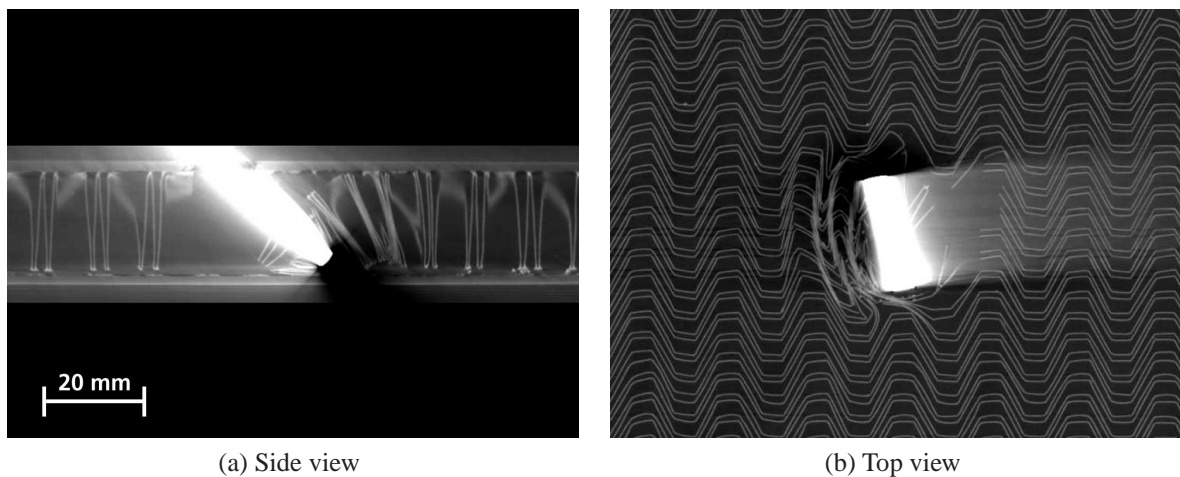
(b) Top view

Figure 5.26.: The 2D computer tomographies show the side view (a) and top view (b) of the target specimen's cross-section which was impacted by a kinetic energy of 78.7 J.

form of a 4 mm thick steel plate impacting edge onto the panel and thus able to pass between the folds of the foldcore with little energy absorption possible.

The photographies in figure 5.25 show the front and back side of the impact with 234.7 J, where the specimen passed straight through the target specimen. Similar to the observations made for the steel cube the size and shape of the damage in the outer composite face sheet was considerably localised and corresponded to the circumference of the steel beam projectile. However the inner face sheet showed extensive damage and delamination in a region of about 100–200 mm in diameter.
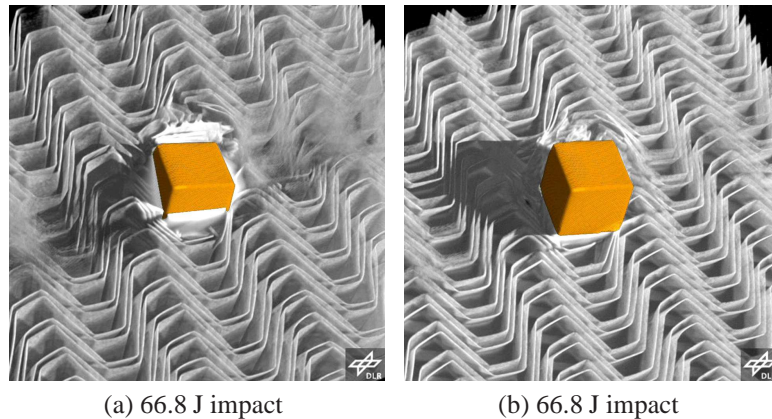
(a) 78.7 J impact   (b) 78.7 J impact
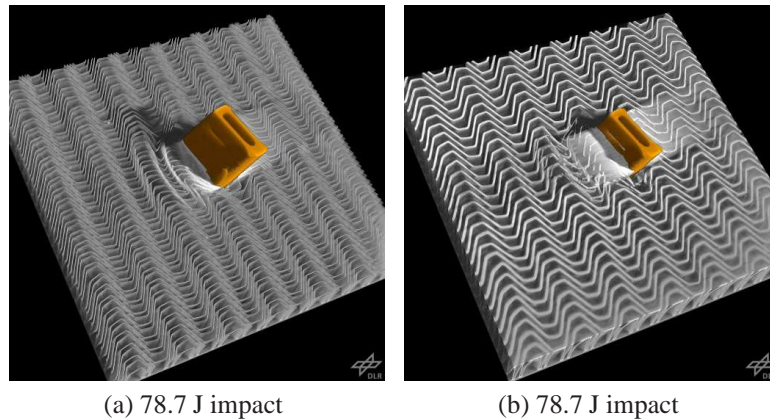
Figure 5.27.: 3D computed tomography of 78.7 J impact. The images show an iso-view, with a cut-plane (a) adjacent to the outer composite face sheet (b) adjacent to the midplane of the sandwich specimen.

The computed tomography in figure 5.26 indicates, that for a kinetic energy of 78.7 J the sandwich's interior damage was comparable to the damage pattern observed for the steel cube at similar energy levels. The projectile remained stuck in the core. Again, the damage in the outer face sheet and foldcore was very localised. Due to the inclined impact angle, the front end of the beam projectile slided along the inner face sheet and compressed and sheared off the foldcore along a distance of about 30 mm. The inner face sheet was also considerably debonded from the core in a region of about 120–150 mm. No damage was detected on the inner face sheet itself. Figure 5.27 depicts two 3D computer tomographies of the same impact event. The visible parts of the beam projectile are coloured in yellow. It is evident, that the foldcore was only damaged in close proximity to the stuck projectile.

Rubber beam impact

The difference between impact damage from hard bodies and soft elastic projectiles was highlighted by three impact tests with rubber beams. For that purpose, the target specimen was impacted by rubber beam projectiles with dimensions of 132x30x25 mm. These had a similar mass to the steel beams of 103 g. The velocities, impact energies and test observations of each shot are listed in table 5.7. The projectiles hit the target specimen with an impact angle of $90°$. The beam was aligned with the sabot so that it impacts the panel end on. By rotating the beam in the sabot, it was possible to vary the angle between the face of the beam and the foldcore directions.

The target specimen was impacted with kinetic energies of 350–814 J, however there was no outer face sheet penetration. This was due to the rubber material storing kinetic energy as elastic strain energy on contact, so less energy was available to damage the panel, and because there was no immediate penetration, the panel itself was able to deform globally to resist the impact. Here the only observed damage by computed tomography was delamination in the

Table 5.7.: Overview on performed impact test with rubber beam projectiles.

Shot	Mass [g]	Velocity [m/s]	Energy [J]	Comments
1	103	82.9	353.9	No damage was visible. The outer face sheet was slightly deformed and yielded to pressure (~0.5 mm in depth)
2	103	105.0	568.1	No damage was visible. The outer face sheet was deformed and yielded to pressure in a region of approximately 2 mm in depth and 50 mm in diameter
3	103	125.7	814.2	No damage was visible. The outer face sheet was deformed and yielded to pressure in a region of approximately 3 mm in depth and 60–70 mm in diameter
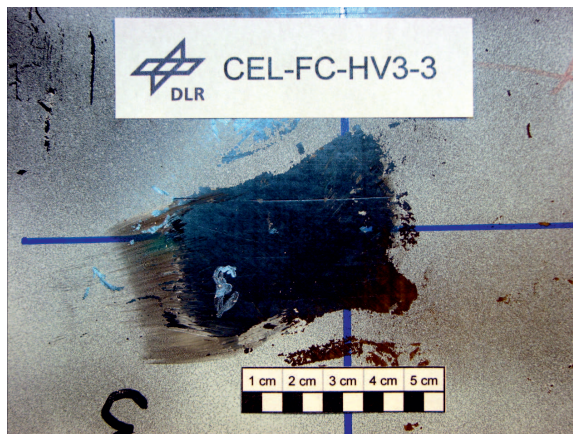
(a) Photography of impact region
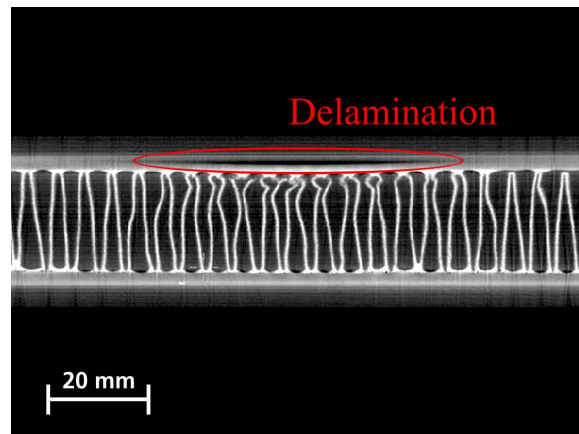
(b) 2D computed tomography

Figure 5.28.: (a) Photography of the front side of the impact specimen (814 J) (b) 2D computed tomography of impact region (814 J).

carbon composite face sheet at the impact region, with small local kinking of the foldcore on contact. This was manifested by a soft spot on the sandwich face sheet which could be indented by finger pressure. Depending on kinetic energy of the projectile, the size of the delaminated area changed. Photography and computed tomography of the impact with the largest kinetic energy (814 J) is provided in figure 5.28. In this case, the face sheet was delaminated in a region of about 90–100 mm in diameter. In a similar area the upper parts of the foldcore showed local kinking and some small cracks directly below the region of impact.

Conclusions

Based on the experimental results typical characteristics of the dynamically loaded sandwich structure have been identified for the effective impact conditions. The observed characteristics are used to assess the quality of the subsequently presented finite element model. Significant observed characteristics in case of hard body impact (Steel cube and steel beam) are:

- Steel cube and steel beam impact caused similar damage characteristics.

- Outer face sheet perforation was in the range 20–40 J, at 45–70 J the projectile was stopped by the foldcore, at kinetic energies larger than 50–70 J the projectile was stopped by the inner face sheet. At 235 J complete penetration of the sandwich specimen was observed. However it was expected that penetration can occur at considerably lower energy levels in the range of of 100–200 J. This kinetic energy range was not investigated in this test series.

- For all energy levels the observed outer face sheet and foldcore damage was localised to a region of which is not much larger than the size of the projectile.

- In case of kinetic energies of 50 J and above, the energy, which was not absorbed by outer face sheet and foldcore, caused considerable deformation of the inner face sheet. As a result, extensive debonding of inner face sheet and foldcore was observed at > 70 J. In case of complete penetration the delamination and damage in the inner face sheet was considerably larger than in the outer face sheet.

Significant observed characteristics in case of soft body impact (Rubber beam) are:

- The face sheet was not penetrated in case of kinetic energies up to 814 J.

- The impact energy was mainly absorbed by global deformation, which was accompanied by delamination of the outer face sheet and small local kinking of the upper foldcore in the impact region.

- The size of delamination correlated to the impact energy.

The difference in damage modes for a soft compliant projectile, which results in shallow crushing of the core whereas a hard body projectile creates deeper damage that conforms to the shape of the projectile was also observed by Horrigan et al. [84].

5.3. Numerical model

In this section the numerical foldcore model is applied to impact loads. For that purpose a brief introduction to impact modelling and the setup of the impact model is given. In succession the implementation of the composite face sheet, of the face sheet-core interface, of the different impactor types and support frame is reviewed. The modelling approach of the composite face sheet is delineated and an estimation of its validity is given by comparing simulation and experiment of a low-velocity composite panel impact case. The setup of further model characteristics, e.g. face sheet-core interface, impactor types, support frame is briefly sketched subsequently. Finally, the dependency of the presented impact model on several modelling factors such as element size, impact location, size of target specimen and friction coefficients is quantified by means of a parameter study and the consequences on the numerical adequacy and reliability of the model are discussed.

5.3.1. Setup of impact model

In the subsequent section the adaption of the numerical foldcore model to impact scenarios is presented. For that purpose the foldcore model has to be extended to give a precise reproduction of the mechanical and structural behaviour required for an impact load scenario. To that end it is necessary to represent the different components of a sandwich structure as well as the material behaviours and relevant physical mechanisms into the model. A schematic overview on the necessary model extensions is given in figure 5.29. These extensions including the modelling of the composite face sheets, the modelling of impactor and support and the interface between core and face sheet are discussed in the following sections.

5.3.2. Modelling of the composite face sheet

Modelling approach

The modelling of the carbon composite face sheet presented in the following mainly bases on previously existing material data and modelling approaches employed by the DLR, which are extensively summarised and discussed by Johnson et al. [89,94]. The challenge of composites modelling is to predict material behaviour at global structural scale level, which incorporates the micromechanic failure mechanisms occurring at local scale level. Typically the length scale for impact simulations measures in 10–10^3 mm, whereas the length scale of the occurring failure mechanisms, such as fibre pull-out, fibre/matrix debonding, matrix cracking, fibre bridging, fibre fracture, microbuckling, interply delamination, etc., is in the regime of μm. The modelling and simulation of damage in composite structures have been extensively researched and the number of research work dealing with this topic is far to enourmous to be covered in this work. A comprehensive review of the different philosophies on damage mechanics in composite materials is given in the research of Talreja [144]. The reader is also referred to the comprehensive investigation into the capacity of existing failure criteria provided in the work

Representation of impactor
(Geometry, material behaviour,
impact location and velocity)

Interaction of impactor and skin/core
(Contact and sliding interface)

Support conditions and interaction
(Contact and sliding, boundary
conditions, geometry and material
behaviour)

**Representation
of composite skin**
(Geometry, material
behaviour, composite
damage mechanism)

Representation of foldcore
(Geometry, material behaviour,
irregularities, self interaction)

Interaction of core and skin
(Core-skin bond, contact and
sliding interface)

Figure 5.29.: Schematic overview on adopted modelling methods which are necessary to reproduce an impact load case.

of Hinton et al. [81]. An overview on modelling approaches in commercial FE codes is found in the review of Zhang and Yang [162]. Impact failure mechanisms in composite structures are discussed and a general view on several impact modelling approaches is given in the review of Abrate [7].

This work uses a meso-model in which the face sheet is idealised as a stacking of two entities: plies and interfaces. In-ply failure is represented by a continuum damage mechanics (CDM) formulation and inter-ply failure is represented by a cohesive interface model. A schematic overview on the representation of failure mechanisms in the meso-model is given in figure 5.30. The CDM formulation follows the approach proposed by Ladevèze [109, 110] in which the damage evolution is related to the damage energy release rate in the ply. The CDM approach can be coupled with a cohesive interface delamination model as fundamentally described by Allix and Ladevèze [13]. Interface models are an intensively investigated field of research and numerous approaches which consider delamination in composite structures have been proposed. A good overview on exising interface modelling approaches is given in the comprehensive review by Wisnom [154]. The employed cohesive interface model bases on the approach suggested by Crisfield et al. [36] which uses fracture mechanic concepts to relate the energy absorbed in the damaging process to the interfacial fracture energy.

The CDM ply and delamination models have been implemented by ESI GmbH in their explicit FE crash and impact code PAM-CRASH, as described in [48, 49]. The CDM ply damage model is supported by layered composite shell elements. A layered composite shell element is a stacked sequence of composite plies with different in-plane orientations. Each ply is modelled on basis of the CDM formulation as homogeneous orthotropic elastic-damaging
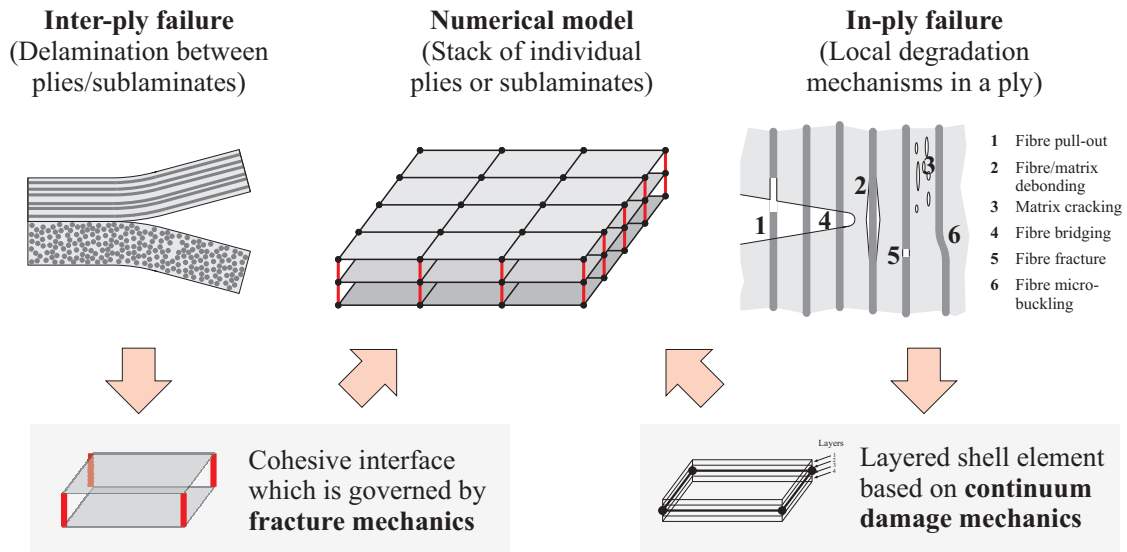
Figure 5.30.: Schematic illustration of composite model's composition. The illustration of in-ply failure is based on a figure found in the work of Anderson [17].

material. The ply damage is described by three scalar damage parameters representing modulus reductions under different loading conditions due to microdamage in the ply.

Delamination can then be defined between layered shell elements which represent sublaminate ply groups of a composite structure. For that purpose the shell elements are tied together using a 'sliding interface' with an interface traction-displacement law. Full details of the implementation of the delamination model as sliding interface with failure between stacked shell elements is given by Greve and Pickett [66]. The advantage of this approach is that the critical integration time step is larger since it depends on the cross-sectional area of the shell elements. Thus large composite structures may be modelled efficiently with shell or stacked shells, requiring fewer elements than solid models, and computationally expensive interface solid elements are eliminated. It is noted that under certain circumstances this approach can overestimate the magnitude of delamination. This is due to delamination only being considered between sublaminates, whereas in real composite materials delamination may occur between individual plies. Thus, in specific cases, the energy in the model has to be absorbed by less interfaces compared to the reality.

Implemented face sheet material model

In the present work, the composite lay-up of 16 UD ply layers is modelled by four stacked layered composite shell elements with cohesive interfaces which may fail by delamination. Each shell element represents four unidirectional ply layer with [0/45/90/-45] orientation. Principal properties of a single UD ply (Cytec Carbon UD 977-2) are given in table 5.8. The

Table 5.8.: Basic properties of single Carbon UD 977-2 ply, as used in the material model.

Longitudinal tensile modulus E_1^T	141	GPa
Longitudinal compressive modulus E_1^C	117	GPa
Transverse modulus E_2	9.7	GPa
In-plane shear modulus G_{12}	4.6	GPa
Major Poisson's ratio ν_{12}	0.31	
Longitudinal tensile failure strain ε_1^T	0.015	
Longitudinal tensile strength σ_1^T	2087	MPa
Longitudinal compressive failure strain ε_1^T	0.012	
Longitudinal compressive strength σ_1^T	1440	MPa
Strain energy release rate (Mode I) G_{IC}	400	J/m^2
Strain energy release rate (Mode II) G_{IIC}	1000	J/m^2
Density ρ	1.65	g/cm^3
Ply thickness t_{Ply}	0.125	mm

stacked shell elements are connected by cohesive interfaces governed by fracture mechanics to represent skin delamination. The critical energies for mode I and mode II failure of C-977 UD composites have been measured in a second DLR test series [95].

The quality of the numerical face sheet material implementation was estimated by comparing impact simulations to existing data on composite plates under impact load provided by EU-Project HICAS [139]. Here a carbon/epoxy composite plate fabricated in a lay-up [0/90]$_{20}$ of Carbon UD 977-2 plies was impacted with a 50 mm spherical impactor of a mass of 21 kg. In the case presented here the impactor hit the target plate with a velocity of 3.11 m/s, which corresponds to a kinetic energy of 102 J. The setup of the plate, impact tests and the instrumentation was the same as that shown in figure 5.5, except that in this case the sandwich panel was replaced by a flat CFRP plate. The impactor damaged the plate and rebounded without penetrating it. The plate was extensively delaminated and fibre fracture occurred at the rear side. The fibre fracture visible on the rear adopted a crosswise shape with the fracture length measuring about half of the plates side length.

The composite plate was modelled as a stacked setup of four sublaminates where each sublaminate represents 10 plies in a [0/90]$_5$ layup. The parameters of the individual UD ply and the delamination interface are identical to those used in the simulations presented in section 5.4. The setup of the numerical model is illustrated in figure 5.31 where a side view of the model is shown briefly before impact and during the impact event, where the impactor has reached the deepest penetration depth prior to rebounding. In figure 5.32 the corresponding load-displacement curves of numerical model and experiment are depicted, where the load on the impactor is plotted against the penetration depth.

Both load curves show comparatively linear increase until a peak load is met, which signifies the onset of fracture in the plate. The load then drops and remains at a lower level until the impactor begins to rebound at a penetration depth of about 24 mm. Generally a good

Sideview briefly before impact

Moment of deepest penetration
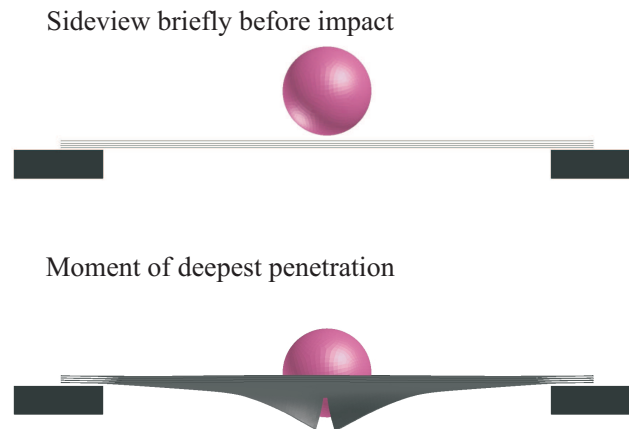
Figure 5.31.: Side views of the numerical model.
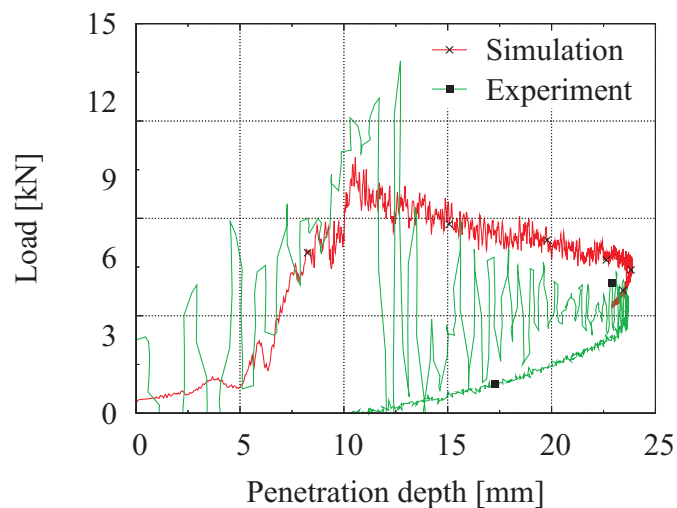
Figure 5.32.: Curve plots of the impactor load vs. penetration depth for simulation and expe-
riment.

agreement of both curves is observed. However, the numerical model underestimates to some
extend the load peak prior to plate fracture and delamination, which amounts to about 12.5 kN
in the experiment and 9.5 kN in the simulation. In contrast the numerical model overestimates
the residual load level in the second phase in which crosswise cracks are forming and extensive
delamination occurs.

The corresponding delamination patterns of simulation and experiment are plotted in
figure 5.33. In the contour plot of the simulation as depicted in figure 5.33a the crosswise shape
of fracture is clearly visible. The extent of delamination is indicated by the purple rhombus,

(a) Simulation   (b) Experiment
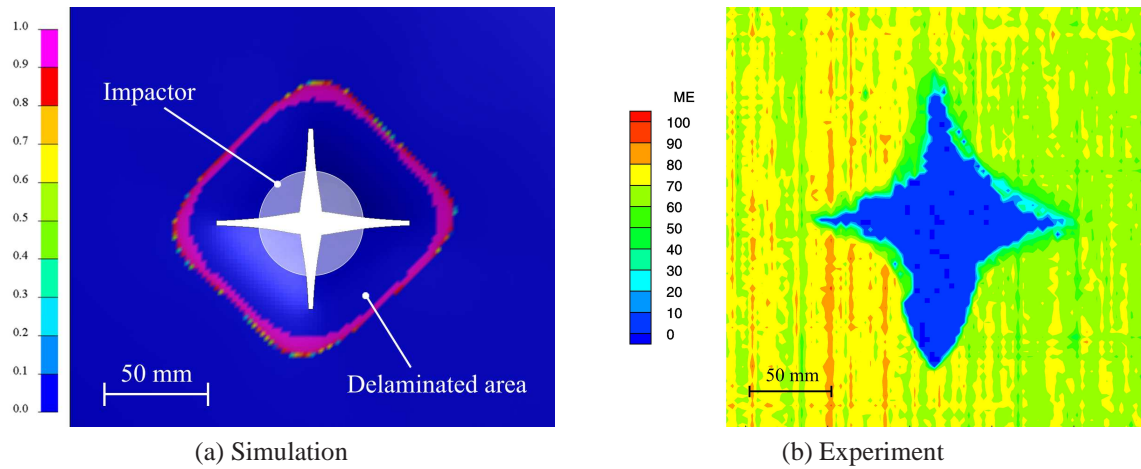
Figure 5.33.: The figures depict the amount of delamination in simulation (Contour plot of interface damage) and experiment (C-Scan of impacted composite panel).

which signifies degraded interfaces. It is noted that the state of the delamination interfaces enclosed by the rhombus is not plotted, as they are eliminated after full failure (damage scalar $d = 1$). The shape of the delamination is mainly governed by the buckling of the corners formed by the crosswise fracture during the impact event. The shapes of delamination predicted by each delamination interface are comparable. If now compared to the C-scan of the experiment in figure 5.33b it is found that the size and shape of the delamination is well represented. However it is noted, that in the numerical model exactly three delamination planes are forming, as this is the number of delamination interfaces defined between the sublaminates. In the experiment a larger amount of delamination planes is observed.

In summary, it is shown that the presented composite model provides sufficient accuracy in modelling the inter-ply and intra-ply damage and failure of a composite panel. It is therefore expected to provide a good prediction capability of the face sheet behaviour in order to model of the impact cases of section 5.2. However it is noted, that, as discussed above, some moderate deviances are existing between the numerical prediction and the experimental observations.

5.3.3. Modelling of impactors and support conditions

In the following a brief overview on the modelling of the different impactor types as well as on the representation of the different impact support conditions is given. It is noted that in case of contact between impactor/support and the target specimen the friction values measured in section 4.2.3 are used.

Table 5.9.: Properties of hard body impactor models.

Type	Mass [kg]	Length [mm]	Width [mm]	Height [mm]	Modulus [GPa]	Poisson's ratio [-]
Steel sphere (LVI)	23.54	Diameter: 50 mm			210	0.28
Steel cube (HVI)	0.0134	12	12	12	210	0.28
Steel beam (HVI)	0.1014	109	30	4	210	0.28

Modelling of impactors

Both hard body impact (steel impactors) and soft body impact (rubber impactors) are investigated in this work. The modelling of hard body impactors at low and moderate velocity conditions (<300 m/s) is straightforward and most reported research on impact concentrates on impact damage and modelling from hard body impactors [11, 33, 59, 106, 118, 121]. Typically a hard body impactor is considerably stiffer than the target specimen and is modelled as rigid (i. e. non-deformable). However, in the PAM-CRASH code elastic properties are assigned to this 'rigid' body, as they are used in the formulation of the penalty forces in the contact law between impactor and target specimen. The dimensions and elastic properties of the (rigid) hard body impactors used in this work are given in table 5.9.

By contrast soft body impactors such as gelatine (substitute bird), ice (hailstones) and rubber (tyre fragments) demonstrate considerable deformability and typically flow over the structure on impact. Considerable effort is necessary to develop modelling techniques and experimental input data for this type of impactors. Both ice and bird impact have been modelled on basis of Lagrangian elements (Ice impact: Park et al. [128], Bird strike: Hanssen et al. [72], Smojver and Ivancevic [140]) as well as on basis of smooth particle hydrodynamics (SPH) (Bird strike: Johnson and Holzapfel [90], Georgiadis et al. [62] and Guida et al. [67]). In contrast most rubber materials are modelled on basis of Langrangian elements, as for example in the research of Karagiozova and Mines [96]. Their main characteristics is the hyperelasticity.

The PAM-CRASH material model for tyre rubber eployed here is based on the hyperelastic Odgen formulation, as described by Odgen [124] and in the PAM-CRASH Solver Notes [48]. By using the two first terms of the Ogden series with exponents of $\alpha_1 = 2$ and $\alpha_2 = -2$ the model reduces to a Mooney-Rivlin material in form of

$$W = \sum_{n=1}^{3} \mu_1 \left(\overline{\lambda}_n^2 - 1 \right) - \mu_2 \left(\overline{\lambda}_n^{-2} - 1 \right) + \frac{K}{2} \left(J - 1 \right)^2, \qquad (5.1)$$

where W is the strain energy functional, K is the respective bulk modulus, J signifies the determinant of the deformation gradient matrix and λ_n are the eigenvalues of the deformation gradient matrix. The factor $\overline{\lambda}_n$ is equal to $J^{-1/3}\lambda_n$. The material parameters μ_1 and μ_2 have been identified in an independent DLR research work. The properties of the rubber beam impactor are given in table 5.10.

Table 5.10.: Properties of soft body impactor model (Tyre rubber).

Mass m	0.103	kg
Length L	132	mm
Width W	30	mm
Height H	25	mm
Poisson's ratio ν	0.499	
Terms in Odgen series		
First coefficient μ_1	0.26	MPa
Second coefficient μ_2	-0.63	MPa
First exponent α_1	2	
Second exponent α_2	-2	

Table 5.11.: Properties of support frame model.

Type	Outer length [mm]	Outer width [mm]	Inner length [mm]	Inner width [mm]	Frame-target specimen interaction [-]
Low-velocity impact	350	350	250	250	Contact interface
Steel cube impact (HVI)	179	166	139	126	TIED interface
Steel beam impact (HVI)	225	226	185	186	TIED interface
Rubber beam impact (HVI)	225	226	185	186	TIED interface

Modelling of support conditions

The support conditions of the numerical model aim to reproduce the suspension of the target specimen during the impact test. For that purpose the steel frame is modelled as a rigid body with nominal elastic properties of steel, Young's modulus is 210 GPa and the Poisson's ratio is equal to 0.28. The rigid support frame interacts either via a contact model or via a TIED interface with the target specimen. The principle of a TIED interface is briefly sketched in section 5.3.4. In case of low-velocity impact presented in section 5.4.1 the interaction between frame and target specimen is modelled by a contact model as the target specimen is placed on the support frame without fixation in the experiment. In case of the high-velocity tests presented in section 5.4.2 the two outer sublaminates of the inner face sheet are connected to the support frame via a TIED interface. This approach approximates the bolting between target specimen and frame used in the experiment. The dimensions of the support frame for the numerical impact models with different impactor types are summarised in table 5.11.

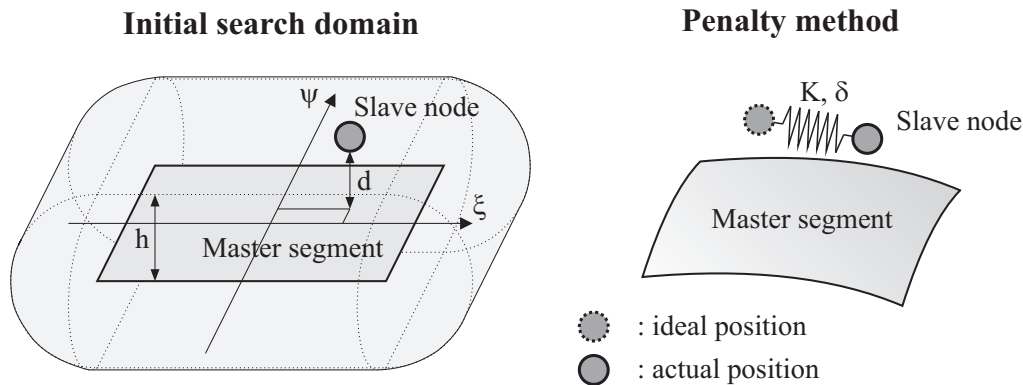**Initial search domain**   **Penalty method**

Figure 5.34.: Schematic illustration of node-surface TIED interface as provided by PAM-CRASH. The figures in the illustration are taken from PAM-CRASH Solver Notes [48].

5.3.4. Interface between foldcore and face sheet

The sandwich specimen investigated here are fabricated in two production steps. In the first step foldcore and face sheets are assembled separately. In the second step the cured foldcore and face sheets are adhesively bonded together with the epoxy-based film adhesive Redux® 319. In the numerical model, the bond between foldcore and face sheets is described on basis of the TIED node-surface interface provided by PAM-CRASH [48, 49]. This fundamental method of the TIED node-surface interface is illustrated in figure 5.34.

The TIED node-surface interface initially searches for nodes close to a surface or master surface within a search distance h. All so-called slave nodes found within the search domain are coupled to the master surface via a penalty algorithm. For that purpose the position of the nodes is computed by determining the minimum distance d between node and master surface on basis of the local, projected coordinates ξ and ψ. During analysis, a new ideal position is computed each time step based on the initial position of the slave nodes relative to the master surface. The interface approximates the ideal position by modifying the actual position of a slave node on basis of a penalty force. The magnitude of the penalty force depends on the difference between actual position of the slave node and its ideal position. Due to limited experimental data on bondline properties a very basic interface is implemented using a linear penalty algorithm with spring constant K.

A perfect bond between face sheet and foldcore is assumed and bond degradation as well as rupture are neglected. It is noted that similar foldcore sandwich specimens with four different epoxy-based film adhesive systems were investigated in flatwise tensile and shear tests by Drechsler et al. [44]. It was shown that in case of quasi-static loads the dominating failure was a separation of the phenolic impregnation of the aramid fibres. In case of the present work it was therefore expected that the dominant failure mode is in the cell wall material at the bondline and the failure of the adhesive layer is not considered important.
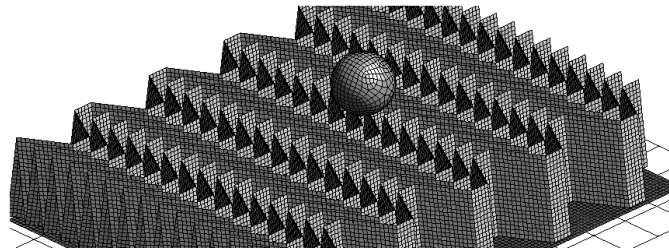
Figure 5.35.: Iso-view of the parametric model (Outer skin is made transparent).

5.3.5. Parameter study on impact conditions

In this subsection the effect and influence of several numerical quantities are estimated. These include element size, impact location in relation to foldcore structure, model size and influence of different friction coefficients. For that purpose a basic impact scenario was realised allowing comparison of the effect of the individual parameters. The scenario represents a spherical projectile of 14 mm in diameter impacting a type 30 foldcore sandwich panel which has the size of 5x15 unit cells. The complete face sheet laminate is modelled with a layered shell as proposed in section 5.3.2. A delamination interface is not included. A square frame supports the edges of the sandwich panel. The impactor and the frame support are rigid bodies. For comparability reasons the velocity of the impactor was held constant at 25 m/s during the whole simulation. It is noted that a constant velocity of the impactor is not consistent with a realistic impact occurrence, in which a projectile is decelerated. Figure 5.35 depicts the setup of the parametric model. The outer skin is made transparent in order to provide insight into the subjacent foldcore structure.

Element size

Similar to the mesh size studies in section 4.3.4 the element size dependency of an exemplary impact model was investigated. For this purpose the impact model (foldcore, face sheets, impactor and support) was meshed with element sizes ranging from 0.5–2.0 mm side length. In figure 5.36 the force acting on the impactor is plotted against the penetration depth. The distinctive peaks in force magnitude signify the penetration of the outer and inner face sheet. The domain between both peaks indicates core crushing at a comparably low force level.

As in the parameter studies of core crushing in section 4.3.4 a considerable influence on model behaviour is observed. The smaller the element size, the softer the model becomes. The force which was computed with the smallest element size (side length 0.5 mm) is about twice the magnitude of the force which was computed with largest element side length (side length 2.0 mm). Very small element sizes (< 0.5 mm) result in unstable simulation behaviour, which is mainly caused by the characteristic element length approaching the element thickness.

Figure 5.36.: Load acting on the impactor vs. penetration depth of the impactor plotted for varying element sizes.

Location of impact

Another parameter which can possibly influence the simulation results is the impact position with respect to the foldcore geometry. In particular for small impactors it was uncertain if the impact behaviour is affected by positioning a fold ridge or fold gap directly beneath the impact position. For this purpose the parameter model was impacted between the foldcore ridges (1), directly on a foldcore ridge (2) and on a ridge corner, where two folds meet (3) as depicted in figure 5.37.

The force acting on the impactor against the penetration depth is given in figure 5.38. It was expected that case (1) exhibits the lowest impact resistance and case (3) demonstrates the highest impact resistance. Instead of that it was found that all three curves are very similar. The peak of the penetration of the outer skin is slightly larger for the case (3) and the lower skin is penetrated at an slightly larger penetration depth (~1 mm) for case (1) compared to case (2) and case (3). In general the impact position in regard to foldcore geometry has a small influence on the numerical results. With 14 mm in diameter, the impactor size in the parameter study correlates to the minimal impactor size investigated in the subsequent numerical study. It is noted that in case of larger impactor sizes the effect of impact location is expected to be even more marginal.

Panel size

Due to the dense packing of foldcore faces the meso-model can become considerably complex, especially if large target specimen need to be modelled. In order to save computation time it is therefore of interest to reduce the modelled foldcore size as much as feasible. However, the

1: between ridges
2: midway on ridge
3: on corner of ridge
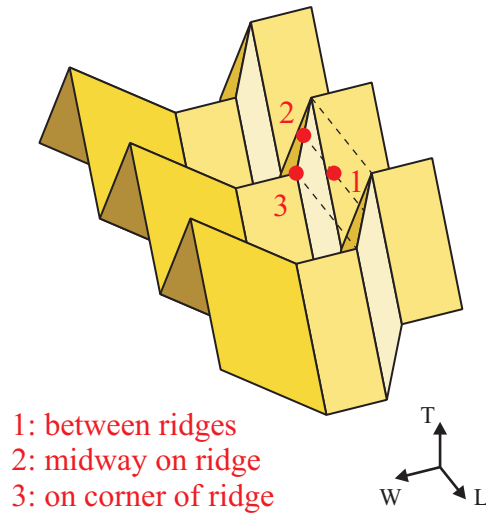
Figure 5.37.: Position of impactor.
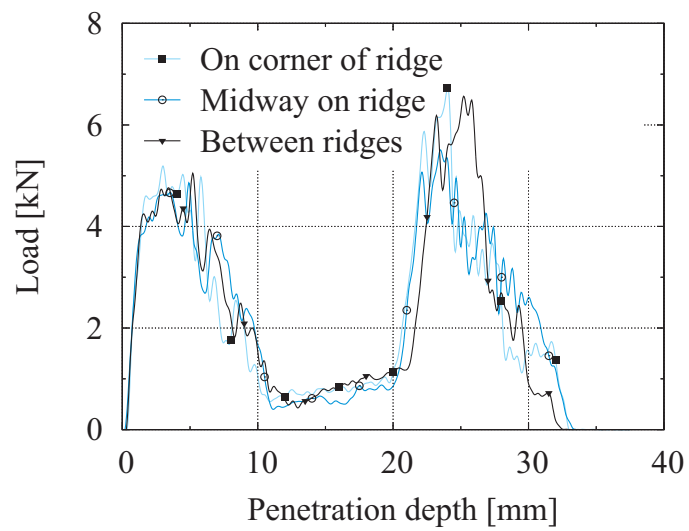
Figure 5.38.: Load acting on the impactor vs. penetration depth of the impactor plotted for
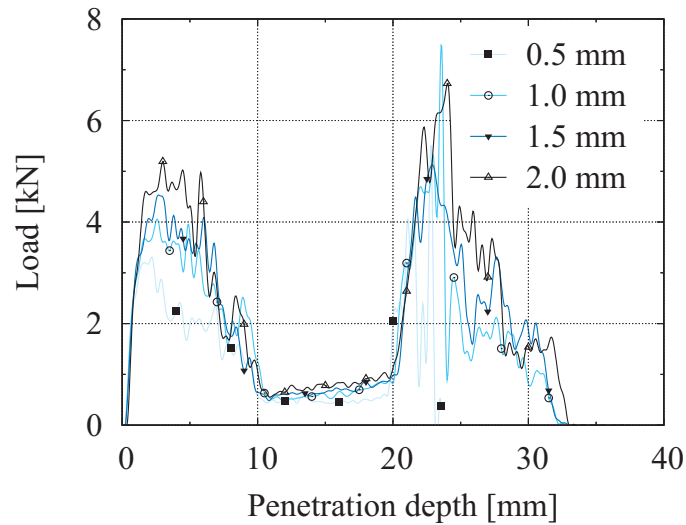varying impact locations.
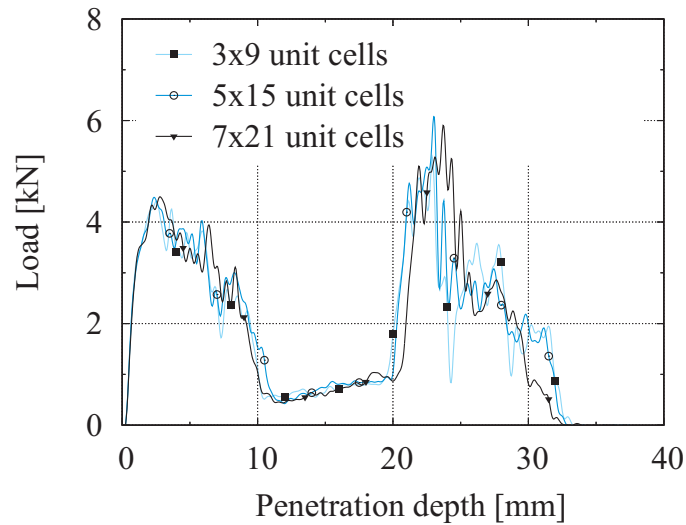
Figure 5.39.: Load acting on the impactor vs. penetration depth of the impactor plotted for
varying model sizes.

reduction of the target specimen size affects global properties such as buckling modes of the
sandwich structure and correct application of boundary conditions, as the size of the support
has to be adapted to the size of the target specimen. To assess these effects on global properties
the impact on several panel sizes has been investigated.

For that purpose three models were generated with the dimensions of 3x9, 5x15 and 7x21
unit cells. The model size was then 68x58 mm, 113x100 mm and 158x125 mm, respectively.
The inner dimensions of the support frame were 50x41 mm, 95x74 mm and 141x106 mm. It
is noted, that the inner face sheet is fixed to the support frame to represent the in reality bolted
fixation of panel and support. Figure 5.39 shows the load on the impactor against the pene-
tration depth for the different panel sizes. The different panel sizes demonstrate negligible
influence during outer face sheet penetration and foldcore crushing. In case of the 7x21 unit
cell panel the loading and failure of the inner face sheet occurred at a slightly larger penetra-
tion depth (~1 mm) which indicates that there was some compliance due to increased global
buckling.

Coefficient of friction

The influence of the friction on the sliding interfaces was investigated. The friction coefficient
for composite surface on folded core contact and for folded core self contact was varied.
For this parameter study both friction coefficients were assumed to be identical and ranging
between 0.0 and 0.4. It is noted that the friction coefficient for folded core self contact is
usually larger than the friction coefficient for surface to core contact. The folded core and
surface element size was 1.5 mm.
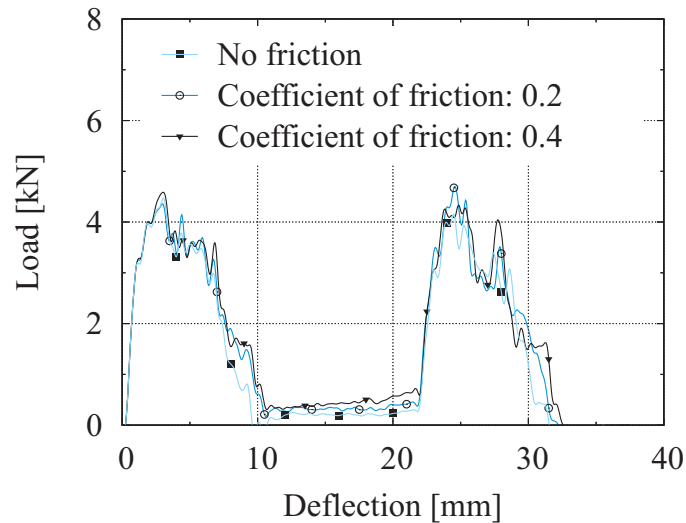
Figure 5.40.: Load acting on the impactor vs. penetration depth of the impactor plotted for
varying coefficients of friction.

Figure 5.40 depicts the force vs. displacement curve for different friction values. The
force-displacement behaviour for the first and second force peak is comparable for all friction
cases, although the cases with larger friction display a slightly larger force level. During core
compaction different force levels can be observed for the investigated friction coefficients.
Larger friction coefficients lead to an increase of crush force level. This indicates that es-
pecially extensive core compaction and substantial force levels may result in a considerable
effect of friction. However, the crush force and thus the observed differences in the investi-
gated model setup are very small. Therefore a uncertainess towards this observations exits. It
is also noted that in case of zero friction the force level drops into negative regions after the
outer surface is penetrated.

Summary of parameter study

In the parameter study the modelling of a small, hard body impactor on a folded core sandwich
was investigated. In general, the simulations showed a limited amount of outer skin elastic
loading, then a localised penetration of the outer skin followed by localised core crushing and
finally inner skin penetration. As the impactor was small compared to the folding pattern of
the core the energy absorbed by the folded core was small.

The conclusion in regard to element size are similar to those made in section 4.3.4: The
element sizes employed by the numerical model need to be limited to side lengths of 1.0–1.5
mm, as there is a considerable effect of mesh size. The impact location is considered to have
no relevance for the impact modelling, as the simulations with comparably large foldcore unit
cells and a comparably small impactor showed negligible influence of position of impact.
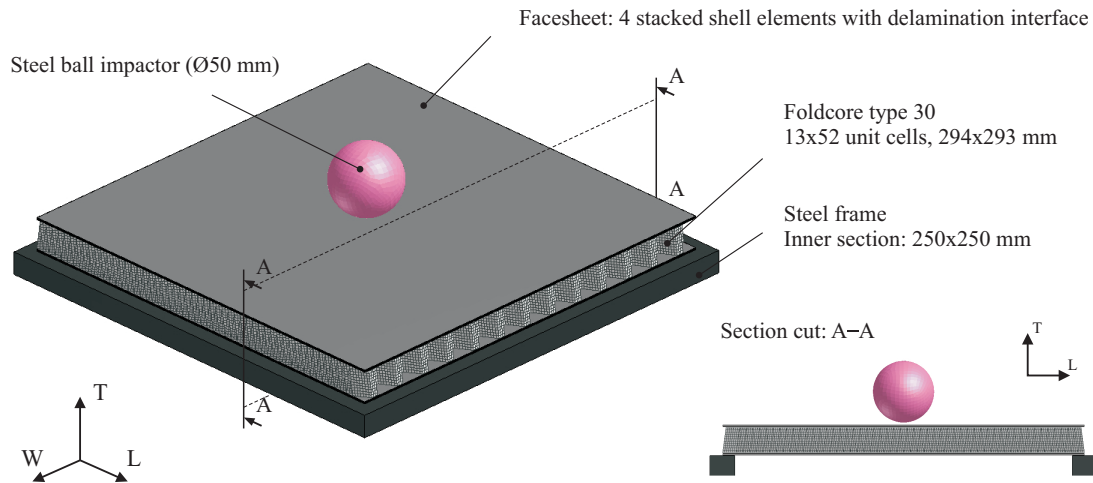
Figure 5.41.: Iso-view and side view on the low-velocity impact model. The mesh of impactor, frame and face sheets is transparent.

5.4. Model evaluation

In section 5.3 the foldcore meso-model developed in section 4.3 is applied to impact loads. In order to evaluate the accurateness and capacity of the application to impact loads, the numerical predictive model is comprehensively compared to the drop tower and gas gun tests delineated in section 5.2. The first part of the present section covers low-velocity impact (drop tower tests). Subsequently high-velocity impact (gas gun tests) is discussed. Evaluation criteria are accurate representation of the course of events during impact, a correct prediction of energy absorption and a good reproduction of the resulting damage patterns in foldcore and face sheets. Additionally the force and displacements path of experiment and simulation are compared in case of the low-velocity impact tests.

5.4.1. Low-velocity impact

Setup

In this section, the numerical predictions are compared to the low-velocity impact tests discussed in section 5.2.1. For that purpose the numerical model was adopted to the experimental setup corresponding to the modelling approach delineated in section 5.3. The initial set-up of the numerical model is depicted in figure 5.41. The spherical impactor is positioned just beyond the contact distance of the face sheet mesh at a given initial velocity.

The geometric dimensions of the numerical model correspond exactly to the dimensions of the sandwich panel in the experiment. The sandwich core is a type 30 with 13 x 52 unit cells,

which results in about $3 \cdot 10^5$ elements to represent the core in combination with an element side length of 1.5 mm. The total number of elements in the whole model is about $4 \cdot 10^5$. The face sheets consist of four stacked layered elements. Each individual layered element represents four plies which gives a total of 16 plies per face sheet. Delamination between the stacked elements is considered. The spherical impactor is a rigid body with 50 mm in diameter. The support frame is also a rigid body with inner section dimensions of 250x250 mm. Between support frame and inner face sheet a contact and friction interaction is defined. Further model parameters are summarised in table 5.12, where references are given to sections in which the individual parameters are discussed in detail.

Comparison

The initial velocities of the spherical impactor are set to 2.21 m/s, 3.42 m/s and 5.77 m/s which correlates to the velocities measured in the drop tower test series. It is noted, that the kinetic energies corresponding to these velocities are somewhat smaller than the specified energies of 60 J, 140 J and 400 J. The numerical model is evaluated on basis of several benchmark characteristics, such as representation of the course of events during impact and the accurate prediction of force, displacement and energy behaviour during the impact occurrence. A further benchmark characteristic is the representation of the observed damage patterns in foldcore and face sheets. Relevant damage patterns of the foldcore are face and fold buckling and fracture, foldcore crushing and damage expansion. Relevant damage patterns of the face sheet are mainly ply damage and delamination between plies.

Comparing the course of impact events, simulation and experiment demonstrate satisfying conformance for all investigated load cases. As an example the impact courses of the 140 J impact are compared in figure 5.42. The images at time interval t=0 ms show the ball impactor and target specimen just before impact. In both simulation and experiment the ball impactor has reached the maximum penetration depth at time interval t=8 ms and begins to rebound. The images at time interval t=12 ms depict the retreating ball impactor. These elementary impact characteristics are well reproduced by the numerical model. It is noted that considerable oscillations in the sandwich structure were observed in the experiments which are caused by a 'rebounding' of the face sheets after penetration. This rebounding of face sheets and associated oscillations is not reproduced by the numerical model.

However, if the load-displacement and energy-displacement curves in figure 5.43 are considered, in which the force on the ball impactor and the energy absorbed in the process is plotted against the penetration depth, some divergence between simulation and experiment is observable. Generally the load-displacement-curve of a hard body impact is signified by two load peaks in which the face sheets are penetrated and a phase in-between, which is dominated by foldcore crushing at a constant load. In the experimental force-displacements curves the load peaks, which indicate the failure of face sheets are clearly recognisable. In contrast the respective load peaks are hardly discernable in the curves of the numerical model. For instance the outer face sheet fails at about 12–13 kN in the experiment, whereas the numerical model predicts magnitudes of 9–12 kN. In case of a 400 J impact, the experiment showed inner face

Table 5.12.: Properties of low-velocity impact model.

Foldcore	
Geometric dimensions	Type 30, 13x52 unit cells, H = 20 mm, a = 12.5 mm, γ = 30.5°, s = 5 mm, $\rho*$ = 137.5 kg/m^3 (for CELPACT type definition see table 4.5 on page 81)
Material properties	Aramid paper model (for elastic properties of fibre reinforced layer see table 3.15 on page 54 and for elastic properties of resin film layer see table 3.14 on page 52; damage on basis of a scalar damage function is modelled separately for each layer, an overview on the stress-strain behaviour of each layer is found in figures 3.31 and 3.32 on page 60 f.)
Element side length	1.5 mm (for an investigation of the influence of element size see section 4.3.4 on page 90ff.)
Contact and friction	Coefficient of friction: $\mu_{(FC-FC)}$ = 0.2, $\mu_{(FC-Steel)}$ = 0.4, $\mu_{(FC-CFRP)}$ = 0.4 (see section 4.2.3 on page 75ff.)
Irregularities	Node-shaking, Max. deflection: Normal = 2.5 μm, Lateral = 50 μm (see section 4.3.2 on page 80ff.)
Face sheet	
Geometric dimensions	300x300 mm, thickness: 2 mm (16 plys, each with 0.125 mm)
Material properties	Four stacked shell elements with CDM ply damage model and three cohesive interfaces; each shell element represents four CFRP plies (material properties used in model are given in table 5.8 on page 137)
Element side length	1.5 mm (and investigation on element size effects can be found in section 5.3.5 on page 143f.)
Contact and friction	Coefficient of friction: $\mu_{(CFRP-CFRP)}$ = 0.2, $\mu_{(CFRP-FC)}$ = 0.4, $\mu_{(CFRP-Steel)}$ = 0.3 (see section 4.2.3 on page 75ff.)
Irregularities	Node-shaking, Max. deflection: Normal = 0 μm, Lateral = 50 μm, (see section 4.3.2 on page 80ff.)
Ball impactor/support frame	
Geometric dimensions	Ball Impactor: Ø50 mm Frame: 250x250 mm (interior), 350x350 mm (exterior) (see table 5.11 on page 141)
Material properties	Ball impactor: E = 210 GPa, ν = 0.28 (see table 5.9 on page 140) Frame: E = 210 GPa, ν = 0.28
Element side length	Ball impactor: 1.5 mm Frame: 10.0 mm
Contact and friction	Coefficient of friction: $\mu_{(Steel-FC)}$ = 0.4, $\mu_{(Steel-CFRP)}$ = 0.3 (see section 4.2.3 on page 75ff.)
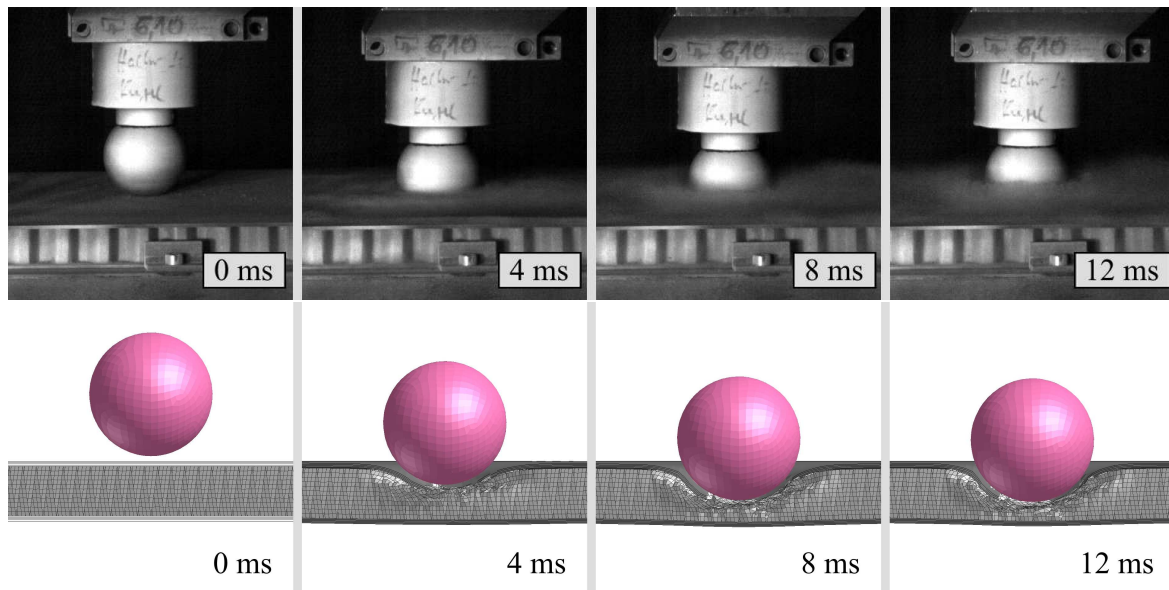
Figure 5.42.: The image sequences depict the impact occurrence of numerical model and experiment in case of a 140 J low-velocity impact.

sheet loading up to 21 kN until the impactor began to rebound. However, the numerical model predicted failure at a peak load of 17.5 kN.

A certain difference in peak loads of simulation and experiment was also observed in the validation study of the composite skin model in section 5.3.2. In the validation study the peak load is underestimated, whereas the subsequent load path was slightly larger compared to the magnitudes observed in the experiment. This indicates that the composite skin model predicts a premature initiation of fracture, which correlates to the drop in stress level after reaching peak load. After fracture initiation the composite skin model overestimates the work needed for subsequent crack propagation and associated delamination between plys.

It is also observed, that the penetration depths predicted by the numerical model exceed the penetration depths measured in the experiment by about 12 % (60 J), 19 % (140 J) and 3 % (400 J). This overestimation is to a certain point caused by the reduced energy absorption in the face sheet. The main factor however is that although the kinetic energy imposed in experiment and simulation is equal, the amount of energy absorbed by the target specimen is different for experiment and simulation. In the simulation, all energy has to be absorbed by the target specimen, whereas in the experiment several additional factors are affecting the amount of energy absorbed by the target specimen. For instance, a fraction of the initial kinetic energy can be absorbed by the support and the impactor mass, by friction between slide carriage and rail, etc. As a result the absorbed energy measured in the experiment is 17 % (60 J), 18 % (140 J) und 11 % (400 J) lower than the initial kinetic energy, which correlates to the observed differences in penetration depth.
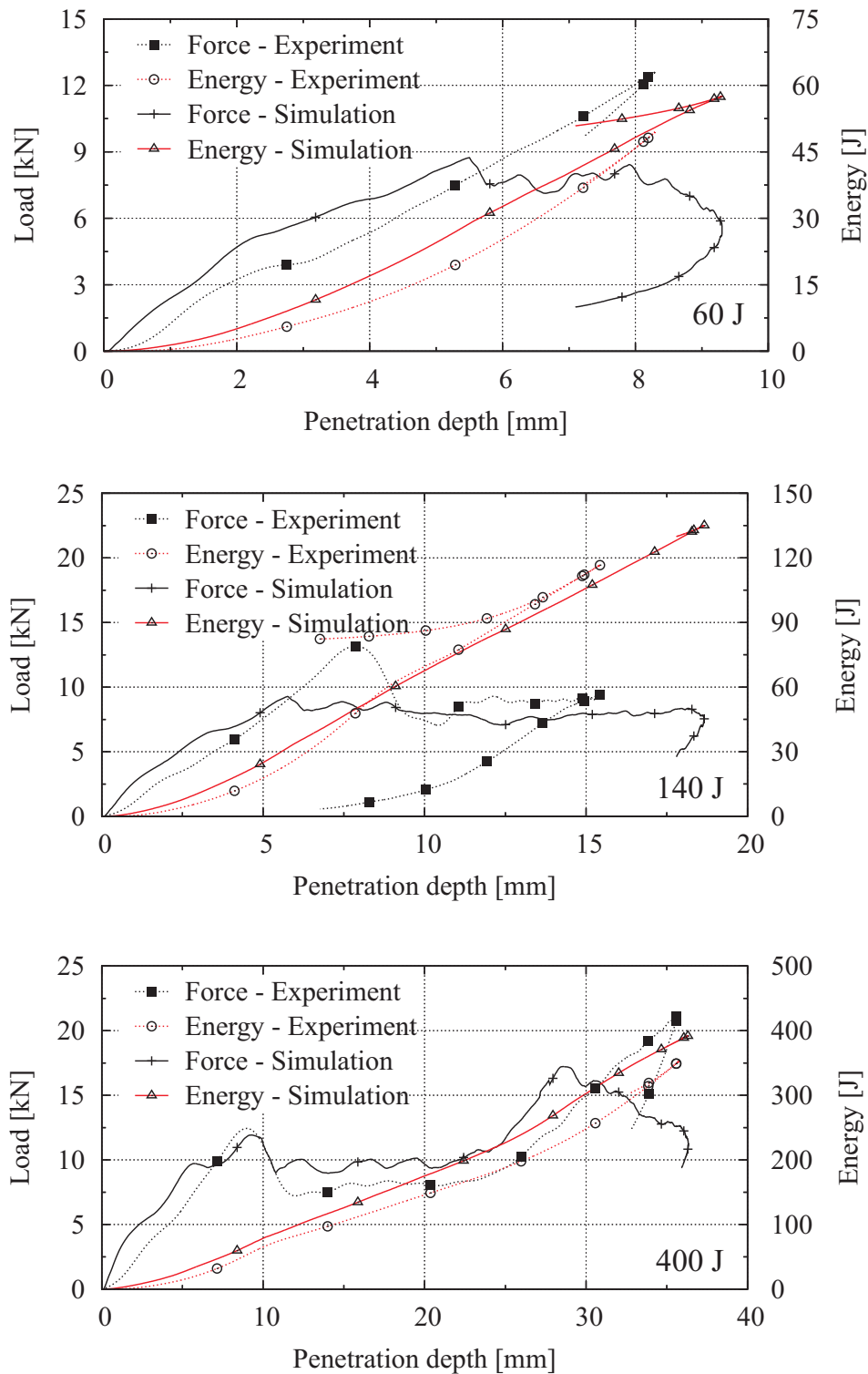
Figure 5.43.: Load-deflection and Energy-deflection curves of the 60 J, 140 J and 400 J impact
            test.

The load-displacement and energy-displacement of numerical model and experiment show good agreement for the phase after outer face sheet penetration and before inner face sheet penetration, where the response is mainly governed by foldcore collapse and crushing in combination with face sheet bending. In particular the conformance of the load levels in the foldcore crushing dominated phase is noted. A good representation of the foldcore behaviour is also found in case of cell wall damage occurrence, as observable in figure 5.44. Here, contour plots of the damage in the fibre reinforced layer of the aramid paper model is compared to post-impact CT-scans. The contour plots depict the moment in which the projectile has reached the maximum penetration depth. The CT-scans were performed subsequently to the completion of the impact tests. A damage value of up to 0.18 represents the continuous damage caused by micro processes such as fibre segment realignment and associated local matrix damage. A damage value of 1.0 signifies full failure of the aramid paper. If the contour plots are considered it is observed that the numerical model predicts a very localised damage in the foldcore. This is in good agreement with the CT-scans of the impacted specimen:

In case of a 60 J impact (Figures 5.44a and 5.44b) local failure of the cell wall is evident directly below the position of impact. The extent of failure correlates roughly the diameter of the spherical impactor. Moderate damage is observed in the upper two-thirds of the core. Local buckling is found in the upper half of the foldcore core. This coincides with the damage identified in the CT-scan. Here a permanent deformation of the foldcore with sharp kinks and local fractures in the aramid paper is observed in the upper part of the foldcore in an area which correlates roughly with the diameter of the impactor.

In case of a 140 J impact (Figures 5.44c and 5.44d) the numerical model also shows cell wall failure directly below the impactor in a region of about 1.5–2 times the diameter of the impactor. The upper two-thirds of the foldcore are fully densified and the impactor has penetrated the foldcore to a depth of about 10 mm. Below the impactor the aramid paper is damaged almost up to the inner face sheet. The considerable amount of kinks and fractures in the CT-scan approximately corresponds to the damage prediction in the numerical model.

The comparison of simulation (Figure 5.44e) and experimental results (Figure 5.44d) of the 400 J impact exhibits in both cases a full densification of the foldcore below the impactor. The numerical model predicts damage of the aramid paper in a region of 2–2.5 times the diameter of the impactor. Full failure occurs close to the impactor as well as along of the face sheets, in particular the inner face sheet. In the experiment mainly face sheet-core debonding was observed in this region. It is noted, that the numerical model assumes a perfect bond between face sheet and core. The foldcore elements failed along the interface in regions where debonding of skin and core was observed in the experiments (as can be seen in 5.44e). However the extent and size of this debonding zone was still underestimated by the model.

Figure 5.45 shows the course of the kinetic and internal energies predicted by the numerical model for the 140 J impact. The blue colour signifies the kinetic energy of the impactor, which is initially about 135 J. At about t=10 ms the kinetic energy is fully absorbed by the sandwich structure and the impactor begins to rebound. The grey colour indicates the internal (and kinetic) energies of the inner and outer face sheets. The yellow colour corresponds to the internal (and kinetic) energy stored in the foldcore. It is noted that the magnitude of the

(a) Simulation (60 J)   (b) Experiment (60 J)

(c) Simulation (140 J)   (d) Experiment (140 J)

(e) Simulation (400 J)   (f) Experiment (400 J)
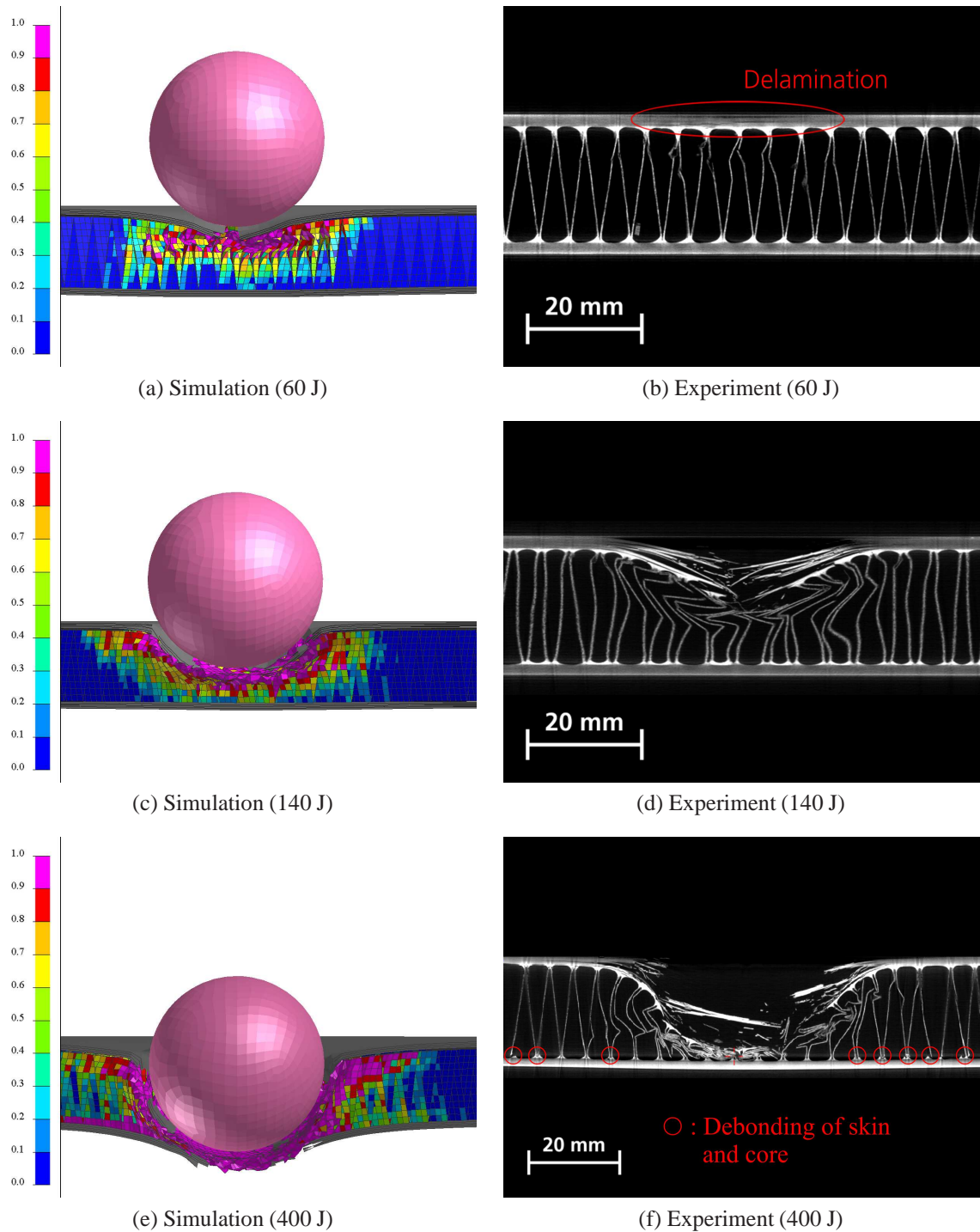
Figure 5.44.: Comparison of numerically predicted foldcore deformation and damage with CT-scans of the 60 J, 140 J and 400 J impact. The numerical contour plot show the damage scalar of the fibre reinforced layer. a) The contour plot depicts the foldcore target specimen at maximum penetration depth of the ball impactor (60 J impact) b) Post-impact CT-scan (60 J impact) c) The contour plot depicts the foldcore target specimen at maximum penetration depth of the ball impactor (140 J impact) d) Post-impact CT-scan (140 J impact) e) The contour plot depicts the foldcore target specimen at maximum penetration depth of the ball impactor (400 J impact) f) Post-impact CT-scan (400 J impact).
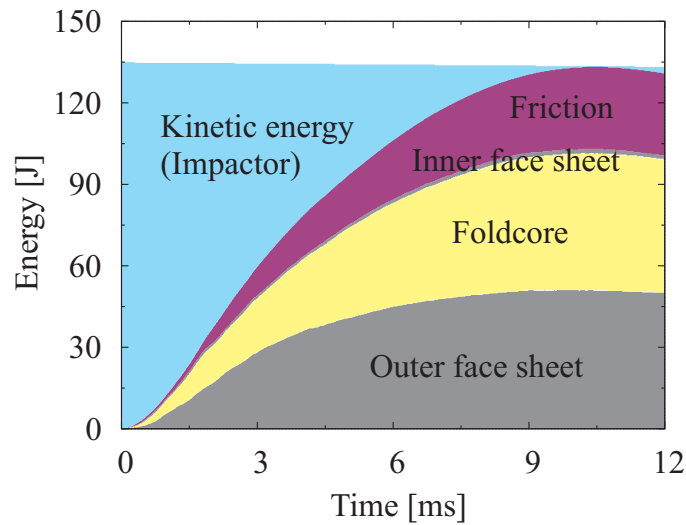
Figure 5.45.: Energies predicted by the numerical model for a 140 J impact.

kinetic energy in the sandwich structure is very small compared to the internal energy (less than 1 %). The purple colour signifies the energy which is absorbed by friction.

The kinetic energy of the impactor is absorbed to about 40 % by foldcore and outer face sheet respectively, whereas 20 % of the energy is absorbed by friction occurring between the fold cell walls and -to some extent- the face sheets. The energy absorbed by the inner face sheet is small due to the impactor being stopped by outer face sheet and foldcore. It is noted that there is a small decrease in total energy which roughly corresponds to the energy associated with hourglassing.

5.4.2. High-velocity impact

Setup

In this section, the numerical predictions of high-velocity-impact are compared to the experiments discussed in section 5.2.2. Similarly to the low-velocity impact simulations a numerical model was generated in correspondence to the modelling approach delineated in section 5.3. The initial model setups for the different impactor types are depicted in figure 5.46.

The different impactor types are positioned such that they are located just beyond the contact distance of the face sheet mesh at a given initial velocity. The geometric dimensions of the sandwich panel are reduced in order to reduce computation time. The foldcore geometry conforms to the type 30 specification. The size of the core model is 7 x 25 unit cells in case of the cubic impactors and 9 x 36 unit cells in case of the beam impactors. It is noted that the sandwich panel size of the numerical model is significantly smaller than the size of the sandwich panel used in the experiment. The reason for this deviance is that the parameter
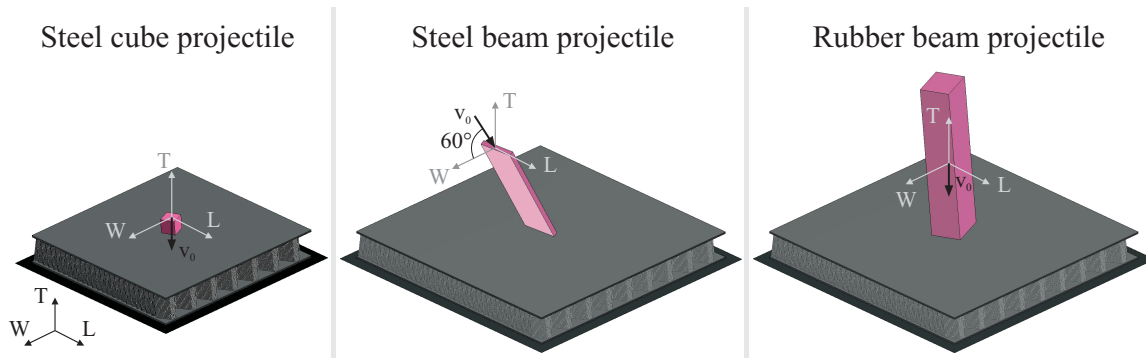
Figure 5.46.: Iso-view and side view on the high-velocity impact model. The mesh of impactor, frame and face sheets is transparent.

study in section 5.3.5 indicated, that a moderate reduction of panel size has no significant influence on the numerical results. The element number in the sandwich panel ranges from $2.6 \cdot 10^5$ to $5 \cdot 10^5$ elements for an average element side length of 1.0 mm. The total number of elements of the whole model ranges from $5 \cdot 10^5$ to 10^6. The face sheets are setup similarly to the face sheets in the low-velocity impact model. This means a stack of four layered elements with four plies each which gives a total of 16 plies per face sheet. Delamination between the stacked elements is considered by a cohesive interface.

The impactor types are modelled as rigid bodies in order to reproduce steel cube and steel beam projectiles. The rubber beam impactor is modelled as an hyperelastic material based on the Odgen formulation. The orientation of steel cube, steel beam and rubber beam before impact has been roughly adapted to the orientation observed in the experimental video sequences. The support frame is a rigid body with inner section dimensions adapted to the sandwich dimensions so that there is an overlap of about 10 mm between frame and sandwich panel. As for the low-velocity impact simulations no damage/fail condition was implemented for skin-core bonding. Between support frame and inner face sheet a perfect bond was defined to represent the bolting of the sandwich panel to the frame. The model parameters are summarised in table 5.13, where references are given to sections in which the individual parameters are discussed in detail.

Comparison

In the following, the predictions of the numerical model are compared to high-velocity impact test results in section 5.2.2 for steel cube impact at 55.6 m/s (20.9 J), at 81.8 m/s (45.2 J) and at 108.1 m/s(77.2 J), steel beam impact at 39.3 m/s (78.7 J) and at 67.9 m/s (234.7 J) as well as rubber beam impact at 125.7 m/s (814.2 J). The numerical model is evaluated on basis of several benchmark characteristics, such as representation of the course of events during impact. A further benchmark characteristic is the representation of the observed damage patterns in foldcore and face sheets. Relevant damage patterns of the foldcore are face and fold buckling

Table 5.13.: Properties of high-velocity impact model.

Foldcore	
Geometric dimensions	Type 30, Hard body impact: 7x25 unit cells, soft body impact: 7x25 unit cells (for CELPACT type definition see table 4.5 on page 81)
Material properties	Aramid paper model (for elastic properties of fibre reinforced layer see table 3.15 on page 54 and for elastic properties of resin film layer see table 3.14 on page 52; an overview on the stress-strain behaviour of each layer is found in figures 3.31 and 3.32 on page 60 f.)
Element side length	1.0 mm (for an investigation of element size see section 4.3.4 on page 90ff.)
Contact and friction	Coefficient of friction: $\mu_{(FC-FC)} = 0.2$, $\mu_{(FC-Steel)} = 0.4$, $\mu_{(FC-CFRP)} = 0.4$, $\mu_{(FC-Rubber)} = 0.4$ (see section 4.2.3 on page 75ff.)
Irregularities	Node-shaking, Max. deflection: Normal = 2.5 μm, Lateral = 50 μm (see section 4.3.2 on page 80ff.)
Face sheet	
Geometric dimensions	Hard body impact: 160x140 mm, soft body impact: 160x140 mm, thickness: 2 mm (16 plys, each with 0.125 mm)
Material properties	Four stacked shell elements with CDM ply damage model and three cohesive interfaces; each shell element represents four CFRP plies (material properties used in model are given in table 5.8 on page 137)
Element side length	1.0 mm (and investigation on element size effects can be found in section 5.3.5 on page 143f.)
Contact and friction	Coefficient of friction: $\mu_{(CFRP-CFRP)} = 0.2$, $\mu_{(CFRP-FC)} = 0.4$, $\mu_{(CFRP-Steel)} = 0.3$, $\mu_{(CFRP-Rubber)} = 0.4$ (see section 4.2.3 on page 75ff.)
Irregularities	Node-shaking, Max. deflection: Normal = 0 μm, Lateral = 50 μm, (see section 4.3.2 on page 80ff.)
Hard/soft body impactors/support frame	
Geometric dimensions	Steel cube: 12x12x12 mm, Steel beam: 109x30x4 mm, Rubber beam 132x30x25 mm, Frame (cube impact): 139x126 mm (interior), Frame (beam impact): 185x186 mm (interior) (see table 5.11 on page 141)
Material properties	Steel impactors: E = 210 GPa, $\nu = 0.28$ (see table 5.9 on page 140) Rubber impactor: Odgen formulation (see table 5.10 on page 141) Frame: E = 210 GPa, $\nu = 0.28$
Element side length	Impactors: 1.0 mm Frame: 10.0 mm
Contact and friction	Coefficient of friction: $\mu_{(Steel-FC)} = 0.4$, $\mu_{(Steel-CFRP)} = 0.3$, $\mu_{(Rubber-FC)} = 0.4$, $\mu_{(Rubber-CFRP)} = 0.4$ (see section 4.2.3 on page 75ff.)

and fracture, foldcore crushing and expansion of damaged region. Relevant damage patterns of the face sheet are mainly ply damage and delamination between plies.

In figure 5.47 the impact course of simulation and experiment are shown for impact with the three different projectile types, namely a steel cube (45J), a steel beam (235 J) and a rubber beam (814 J). The images at time interval t=0 ms show the projectiles and target specimens just before impact. The subsequent images depict experiment and simulation at similar t until the projectile is either rebounding or has penetrated the sandwich panel. As for the low-velocity impact case a good agreement between numerical model and experiment is observed. The steel cube projectile in both test and simulation penetrated through the outer skin, crushes the foldcore and is stopped by the inner skin on reaching the maximum penetration depth at about t=1 ms then begins to rebound. In the experiment the projectile was trapped in the core, whereas the numerical model predicts it rebounding through the outer skin. The main reason it is not trapped in the simulation is, that many elements of the target specimen were eliminated along the path of the projectile and are therefore not able to trap it as in the test.

The picture sequences of the steel beam projectile both depict a penetration of the target specimen during a time period of about 3 ms. The positions of the projectile in numerical model and experiment at different t show good agreement. Finally picture sequences of a rubber beam impact are presented. Both, numerical model and experiment, show a rebound of the projectile at about t=0.8 ms. In both events a considerable deformation of the rubber projectile is observed. In summary it is evident that the elementary characteristics of the impact event are well reproduced by the numerical model.

In figures 5.48 and 5.48 the load on the projectile versus the penetration depth is plotted for selected steel cube and steel beam impact simulations. There are no corresponding experimental curves, as the force-time response was not measured during the gas gun tests. The load-penetration depth curves of both types of projectile demonstrate similar characteristics. Face sheet loading and penetration is recognised by two distinctive load peaks with magnitude of about 8–12 kN. The peak corresponding to the inner face sheet is lower in case of the steel cube impacts and the steel beam impact with 79 J as the projectile rebounded before inner face sheet failure. Penetration depth between 5 mm and 20 mm signify foldcore crushing at a relatively low, constant stress level of about 1–2 kN.

In figures 5.50 and 5.51 the deformation and damage behaviour of the foldcore model are compared to post-impact CT-scan. Figure 5.50 shows three impact case with hard body impactors (steel cube and steel beam). Figure 5.51 depicts an impact case with a soft body impactor (rubber beam). The numerical images are taken at the moment, where the projectile reached the deepest penetration depth prior to rebound. The corresponding CT-scans were performed subsequently to the impact tests. The contour plots depict the damage scalar of the fibre reinforced layer of the aramid paper model. A damage value of up to 0.18 signifies the continuous damage processes caused by micro processes such as fibre segment realignment and associated local matrix damage (see chapter 3.3). A damage value between 0.18 and 1.0 indicates the rapid decrease in local aramid paper structure until failure at an damage value of 1.0.
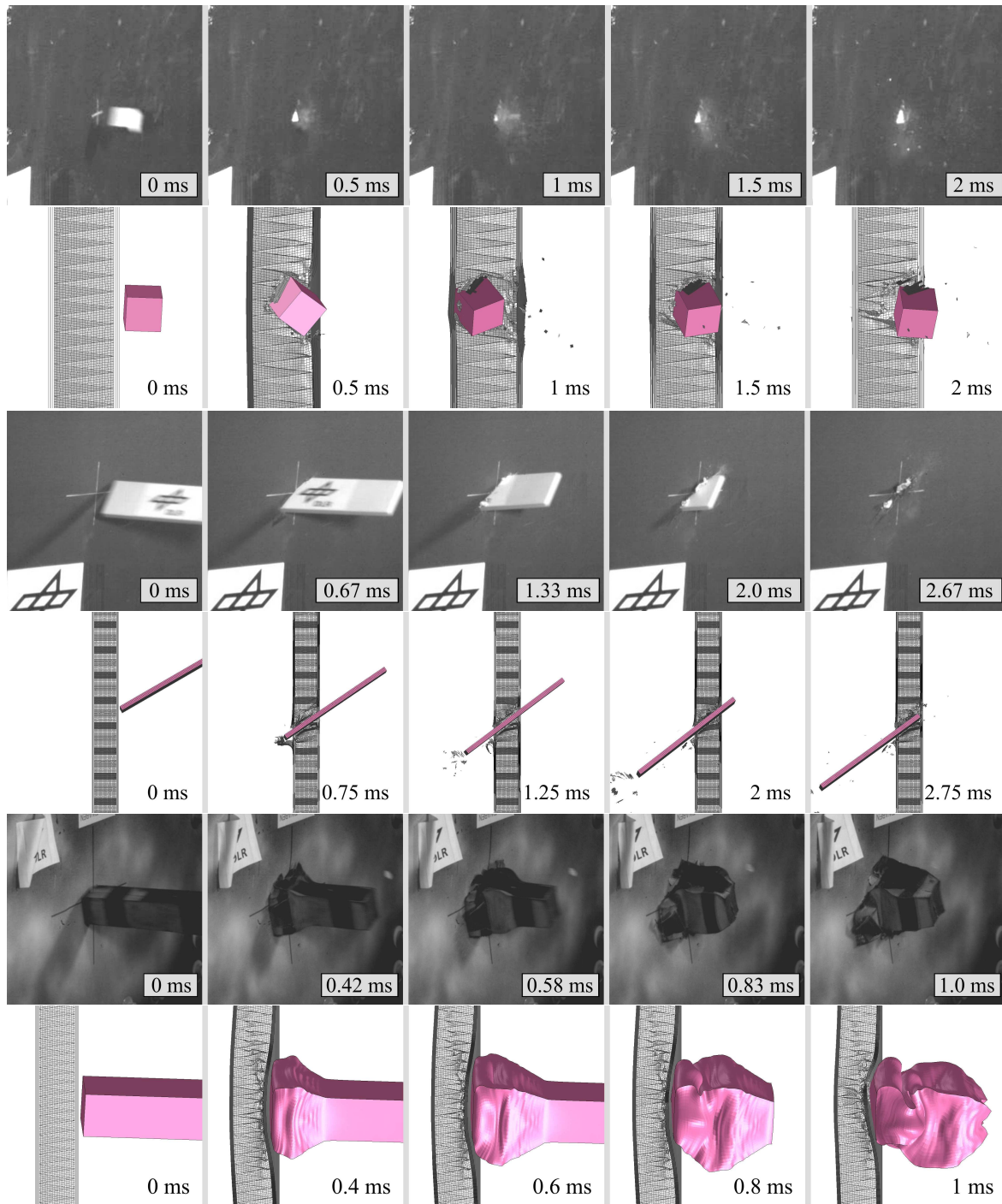
Figure 5.47.: The image sequences depict the impact event of numerical prediction and experiment in case of a 45 J steel cube impact, a 235 J steel beam impact and a 814 J rubber beam impact.
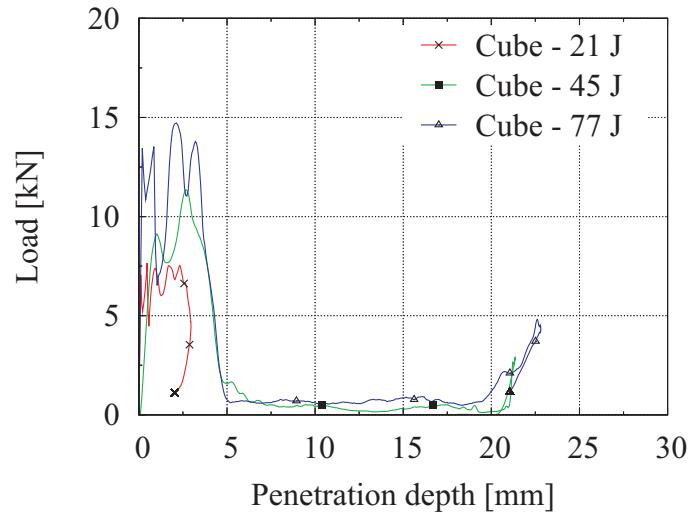
Figure 5.48.: Force vs. penetration depth curves computed for steel cube impact.
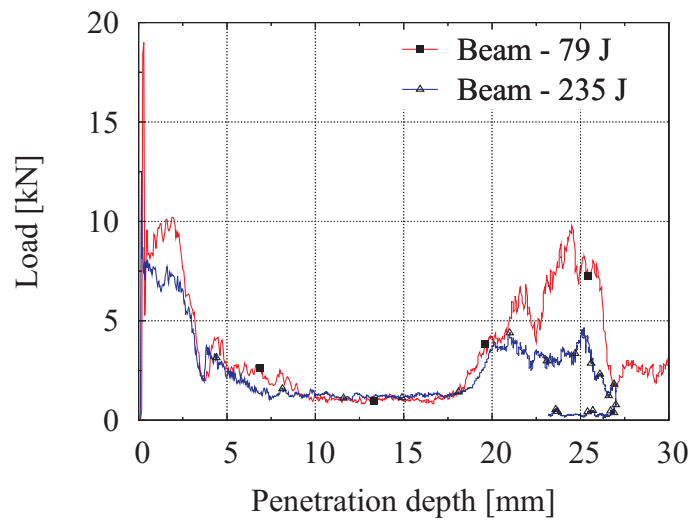
Figure 5.49.: Force vs. penetration depth curves computed for steel beam impact.

(a) Simulation (21 J)

(b) Experiment (21 J)

(c) Simulation (77 J)

(d) Experiment (77 J)

(e) Simulation (79 J)

(f) Experiment (79 J)

Figure 5.50.: Comparison of numerically predicted foldcore deformation and damage with CT-scans of high-velocity impact tests. The numerical contour plots show the damage scalar of the fibre reinforced layer in the moment where the projectile has reached the maximum penetration depth. a) Damage contour plot of a steel cube impact with 21 J b) Post-impact CT-scan (21 J steel cube impact) c) Damage contour plot of a steel cube impact with 77 J d) Post-impact CT-scan (77 J steel cube impact) e) Damage contour plot of a steel beam impact with 79 J f) Post-impact CT-scan (79 J steel beam impact).

| (a) Simulation (814 J) | (b) Experiment (814 J) |
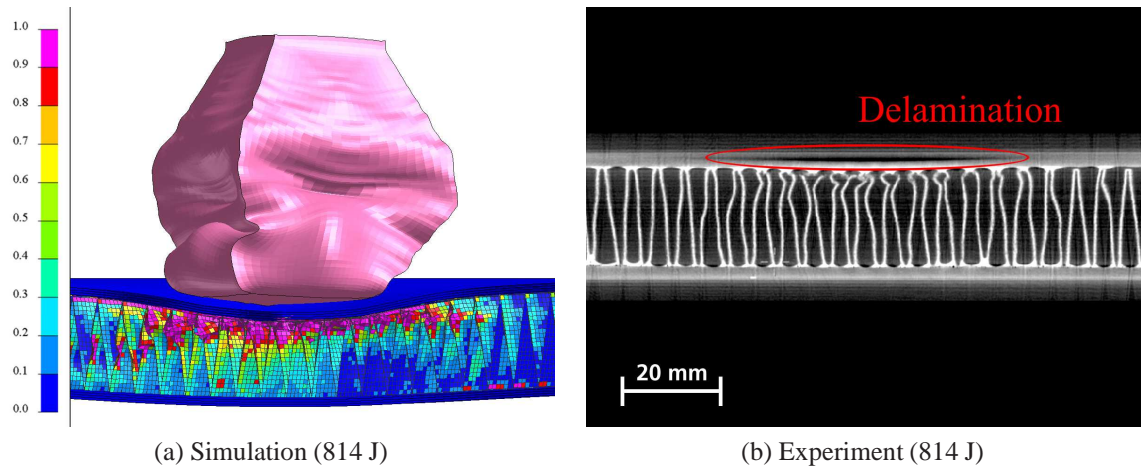
Figure 5.51.: Comparison of numerically predicted foldcore deformation and damage with CT-scans of a rubber beam impact. The numerical contour plots show the damage scalar of the fibre reinforced layer in the moment where the projectile has reached the maximum penetration depth. a) Damage contour plot of a rubber beam impact with 814 J b) Post-impact CT-scan (814 J rubber beam impact).

The numerical model of a 21 J impact of a steel cube projectile (Figures 5.50a) demonstrates local failure of the foldcore directly below the point of impact. In adjacent parts a moderate degradation is observed, which spreads to the foldcore midline and which has a extension of 3–4 times the projectiles diameter. This characteristics are roughly reflected by the CT-scan in figure 5.50b. Here the foldcore depicts sharp kinks and some fractures directly below the position of impact. The foldcore is also deformed and shows buckling in a region of about 50 mm in diameter.

The second case is a steel cube impact, where the kinetic energy of the projectile has been increased to 77 J. The numerical model in figure 5.50c predicts a fully crushed foldcore by the projectile. At the same time failure of the aramid paper is only occurs in close proximity to the projectile. This coincides with the damage pattern observed in the CT-scan as depicted in figure 5.50d. However, in the experiment extensive debonding of foldcore and inner face sheet was evident. Because of the assumed perfect bond between face sheet and core this cannot be reproduced by the numerical model. In contrast, the numerical model predicts a larger extent of failure at the upper foldcore surface where the foldcore is connected to the outer face sheet. Altogether the numerical anticipates a larger extent of damage as observed in the CT-scan of the 77 J impact.

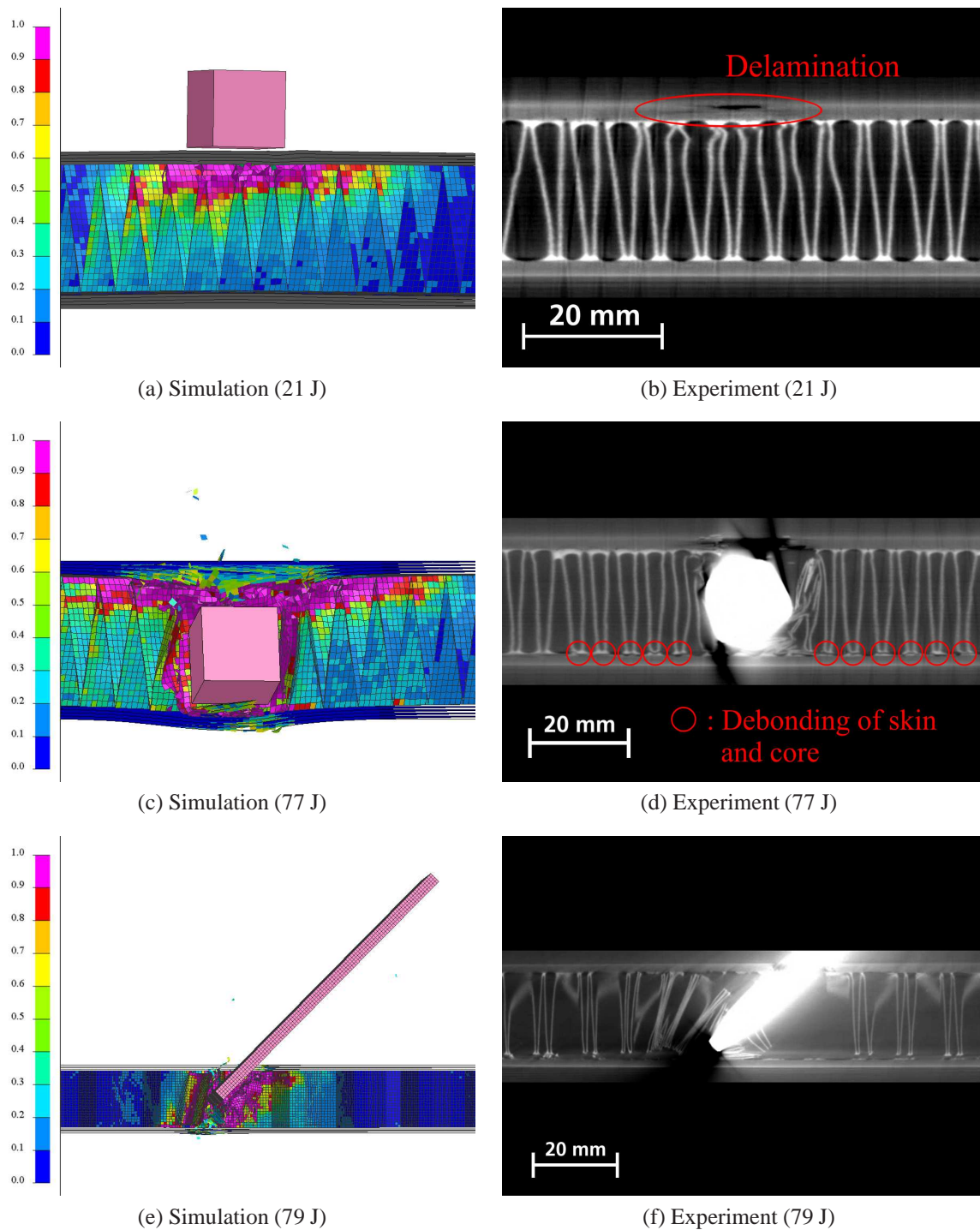Figures 5.50e and 5.50f depict the damage contour plot and CT-scan of a steel beam impact with comparable kinetic energy (79 J) as above steel cube impact. It is noted that in this case, the impact angle is $60°$. The extent of damage is marginally larger than observed in the steel cube impact with comparable kinetic energy. This is due to the shovel-like movement of the beam during the impact event, which shears the foldcore from the inner face sheet. Apart from this mechanism the damage is again localised very close to the path of the projectiles.

Similar to the previous case of a steel cube impact a difference between experiment and simulation is the neglect of face sheet-core debonding in the numerical model. Apart from that the reproduction of foldcore deformation and damge shows good agreement with the CT-scan of the experiment.

In above cases of hard body impact the numerical model indicates a very local damage in the foldcore which corresponds to the experimental observations. In figure 5.51 the behaviour of the foldcore in case of a soft body impact is depicted for simulation (5.51a) and experiment (5.51b). In case of a soft body impact the kinetic energy is absorbed by the target specimen during a time period which is considerably larger than in case of hard body impacts with comparable kinetic energy. Therefore the damage pattern of a soft body impact differs from the damage pattern of a hard body impact. In case of the rubber beam impact presented here with a kinetic energy of 814 J the numerical model shows extensive outer face sheet delamination and cell wall failure in vicinity of the outer face sheet in a diameter of about 120 mm. If compared with the CT-scan it is found that fold kinking and fracture is observed in a similar area. Furthermore the region in which the numerical model predicts moderate damage values of 0.2–0.7 roughly correlates to the region in which permanent local foldcore buckling was observed in the experiment.

Face sheet degradation and failure in the FEM model has to include several damage modes, which are either classified as intraply failure (fibre pull-out, fibre/matrix debonding, matrix cracking, fibre bridging, fibre fracture, microbuckling) or interply failure (mainly delamination between plies). The quality of the modelling of interply failure (delamination) can be well assessed by comparing the extent of delamination in the soft body impact cases, as soft body impact typically leads to extensive amounts of delamination. Figure 5.52a depicts a contour plot of the interface damage scalar of the simulation of a 814 J rubber beam impact. If compared to the CT-scan in figure 5.52b, which shows the sandwich specimens cross-section with the largest delamination diameter, it can be observed that the by the simulation predicted extent of delamination compares well with the results of the experiment. However it is noted that the FE model predicted similar delaminations zones in all three interface layers of the outer face sheet, whereas in the CT picture a single extensive delamination zone was observable. However there might exist smaller delaminations, which were not detectable due to CT scan resolution.

In order to evaluate the FE models prediction of face sheet intraply failure, simulation and experiment of hard body impact cases can be compared. Hard body impact typically shows intraply failure, whereas the amount of delamination is often small. However, the intraply failure is mainly governed by fibre fracture, which are sheared off by the edges of the hard impactor. Therefore the assessment of the intraply failure is here limited to this failure mode. In figure 5.53 the typical damage in the outer face sheet in case of a hard body impact is shown for simulation and experiment. Both demonstrate localised face sheet failure in very close proximity to the impactors path. This face sheet failure behaviour was observed in all experimental and numerical investigation of hard body impact.

In figure 5.54 the predicted kinetic and internal energies of a 68 J cube impact are depicted. At t=0 ms the initial kinetic energy of the impactor (blue colour) corresponds to the

(a) Simulation (814 J)

(b) Experiment (814 J)
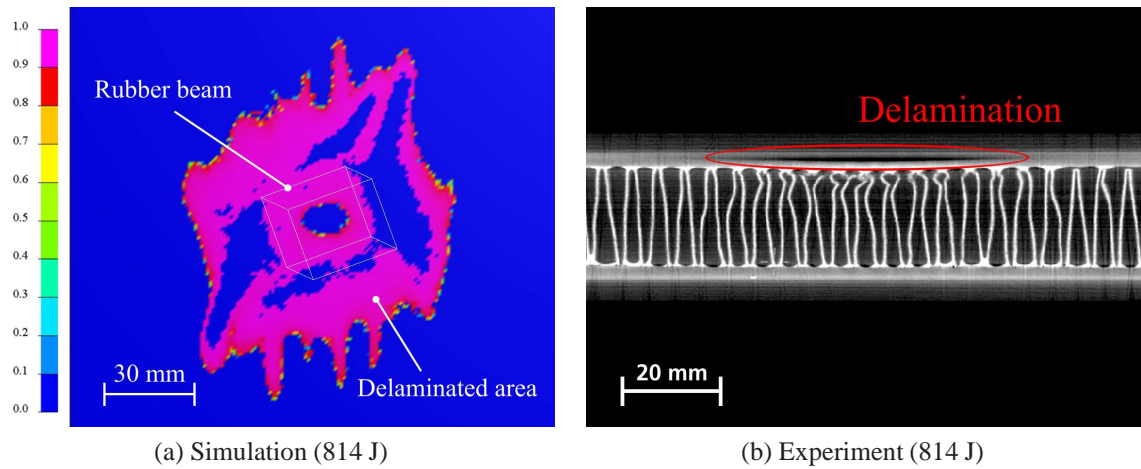
Figure 5.52.: a) Plot of the damage scalar of the interface region in the outer face sheet of the 814 J rubber beam impact b) Side view of a CT-scan showing the delaminated area of the sandwich structure impacted by a rubber beam (814 J).

(a) Simulation (235 J)

(b) Experiment (235 J)
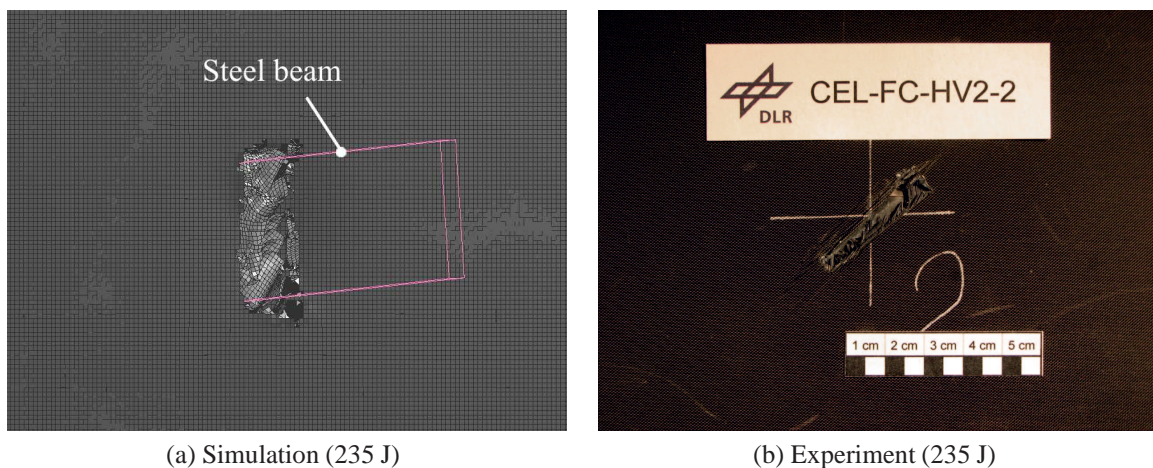
Figure 5.53.: a) Deformation plot showing the extend of eliminated elements on the outer face sheet in case of a steel bar, which penetrated the whole specimen (235 J) b) Photography of the front side of an impacted specimen (Steel bar, 235 J).

total energy. The kinetic energy decreases during penetration of outer face sheet (0–0.4 ms) and foldcore (0.4–3 ms). At t=4 ms the impactor is stopped and begins to rebound. Grey colours signify the internal (light grey) and kinetic energy (dark grey) of the face sheets. Yellow colours indicate internal (light yellow) and kinetic energy (dark yellow) energies stored by the foldcore. The purple area corresponds to the energy absorbed by frictional effects.

About 50 % of the total energy is absorbed by elastic deformation and permanent degradation of the foldcore at the time the impactor is stopped. 30-35 % of the total energy is absorbed by elastic deformation and permanent degradation of the face sheets. The remaining
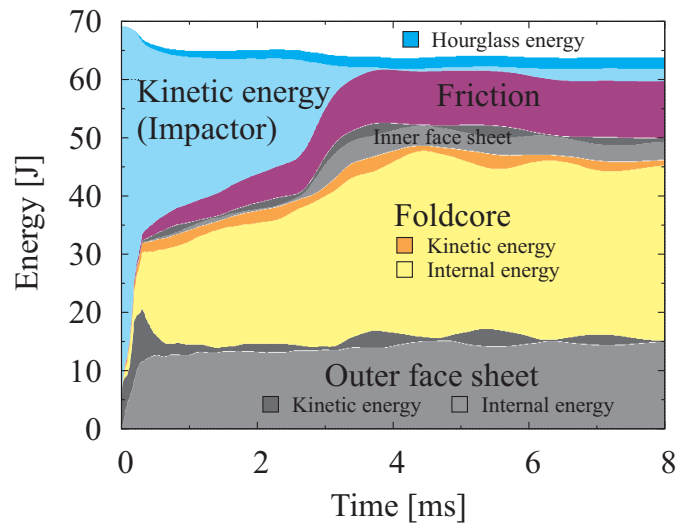
Figure 5.54.: Energies predicted by the numerical model for a 68 J impact (Cubic impactor).

energy is absorbed by friction between foldcore cell walls and also face sheets. The energy associated with hourglass modes is less than 3 % of the total energy. However there is a small drop in total energy at the beginning of the impact event (0–0.5 ms), which is not fully understood, but could be explained by energy disipated at the several contact interfaces in the model

6. Discussion

6.1. Overview

The numerical description of an aramid paper foldcore sandwich structure is a complex subject, mainly due to the heterogeneous nature of its constituents and the multiple failure mechanisms that can occur in facesheet and foldcore and their interactions. The research thesis has presented experimental research to investigate the mechanical properties of a promising foldcore base material -aramid paper- and of foldcore geometries made therefrom. Furthermore the failure mechanisms of foldcore structures with carbon composite skin subjected to different types of impact loads has been experimentally examined. This experimental work has been used to develop and assess a modelling strategy in the commercial FE code PAM-CRASH to represent various quasi-static and dynamic load cases. The FE modelling is established in a step-by-step approach, where the numerical model is in each step gradually extended and evaluated. These steps include the modelling of aramid paper, the modelling of foldcore structures made of aramid paper and the modelling of foldcore sandwich structures subjected to impact. This Chapter discusses the investigations and findings presented in this research thesis. The limitations of the experimental and numerical work are highlighted.

6.2. Investigation of aramid paper

6.2.1. Experimental determination of the mechanical properties of aramid paper

A comprehensive test programme was performed to characterise the mechanical behaviour of aramid paper. In order to provide a foundation for the constitutive modelling the elastic properties as well as degradation and failure behaviour was measured. The adopted experimental method followed in many ways approaches used in experimental investigations of traditional paper structures made from cellulose fibres [29, 51, 133]. Most experimental investigations in the literature focus on the determination of the in-plane stiffness and strength properties [58, 80, 116]. The out-of-plane properties are difficult to measure and of secondary importance, as paper behaviour is usually approximated by thin shell theory.

The elastic in-plane properties in orthogonal directions were measured using tensile coupon tests and ring crush tests. A moderate difference between the in-plane stiffnesses in machine and cross-machine directions was observed. The stiffnesses observed in tension were

considerably larger than those measured for compression. Furthermore it was noticed that the elastic properties measured in tension (coupon tests), compression (ring crush tests) and bending (beam vibration tests, provided by Baranger et al. [20]) were not conforming to the assumption of homogeneous material in thickness direction. This observation was supported by microsopic cut-images, which showed a layered setup in the paper's out-of-plane direction. The fibres were concentrated in an inner layer of about 0.2 mm thickness, whereas the outer layers were composed of a irregular pure resin film with varying thickness.

The degradation and failure mechanism were measured in tension (coupon tests) and compression (ring crush tests). In both load directions an almost instantaneous, continuous degradation of material properties was observed. In cyclic loading test it was found that this degradation is composed of both, plasticity and modulus damage. It was associated to realignment of fibres in direction of loading and (irreversible) microdamage in the resin matrix. The realignment of fibres was to a considerable extend reversible, as the fibres in the fibre layer were only partly embedded in the matrix and a large number of voids existed. Different failure mechanism for tension and compression were observed. In tension the paper fails suddenly by fracturing. In compression the specimen typically failed by instability before the material was fully degraded. However the dimension of the ring crush specimen was chosen such that the stress at which instability occured was equal to the compression strength of the material and the cylinder was crushed before it buckled. By this means a compressive strength was identified, which was assumed to be constant once paper crushing was initiated.

The in-plane shear properties were determined using thick-walled beam shear test results provided by Universität Stuttgart, Institute of Aircraft Design. The elastic and degradation properties in shear direction corresponded to above observations: the measured shear modulus was in the range expected from the in-plane moduli and in-plane Poisson's ratios discussed above. Furthermore the stress-strain-curve showed a similar continuous degradation of material properties as observed in the tensile and compressive tests. For large strains the shear stress approached a constant stress level.

However there exists a range of limitations in the experimental characterisation of mechanical properties of the aramid paper. It was difficult to identify the elastic properties as the material began to degrade at considerable low strains. Therefore the elastic properties were measured at very small strains where initial inaccuracies during test start-up could not be entirely excluded. Furthermore it was difficult to avoid structural instability in case of compression and shear loading. The compression specimen (ring crush) and shear specimen (thick-walled beam) consisted of several layers of joined paper in order to increase their stability. This might have affected their inherent material properties.

In case of the ring crush test it was also assumed that the stress at which the cylinder crushes is the maximum compressive strength of the paper material. However Uesaka [148] stated that although this approach is often used in the paper industry its reliability is limited as the results often tend to scatter significantly. Also the ring crush specimen failed by initial delamination between the paper layers and successive local buckling of the seperated parts of the cylinder wall, which was a failure of the bond between the paper layers and not of a paper layer itself. The subsequent buckling was a structural failure by instability. Therefore

it is possible that the compressive strength of a single aramid paper layer was larger than the measured value.

6.2.2. Modelling of aramid paper

Based on the experimental findings a modelling approach was developed in order to represent the aramid paper by a shell-based meso-model. In contrast to previous research works, which approximated similar materials with single layered shells [12, 14, 32, 34, 59, 76, 77, 121], the present work considered the non-uniform nature of the aramid paper in out-of-plane direction on basis of a multi-layered shell model. This approach allowed to represent the fibre rich region in the paper's centre and the resin films on the paper's surfaces by individual layers.

The elastic in-plane properties of both layers types were determined by an inverse approach from the tensile, compressive and bending stiffnesses of the whole aramid paper. It is noted that the compressive modulus of the fibre reinforced layer was calculated to be equal or even slightly below the modulus of the resin film layer depending on layer thickness. This was attributed to local buckling of aramid fibres in the fibre reinforced region which was not fully infiltrated by the resin. Due to the missing support by the matrix the fibres in these void zones carried significantly less load in compressive direction. The elastic out-of-plane properties of the layers were approximated by assuming isotropic material behaviour in the resin film layer and negligible fibre reinforcement in out-of-plane direction in the fibre reinforced layer. It is noted that the out-of-plane properties were of secondary importance as the layered shell model is based on Mindlin/Reissner plate theory.

The degradation and failure behaviour of the aramid paper was modelled by modulus damage functions, which use a single, independent variable describing the damage in each layer. The shapes of the damage functions were fitted to the in-plane degradation and failure behaviour observed in the experiments. For that purpose they considered the continuous degradation by microdamage of an aramid paper subjected to increasing loads as well as the different failure modes in tension and compression. The continuous degradation was assumed to be evenly distributed in the individual layers. The failure progression in the fibre reinforced layer was adopted to the characteristics observed in aramid fibre reinforced composites whereas the failure progression in the resin film layer followed the characteristics observed for pure phenolic resin.

In order to evaluate the shell model the tensile coupon tests and cylinder collapse test were modelled on basis of the layered shell model. The resulting stress-strain behaviour of a complete layered shell setup was able to reproduce the experimentally measured curves in tension and compression up to failure.

However, there are some intrinsic limitations of the damage model, which have to be mentioned. In case of unloading a damaged material relaxed completely to its original shape based on the reduced moduli. The model did not consider permanent deformation whereas during testing permanent deformation was observed (as for example in the cyclic tension test in figures 3.10 and 3.11 plastic deformation of 14 % to 23 % was observable). This discrepancy

was acceptable as the occurrence of unloading is insignificant for the load cases studied in this work.

The damage evolution model used depends exclusively on the deviatoric strain components. However, the brittle failure at large strains in tension could have a dependence on hydrostatic pressure.

The different damage characteristics in a specific layer were homogenised and controlled by a scalar damage parameter which proportionally reduced the modulus values. In reality a material damaged due to loading in a distinctive direction was not necessarily degraded to the same extent when loaded in a perpendicular direction. Additionally, as the damage function was isotropic, the difference in respective stress-strain relations was directly proportional to the ratio of moduli in the same directions. This proportionality contradicted to some extend the values observed in the experiments (as for example between tension behaviour in machine and cross-machine direction), which seemed to evolve differently depending on direction.

In case of tensile loading fracture formation and propagation was represented by full degradation and subsequent elimination of shell elements. However a shell corresponded to a comparatively large area whereas a fracture was typically localised to a very small region. This difference could result in an overestimation of failure, especially if multiple cracks were forming.

6.3. Investigation of aramid paper foldcores

6.3.1. Experimental determination of the mechanical properties of foldcores

An experimental characterisation of foldcore sandwich structures was performed in order to provide a sufficient basis for the evaluation of the numerical foldcore model. For that purpose the mechanical foldcore behaviour along its principal load directions (T-, TL- and TW-direction) was investigated. The foldcore behaviour was tested up to large strains, at which considerable non-linear behaviour and numerous failure modes were observable. Similar test programs were performed by Heimbs [75] who examined compression and shear properties of aramid paper and carbon composite foldcores. Research by Kintscher et al. [102, 103] also investigated aramid paper foldcores subjected to mixed load conditions. However, these material characterisations were based on different types of aramid paper and foldcore specifications and therefore provided an insufficient basis for evaluation.

The mechanical response of the experimentally investigated foldcores agreed in shape and semblance to the characteristics of above mentioned research works. The behaviour was qualitatively comparable to that of honeycomb cores, with an initial stiff response followed by a collapse response at lower stress level. However it is noted that foldcores provide additional potential to tailor the mechanical response in its principal load directions. The potential to tailor the foldcore behaviour was investigated and discussed in an optimisation study performed by Lülf [113] based on the foldcore material model developed here.

It is noted that the foldcore compression and shear tests were limited to quasi-static load cases which were believed to be reasonably representative of the deformation and failure mechanisms in a foldcore structure during an impact test. However it was thought to be possible that the response of a foldcore structure can vary if high loading rates are applied. For example, an influence of high strain rates in honeycomb sandwich structures was observed by Heimbs et al. [78]. In the present work these strain-rate effects in foldcore structures were assumed to be caused by inertial effects. Nevertheless a characterisation of rate dependent material behaviour in aramid paper and in foldcores would be a valuable study for future work.

It might also be arguable that mixed load cases on foldcore structures were not investigated. However the stress-strain response and damage characteristics in the compression and shear experiments were comparable in their principal form and shape. Therefore it was assumed that mixed load cases in general demonstrate qualitative similar stress-strain responses and damage characteristics and did not provide added data for evaluation.

In addition to above characterisation of the mechanical properties the friction between aramid paper and a range of materials was determined. These properties were necessary for a good representation of foldcores subjected to large deformation, which typically demonstrated significant interaction between their cell walls. However, the determined friction properties have to be used with caution as the presented tests only measured friction properties on the surface of the material. As discussed in section 3.2.4 the surface of aramid paper consisted purely of a resin film. However, in case of a interfolding and crushing foldcore the interacting cell wall structures might be damaged. Therefore the friction properties could also depend on the properties of exposed aramid fibres as well as on changed surface texture.

6.3.2. Modelling of aramid paper foldcores

To represent the foldcore structure with the developed aramid paper model a parametric geometry model was presented and evaluated using above discussed experimental investigation of foldcores. The parameter model was based on the mathematical description presented by Hachenberg et al. [71]. The various forms of irregularities in foldcores were considered by the so-called 'node-shaking' approach.

The thus created foldcore model was verified by several benchmark studies investigating the effect of differnt element formulations, element sizes, etc. It was found that a simple Belytschko-Tsay formulation with reduced integration was sufficient to represent a collapsing and interfolding foldcore structure, if an appropriate hourglass control was chosen. It was also observed that the accuracy of the numerical prediction is very sensitive to element size. As a consequence every change in element size from the original element size, in which the layered shell model was verified, needed to be carefully considered. To minimise this effect element size in this work were limited to a range of 1–2 mm side length.

The foldcore model was then evaluated by comparison to the previously discussed experiments on foldcore behaviour. The collapse behaviour comprising of buckling, bending and kinking of cell walls was well captured if compared to the experimentally examined cases.

The predicted strength in the modelling was shown to give adequate values comparable to the measured T-directional compressive strengths and TL- and TW-directional shear strengths. Although no strain rate dependencies were considered in the constitutive material model the numerical foldcore model predicted rate dependencies caused by inertia effects which were in tendency similar to those observed by Heimbs et al. [78].

However, there exists a number of limitations in the developed foldcore model. The representation of the irregularities by the 'node-shaking' approach basically introduced a minor random variance of nodal positions which prevented the fold cells from uniform buckling. The presented implementation of 'node-shaking' was by no means based on a physically measured quantity. Although the comparison to the 'geometry-shaking' indicated that size and form of a geometrical or a local material deviance had no large influence on the predicted results the simplified consideration of irregularies still might lead to inaccuracies in the numerical results. Furthermore 'node-shaking' was not able to capture every type of irregularity. For example the cuts in the fold edges caused by the embossing process were not adequately represented. However, in particular these cuts in the fold edges were observed to lead to the formation of fractures.

A second limitation is underestimation of the stresses which occured if a foldcore was densified during compression loading. A reason was that the cell wall of a compacted foldcore was typically permeated by many cracks and sharp kinks, whereas the cell wall parts in between were relatively undamaged. In contrast the shell model overestimated the extension of damage as it degraded the whole element. In case of densification the large number of degraded elements resulted in a considerably lower stiffnesses compared to those observed in the experiments. This effect was magnified if the shell element was eliminated. The elimination of fully degraded shell elements led to a further unnatural weakening of the compacted foldcore region, as eliminated elements were no longer considered in the computation of sliding interaction. An elimination basically led to 'vanishing' of the material represented by the element, whereas in reality the damaged material remains in the foldcore and can interact with surrounding debris through frictional contact.

6.4. Impact on foldcore structures

6.4.1. Experimental investigation of impact on foldcore sandwich structures

A series of experimental studies were conducted to investigate the behaviour of foldcore sandwich structures subjected to impact. The objective was to identify and characterise the deformation and failure mechanisms in foldcore and face sheets. The knowledge gained was used to improve the modelling of impact cases as well as for the evaluation of the modelling approach presented in this work. The nature of damage and failure caused by impact can vary significantly and depends on several different factors such as impactor properties, velocity, impact angle, impact energy, etc. Therefore, in order to provide comprehensive experimental

data a broad range of impact conditions were investigated including hard and soft body impact, impact velocities ranging from 2–125 m/s as well as impact energies ranging from 21–814 J. The experimental studies were performed in a drop tower apparatus and in a gas gun facility.

In drop tower tests the impact of a hard, spherical drop weight on foldcore sandwich structures at velocities ranging from 2 m/s to 6 m/s was investigated. These velocities were estimated on basis of a quasi-static pre-test to cause specific failure mechanism. Both the quasi-static and the low-velocity impact tests showed similar failure modes with outer face sheet penetration, core crushing and finally inner face sheet deformation and, in case of the quasi-static test, penetration. The face sheets failed by interlaminar delamination and subsequent ply fracture. The foldcore crushed until full compaction under formation of sharp kinks and fractures at face edges. The observed damage and failure was localised close to the impact region, which corresponded to observations made for similar impact conditions by Anderson and Madenci [16] and Park et al. [128].

It is noted that the stress-strain response measured in the quasi-static and low-velocity impact tests always followed a similar pattern: Two definite peak loads correlated to outer and inner face sheet failure. In between the foldcore crushed at a lower, constant load. The similarity of quasi-static and low-velocity impact response supported that low-velocity impact is generally quasi-static in nature except for localised damage, as discussed in the research papers of Dear et al. [39] and Abrate [6].

It appears that in the drop tower test the dynamic failure of the face sheets and core crushing were triggered at lower loads than in the quasi-static tests. However, the maximum deflection as observed for the 400 J test by the high-velocity camera and displacement-time sensor respectively was about 2 mm larger than the deflection at full penetration of the quasi-static test. This is unexpected, as dynamically loaded composites typically show a more brittle failure behaviour than quasi-statically loaded composites. However, the measured lower dynamic core crush loads are consistent with experimental data reported in the research thesis of M. David [38]. The observed lower failure stresses of the composite face sheets might be explained by the existence of additional boundary effects.

Another observation was that the absorbed energy measured in the drop tower tests is about 10 % less than the initial kinetic energy calculated for the impacting drop weight. This difference was thought to be caused by a range of experimental interferences such as previous deceleration of drop weight carriage, compliance of the sandwich panel's support structure, partial absorption of energy in drop weight structure and support structure, etc. It was observed in almost every drop weight test and difficult to circumvent. In the present work it was assumed that the absorbed energy calculated from the stress-strain response corresponded to the energy absorbed by the sandwich structure and therefore was taken as basis for the numerical modelling approach. However, the existence of a certain inaccuracy could not be fully excluded.

It should also be noted that the presented load case is only a generalisation of the low velocity, high mass blunt impact scenario for an aircraft fuselage. The reason for choosing a ~25 kg drop weight and spherical impactor tip was mainly the expectation that a broad range of failure modes would be caused by this drop tower setup, which were required to evaluate

the numerical model. However, the restriction to a single type of hard body impactor limited the universality of the observations to a specific type of impact.

In the gas gun tests the impact response of a foldcore sandwich structure to hard body impact (steel cubes and steel beams) and to soft body impact (rubber beams) were investigated. In the test series the energies required for characteristic damage patterns such as face sheet delamination and perforation as well as foldcore compaction and densification were determined. These critical energy levels were then used in the numerical model to evaluate the modelling approach. The load-displacement response caused by identical impactors and different kinetic energies generally followed a similar path until the energy was fully absorbed. However, considerable diffence in damage patterns were observed for hard body and soft body impact.

Hard body impactors with different geometry typically caused comparable damage patterns for similar kinetic energies. The damage was very localised and the face sheets/sandwich structure was penetrated at comparatively low velocities. Soft body impactors mainly caused delamination in the face sheets as well as compliance and crushing in the foldcore. The damage was widespread in area and the face sheet were not penetrated even at large velocities. These findings corresponded to experimental observations made by Horrigan et al. [84] for honeycomb sandwich structures.

6.4.2. Modelling of impact on foldcore sandwich structures

The foldcore meso-model presented in section 4.3 was applied to impact load scenarios as discussed in section 5.3. For that purpose the behaviours and interaction of face sheets, impactor and support had to be considered in the modelling approach. These were implemented into the model on basis of existing modelling capabilities in PAM-CRASH.

The fibre reinforced composite model of the face sheets was based on a stacked shell model approach with a continuum damage model representing in-ply failure and a cohesive interface model representing inter-ply failure. The rather complex adaption of the composite model to experimental data was realised in earlier DLR programmes and is not adressed in this work, but see publications of Johnson et al. [89, 90, 94] for further details. However, the reliability of the approach was investigated here by comparing numerical predictions based on the stacked shell model to experimental data on composite plate impact. The experimental data was taken from the research project HICAS [139]. The shapes of panel fracture and delamination predicted in this context were in good agreement with the experiments. The load-displacement responses of the impactor in simulation and experiment compared well. However, it was noted that the composite model predicted fracture initiation at a too low load level and in contrast underestimated to a certain extend the subsequent propagation of fracture and associated ply delamination.

The impact model was verified on basis of a parameter study. For that purpose, the effect of element size, impact location, target panel size and magnitude of friction on the model behaviour was estimated and the consideration of those findings in the modelling approach was discussed. It was found that the accuracy of the numerical prediction was very sensitive

to element size. This observation confirmed the conclusions made during foldcore model verification, which stated, that the element size has to be limited to a certain range (1–2 mm side length). Another observation was that impact location (with respect to the foldcore geometry) and target panel size have negligible influence on the simulation results. However this observation was made for a small, hard body impactor and might not be valid for a large, soft body impactor which usually causes considerably larger global bending of the panel. Rarely discussed in the literature is also the effect of the coefficent of friction between impactor, foldcore and face sheets on the load-displacement response and absorbed energy. The parameter study indicated that in particalur the friction behaviour of the foldcore had an influence on the computed load level.

To assess the impact model's capability numerical predictions were compared to the experimentally investigated load scenarios presented in section 5.2. In case of the drop tower test series, the experimental and numerical results demonstrated good agreement. The numerical prediction produced a good representation of the experimentally observed impact sequences: Timing and extent of characteristic failure modes such as skin penetration, foldcore crushing, slowing and stopping of the impactor, etc. were well captured for almost all investigated load cases. An exception was the 400 J impact case for which the numerical model predicted considerable inner face sheet failure in contrast to negligible inner face sheet failure observed in the experiment.

Comparison of the experimentally and numerically determined load-displacement responses yielded some differences between the predicted response and the measured response. The numerically computed penetration depths of the impactor and energies absorbed in the sandwich structure were 10–20 % larger than those observed in the experiment. The overestimation of penetration depth and absorbed energy was thought to be caused by the confinement of the dynamic load scenario to a deformable foldcore structure and idealised impactor and support. In reality a part of the initial kinetic energy was absorbed by the surrounding environment, test rig cross-head, rails, support frame, etc. , whereas in the model all energy had to be absorbed in the modelled structure: the foldcore sandwich. Therefore the energy acting on the foldcore structure was overrated in the model. The increase in absorbed energy led to an increase in penetration depth, as the load curves of the impactor typically followed similar paths until the initial kinetic energy was fully absorbed.

If the load magnitude is considered it can be observed that the model also underestimated the loads corresponding to face sheet failure to some extend, whereas the loads corresponding to foldcore crushing seemed to be well represented. Similar difference in predicted and measured peak load was found in the preliminary study (Section 5.3.2) in which the capability of the face sheet material model to represent impact on composite plates was investigated. However an additional factor might be that the support of the face sheet by the foldcore structure was underestimated by the model, which assumed considerable cell wall degradation in the foldcore close to the interface.

During the quasi-static validation tests discussed above a substantial overestimation of the damaged zone by the foldcore model was observed in case of fracture and foldcore densification. This was mainly caused by the degradation of whole elements compared to very

localised damage (sharp kinks, fracture) in the experiments. Similar overestimation of the damaged zone was seen in the low-velocity impact model, most noticeably in case of the fully degraded region below the impactor. However, these regions were in most cases considerably smaller than the densified region in the quasi-static model and therefore the effect is much less prominent in the force-displacement response. An exception was the 400 J impact, where the region below the impactor was fully compacted and the resulting overestimation of damaged zone might have contributed to the low magnitude of the predicted load at inner skin penetration.

Predictions of the numerical model were also compared to the gas gun test series investigating hard and soft body impact on foldcore sandwich structures. It is noted that no stress-strain response was measured during the high-velocity impact tests. This limited the evaluation of the numerical modelling to a comparison of the observed impact sequences and characteristic damage patterns in simulation and experiment. However as a specific damage pattern typically occured in a rather large range of impact velocities the accuracy of such an evaluation was limited. Nevertheless the correct predictions of the experimentally observed impact sequences and damage patterns indicated a good representation of damage and failure mechanics in the numerical model.

In case of hard body impact the damage was typically localised and governed by the face sheet behaviour. The energy absorbed by the foldcore was comparatively low. In contrast, soft body impact mainly caused delamination in the outer face sheet and buckling/kinking in the subjacent foldcore structure. Expansion of delamination was well predicted however the number of delaminated areas was overestimated and depended on the number of implemented delamination interfaces.

Another limitation is that the impact model was not able to capture the full extent of debonding due to the neglect of interface degradation in the model. This resulted especially for large impact energies in low-velocity impact (400 J) and high-velocity impact (hard body impact >70J) in difference between predicted and measured damage patterns. Nevertheless the numerical model showed to some extent degradation of the foldcore elements adjacent to the interface for these impact energies, which could be interpreted as 'interface debonding'.

An important finding was, that, although the material properties of the foldcore were significantly lower than those of the face sheets, the numerical model predicted that a considerable amount of kinetic impactor energy was absorbed by elastic deformation and permanent degradation of the foldcore. The energy stored in the foldcore was predicted to be 40–50 % of the total energy without considering friction energy in both low-velocity and high-velocity impact events. The main reason for the large magnitudes was the extensive foldcore deformation and degradation in large areas compared to small deformation (bending) and localised degradation in the face sheets: The face sheets were often seen to be pushed into the foldcore by the impactor. This led to comparatively widespread bending of the sandwich structure and subsequent local penetration. Bending of the sandwich structure resulted in bending of the face sheets accompanied by considerable buckling and crushing of the adjacent foldcore depending on degree of relative deformation between the face sheets. The energy stored in

the foldcore by this buckling and crushing behaviour was significantly larger than the energy stored in the face sheets due to bending.

In the presented simulations typically 15–20 % of the initial kinetic energy was dissipated due to friction. The numerically predicted energy absorbtion due to friction was highly dependent of the implemented friction parameters, as also had been observed in the previously performed parameter study in section 5.3.5. In order to provide a good estimation of the energy dissipated, the Coloumb friction of the investigated materials was determined experimentally. However the validity of the measured friction parameters was questionable, as they are based on friction between undamaged materials. In contrast, most energy due to friction were dissipated through considerably damaged foldcore cell walls and face sheets. In a damaged material the smoothness and composition of surface was changed. For example in the undamaged aramid paper, the surface consisted purely of phenolic resin whereas in the damaged paper regions aramid fibres were exposed on the surface. The coefficients of kinetic friction measured here were considered as a first approximation and it is noted that further research is required to improve the representation of friction.

7. Contributions and future research

In the following the main contributions of this research work to existing knowledge are summarised. Subsequently possible directions of future research that could address limitations and further extend the presented approaches are pointed out.

7.1. Contributions

Contributions to the knowledge of aramid paper material properties

- The in-plane stiffness and strength properties of aramid paper have been determined. In particular the properties in compression were previously unknown due to the complex interaction of material and structural behaviour in paper specimen under compression. Here, ring crush tests used in cellulose paper structures were adapted to determine the compressive stiffness and strength of aramid paper.

- A layered structure of aramid paper was identified by microscopy consisting of a fibre rich region in the paper's centre and regions of pure resin on the paper's surfaces. The different magnitudes of tensile, compressive and bending properties measured for aramid paper are caused by the layered structure. In current literature the distribution of fibres in the paper's thickness direction is assumed to be homogeneous [58, 75, 80].

- A metholodogy to derive stiffness and strength properties of the individual paper layers has been presented. The approach is based on the globally measured paper properties and the knowledge of the fundamental behaviour of pure phenolic resin and traditional aramid fibre reinforced materials.

Contributions to the numerical modelling of aramid paper

- A shell-based element material model originally used in PAM-CRASH to describe layered composite materials has been adopted to the determined aramid paper behaviour. For that purpose the stiffness and strength properties derived for the individual paper layers (fibre reinforced layer and resin film layer) have been used to define the orthotropic and elastic-damage softening behaviour of the material model. Current numerical approaches in the literature do not consider the inhomogeneous setup of the aramid paper in thickness direction [10, 34, 59, 77, 121].

- By comparison to tensile coupon and cylinder collapse tests it was shown that the modelling approach satisfactorily reproduces the relevant tensile and compressive failure mechanism.

- The limitations of the modelling approach were discussed. The main limitations are the disregard of plastic deformation, the description of damage in each layer by a single, isotropic damage scalar and the overestimation of damaged area in case of fracture.

Contributions to the knowledge of degradation and failure behaviour of foldcores subjected to quasi-static and dynamic loads

- Foldcore sandwich structures were comprehensively tested under quasi-static (compression, shear, indentation) and dynamic load conditions (low-velocity impact, high-velocity impact). A variety of characteristic deformation and failure mechanism were observed and documented. These include foldcore collapse and crushing modes until full densification as well as different cell wall fracture modes. In general the observed deformation and failure behaviour is similar to the behaviour observed for honeycomb structures. It is noted, that the existing studies on the impact response of foldcore structures tended to neglect the effect of foldcore structure and failure mechanisms as they mainly focussed on the role of the face sheets on the impact behaviour of the whole sandwich structure [16, 32, 39, 128, 138].

- In case of compression and shear loads the foldcore typically demonstrates an initial linear elastic response. If a certain peak load is reached the foldcore cell walls begin to buckle and collapse which is accompanied by a significant drop in load level. At very large compressive strains the densification of the cell wall material leads to a large increase of load level.

- Hard body impact at both low and high velocities was found to result in very localised damage and penetration of specimen at low and moderate kinetic energy levels. The main observed failure modes are the collapse, crushing and densification of the foldcore beneath the impactor as well as buckling of foldcore cells adjacent to the impact location.

- Soft body impact was observed to mainly cause delamination in the face sheets and widespread collapse and crushing in the foldcore. The target specimen was not penetrated even at high kinetic energy levels.

Contributions to the numerical modelling of foldcore structures subjected to quasi-static and dynamic loads

- A shell-based foldcore model was presented using the layered material model discussed above. The foldcore geometry is generated based on the geometric description proposed by Hachenberg et al. [71]. In order to correctly reproduce the interaction of face sheets and foldcore in impact cases an existing composite model based on a continuum damage model with cohesive interface was adopted to the carbon composite face sheets used in the experiments. A strength of this study is that the aramid paper foldcore was investigated numerically over a wide range of quasi-static and dynamic load cases, which permitted a extensive investigation of the model's validity. This is an improvement of existing numerical studies in the literature which focussed on a narrow range load cases/foldcore geometries and were therefore limited in their comprehensiveness [10, 14, 25, 33, 60, 75, 83, 118].

- The representation of irregularities in the foldcore is important in order to prevent uniform buckling of foldcore cells. It was shown that a certain measure of geometrical irregularity can be introduced by 'node-shaking' which applies a minor random variance to nodal positions. In current literature structures with cellular cores are typically assumed to be of perfect geometry.

- The foldcore model was compared to quasi-static compression and shear tests and it was demonstrated that compressive and shear strengths as well as the foldcore collapse behaviour are well represented. However it was observed that the model overestimates the damage in case of final foldcore densification.

- The foldcore model extended to impact was evaluated by comparison of the numerical predictions to the observations made in the low-velocity and high-velocity impact tests. Generally a good agreement was found, in particular the crushing behaviour of the foldcores is well represented. However the numerical model underestimates the loads for carbon/epoxy skin penetration which influences the failure sequence.

- The effects of several numerical parameters were investigated in parameter studies based on a foldcore compression case and a hard body impact case. Notable results were that the numerical model demonstrates considerable dependency on mesh size and friction parameters.

- Based on the numerical predictions it was found that a significant part (40–50 %) of the kinetic impactor energy is absorbed by the foldcore. The reason is that although the face sheet material has higher stiffness and strength the extent of deformation and damage is considerable smaller than in the foldcore. This is an important finding as it indicates that the resistance of a sandwich structure can be considerably increased by an improvement of sandwich core properties and that foldcore has the potential to improve impact resistance in aircraft sandwich structures.

7.2. Future research

This section presents potential future research that could build on the results of this research work. Some of the limitations encountered during the research and suggestions for further work are discussed in the following.

Adressing limitations of the aramid paper model

Although the modelling of aramid paper has been comprehensively examined in the present work there remain several aspects which have not been adressed. Further recommended experimental and numerical investigations on aramid paper behaviour are:

- **Consideration of strain rate effects in the material model in case of dynamic loading events:** The conducted experimental and numerical investigations covered load events with strain rates of up to 10 s^{-1}. Effect of strain rates on the material behaviour are not considered in the aramid paper model. However in particular the larger strain rates encountered during the high-velocity impact tests make this assumption arguable. To further improve the representation of aramid paper behaviour at strain rates $> 1 \text{ s}^{-1}$ it is suggested to experimentally characterise the rate dependent material behaviour (Test methods: High-speed tension tests, drop tower, Split Hopkinson pressure bar). The findings from this investigation can then be used to introduce rate dependent material behaviour to the aramid paper model.

- **Improved constitutive modelling:** The degradation of the aramid paper has been characterised by uniaxial material tests. However there may exist a dependency from mixed load conditions and the triaxiality of the material behaviour should be investigated experimentally. Furthermore substantial plasticity was observed in the experimental studies and it is suggested to expand the aramid paper material to represent plastic material behaviour. A third possibility of improvement is to substitute the isotropic damage model by an orthotropic damage model which allows to deal with multi-directional material degradation.

- **Improved representation of friction:** Kinetic friction coeffcents were measured for the investigated materials (Aramid paper, carbon composite, Aluminium, Steel) in undamaged condition. However a considerable amount of friction energy is dissipated between considerably damaged material surfaces. By consideration of this changed surface conditions it is expected that the prediction of dissipated friction energy can be improved. This will also result in a better reproduction of the impact event as a considerable part (20–25 %) of the kinetic impactor energy is typically absorbed by friction.

Investigation of the aramid paper behaviour on basis of an representative volume element (RVE) approach

Another avenue to research aramid paper properties is the use of an RVE approach, as for example discussed in the works of Böhm [26] and Kwon et al. [108]. An RVE model allows to numerically study the influence of microstructure on the macroscopic behavior of a heterogeneous composite such as the aramid paper. An RVE study could provide better understanding of the elemental micro-mechanic processes at the micro-level. This knowledge can then be used to improve the numerical aramid paper model. Furthermore it permits the identification of strategies to improve the material properties of the aramid paper.

Improvements of foldcore modelling

There are also some unanswered questions concerning the modelling of foldcore sandwich structures made from aramid paper, which have not been adressed in this work. These potential studies include:

- **Improved consideration of irregularities:** The current foldcore model accounts for irregularities only by a random offset of nodal positions, which is not based on physically measured properties. In future research the geometrical foldcore structure could be directly derived from three-dimensional CT-scans coupled with a numerical mapping algorithm. Furthermore it was observed that fracture is often initiated at cell folds, where the aramid paper material is weakened by the fold cut. As the occurrence of fracture considerably weakens the foldcore structure it is recommended to consider these initial local flaws due to pre-cutting in the material model.

- **Consideration of skin-core debonding:** In this work, debonding between core and face sheets was not considered. However in several impact load cases considerable debonding between inner face sheet and core was observed. Based on a experimental characterisation of bond properties as for example performed by Heimbs [75] the interfacial degradation and rupture could be implemented into the foldcore model.

- **Implementation of a multi-model approach:** In order to reduce computation time a coupling between different scales of foldcore models is suggested. Initial research based on the shell-based foldcore model proposed here and a solid-based foldcore model with homogenised material properties was investigated in the research project CELPACT [92]. Large reductions in computation time are expected in particular for load cases which can be partitioned in a small region where damage occurs with detailed fine scale model and a large region away from the damage zone based on a simplified large scale model.

Foldcore geometry optimisation

A potential future application is the possibility to optimise foldcore structures to certain load cases based on a numerical procedure. The aramid paper foldcore model presented here was used by Lülf [113] to investigate the feasibility of such an approach. It was shown that there is considerable potential to improve foldcore geometries to load states such as foldcore compression, shear and hard body impact. In future research this approach could be adopted to optimise complex foldcore structures to load cases required by specific design specifications.

Appendix A.

Newton-Raphson method

In section 3.4.3 on pages 47ff. a multi-dimensional Newton-Raphson method was used to compute the stiffnesses E_{Fr}^T, E_{Fr}^C and E_{Film} and the position of the neutral line $\overline{z}$. A comprehensive introduction to Newton methods is given in the textbook of Deuflhard [40]. In the following the iterative solution of the two-dimensional nonlinear equation system on basis of the Newton-Raphson method is briefly summarised. Principially, the roots of an equation system with the functions $f_1(x_1, x_2)$ and $f_2(x_1, x_2)$ can be solved iteratively using

$$\mathbf{x}^{(n+1)} = \mathbf{x}^{(n)} - \mathbf{J}_n^{-1}\mathbf{F}\left(\mathbf{x}^{(n)}\right), \qquad n = 0, 1, \cdots, \tag{A.1}$$

where J_k is the Jacobean matrix. The vectors $\mathbf{x}^{(n)}$ and $\mathbf{F}\left(\mathbf{x}^{(n)}\right)$ are defined as

$$\mathbf{x} = \begin{pmatrix} x_1 \\ x_2 \end{pmatrix} \quad \text{and} \quad \mathbf{F}\left(\mathbf{x}\right) = \begin{pmatrix} f_1(x_1, x_2) \\ f_2(x_1, x_2) \end{pmatrix}. \tag{A.2}$$

In the presented case the inverse of the Jacobean matrix J_n^{-1} is given by

$$J_n^{-1} = \frac{1}{\frac{df_1}{dx_2}\frac{df_2}{dx_1} - \frac{df_1}{dx_1}\frac{df_1}{dx_1}} \begin{pmatrix} -\frac{df_2}{dx_2} & \frac{df_1}{dx_2} \\ \frac{df_2}{dx_1} & -\frac{df_1}{dx_1} \end{pmatrix}. \tag{A.3}$$

Using above equations, equation A.1 can be solved if the functions $f_1(x_1, x_2)$ and $f_2(x_1, x_2)$ and their partial derivatives as well as initial estimations $x_1^{(0)}$ and $x_2^{(0)}$ for the roots are known. To provide an equation system and derivatives similar to the one presented above equations 3.9 and 3.10 on pages 50f. were used to eliminate the variables E_{Fr}^T and E_{Fr}^C from equations 3.8 and 3.11. The resulting equations

$$
\begin{aligned}
f_1 &= 4\left(E_{Paper}^T - E_{Paper}^C\right)\overline{z}^2 - 4\left(E_{Paper}^T + E_{Paper}^C\right)t_{Fr}\overline{z} + \left(E_{Paper}^T - E_{Paper}^C\right)t_{Fr}^2,
\end{aligned}
$$

$$
\begin{aligned}
f_2 &= \left(4t_{Film}^3 t_{Fr} + 6t_{Film}^2 t_{Fr}^2 + 3t_{Film}t_{Fr}^3 + 12t_{Film}t_{Fr}\overline{z}^2\right)\left(E_{Paper}^F - E_{Film}\right) + \cdots \\
&\quad + \left(\frac{t_{Fr}}{2} - \overline{z}\right)^3\left(2E_{Paper}^F t_{Fr} - 2E_{Paper}^T(2t_{Film} + t_{Fr}) + 4E_{Film}t_{Film}\right) + \cdots \\
&\quad + \left(\frac{t_{Fr}}{2} + \overline{z}\right)^3\left(2E_{Paper}^F t_{Fr} - 2E_{Paper}^C(2t_{Film} + t_{Fr}) + 4E_{Film}t_{Film}\right). \tag{A.4}
\end{aligned}
$$

Table A.1.: Elastic layer properties determined by the Newton-Raphson-method.

Orientation	E_{Fr}^T [GPa]	E_{Fr}^C [GPa]	E_{Film} [GPa]	$\overline{z}$ [mm]
MD	9.2	5.1	4.71	0.0108
CD	8.3	4.7	4.67	0.0105

have two unknown variables E_{Film} and $\overline{z}$. The derivatives of functions f_1 and f_2 then were

$$\frac{df_1}{dE_{Film}} = 0,$$

$$\frac{df_1}{d\overline{z}} = 8\left(E_{Paper}^T - E_{Paper}^C\right)\overline{z} - 4\left(E_{Paper}^T + E_{Paper}^C\right)t_{Fr},$$

$$\frac{df_2}{dE_{Film}} = -4t_{Film}^3 * t_{Fr} - 6t_{Film}^2 t_{Fr}^2 - 2t_{Film}t_{Fr}^3 \qquad \text{and}$$

$$\begin{aligned}
\frac{df_2}{d\overline{z}} = \ & 24t_{Film}t_{Fr}\left(E_{Paper}^F - E_{Film}\right)\overline{z} + \cdots \\
& + \ 3\left(\frac{t_{Fr}}{2} - \overline{z}\right)^2\left(2E_{Paper}^F t_{Fr} - 2E_{Paper}^T(2t_{Film} + t_{Fr}) + 4E_{Film}t_{Film}\right) + \cdots \\
& + \ 3\left(\frac{t_{Fr}}{2} + \overline{z}\right)^2\left(2E_{Paper}^F t_{Fr} - 2E_{Paper}^C(2t_{Film} + t_{Fr}) + 4E_{Film}t_{Film}\right). \quad \text{(A.5)}
\end{aligned}$$

With equations A.4 and A.5 applied to relation A.1 the values of E_{Film} and $\overline{z}$ were iteratively determined. For that purpose a routine was written in Fortran 90. The global paper stiffness properties E_{Paper}^T, E_{Paper}^C and E_{Paper}^F were corresponding to the magnitudes given in table 3.11 on page 45. The layer thicknesses t_{Film} and t_{Fr} were equal to 0.05 mm and 0.2 mm respectively. The initial estimations adopted for $E_{Film}^{(0)}$ and $\overline{z}^{(0)}$ were 3.8 GPa and 0.01 mm. With the determined magnitude of E_{Film} the values of E_{Fr}^T and E_{Fr}^C were calculated from equations 3.9 and 3.10. The thus computed magnitudes of the elastic properties are summarised in table A.1.

Appendix B.

Model setup in PAM-CRASH

The present work has been realised using the explicit solver PAM-CRASH in order to model quasi-static and dynamic load cases on foldcore structures. PAM-CRASH is provided by the ESI Group and is one of several commercially available explicit FE-codes. A finite element simulation is typically composed of pre-processing, solution and post-processing phase. The sequence of these phases as adopted in the presented work is schematically depicted in figure B.1. Commonly, the numerical model was generated in the pre-processing phase and then numerically solved in the solution phase. During post-processing the numerical results were graphically and tabularly interpreted.

PRE-PROCESSOR

As illustrated in figure B.1 the pre-processing in this work was split into two steps. In the first step the numerical mesh was generated on basis of a parameter script, which was developed within the scope in this work using the ANSYS parameter design language (*apdl*) and the ANSYS pre-processor. The *apdl* programming language allowed to build the model in terms of variables. The *apdl* script can use all ANSYS commands as part of the scripting language and also has access to vector operations and numerical routines such as branching and looping. Several *apdl* script files were programmed in order to generate the foldcore sandwich structures investigated in this work. The script generated a *cdb* file (ANSYS input file format) as output, which stored nodal coordinates and the respective assignment of elements. In this work primarily four-point-quadrangular shell elements and eight-point-hexagonal brick elements were used to represent the foldcore sandwich structure, support frames and projectiles. The *cdb* file was transformed to a *pc* file (PAMCRASH input file format) on basis of an available cdb2pc script written in perl programming language.

In the second step the necessary simulation parameters were added to the *pc* file via the PAMCRASH pre-processor. These included definitions of load conditions, constraint conditions, bond interfaces, model organisation, material models and composite ply models (which are a kind of sub-class of material models). In the present work the input parameters for a model 'NAME' were typically organised in a main file (NAME_main.pc), a material file (NAME_parts.inp), a file defining the boundary conditions (NAME_BC.inp) and a file containing all nodal and mesh information (NAME.pc). In the main file the global simulation parameter and the file structure were assigned. The part file included the definitions of the material
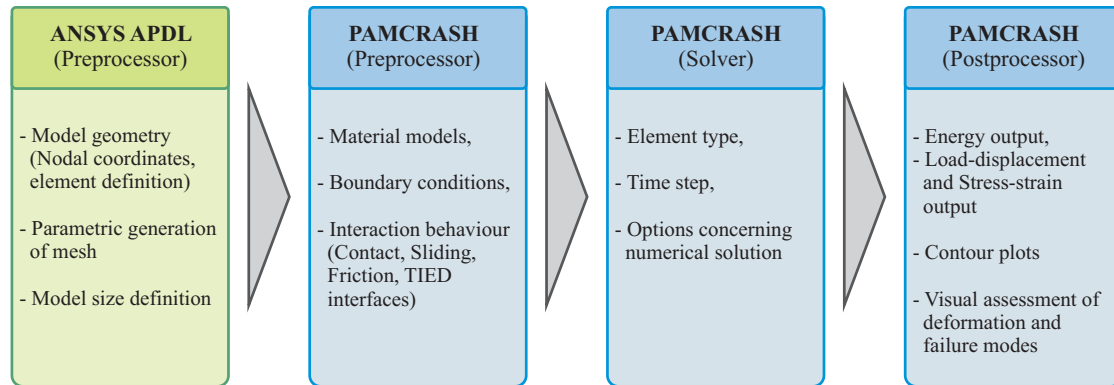
Figure B.1.: Basic scheme of the finite element procedure adopted in this work.

Table B.1.: Consistent set of unit employed in this work.

Length unit:	1	[mm]
Time unit:	1	[ms]
Mass unit:	1	[kg]
Force unit:	1	[kN]
Acceleration of gravity:	9.81E+03	[mm/ms^2]
Young's modulus of aluminium:	70	[GPa]
Yield stress of aluminium:	0.052	[GPa]
Density of aluminium:	2.7E-06	[kg/mm^3]

properties and the model organisation in different parts. It is noted that a consistent set of units was used as illustrated in table B.1. The boundary condition file specified the load and displacement constraints acting on the model as well as the contact and bond interactions. The file containing the nodal and mesh information was sometimes divided into several files to allow for reasonable access and editing options of model sub-structures.

SOLVER

The individual simulation jobs were executed at the DLR Beowulf cluster system with 13 nodes which add up to a total of 28 64bit AMD Opteron CPU's. The cluster system was accessed with the open source terminal emulator *PuTTy* which acted as a remote client for the SSH computer protocol. The executed simulation jobs ran on one to four processors with mesh sizes of up to 10^6 elements. Jobs using one or two CPU's generally ran with a 'Shared memory parallel' (SMP) method, where the CPU's shared the same memory. Jobs requiring more than two CPU's were parallelised with the 'Distributed memory parallel' (DMP) method, where the individual CPU relied on its own respective memory area. The quasi-static models in this work used the PAMCRASH solver version 2006.0.2, whereas the dynamic impact models

were realised with version 2009. All models were computed with single precision, which was signified the IEEE-754 32-bit format.

The employed explicit dynamic finite element formulation is generally suitable for modelling brief, transient dynamic events such as impact problems and is also very efficient for highly nonlinear problems. However, it is noted that the explicit solution scheme can only reproduce a very brief model time period with acceptable accuracy compared to a implicit solution scheme. The model time period usually measures in the domain of miliseconds. In this work the time period of the implemented quasi-static simulations ranged between 50–100 ms with time steps of about 10^{-4} ms whereas for the examined dynamic cases the modelled time periods ranged between 10–15 ms in case of drop tower models and 1–3 ms in case of gas gun models.

POSTPROCESSOR

After completion of the numerical processing of the FE model the results were evaluated, which as done interactively using the PAMCRASH visual environment, which read the binary output database files .THP and .DSY. The .THP file contained information on the model (global) time history. The mesh file (.DSY) recorded the output of nodal and elemental variables. The output data as stored at defined time intervals with the time interval of the mesh file usually being considerably larger than the time interval of the time history file.

On the basis of the output the model was compared and evaluated to analytical and experimental results. The output also offered insight into the mechanical and phenomenological behaviour of the investigated structures. Typical forms of output were curve plots which related two measured variables to each other as for example stress, forces, strain, displacement, energy, time, damage information. Additionally geometry and contour plots were provided, which gave an easily accessible overview on structure deformation and in case of contour plots an insight into the global geometrical evolution of a defined variable.

Bibliography

[1] Engineering mehrfunktionaler Integralstrukturen CFK-Rumpf (EMIR), 2003–2007.

[2] Coordination Action on Advanced Sandwich Structures in the Transportation Industry (SANDCORE). European Research Project, 2004-2006.

[3] Cellular Structures for Impact Performance (CELPACT). European Research Project, 2006-2009.

[4] Developing Lightweight Modules for Transport Systems Featuring Efficient Production and Lifecycle Benefits at Structural and Functional Integrity using Risk based Design (DE-LIGHT). European Research Project, 2006-2010.

[5] Beechcraft Premier Ia - Full Brochure. http://www.hawkerbeechcraft.com, 2011.

[6] S. Abrate. Localized impact on sandwich structures with laminated facings. *Applied Mechanics Reviews*, 50(2):69–82, 1997.

[7] S. Abrate. *Impact on Composite Structures*. Cambridge University Press, 1998.

[8] S. Abrate. Modeling of impacts on composite structures. *Composite Structures*, 51(2):129–138, 2001.

[9] R. Aitken. *Damage due to Soft Body Impact on Composite Sandwich Aircraft Panels*. PhD thesis, University of Auckland, 2000.

[10] L. Aktay. *Improved Simulation Techniques for Modelling Impact and Crash Behaviour of Composite Structures*. PhD thesis, Universität Stuttgart, 2010.

[11] L. Aktay, A. F. Johnson, and M. Holzapfel. Prediction of impact damage on sandwich composite panels. *Computational Materials Science*, 32(3-4):252–260, 2005.

[12] L. Aktay, A. F. Johnson, and B.-H. Kröplin. Numerical modelling of honeycomb core crush behaviour. *Engineering Fracture Mechanics*, 75:2616–2630, 2008.

[13] O. Allix and P. Ladevèze. Interlaminar interface modelling for the prediction of delamination. *Composite Structures*, 22(4):235–242, 1992.

[14] Y. Aminanda, B. Castanié, J.-J. Barrau, and P. Thevenet. Experimental analysis and modeling of the crushing of honeycomb cores. *Applied Composite Materials*, 12:213–227, 2005.

[15] Y. Aminanda, B. Castanié, J.-J. Barrau, and P. Thevenet. Experimental and numerical study of compression after impact of sandwich structures with metallic skins. *Composites Science and Technology*, 69(1):50–59, 2009.

[16] T. Anderson and E. Madenci. Experimental investigation of low-velocity impact characteristics of sandwich composites. *Composite Structures*, 50(3):239–247, 2000.

[17] T. A. Anderson. An investigation of SDOF models for large mass impact on sandwich composites. *Composites Part B: Engineering*, 36(2):135 – 142, 2005.

[18] M. C. Andrews, D. Lu, and R. J. Young. Compressive properties of aramid fibres. *Polymer*, 38(10):2379–2388, 1997.

[19] ASTM E9-09. Standard test methods of compression testing of metallic materials at room temperature.

[20] E. Baranger, C. Cluzel, P. A. Guidault, and O. Allix. Modelling of the behaviour of aramid folded cores up to global crushing. In *17th International Conference on Composite Materials (ICCM)*, Edinburgh, UK, 2009.

[21] E. Baranger, C. Cluzel, D. Winterberger, M. Klaus, S. Fischer, S. Kilchert, A. F. Johnson, S. Heimbs, and P. Middendorf. CELPACT D31-2: Baseline Composite and CHC Core Properties. In *Cellular Structures for Impact Performance (CELPACT), Contract No.: FP6-031038*. Sixth Framework Programme FP6-2005-Aero-1, 2008.

[22] T. Belytschko and I. Leviathan. Projection schemes for one point quadrature shell elements. *Computer Methods for Applied Mechanics and Engineering*, 115:277–286, 1994.

[23] T. Belytschko, J. I. Lin, and C. Tsay. Explicit algorithms for the nonlinear dynamics of shells. *Computer methods for applied mechanics and engineering*, 42:225–251, 1984.

[24] T. Belytschko, B. L. Wong, and H. Chiang. Advances in one point quadrature shell elements. *Computer Methods for Applied Mechanics and Engineering*, 96:93–107, 1992.

[25] T. Besant, G. A. O. Davies, and D. Hitchings. Finite element modelling of low velocity impact of composite sandwich panels. *Composites Part A: Applied Science and Manufacturing*, 32(9):1189 – 1196, 2001.

[26] H. J. Böhm. A Short Introduction to Basic Aspects of Continuum Micromechanics. Ilsb report 206, Institute of Lightweight Design and Structural Biomechanics, Vienna University of Technology, 1998.

[27] T. Bitzer. *Honeycomb Technology*. Chapman & Hall, 1997.

[28] B.J. Briscoe and F. Motamedi. The ballistic impact characteristics of aramid fabrics: The influence of interface friction. *Wear*, 158(1-2):229–247, 1992.

[29] J. A. Bristow and P. Kolseth. *Paper - Structure and Properties*. International fiber science and technology series. M. Dekker, 1986.

[30] I. F. Brown and C. J. Burgoyne. The friction and wear of Kevlar 49 sliding against aluminium at low velocity under high contact pressures. *Wear*, 236(1-2):315–327, 1999.

[31] J. A. Brydson. Phenolic Resins. In J. A. Brydson, editor, *Plastic Materials*, pages 635–667. Elsevier, 1999.

[32] B. L. Buitrago, C. Santiuste, S. Sánchez-Sáez, E. Barbero, and C. Navarro. Modelling of composite sandwich structures with honeycomb core subjected to high-velocity impact. *Composite Structures*, 92(9):2090–2096, 2010.

[33] B. Castanié, C. Bouvet, Y. Aminanda, J.-J. Barrau, and P. Thevenet. Modelling of low-energy impact on Nomex honeycomb sandwich structures with metallic skins. *International Journal of Impact Engineering*, 35(7):620–634, 2008.

[34] A. Chawla, S. Mukherjee, D. Kumar, T. Nakatani, and M. Ueno. Prediction of crushing behaviour of honeycomb structures. *IJCrash*, 8(3):229–235, 2003.

[35] J. Christopherson, M. Mahinfalah, G. Nakhaie Jazar, and M. Rastgaar Aagaah. An investigation on the effect of a small mass impact on sandwich composite plates. *Composite Structures*, 67(3):299–306, 2005.

[36] M. A. Crisfield, Y. Mi, G. A. O. Davies, and H. B. Hellweg. Finite element methods and the progressive failure modelling of composite structures. In *Computational Plasticity-Fundamentals and Applications (CIMNE)*, pages 239–254, Barcelona, Spain, 1997.

[37] I. M. Daniel and O. Ishai. *Engineering Mechanics of Composite Materials*. Oxford University Press, 2006.

[38] M. David. *Experimental and numerical investigation of composite energy absorbers under dynamic loading*. PhD thesis, Universität Stuttgart, in preperation.

[39] J.P. Dear, H. Lee, and S.A. Brown. Impact damage processes in composite sheet and sandwich honeycomb materials. *International Journal of Impact Engineering*, 32(1-4):130–154, 2005.

[40] P. Deuflhard. *Newton Methods for Nonlinear Problems*. Springer, 2004.

[41] R. M. Digilov. Flexural vibration test of a cantilever beam with a force sensor: Fast determination of Young's modulus. *European Journal of Physics*, 29:589–597, 2008.

[42] DIN 53134:2005-4. Prüfung von Papier und Pappe - Bestimmung des Ringstauchwiderstandes.

[43] DIN EN ISO 1924-2:2008. Paper and board – determination of tensile properties, part 2: Constant rate of elongation method.

[44] K. Drechsler, P. Middendorf, B. Van den Broucke, and S. Heimbs. Advanced composite materials - technologies, performance and modelling. In *Course on emerging techniques for damage prediction and failure analysis of laminated composite structures*, Cachan, France, 2007.

[45] DuPont. *Technical Guide - KEVLAR Aramid Fiber*, 2009.

[46] R. E. Dyke and G. A. Hrinda. Structural design for a Neptune aerocapture mission. In *AIAA Atmospheric Flight Mechanics Conference and Exhibit*, Providence, Rhode Island, USA, 2004.

[47] ESI Group. *PAM-Crash 2000 Theory Notes*, 2000.

[48] ESI Group. *PAM-Crash 2009 Solver Notes Manual*, 2009.

[49] ESI Group. *PAM-Crash 2009 Solver Reference Manual*, 2009.

[50] C. Fellers. Edgewise Compression Strength of Paper. In *Handbook of Physical and Mechanical Testing of Paper and Paperboard*. M. Dekker, 1983.

[51] C. Fellers and D. W. Coffin. Paper: Strength and Stiffness. In J. K. H. Buschow, editor, *Encyclopedia of Materials: Science and Technology*, pages 6720–6725. Pergamon, 2001.

[52] J. K. Fink. *High Performance Polymers*. W. Andrew Inc., 2008.

[53] S. Fischer and K. Drechsler. Aluminium foldcores for sandwich structure application. In *Cellular Metals for Structural and Functional Applications (CELLMET)*, Dresden, Germany, 2008.

[54] S. Fischer, K. Drechsler, S. Kilchert, and A. Johnson. Mechanical tests for foldcore base material properties. *Composites: Part A*, 40(12):1941–1952, 2009.

[55] S. Fischer, S. Heimbs, S. Kilchert, M. Klaus, and C. Cluzel. Sandwich structures with folded core: Manufacturing and mechanical behaviour. In *SAMPE Europe 30st International Technical Conference*, Paris, France, 2009.

[56] D. Flanagan and T. Belytschko. A uniform strain hexahedron and quadrilateral with orthogonal hourglass control. *International Journal of Numerical Methods for Engineering*, 17:679–706, 1981.

[57] M. Flemming, G. Ziegmann, and S.Roth. *Faserverbundbauweisen: Fasern und Matrices*. Springer, 1995.

[58] C. C. Foo, G. B. Chai, and L. K. Seah. Mechanical properties of Nomex material and Nomex honeycomb structure. *Composite Structures*, 80:588–594, 2007.

[59] C. C. Foo, G. B. Chai, and L. K. Seah. A model to predict low-velocity impact reponse and damage in sandwich composites. *Composite Science and Technology*, 68:1348–1365, 2008.

[60] C.C. Foo, L.K. Seah, and G.B. Chai. A modified energy-balance model to predict low-velocity impact response for sandwich composites. *Composite Structures*, 93(5):1385–1393, 2011.

[61] Herbert Funke. *Systematische Entwicklung von Ultra-Leichtbaukonstruktionen in Faserverbund-Wabensandwichbauweise am Beispiel eines Kleinflugzeuges*. PhD thesis, Universität-Gesamthochschule Paderborn, 2001.

[62] S. Georgiadis, A. J. Gunnion, R. S. Thomson, and B. K. Cartwright. Bird-strike simulation for certification of the Boeing 787 composite moveable trailing edge. *Composite Structures*, 86(1-3):258–268, 2008.

[63] W. Goldsmith and D. L. Louie. Axial perforation of aluminum honeycombs by projectiles. *International Journal of Solids and Structures*, 32(8-9):1017–1046, 1995.

[64] W. Goldsmith and J. L. Sackman. An experimental study of energy absorption in impact on sandwich plates. *International Journal of Impact Engineering*, 12(2):241–262, 1992.

[65] M. Grediac. A finite element study of the transverse shear in honeycomb cores. *International Journal of Solids and Structures*, 30(13):1777–1788, 1993.

[66] L. Greve and A.K. Pickett. Delamination testing and modelling for composite crash simulation. *Composites Science and Technology*, 66(6):816–826, 2006.

[67] M. Guida, F. Marulo, M. Meo, A. Grimaldi, and G. Olivares. SPH - Lagrangian study of bird impact on leading edge wing. *Composite Structures*, 93(3):1060–1071, 2011.

[68] N. Gupta. *Characterisation of Syntactic Foams and their Sandwich Composites: Modelling and Experimental Approaches*. PhD thesis, Louisiana State University, 2003.

[69] N. K. Gupta, G. S. Sekhon, and P. K. Gupta. A study of fold formation in axisymmetric axial collapse of round tubes. *International Journal of Impact Engineering*, 27(1):87–117, 2002.

[70] N. K. Gupta and R. Velmurugan. Consideration of internal folding and non-symmetric fold formation in axisymmetric axial collapse of round tubes. *International Journal of Solids and Structures*, 34(20):2611–2613, 1997.

[71] D. Hachenberg, C. Mudra, and M. Nguyen. Folded structures - An alternative sandwich core material for future aircraft concepts. In *Deutscher Luft- und Raumfahrtkongress (DGLR)*, München, Germany, 2003.

[72] A.G. Hanssen, Y. Girard, L. Olovsson, T. Berstad, and M. Langseth. A numerical model for bird strike of aluminium foam-based sandwich panels. *International Journal of Impact Engineering*, 32(7):1127–1144, 2006.

[73] T. Haraldsson, C. Fellers, and P. Kolseth. A method for measuring the creep and stress-strain properties of paperboard in compression. *Journal of pulp and paper science*, 20(1):J14–J20, 1994.

[74] J. Hecht. Ermittlung der mechanischen Kennwerte gefalteter Kernstrukturen aus Folien verschiedener Metalle. Master's thesis, Universität Stuttgart, Institute of Aircraft Design, 2006.

[75] S. Heimbs. *Sandwichstrukturen mit Wabenkern: Experimentelle und numerische Analyse des Schädigungsverhaltens unter statischer und kurzzeitdynamischer Belastung.* PhD thesis, Technische Universität Kaiserslautern, 2008.

[76] S. Heimbs, J. Cichosz, M. Klaus, S. Kilchert, and A.F. Johnson. Sandwich structures with textile-reinforced composite foldcores under impact loads. *Composite Structures*, 92(6):1485–1497, 2010.

[77] S. Heimbs, P. Middendorf, S. Kilchert, A. F. Johnson, and M. Maier. Experimental and numerical analysis of composite folded sandwich core structures under compression. *Applied Composite Materials*, 14:363–377, 2007.

[78] S. Heimbs, S. Schmeer, P. Middendorf, and M. Maier. Strain rate effects in phenolic composites and phenolic-impregnated honeycomb structures. *Composites Science and Technology*, 67:2827–2837, 2008.

[79] A. S. Herrmann, P. C. Zahlen, and I. Zuardy. Sandwich Structures Technology in Commercial Aviation. In *Proceedings of the 7th International Conference on Sandwich Structures (ICSS-7)*, Aalborg, Denmark, August 29-31 2005.

[80] F. Hähnel and K. Wolf. Evaluation of the material properties of resin-impregnated nomex paper as basis for the simulation of the impact behaviour of honeycomb sandwich. In *Proceedings of the 3rd International Conference on Composites Testing and Model Identification (CompTest)*, Porto, Portugal, 2006.

[81] M. J. Hinton, A. S. Kaddour, and P. D. Soden. *Failure Criteria in Fibre Reinforced Polymer Composites: The World-Wide Failure Exercise*. Elsevier, 2004.

[82] S.-T. Hong, J. Pan, T. Tyan, and P. Prasad. Quasi-static crush behavior of aluminum honeycomb specimens under compression dominant combined loads. *International Journal of Plasticity*, 22(1):73–109, 2006.

[83] M. S. Hoo Fatt and D. Sirivolu. A wave propagation model for the high velocity impact response of a composite sandwich panel. *International Journal of Impact Engineering*, 37(2):117–130, 2010.

[84] D. P. W. Horrigan, R. R. Aitken, and G. Moltschaniwskyj. Modelling of crushing due to impact in honeycomb sandwiches. *Journal of Sandwich Structures and Materials*, 2(2):131–151, 2000.

[85] T. J. R. Hughes, M. Cohen, and M. Haroun. Reduced and selective integration techniques in finite element analysis of plates. *Nuclear engineering and design*, 46:203–222, 1978.

[86] T. J. R. Hughes and T. E. Tezduyar. Finite element based upon Mindlin plate theory with particular reference to the four-node bilinear isoparametric element. *Journal of Applied Mechanics*, 48:587–591, 1981.

[87] A. Idlbi, M. Karama, and M. Touratier. Comparison of various laminated plate theories. *Composite Structures*, 37:173–184, 1997.

[88] ISO 9895:2008. Paper and board – compressive strength – short-span test.

[89] A. F. Johnson. Modelling Impact Damage in Composite Structural Elements. In C. Soutis and P.W.R. Beaumont, editors, *Multi-scale Modelling of Composite Material Systems: The Art of Predictive Damage Modelling*. Woodhead, 2005.

[90] A. F. Johnson and M. Holzapfel. Modelling soft body impact on composite structures. *Composite Structures*, 61(1-2):103–113, 2003.

[91] A. F. Johnson, S. Kilchert, H. Abu El-Hija, H. Kraft, and R. Jemmali. CELPACT D32-1: Low Velocity Impact Tests on Sandwich Panels. In *Cellular Structures for Impact Performance (CELPACT), Contract No.: FP6-031038*. Sixth Framework Programme FP6-2005-Aero-1, 2008.

[92] A. F. Johnson, S. Kilchert, P. Guidault, E. Baranger, S. Heimbs, and P. Middendorf. CELPACT D22-3: Multiscale Modelling Strategies for Sandwich Structures. In *Cellular Structures for Impact Performance (CELPACT), Contract No.: FP6-031038*. Sixth Framework Programme FP6-2005-Aero-1, 2009.

[93] A. F. Johnson, G.D. Sims, and F. Ajibade. Performance analysis of web-core composite sandwich panels. *Composites*, 21(4):319–324, 1990.

[94] A. F. Johnson and N. Toso-Pentecôte. Determination of Delamination Damage in Composites under Impact Loads. In S. Sridharan, editor, *Delamination Behaviour of Composites*. Woodhead, 2008.

[95] G. Jourdain. Delamination Studies on Composite Materials: C-Peek, C-977-UD and C-Geb-977. Internal report, Deutsches Zentrum für Luft- und Raumfahrt, 2008.

[96] D. Karagiozova and R. A. W. Mines. Impact of aircraft rubber tyre fragments on aluminium alloy plates: II–numerical simulation using LS-DYNA. *International Journal of Impact Engineering*, 34(4):647–667, 2007.

[97] R. Kehrle and K. Drechsler. Manufacturing of folded core structures for technical applications. In *SAMPE Europe 25th International Conference*, pages 508–513, Paris, France, 2004.

[98] C. Keindorf. *Tragverhalten und Ermüdungsfestigkeit von Sandwichtürmen von Windenergieanlagen*. PhD thesis, Gottfried Wilhelm Leibnitz Universität Hannover, 2009.

[99] S. Kilchert. Ermittlung der Harzaufnahme von Schaumkernen bei der Infiltration im VARI-Verfahren. Master's thesis, Universität Stuttgart, Institute of Aircraft Design, 2004.

[100] S. Kilchert, A. F. Johnson, A. Reiter, and R. Jemmali. CELPACT D32-2: Gas Gun Impact Tests on Sandwich Panels. In *Cellular Structures for Impact Performance (CELPACT), Contract No.: FP6-031038*. Sixth Framework Programme FP6-2005-Aero-1, 2008.

[101] S. Kilchert, A. F. Johnson, and H. Voggenreiter. FE modelling of phenolic resin impregnated aramid paper adopted in foldcore sandwich cores. In *The Ninth International Conference on Computational Structures Technology (CST)*, Athens, Greece, 2008.

[102] M. Kintscher and L. Kärger. Versagen von Faltwaben- und Honigwabenkernen unter kombinierter Druck-Schub-Belastung - Entwicklung von Materialmodellen und Versagenskriterien. Technical Report IB 131-2006/07, Deutsches Zentrum für Luft- und Raumfahrt, 2007.

[103] M. Kintscher, L. Kärger, A. Wetzel, and D. Hartung. Stiffness and failure behaviour of folded sandwich cores under combined transverse shear and compression. *Composites Part A: Applied Science and Manufacturing*, 38(5):1288–1295, 2007.

[104] Y. Klett, K. Drechsler, R. Kehrle, and M. Fach. Cutting Edge Cores: Multifunktionale Faltkernstrukturen. In *Landshuter Leichtbau-Colloquium*, Landshut, Germany, 2008.

[105] Y. Klett, K. Drechsler, M. Kolax, H. Wentzel, and R. Kehrle. Design of multifunctional folded core structures for aerospace applications. In *1st European Air and Space Conference (CEAS)*, Berlin, Germany, 2007.

[106] L. Kärger, J. Baaran, and J. Teßmer. Efficient simulation of low-velocity impacts on composite sandwich panels. *Computers and Structures*, 86:988–996, 2008.

[107] A. A. Kritsuk. Sandwich shear test revisited. *International Applied Mechanics*, 37(9):1229–1232, 2001.

[108] Y. W. Kwon, D. H. Allen, and R. Talreja. *Multiscale Modeling and Simulation of Composite Materials and Structures*. Springer, 2008.

[109] P. Ladevèze. Inelastic Strains and Damage. In *Damage Mechanics of Composite Materials*. Elsevier, 1994.

[110] P. Ladèveze and E. LeDantec. Damage modelling of the elementary ply for laminated composites. *Composites Science and Technology*, 43(3):257–267, 1992.

[111] A. J. Lamb. *Experimental Investigation and Numerical Modelling of Composite-Honeycomb Materials used in Formula 1 Crash Structures*. PhD thesis, Cranfield University, 2007.

[112] M. Leekitwattana, S. W. Boyd, and R. A. Shenoi. An alternative design of steel-concrete-steel sandwich beam. In *9th International Conference on Sandwich Structures (ICSS)*, Pasadena, California, USA, 2010.

[113] F. A. Lülf. Optimisation of folded core geometry by fe models for different load cases. Master's thesis, Universität Stuttgart, Institute of Statics and Dynamics of Aerospace Structures, 2008.

[114] A. G. Mamalis, D. E. Manolakos, G. A. Demosthenous, and M. B. Ioannidis. Analysis of failure mechanisms observed in axial collapse of thin-walled circular fibreglass composite tubes. *Thin-Walled Structures*, 24(4):335–352, 1996.

[115] V. Manet. The use of ANSYS to calculate the behaviour of sandwich structures. *Composites Science and Technology*, 58(12):1899 – 1905, 1998.

[116] R. W. Mann, G. A. Baum, and C. C. Habeger. Determination of all nine orthotropic elastic constants for machine-made paper. *Tappi*, 63(2):163–166, 1980.

[117] P. Mastrogiuseppe. The effects of core material and thickness on the performance and behaviour of a ski. Master's thesis, McGill University, Department of Civil Engineering and applied Mechanics, 2007.

[118] M. Meo, R. Vignjevic, and G. Marengo. The response of honeycomb sandwich panels under low-velocity impact loading. *International Journal of Mechanical Sciences*, 47:1301–1325, 2005.

[119] R. D. Mindlin. Influence of rotatory inertia and shear on flexural motions of isotropic, elastic plates. *Journal of Applied Mechanics*, 18:31–38, 1951.

[120] L. L. Mishnaevsky and S. Schmauder. Continuum mesomechanical finite element modeling in materials development: A state-of-the-art review, 2001.

[121] M. Q. Nguyen, S. S. Jacombs, D. Hachenberg R. S. Thomson, and M. L. Scott. Simulation of impact on sandwich structures. *Composite Structures*, 67:217–227, 2005.

[122] A. K. Noor and W. S. Burton. Assessment of computational models for multilayered composite shells. *Applied Mechanics Review*, 43:67–97, 1990.

[123] NPCS Board of Consultants & Engineers. *Phenolic Resins Technology Handbook*. ISBN 978-81-905685-0-0. Niir Project Consultancy Services, 2000.

[124] R. W. Ogden. *Non-Linear Elastic Deformations*. Dover Publications, 1997.

[125] R. Olsson. Closed form prediction of peak load and delamination onset under small mass impact. *Composite Structures*, 59(3):341–349, 2003.

[126] S.-D. Pan, L.-Z. Wu, and Y.-G. Sun. Transverse shear modulus and strength of honeycomb cores. *Composite Structures*, 84(4):369–374, 2008.

[127] S.-D. Pan, L.-Z. Wu, Y.-G. Sun, Z.-G. Zhou, and J.-L. Qu. Longitudinal shear strength and failure process of honeycomb cores. *Composite Structures*, 72(1):42–46, 2006.

[128] J.H. Park, S.K. Ha, K.W. Kang, C.W. Kim, and H.S. Kim. Impact damage resistance of sandwich structure subjected to low velocity impact. *Journal of Materials Processing Technology*, 201(1-3):425–430, 2008.

[129] R. Perkins. Paper: Structure. In J. K. H. Buschow, editor, *Encyclopedia of Materials: Science and Technology*, pages 6725–6732. Pergamon, 2001.

[130] F. Pled, W. Yan, and C. Wen. Crushing modes of aluminium tubes under axial compression. In *5th Australasian congress on applied mechanics (ACAM)*, Brisbane, Australia, 2007.

[131] M. S. Qatu, R. W. Sullivan, and W. Wang. Recent research advances on the dynamic analysis of composite shells: 2000–2009. *Composite Structures*, 93:14–31, 2010.

[132] J. N. Reddy. An evaluation of equivalent-single-layer and layerwise theories of composite laminates. *Composite Structures*, 25:21–35, 1993.

[133] W. Richard and J. Perkins. Models for Describing the Elastic, Viscoelastic and Inelastic Mechanical Behaviour of Paper and Board. In *Handbook of Physical and Mechanical Testing of Paper and Paperboard*. M. Dekker, 1983.

[134] M. Rigdahl and H. Hollmark. Network Mechanics. In J. A. Bristow and P. Kolseth, editors, *Paper - Structures and Properties*. M. Dekker, 1986.

[135] J. Schön. Coefficient of friction for aluminum in contact with a carbon fiber epoxy composite. *Tribology International*, 37(5):395–404, 2004.

[136] S. J. Scotti, C. Clay, and M. Rezin. Structures and materials technologies for extreme environments applied to reusable launch vehicle. In *AIAA/ICAS International Symposium and Exposition*, Dayton, Ohio, USA, 2003.

[137] H. F. Seibert. Applications for PMI foams in aerospace sandwich structures. *Reinforced Plastics*, 50(1):44–48, 2006.

[138] K. B. Shin, J. Y. Lee, and S. H. Cho. An experimental study of low-velocity impact responses of sandwich panels for Korean low floor bus. *Composite Structures*, 84(3):228–240, 2008.

[139] J. Simon, A.F. Johnson, and H. Weissinger. HICAS D41-1a: Impact Tests on Composite Plates and Shells. Part I: Drop Tower Tests. In *High Velocity Impact of Composite Aircraft Structures (HICAS), Contract No.: BRPR-CT97-0543*. BRITE-EURAM III project, 1999.

[140] I. Smojver and D. Ivancevic. Numerical simulation of bird strike damage prediction in airplane flap structure. *Composite Structures*, 92(9):2016–2026, 2010.

[141] P. Soden. Indentation of composite sandwich beams. *The Journal of Strain Analysis for Engineering Design*, 31(5):353–360, 1996.

[142] F.-H. Su, Z-Z. Zhang, F. Guo, K. Wang, and W.-M. Liu. Study on the friction and wear properties of the composites made of surface modified Nomex fabrics. *Materials Science and Engineering: A*, 416(1-2):126–133, 2006.

[143] J. Säynäjäkangas and T. Taulavuori. A review in design and manufacturing of stainless steel sandwich panels. In *Stainless Steel World*, Houston, Texas, USA, 2004.

[144] R. Talreja. *Damage Mechanics of Composite Materials*. Composite materials series. Elsevier, 1994.

[145] V. B. C. Tan, X. S. Zeng, and V. P. W. Shim. Characterization and constitutive modeling of aramid fibres at high strain rates. *International Journal of Impact Engineering*, 35:1303–1313, 2008.

[146] O. T. Thomsen. Sandwich materials for wind turbine blades – Present and future. *Journal of Sandwich Structures and Materials*, 11(1):7–26, 2009.

[147] O. T. Thomsen and E. Bozhevolnayaand A. Lyckegaard, editors. *Sandwich structures 7: Advancing with Sandwich Structures and Materials*, Proceedings of the 7th International Conference on Sandwich Structures, Aalborg, Denmark, August 29-31 2005.

[148] T. Uesaka. Specimen Design for Mechanical Testing of Paper and Paperboard. In *Handbook of Physical and Mechanical Testing of Paper and Paperboard*. M. Dekker, 1983.

[149] Y. Wang and Y. Xia. The effects of strain rate on the mechanical behaviour of Kevlar fibre bundles: An experimental and theoretical study. *Composites Part A*, 29A:1411–1415, 1998.

[150] M. W. Wardle. Aramid Fiber Reinforced Plastics - Properties. In A. Kelly, C. Zweben, R. Talreja, and J.-A. Manson, editors, *Comprehensive Composite Materials: Polymer Matrix Composites*, volume 2, pages 199–229. Pergamon, 2003.

[151] T. Wierzbicki. Crushing analysis of metal honeycombs. *International Journal of Impact Engineering*, 1(2):157 – 174, 1983.

[152] E. L. Wilson. *Three-Dimensional Static and Dynamic Analysis of Structures*. Computers and Structures, Inc., 2002.

[153] D. Winterberger. Analyse multi-échelles d'une âme de sandwich en papier plié. Master's thesis, LMT-Cachan, 2008.

[154] M.R. Wisnom. Modelling discrete failures in composites with interface elements. *Composites Part A: Applied Science and Manufacturing*, 41(7):795–805, July 2010.

[155] P. Wriggers. *Nonlinear Finite Element Methods*. Springer, 2008.

[156] Z. Xu and D. Li. Physical and mechanical properties of the packaging material of sandwich construction with wood facings and a paper honeycomb core. e-Journal, DOI: CNKI:SUN:BZGC.0.2007-01-011, 2007.

[157] H. H. Yang. Aramid Fibers. In A. Kelly, C. Zweben, R. Talreja, and J.-A. Manson, editors, *Comprehensive Composite Materials: Fiber Reinforcements and General Theory of Composites*, volume 2. Pergamon, 2003.

[158] I. M. Zakirov and K. A. Alexeev. New folded structures for sandwich panels. In *SAMPE Europe 27th International Technical Conference*, Paris, France, 2006.

[159] D. Zenkert. *Handbook of Sandwich Construction*. Engineering Materials Advisory Services, 2008.

[160] J. Zhang and M.F. Ashby. The out-of-plane properties of honeycombs. *International Journal of Mechanical Sciences*, 34(6):475–489, 1992.

[161] X. Zhang, X. Pei, and Q. Wang. Friction and wear properties of combined surface modified carbon fabric reinforced phenolic composites. *European Polymer Journal*, 44(8):2551–2557, 2008.

[162] Y.X. Zhang and C.H. Yang. Recent developments in finite element analysis for laminated composite plates. *Composite Structures*, 88(1):147 – 157, 2009.

[163] D.W. Zhou and W.J. Stronge. Low velocity impact denting of HSSA lightweight sandwich panel. *International Journal of Mechanical Sciences*, 48(10):1031 – 1045, 2006.